

NUMERICAL SIMULATION OF  
MEAN CROSS-SHORE CURRENTS:  
A STREAM FUNCTION APPROACH

by

ALBERT E. BROWDER

A DISSERTATION PRESENTED TO THE GRADUATE SCHOOL  
OF THE UNIVERSITY OF FLORIDA IN PARTIAL FULFILLMENT  
OF THE REQUIREMENTS FOR THE DEGREE OF  
DOCTOR OF PHILOSOPHY

UNIVERSITY OF FLORIDA

2000

## ACKNOWLEDGMENTS

I wish to express my sincere appreciation and utmost respect to the chairman of my graduate committee, Robert G. Dean, for his guidance, trust, and friendship. Working for someone who grants you the latitude to pursue your own interests and always teaches you something at each stage of the process has been the most rewarding aspect of my dissertation work. For providing me the experience of teaching and always being there to answer my “real quick” questions, I wish to thank committee member Robert J. Thieke. To the other members of my graduate committee, who have provided me great insight and guidance in my education and the completion of this document, I express my gratitude.

I am fortunate to have had many dedicated classmates and friends in this endeavor, almost too many to list. Thanks go to Mark and Eric, qualifier coaches extraordinaire, for their support and friendship. To Becky, I express my thanks for keeping me on track and being my friend. Jamie, Justin, Kevin, Bill, Matt, Sean, Dave, Jon, Heather, Beth, and Chris deserve thanks for all the encouragement, and distractions necessary to complete this task. For teaching me the basics, I thank Jack Kinder. Thanks are in order for all at Olsen Associates for their understanding and encouragement. If I have left anyone out, it is by no means intentional, just a sign of how fortunate I am to have so many good friends.

I am ever grateful to my parents, Susan and Larry, for their never ending support. Finally, none of this would have been possible without the love and undying support of my wife, Keeley. This is as much yours as it is mine.

## TABLE OF CONTENTS

	<u>page</u>
ACKNOWLEDGMENTS .....	ii
LIST OF TABLES .....	vi
LIST OF FIGURES .....	vii
KEY TO SYMBOLS .....	xii
ABSTRACT .....	xv
CHAPTERS	
1 INTRODUCTION .....	1
1.1 Objectives and Rationale .....	3
1.2 Present Approach to Return Flow Modeling .....	4
2 LITERATURE REVIEW .....	8
2.1 Motivating Literature .....	9
2.2 Return Flow Models .....	13
2.3 Turbulent Eddy Viscosity .....	18
2.4 Return Flow Measurements .....	25
3 DERIVATION OF GOVERNING EQUATION AND NUMERICAL MODEL DEVELOPMENT .....	29
3.1 Derivation of Governing Equation .....	30
3.2 Development of One-Dimensional Model .....	37
3.2.1 Boundary Conditions for One-Dimensional Model .....	40
3.2.2 Solution Scheme for One-Dimensional Model .....	41
3.3 Development of Two-Dimensional Return Flow Model .....	43
3.3.1 Transformation of the Partial Differential Equation .....	43
3.3.2 Discretization of the Two-Dimensional PDE .....	45
3.3.3 Boundary Conditions for Two-Dimensional Model .....	48
3.3.4 Solution Scheme for Two-Dimensional Model .....	49

4	BOUNDARY CONDITIONS AND TRANSITION REGION TREATMENT .....	52
	4.1 Wave Height Transformation .....	53
	4.2 Determination of Return Flow Rate .....	58
	4.3 Specification of the Surface Shear Stress Due to Waves .....	62
	4.4 Specification of Bottom and Sidewall Tangential Boundary Conditions ..	64
	4.5 Matching Conditions Across the Transition Region .....	68
5	VALIDATION OF NUMERICAL MODEL .....	75
	5.1 One-Dimensional Analytic Solutions .....	76
	5.1.1 Steady-State Simulations .....	76
	5.1.2 Variable Eddy Viscosity Simulations - Steady State .....	78
	5.1.3 Time-Dependent Simulation .....	81
	5.2 Two-Dimensional Model Validation .....	87
	5.2.1 Comparison to One-Dimensional Results .....	87
	5.2.2 Comparison to Analytic Series Solution .....	88
6	COMPARISON OF NUMERICAL MODEL TO EXPERIMENTAL DATA .....	93
	6.1 Introduction of Model Output and RMS Errors .....	94
	6.2 Simulation of Cox and Kobayashi (1997) Experiments .....	104
	6.3 Simulation of Ting and Kirby (1994) Experiments .....	114
	6.4 Simulation of Nadaoka and Kondoh (1982) Experiments .....	124
	6.5 Simulation of Okayasu and Katayama (1992) Experiments .....	130
	6.6 Simulation of Roelvink and Reniers (1995) Experiments .....	139
	6.7 Simulation of Smith et al. (1992) Experiments .....	147
	6.8 Comments .....	154
7	IMPLICATIONS FOR CROSS-SHORE SEDIMENT TRANSPORT AND FUTURE STUDY .....	156
	7.1 Variation in Predicted Bottom Shear Stress and Shear Stress Profiles ..	158
	7.2 Transition Region Treatment .....	163
	7.3 Onshore Bottom Stresses and Velocities Seaward of the Break Point ..	169
	7.4 Selection of Wave Theory and Phase Speed Definition .....	173
	7.5 Selection of Vertical Distribution of Eddy Viscosity .....	176
8	SUMMARY, CONCLUSIONS, AND RECOMMENDATIONS FOR FUTURE WORK .....	182
	8.1 Summary .....	182
	8.2 Conclusions .....	184
	8.3 Recommendations for Future Work .....	187

## APPENDICES

A	NUMERICAL MODEL DEVELOPMENT .....	189
A.1	Development of One-Dimensional Model .....	190
A.1.1	Boundary Conditions for One-Dimensional Model .....	192
A.1.2	Solution Scheme for One-Dimensional Model .....	195
A.2	Development of Two-Dimensional Return Flow Model .....	196
A.2.1	Transformation of the Partial Differential Equation .....	196
A.2.2	Discretization of the Two-Dimensional PDE .....	201
A.2.3	Boundary Conditions for Two-Dimensional Model .....	207
A.2.4	Solution Scheme for Two-Dimensional Model .....	213
B	FORTRAN CODE LISTING RF_PSI.F90 .....	215
	REFERENCES .....	247
	BIOGRAPHICAL SKETCH .....	251

## LIST OF TABLES

<u>Table</u>		<u>page</u>
6.1	Parameters to be Investigated/Adjusted in Numerical Model for Comparison to Experimental Data. . . . .	94
6.2	Errors in Example Simulation Shown In Figures 6.1 and 6.2 for Cox and Kobayashi (1997) Laboratory Experiment. . . . .	99
6.3	Conditions for Return Flow Measurements Simulated by Numerical Model	100
7.1	Comparison of normalized RMS errors calculated from applying the eddy viscosity distributions in Figure 7.12 for the experiment of Cox and Kobayashi (1997). . . . .	181

## LIST OF FIGURES

<u>Figure</u>		<u>page</u>
1.1 Rendering of wave-induced return flow in the surf zone. . . . .	2	
1.2 Definition sketch of return flow problem. . . . .	5	
2.1 Illustration of the effect of the quadratic mixing length expression employed by Reid (1957). . . . .	22	
2.2 Comparison of mean horizontal velocity profiles as reported by Cox and Kobayashi (1997) and Ting and Kirby (1994). . . . .	28	
3.1 Definition sketch for model development. . . . .	31	
3.2 Definition sketch for one-dimensional model. . . . .	39	
3.3 Example output from one-dimensional return flow model. . . . .	42	
3.4 Definition sketch of coordinate transformation between the physical, $x$ - $z$ , domain and the computational, $\xi$ - $\eta$ , domain. . . . .	44	
3.5 Solution cells for the fourth-order finite difference equation in the $x$ - $z$ domain and the transformed $\xi$ - $\eta$ domain. . . . .	46	
3.6 Flowchart for two-dimensional numerical model. . . . .	51	
4.1 Stream function wave theory shoaling table for normally incident waves. . .	54	
4.2 Demonstration of wave transformation model for two laboratory studies. . .	56	
4.3 Demonstration of the treatment of the transition region in the simulation of the data set of Ting & Kirby (1994). . . . .	71	
5.1 Definition sketch of one-dimensional problem. . . . .	77	
5.2 Comparison of 1-D numerical model to analytic solution for steady-state conditions. . . . .	78	

5.3	Comparison of 1-D numerical model results to those of Reid (1957) for the case of $Q = 0$ . . . . .	80
5.4	Comparison of numerical model results to superimposed analytic solutions to the diffusion equation. . . . .	84
5.5	Time history of the forcing term, A, in Eq. (5.10). . . . .	85
5.6	Investigation of time step dependence on the one-dimensional semi - implicit numerical model. . . . .	86
5.7	Comparison of 2-D numerical model to 1-D analytical results of Eq. (5.4) computed at each vertical section. . . . .	89
5.8	Comparison of numerical model results to Fourier Series solution, Eq. (5.17). . . . .	92
6.1	Example contour and velocity vector plot of laboratory experiments by Cox and Kobayashi (1997). . . . .	95
6.2	Example of cross shore variation in wave height, radiation stress, volumetric transport, and vertical profiles of horizontal velocity for the experiments of Cox and Kobayashi (1997). . . . .	96
6.3	Comparison of cross shore variation in wave height, radiation stress, volumetric transport, and vertical profiles of horizontal velocity for the experiments of Ting and Kirby (1994) ( $\epsilon = 0.001 \text{ m}^2/\text{s}$ ). . . . .	102
6.4	Comparison of present radiation stress transition region patch to the wave surface roller model of Dally and Brown (1995) for the data set of Ting and Kirby (1994) ( $\epsilon = 0.001 \text{ m}^2/\text{s}$ ). . . . .	103
6.5	Comparison of simulations of the data set of Cox and Kobayashi (1997). . . . .	105
6.6	Comparison of predicted radiation stress and volumetric transport for the experiments of Cox and Kobayashi (1997). . . . .	107
6.7	Comparison of normalized RMS errors, $\beta$ , for the experiment of Cox and Kobayashi (1997) employing spatially variable eddy viscosity fields. . . . .	110
6.8	Comparison of vertical profiles of horizontal velocity at station #4 of the Cox and Kobayashi (1997) data set. . . . .	111
6.9	Comparison of vertical profiles of horizontal velocity at station #4 of the Cox and Kobayashi (1997) data set for a zero bottom shear stress boundary condition. . . . .	112

6.10	Predicted flow field for the data set of Cox and Kobayashi (1997). . . . .	113
6.11	Velocity profiles corresponding to the flow field in Figure 6.10 predicted for the data set of Cox and Kobayashi (1997). . . . .	114
6.12	Comparison of simulations for the data set of Ting and Kirby (1994). . . . .	115
6.13	Comparison of predicted radiation stress and volumetric transport for the experiments of Ting and Kirby (1994). . . . .	117
6.14	Comparison of normalized root-mean-square errors, $\beta$ , for the experiments of Ting and Kirby (1994) employing spatially variable eddy viscosity fields. . . . .	119
6.15	Comparison of vertical profiles of horizontal velocity at Station #2 (offshore of the break point) of the Ting and Kirby (1994) data set for a no-slip bottom boundary condition. . . . .	120
6.16	Comparison of velocity profiles at Station #2 (offshore of break point) of the Ting and Kirby (1994) data set. . . . .	121
6.17	Predicted flow field for the data set of Ting and Kirby (1994). . . . .	122
6.18	Velocity profiles corresponding to the flow field in Figure 6.17 predicted for the data set of Ting and Kirby (1994). . . . .	122
6.19	Comparison of simulations of the data of Nadaoka and Kondoh (1982, Case 1). . . . .	125
6.20	Comparison of predicted radiation stress and volumetric transport for the experiments of Nadaoka and Kondoh (1982, Case 1). . . . .	126
6.21	Comparison of normalized root-mean-square errors, $\beta$ , for the experiments of Nadaoka and Kondoh (1982) employing spatially variable eddy viscosity fields. . . . .	128
6.22	Predicted flow fields for the experiments of Nadaoka and Kondoh (1982). . . . .	129
6.23	Velocity profiles corresponding to the flow field in the lower plot of Figure 6.22 predicted for the data of Nadaoka and Kondoh (1982). . . . .	130
6.24	Comparison of predicted RMS wave height, radiation stress, volumetric transport for the random wave experiments of Okayasu and Katayama (1992). . . . .	132

6.25	Comparison of simulations of the data set of Okayasu and Katayama (1992) . . . . .	133
6.26	Comparison of normalized root-mean-square errors, $\beta$ , obtained for the experiments of Okayasu and Katayama (1992) by applying spatially variable eddy viscosity fields. . . . .	135
6.27	Predicted flow field for the experiments of Okayasu and Katayama (1992). . . . .	136
6.28	Comparison of simulations applying random waves averaged over time and applying a monochromatic wave field of RMS height. . . . .	137
6.29	Comparison of simulations of the data set of Roelvink and Reniers (1995) from the Delta flume experiments in Delft, The Netherlands. . . . .	140
6.30	Demonstration of the effect of the choice of surface eddy viscosity. . . . .	141
6.31	Comparison of predicted radiation stress and volumetric transport for the experiments of Roelvink and Reniers (1995). . . . .	143
6.32	Comparison of normalized root-mean-square errors, $\beta$ , obtained for the experiments of Roelvink and Reniers (1995) by applying spatially variable eddy viscosity fields. . . . .	145
6.33	Flow field predicted for the experiments of Roelvink and Reniers (1995). . . . .	146
6.34	Comparison of simulations applying time-averaged random waves versus monochromatic waves of RMS height. . . . .	146
6.35	Comparison of simulations of the data set of Smith et al. (1992). . . . .	148
6.36	Comparison of predicted radiation stress and volumetric transport for the experiments of Smith et al. (1992). . . . .	149
6.37	Comparison of normalized root-mean-square errors, $\beta$ , obtained for the experiments of Smith et al. (1992) by applying spatially variable eddy viscosity fields. . . . .	152
6.38	Comparison of simulations applying time-averaged random waves versus monochromatic waves of RMS height. . . . .	153
7.1	Cross-shore variation in mean bottom shear stress for the experiment of Cox and Kobayashi (1997). . . . .	159

7.2	Cross-shore variation in mean bottom shear stress for the experiment of Cox and Kobayashi (1997). . . . .	161
7.3	Vertical profiles of velocity, shear stress, and eddy viscosity at two measuring stations of the experiment of Cox and Kobayashi (1997). . . . .	162
7.4	Predicted flow field for the experiment of Nadaoka and Kondoh (1982, Case 1). . . . .	165
7.5	Comparison of predicted and measured profiles of vertical velocity for the experiment of Nadaoka and Kondoh (1982, Case 1). . . . .	166
7.6	Predicted flow field for the data set of Cox and Kobayashi (1997). . . . .	167
7.7	Comparison of predicted and measured vertical mean velocities from the experiments of Cox et al. (1995)/Cox and Kobayashi (1997). . . . .	168
7.8	Schematic of the effect of increasing the magnitude of the offshore directed shear stress applied in the shoaling region. . . . .	171
7.9	Predicted flow field in the offshore region for the experiments of Roelvink and Reniers (1995). . . . .	172
7.10	Contours of nondimensional wave induced momentum flux (radiation stress) determined from the 40 cases tabulated for Stream Function Wave Theory by Dean (1974). . . . .	174
7.11	Comparison of predicted velocity profiles applying offshore and onshore directed surface stresses. . . . .	177
7.12	Comparison of non-dimensionalized vertical distributions of eddy viscosity. 179	
7.13	Comparison of predicted velocity profiles applying the eddy viscosity distributions plotted in Figure 7.12. . . . .	181

## KEY TO SYMBOLS

*A#* Steady state term coefficients describing the transformation of coordinates between the  $x$ - $z$  domain and the  $\xi$ - $\eta$  domain (# 1 through 14, units vary).

*A<sub>r</sub>* Cross-sectional area of wave surface roller ( $m^2$ ).

*B#* Time dependent term coefficients describing the transformation of coordinates between the  $x$ - $z$  domain and the  $\xi$ - $\eta$  domain (# 1 through 5, units vary).

*C* Wave celerity (m/s).

*C<sub>j</sub>* Solution coefficients in Fourier Series analytic solution ( $s^{-1}$ ).

*CL#* Steady state term coefficients arising from discretization process on the solution column of cell (# 1 through 5, no units).

*CR#* Steady state term coefficients arising from discretization process off the solution column of cell (# 1 through 16, no units).

*DL#* Time dependent term coefficients arising from discretization process on the solution column of cell (# 1 through 3, no units).

*DR#* Time dependent term coefficients arising from discretization process off the solution column of cell (# 1 through 6, no units).

*D* Total water depth (in Reid, 1957, m).

*E* Total wave energy per unit surface area ( $N/m^2$ ).

*E<sub>RMS</sub>* Root-mean-square error of each predicted velocity profile (m/s).

*g* Acceleration due to gravity ( $m/s^2$ )

*H* Wave height (m).

*H<sub>s</sub>* Significant wave height (m).

*H<sub>o</sub>* Deepwater significant wave height (m).

$h$	Still water depth (m).
$h + \bar{\eta}$	Total water depth (still water depth plus setup/setdown, m)
$i, j$	Horizontal and vertical cell coordinates, respectively, in numerical solution.
$k$	Wave number ( $2\pi/\text{wavelength}$ ).
$k_o$	Von Karman's Constant ( $= 0.4$ ).
$K$	Dimensionless wave decay coefficient.
$L$	Wavelength (m).
$L$	Mixing length (turbulence length scale, m).
$L_o$	Deepwater wavelength (m).
$m$	Ratio of bottom to surface shear stress.
$n$	Time step counter in numerical solution.
$Q$	Wave induced volumetric transport ( $\text{m}^3/\text{s}/\text{m}$ ).
$S_{xx}$	Radiation stress, onshore flux of wave-induced onshore momentum ( $\text{N}\cdot\text{m}/\text{m}^2$ ).
$t$	Time (s).
$T$	Wave period (s).
$U, W$	Horizontal, vertical components of mean velocity (m/s).
$U_b$	Tangential bottom velocity (m/s).
$U_\infty$	Streaming velocity (tangential velocity at upper edge of bottom boundary layer, m/s).
$\tilde{u}, \tilde{w}$	Horizontal, vertical components of wave induced, orbital, velocity (m/s).
$u', w'$	Horizontal, vertical components of turbulence induced velocity (m/s).
$x$	Horizontal coordinate in physical domain (m).
$z$	Vertical coordinate in physical domain (m).
$\alpha$	Wave number in Fourier Series analytic solution ( $\text{m}^{-1}$ ).

$\beta$	Non-dimensional root-mean-square error in each velocity profile.
$\Gamma$	Ratio of stable wave height to local water depth.
$\Delta t$	Time step in numerical solution (s).
$\Delta x$	Horizontal spatial step in physical domain (m).
$\Delta z$	Vertical spatial step in physical domain (m).
$\Delta \eta$	Vertical spatial step in numerical solution (no units).
$\Delta \xi$	Horizontal spatial step in numerical solution (m).
$\epsilon$	Turbulent eddy viscosity ( $\text{m}^2/\text{s}$ ).
$\bar{\eta}$	Setup/setdown of mean water surface from still water surface elevation (m).
$\eta$	Vertical coordinate in transformed computational domain ( $= z/(h+\bar{\eta})$ , no units).
$\theta$	Degree of implicitness in numerical solution.
$\kappa$	Ratio of wave height to local water depth at breaking.
$\nu$	Molecular kinematic viscosity ( $\text{m}^2/\text{s}$ ).
$\xi$	Horizontal coordinate in transformed computational domain (m).
$\rho$	Density of water (freshwater or saltwater, $\text{kg}/\text{m}^3$ ).
$\sigma$	Wave frequency, ( $2\pi/T$ , $\text{s}^{-1}$ ).
$\tau_{ab}$	Viscous shear stress in the $a$ -direction on the $b$ -plane.
$\tau'_{ab}$	Turbulent shear stress in the $a$ -direction on the $b$ -plane
$\tau_b$	Bottom shear stress ( $\text{N}/\text{m}^2$ ).
$\tau_\eta$	Shear stress at instantaneous free surface ( $\text{N}/\text{m}^2$ ).
$\tau_s$	Shear stress at mean water surface ( $\text{N}/\text{m}^2$ ).
$\psi$	Stream function ( $\text{s}^{-1}$ ).
$\nabla$	Del operator (total derivative operator).

Abstract of Dissertation Presented to the Graduate School  
of the University of Florida in Partial Fulfillment of the  
Requirements for the Degree of Doctor of Philosophy

NUMERICAL SIMULATION OF  
MEAN CROSS-SHORE CURRENTS:  
A STREAM FUNCTION APPROACH

By

Albert E. Browder

August 2000

Chairman: Robert G. Dean  
Major Department: Civil & Coastal Engineering

A numerical model applying a stream function formulation is developed and tested to simulate the two-dimensional, wave-induced return flow in the nearshore region, commonly referred to as the undertow. The model is developed using the stream function,  $\psi$ , to represent the wave-induced return flow, and tests are conducted of the effects of various wave theories and boundary conditions on the flow. Solution of  $\psi$  produces the mean velocity in the horizontal and vertical directions, providing a description of the complete flow field in the two-dimensional vertical plane perpendicular to the shoreline.

The governing equation, a fourth-order partial differential equation in  $\psi$ , is not specific to wave-induced flows; therefore, the details of the wave forcing are introduced entirely through the boundary conditions. In this way the model provides a convenient platform to evaluate different combinations of applied boundary conditions. The model includes the ability to study spatial variations in the turbulent eddy viscosity. The present

model also accommodates monochromatic or random wave fields and arbitrary bottom profiles, allowing the modeling of flows over bar-trough beach profiles or any other irregular profile geometry.

Comparison to measurements of wave-induced return flows demonstrates that the model is able to predict the vertical structure and magnitude of the return flow to within 25% to 30% (typical) for most applications. If the return flow rate is properly predicted (or fit), the model can predict the vertical structure of the horizontal velocity to within 10% (typical). Simulation of six laboratory and field experiments demonstrates the capability of the model and highlights the challenges of return flow modeling. The simulations indicate that the most important parameter in return flow modeling is the proper prediction of the wave-induced volumetric transport. Further improvement of the predictive capability of the model inside the surf zone stems from the application of a vertically-varying eddy viscosity field based on the turbulence generated by breaking waves. Comparison of the vertical structure of the return flow seaward and landward of the break point illustrates differences in the appropriate boundary conditions and eddy viscosity distributions that should be applied in return flow modeling.

## CHAPTER 1

### INTRODUCTION

Characterizing fluid flow in the surf zone presents the substantial challenge of identifying many distinctly different processes and attempting to quantify the effects and interactions of each. While the flow field in the nearshore region is at least visually dominated by the passage and breaking of waves on a time scale of seconds to minutes, the mean flows created by these incoming waves also play an important role in the nearshore. Additionally, currents introduced by other phenomena, such as tides or winds, may contribute to the flow field in any nearshore region. On a shorter temporal scale, the effects of turbulence must also be considered. The combination of these factors presents a daunting task to the coastal engineer charged with describing or modeling these flows in order to design coastal structures or predict changes to the nearshore morphology due to waves.

This study focuses on one aspect of the flow field in the surf zone, that being the mean flow in the cross-shore, two-dimensional vertical plane (2-DV), as rendered in Figure 1.1. The desire to understand and accurately predict the mean flow patterns in the nearshore region stems primarily from the interest in predicting changes in the beach profile induced by waves. The mean wave-induced cross-shore and longshore currents act to transport sediment not only by placing stress directly on the seabed, but also by transporting the sediment mobilized and suspended by the passage of other currents, individual waves, or groups of waves (or all three and more in some cases). In the case of

the mean cross-shore flow, mobilization and/or transport of sediment by the mean wave-induced current obviously plays a role in shaping the cross-shore profile and may play a strong role in the formation of longshore bars in the profile.

The mean cross-shore current is frequently referred to as the “undertow” but is more accurately labeled the return flow and shall be discussed as such in this study. The term undertow has been used frequently in the media in conjunction with the occurrence of rip currents, hence the actual definition of the undertow is somewhat vague while the return flow and rip currents are two distinct entities. The return flow always exists in the surf zone, whereas rip currents appear under various conditions but are not always present.

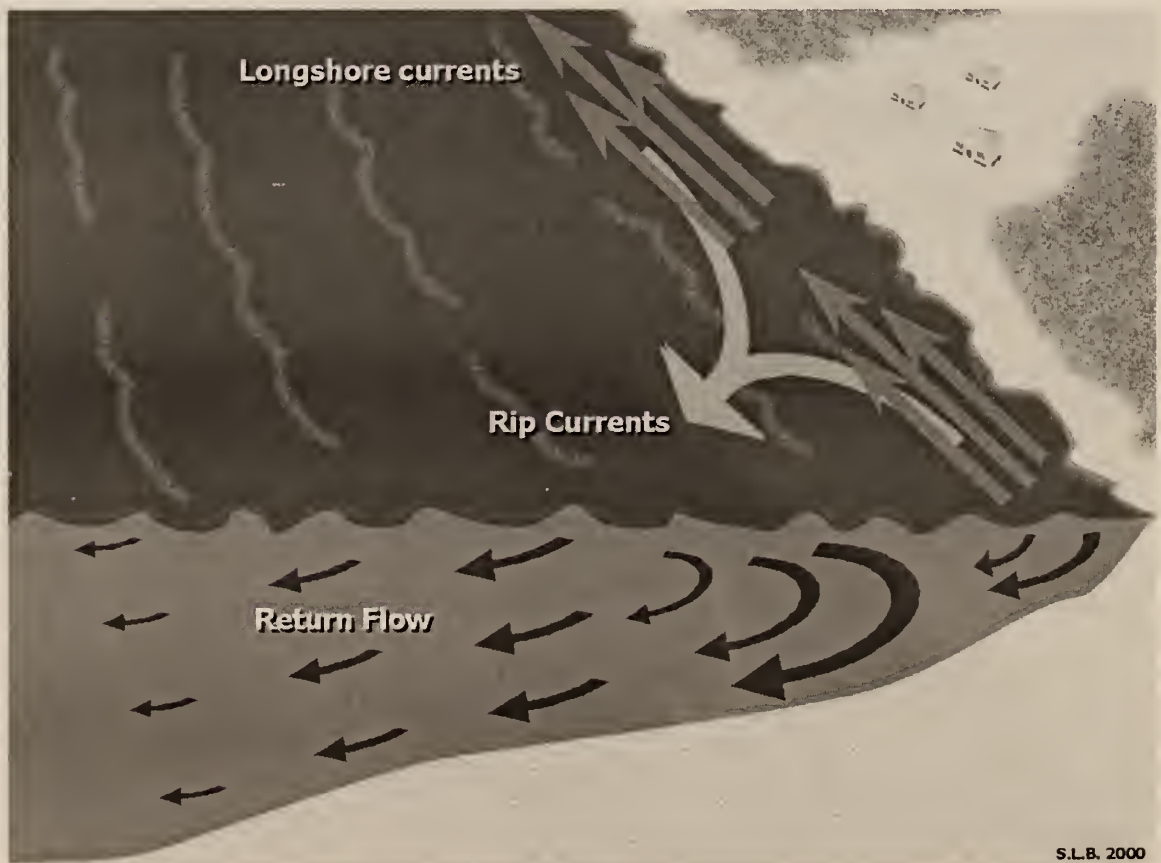


Figure 1.1 Rendering of wave-induced return flow in the surf zone. The return flow is the two-dimensional flow in the vertical plane perpendicular to the shoreline. The relationship of the return flow to longshore currents and rip currents is illustrated.

### 1.1 Objectives and Rationale

The objective of this study is to develop a numerical model of the mean flows in the nearshore region via a stream function formulation and to validate the approach. The driving interest in the development of a stream function return flow model is the desire to investigate various individual aspects of the mean flow. These aspects include the effects of wave transformation, the application of various combinations of boundary conditions, and the effect of spatially variable turbulent eddy viscosity,  $\epsilon$ , in the nearshore region.

In addition, it is of interest to investigate the differences between one-dimensional and two-dimensional formulations of the return flow profile, the role of various formulations for mass transport and shear stress at the water surface, and the possible role of the equilibrium of the moments of the wave induced forces across the beach profile. Dyhr-Nielsen and Sørensen (1970) first hypothesized that the balance of moments at a given vertical section may indeed play a role in the formation of longshore bars. While not much attention has been paid to this possibility, the present model provides a convenient means to demonstrate the idea and its possible alteration of the return flow profile, primarily through the simple application of additional boundary conditions in the model.

Dally (1980) presented an analytic formulation using the stream function to model the vertical variation of the horizontal momentum of fluid dominated by uniform eddy viscosity. The governing equation Dally used is the biharmonic equation, which is also used to describe creeping flows dominated by molecular viscosity. Dally presented a series solution for the horizontal momentum in a channel subjected to a surface stress. The passage of the breaking (or shoaling) wave provided the surface shear stress applied at the mean water surface; flow conservation was achieved by specifying the values of the stream function at the boundaries. The fourth condition specified the bottom velocity ( $= 0$ ).

Dally reported that the resulting flow field included only weak flows away from the point of application of the surface shear stress. The model presented by Dally was developed for a flat bottom and was not coupled horizontally to shear stresses in adjacent cells. The use of the stream function in a fourth-order PDE, however, prompted the interest in creating a two-dimensional model that would accommodate an arbitrary beach profile and would attempt to horizontally couple the flow.

### 1.2 Present Approach to Return Flow Modeling

Figure 1.2 illustrates the basic problem formulation. Longuet-Higgins and Stewart (1962) derive the balance of wave-induced radiation stress and the subsequent uniform pressure gradient caused by the water surface slope (set-up or set-down). Many researchers have discussed that these two forces, while balanced in a depth-averaged sense, are not balanced at every elevation throughout the water column. The gradient in water surface slope acts uniformly throughout the water column, while the radiation stress is greater at the surface than the seabed. This imbalance drives an offshore flow along the lower portions of the water column. This flow is termed the return flow.

Using the scalar stream function,  $\psi$ , in a 2-D return flow model is appealing for a number of reasons. Solving for  $\psi$  produces the velocity components *in both directions*, whereas many models solve only for the horizontal velocity and do not address the vertical velocity. This allows for the solution of the entire 2-DV velocity field across the profile, providing a complete description of the predicted mean flow patterns in the surf zone. Use of the stream function produces one scalar variable,  $\psi$ , to be solved in one equation (the cross-differentiated, time averaged momentum equation). Computationally, the solution for two variables (each velocity component) adds an additional complexity to the problem.

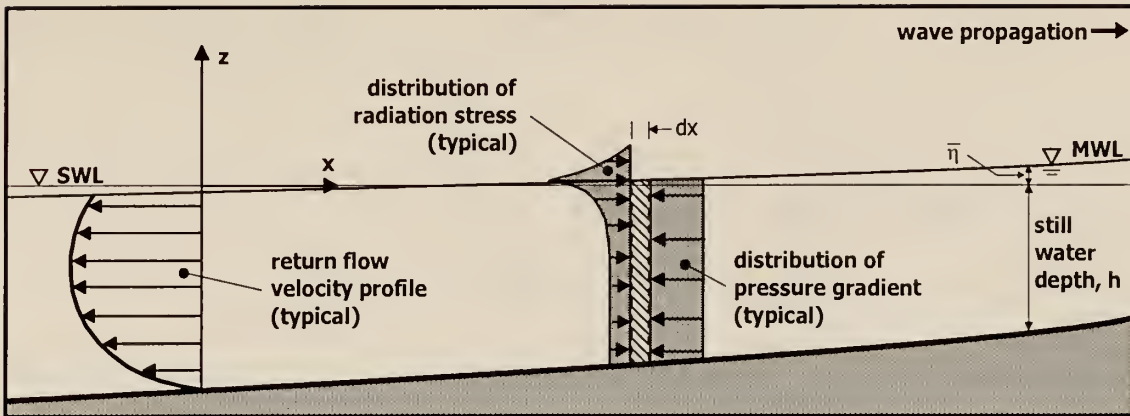


Figure 1.2 Definition sketch of return flow problem. The return flow is created from the vertical imbalance of the wave induced radiation stress in the onshore direction and the uniformly distributed pressure gradient in the offshore direction that arises from the slope in the water surface.

The cross-differentiation process also removes the pressure terms from the equations, eliminating the need to describe the pressure field in the model. Modeling the problem in two dimensions allows for an investigation of the coupling of stresses from one vertical section to the next, as opposed to considering the vertical sections separately. This becomes a particular point of interest in the immediate vicinity of breaking. Non-coupled computations tend to produce a strong discontinuity in the description of the bottom shear stress near the breakpoint. When applied to profile evolution models, the discontinuity can lead to large errors in the predicted behavior of the profile.

The application of the boundary conditions becomes a particularly interesting and potentially beneficial issue. The governing equation is a 2-D, fourth-order PDE in  $\psi$ , hence four boundary conditions are needed in each direction. In the vertical, this provides the ability to prescribe the boundary conditions at the mean water surface and at the seabed while also explicitly dictating that mass (or flow rate) be conserved. This fact provides additional information not available from many previous return flow model formulations.

In the horizontal, the benefit of the inclusion of four boundary conditions is not as significant, although it provides a convenient means for the transfer of fluid into and out of the model domain, as might be the case for an external, non-wave driven current.

One drawback to having the additional boundary conditions is then the need to properly describe these boundary conditions, such as the specification of the velocity or the shear stress at the seabed. The governing equation contains no information that specifically relates to a wave-driven flow, thus all the information regarding the wave forcing must be supplied through the boundary conditions. While the model provides a convenient approach to evaluate these options, application of specific values for these boundary conditions may not be supported by the existing knowledge of the processes near the seabed or the surface.

In addition to the challenges of establishing boundary conditions, another problem that modelers of wave-induced return flow face is the characterization of the flow immediately following breaking. In this area, commonly referred to as the transition region or outer surf zone, the wave undergoes a significant transformation of shape but does not necessarily experience a significant decrease in its momentum. Researchers have studied this problem and at present a common technique is to describe the wave in the surf zone as a turbulent bore, in which the wave form contains a volume of water in front of it referred to as the surface roller (Svendsen, 1984a).

While the surface roller technique developed by Svendsen appears to apply well in the inner surf zone, the details of how this roller forms in conjunction with the conservation of momentum across the entire surf zone are not well defined. It will be demonstrated that momentum is not conserved between the offshore region and the inner surf zone description of Svendsen (1984a), as well as other traditional wave theories (e.g., linear

wave theory). Dally and Brown (1995) introduce a technique to describe the redistribution of momentum and the formation of a wave surface roller in the transition region that does satisfy momentum conservation. In this work, the method of Dally and Brown (1995) is applied and compared to a simple attempt to “patch” the offshore and inner surf zone descriptions by applying a simple conservation of momentum argument between the offshore wave theory and the inner surf zone theories (such as the Svendsen roller model). It will be shown that the conservation of integral wave properties is imperative in creating a smoothly coupled model (more so than the use of a 2-D versus 1-D formulation).

Inclusion of an arbitrary beach profile geometry and a spatially variable turbulent eddy viscosity field precludes an analytic solution of the 2-D problem. Therefore a two-dimensional numerical model is developed to investigate the aforementioned issues. The 2-D numerical model is compared to simple flow situations to check the results against existing 2-D analytic solutions and other return flow models.

The inclusion of a time-dependent component of the mean flow also provides some advantages. The time dependency allows for an investigation of the effects of a random wave field on the return flow since the effects of previous waves are maintained (the model tracks the ‘history’ of the flow). The ability to incorporate random waves is beneficial since it tends to produce bottom velocities and shear stresses that are more uniform and smooth across the profile, which lends itself to the successful coupling to a sediment transport module. Additionally, the ability to model a changing wave and flow field could ultimately lead to the simulation of storm induced changes in a beach profile, where the wave climate builds then diminishes over several hours.

## CHAPTER 2

### LITERATURE REVIEW

A significant amount of literature exists that discusses the mean flow field in the surf zone. Johnson (1919) qualitatively describes the nature of many currents present in the nearshore region, and in describing ‘hydraulic currents’ due to waves he notes that there is a net shoreward movement of water that occurs in shoreward-directed oscillatory waves that must result in the accumulation of water along the coast. Johnson further states:

It is clear that the water piled up against a shore in the manner just described must escape, thereby producing more or less continuous ‘hydraulic currents.’ If the escape is seaward, along the bottom, we have the current known as the *undertow* (p. 104);

Johnson clearly describes the physical mechanisms of interest in the present work and their general cause. A more rigorous explanation of the generating mechanisms of the return flow is provided in the introductory chapter based on the balance of the wave-induced radiation stress and the resultant set-up or set-down of the water surface, as described by Longuet-Higgins and Stewart (1962) (Figure 1.2).

Longuet-Higgins and Stewart (1962, 1964) present the mean horizontal momentum balance, depth-integrated and time-averaged, for the passage of waves over a sloping bottom. As presented graphically in Figure 1.2, the balance equation is:

$$\frac{\partial S_{xx}}{\partial x} = -\rho g(h + \bar{\eta}) \frac{\partial \bar{\eta}}{\partial x} - \bar{\tau}_b \quad (2.1)$$

where  $S_{xx}$  is the wave induced radiation stress (the flux of onshore directed wave momentum in the onshore,  $x$ , direction),  $\bar{\eta}$  is the mean water surface elevation, its gradient in  $x$  represents the water surface slope, and  $\bar{\tau}_b$  is the mean bottom shear stress. The mean bottom shear stress in Eq. (2.1) is frequently labeled as a minor contribution to the momentum balance, and Longuet-Higgins and Stewart discarded the term in their discussion. In a depth integrated sense, the radiation stress and the water surface slope balance, but as a function of depth ( $z$ ), the terms are unbalanced, which creates the return flow in the surf zone.

The objective of this work is to describe the development and application of a stream function formulation to model the mean flow field in the surf zone. With that goal in mind, it is useful to review and describe previous efforts that have prompted the development and use of this particular formulation, as well as the data that exist that allow its demonstration.

Return flow modeling depends strongly on the selection of boundary conditions. In each case presented the choice of boundary conditions is discussed. The application of the boundary conditions to the numerical model and the individual choice of values for each condition are discussed in Chapter 4. Similarly, a variation in the eddy viscosity field in the nearshore region can affect the return flow. These possibilities are demonstrated throughout the present work, and their contributing researchers are noted accordingly.

## 2.1 Motivating Literature

Dyhr-Nielsen and Sørensen (DN&S, 1970) provide a review of nearshore processes that sets the stage for much of the recent work done in this area. DN&S qualitatively describe the balance of wave thrust and pressure gradient and the resultant onshore directed

current along the seabed outside the break point. They also describe the balance inside the surf zone (Figure 1.2) where energy losses due to wave breaking lead to offshore directed currents at the seabed. DN&S hypothesize that this combination of currents contributes to the transport of sediment toward the break point and leads to the development of shore-parallel sand bars.

DN&S present the balance of forces in terms of moments which must be balanced in the water column. The authors conclude that the passage of broken or unbroken waves creates an unbalanced moment within the water column. According to DN&S, this unbalanced moment must be taken up at the bed, resulting in onshore and offshore directed bed stresses seaward and landward of the surf zone, respectively. The possibility of onshore directed stresses caused by wave shoaling seaward of the break point provides one motivation for the development of the present model, which provides a means of clearly demonstrating the effects of the balance of moments and the possibility of onshore directed transport in the shoaling region.

The work of Dally (1980) provides the motivation for the formulation applied in the present study. Dally developed a numerical model to study beach profile evolution (Dally, 1980, and Dally & Dean, 1984). In the development of the profile evolution model, the author derived an expression for the mean return flow profile based on the primitive conservation of fluid momentum equations. The expression was then coupled with a description of the sediment suspension concentration profile to produce a sediment transport model in the surf zone. The return flow model developed by Dally will be discussed elsewhere in this chapter.

In the same work, Dally (1980) presents a brief attempt to model the horizontal momentum of fluid in a flat channel under an applied surface stress. In this effort, Dally

time-averaged and cross-differentiated the equations of motion to produce the biharmonic equation (with some algebraic manipulation):

$$\frac{\partial^4 \Psi}{\partial x^4} + 2 \frac{\partial^4 \Psi}{\partial x^2 \partial z^2} + \frac{\partial^4 \Psi}{\partial z^4} = 0 \quad (2.2)$$

This equation can also be used to describe creeping flows in viscous fluids, and while the analogy with creeping flows does not hold in the present physical situation, the existing mathematical solutions from creeping flows are useful in this work to verify the numerical solutions. The present model builds on the work of Dally (1980) by developing a similar fourth-order partial differential equation (PDE) in terms of the stream function that considers arbitrary geometries and allows a spatially variable eddy viscosity.

Further motivation for the present work arises from the differences between various existing return flow models. The second-order model used by Dally is derived from the time averaged equations of motion and includes the wave trough-to-crest region, a process that produces a second order equation in the mean velocity,  $U$ . This is accomplished by employing linear wave theory, in which the trough-to-crest region is collapsed to the Mean Water Level (MWL), consistent with small amplitude wave theory. Other modelers, e.g., Svendsen (1984b) and Stive and Wind (1986), truncate the model domain at the trough level so as not to invoke linear wave theory. The inclusion of the trough-to-crest region in the derivation incorporates details of the wave momentum flux as an internal forcing mechanism in the development (as opposed to applying this flux as a boundary condition). The other approach, that of truncating the domain at the wave trough level, leaves the momentum contributions in the trough-to-crest region as an option for a surface boundary condition, and thus somewhat separates the flow description from the wave motion.

In the latter approach, a detail of the flow is lost. The need to specify two boundary conditions, without the details of the wave trough-to-crest momentum explicitly included in the governing equation, results in the loss of one of the three pieces of information generally used to describe the problem (flow rate, upper boundary condition, and lower boundary condition). In these cases, previous investigators have generally specified the conservation of flow through the section and either the bottom condition (e.g., Svendsen, 1984a) or the surface shear stress (e.g., Stive and Wind, 1986). The other, unspecified condition is found as a product of the derivation.

The differences in these two approaches leads to confusion with regard to the boundary conditions and the application of a boundary condition versus a constraint on the flow. In the present development, the governing equation is derived from the equations of motion and is somewhat generic (little wave information is evident in the final equation). Wave-related flow characteristics are introduced strictly through the boundary conditions. In this manner the effects of various aspects of the wave passage are elucidated by the use of the fourth-order PDE. The four boundary conditions needed (in the vertical) will be applied at the surface and the bottom to dictate a surface boundary condition, a bottom boundary condition, and the conservation of the flow through any vertical section.

In the well known work of Longuet-Higgins (1953), the author develops a fourth order stream function expression for profiles of the mass transport velocity under water waves. In the ‘conduction solution’ developed, Longuet-Higgins introduces the application of the same four boundary conditions that will be applied in the vertical coordinate in the present model. The author discusses the use of the first- and second-derivative boundary conditions (velocity and shear stress, respectively) where the chosen values correspond to matching conditions at boundary layers at both the free surface and the bottom. It is noted

that the velocity profiles developed by Longuet-Higgins (1953) apply to uniform eddy viscosity flows in relatively deep water (compared to the wave height), and the specific boundary conditions applied are not expected to hold in the present surf zone application (e.g., Longuet-Higgins applied a bottom streaming velocity condition, which, as will be shown, is not well supported by experimental measurements in the surf zone).

It is the efforts of Longuet-Higgins, Dyhr-Nielsen and Sørensen, and Dally that provide the basis and motivation for the present numerical modeling investigation of the mean flow in the surf zone. It is the goal of the present work to combine these efforts into a model that more completely describes the mean flow processes in the nearshore region.

## 2.2 Return Flow Models

Many well-known return flow models are developed directly from the two-dimensional momentum equations and produce a second order differential equation in  $U$  by introducing a turbulent eddy viscosity formulation. Bearing that in mind, it is useful to investigate the full 2-D Reynolds equation of turbulent flow in the  $x$ -direction, where the horizontal velocity components  $u$  and  $w$  have been decomposed into individual mean ( $U$ ,  $W$ ) fluctuating ( $\tilde{u}$ ,  $\tilde{w}$ ), and turbulent ( $u'$ ,  $w'$ ) components:

$$\begin{aligned} \frac{\partial U}{\partial t} + \frac{\partial}{\partial x} [ \overline{(U + \tilde{u} + u')^2} ] + \frac{\partial}{\partial z} [ \overline{(U + \tilde{u} + u')(W + \tilde{w} + w')}] \\ = \frac{1}{\rho} \frac{\partial \bar{P}}{\partial x} + \frac{\partial}{\partial x} [ 2v \frac{\partial}{\partial x} (U + \tilde{u} + u') ] \\ + \frac{\partial}{\partial z} [ v ( \frac{\partial}{\partial z} (U + \tilde{u} + u') + \frac{\partial}{\partial x} (W + \tilde{w} + w') ) ] \end{aligned} \quad (2.3)$$

Generally, in the literature the long-period fluctuation of the mean flow is neglected along with many of the wave induced fluctuating components. Additionally, it is

customary to neglect any turbulent normal stresses. The turbulent shear stresses, known as the Reynolds stresses, can be replaced by a turbulent shear stress representation employing the eddy viscosity,  $\epsilon$ . The introduction of the turbulent shear stress representation then produces a second order equation in  $U$ , resulting in the need for two boundary conditions for solution:

$$\frac{\partial}{\partial x} (\bar{u}^2 - \bar{w}^2) = -g \frac{\partial \bar{\eta}}{\partial x} + \frac{\partial}{\partial z} [\epsilon \frac{\partial U}{\partial z}] \quad (2.4)$$

The reader will note that the depth-integration of Eq. (2.4) produces the original balance shown in Eq. (2.1), where the term on the left-hand side of Eq. (2.4) leads to the horizontal gradient in wave radiation stress,  $S_{xx}$ , and the integration of the second term on the right hand side leads to terms for the surface and bottom shear stress, which are then frequently neglected. Eq. (2.4), or a similar form, is the foundation for many return flow models including Dally (1980), Börekçi (1982), Svendsen (1984b), and Stive and Wind (1986), among others. These investigators applied Eq. (2.4) with a variety of boundary conditions and wave descriptions. A detailed derivation of the Reynolds equations and the substitution of the eddy viscosity representation is included in Chapter 3 as part of the development of the governing equation used in the present model.

Dally (1980) and Dally and Dean (1984) develop an expression for the return flow based on Eq. (2.4). Dally includes the wave trough-to-crest region in the solution domain, retaining the wave momentum flux in that region as an internal forcing mechanism in the governing equation. In linear wave theory, this region is considered to be collapsed to the MWL. This assumption results in the *apparent* application of a surface shear stress without the application of a formal boundary condition. The shear stress at the *instantaneous* free

surface and the velocity at the bottom are then applied as the two boundary conditions. The equation, which contains the term describing the gradient in water surface slope, is constrained such that the net flow through the vertical section,  $Q$ , equals the volumetric transport of the waves (i.e., the Stokes drift). This constraint eliminates the water surface slope term from the equation. The resultant expression for the return flow with uniform eddy viscosity was found to be:

$$\begin{aligned} U(z) = & \frac{gh}{8\epsilon} \frac{\partial H^2}{\partial x} \left[ -\frac{3}{8} \left( \frac{z}{h} \right)^2 - \frac{1}{2} \left( \frac{z}{h} \right) - \frac{1}{8} \right] \\ & + \bar{u}_b \left[ \frac{3}{2} \left( \frac{z}{h} \right)^2 - \frac{1}{2} \right] - \frac{3Q}{2h} \left[ \left( \frac{z}{h} \right)^2 - 1 \right] \end{aligned} \quad (2.5)$$

where the coordinates are defined in Figure 1.2. Dally included the specification of a non-zero bottom velocity to provide a means, if desired, of matching the velocity in the interior of the flow to a boundary layer edge velocity, after Longuet-Higgins (1953).

The first term on the right-hand side of Eq. (2.5) arises from the wave momentum flux in the trough-to-crest region. The use of linear wave theory raises a unique point about the Dally (1980) model. Applying linear wave theory extends the limits of the problem to the free surface. By doing so, Dally is able to include the *effect* of the radiation stress in the trough to crest region as a shear stress on the upper limit of the model domain, *without applying a boundary condition to do so*.

The work of Börekçi (1982) follows the same approach of collapsing the trough-to-crest region down to the MWL. Subsequent researchers have questioned the use of linear wave theory and the application of a zero surface shear stress condition at the free surface in the surf zone setting. The application of a zero surface shear stress at the instantaneous free surface, when in fact the free surface is assumed to be coincident with

the MWL via linear theory, does create a degree of confusion, as evidenced by subsequent discussion of this model (e.g., Svendsen, 1984a; Dally and Dean, 1986).

Dean (1995) employed a similar approach to the Dally (1980) model, but included the possibility of a wind stress. Dean applied the horizontal momentum balance (essentially Eq. (2.4) with the left hand side set equal to zero) with an applied surface shear stress (the wind,  $\tau_n$ ) as one boundary conditions and a set bottom boundary velocity ( $=0$ ). The modified expression from Dean follows:

$$U(z) = \frac{h}{\rho\epsilon} \left[ 2\tau_n - \frac{\partial E}{\partial x} \right] \left[ -\frac{3}{8} \left( \frac{z}{h} \right)^2 - \frac{1}{2} \left( \frac{z}{h} \right) - \frac{1}{8} \right] + \frac{3Q}{2h} \left[ \left( \frac{z}{h} \right)^2 - 1 \right] \quad (2.6)$$

where the flow rate through the section is dictated by substituting for the water surface slope in Eq. (2.4). In this way, Dean constrains the solution to include the bottom and surface boundary conditions and conserve the flow through the vertical section. The first term in Eq. (2.6) includes the wind stress, denoted as  $\tau_n$ , as well as the wave momentum flux in the trough-to-crest region.

Hansen and Svendsen (1984), and Svendsen (1984b) employ a similar approach to return flow modeling in which the net flow and bottom velocity are specified as boundary conditions. In these instances the flow domain is truncated at the wave trough level, and these investigators leave the trough-level boundary condition unspecified. The discussion in these models then focuses on the appropriate choice of the bottom velocity. Svendsen et al. (1987) discuss the need to include the details of the flow near the bottom, where a matching technique is applied to a boundary layer representation. Hansen and Svendsen (1984) note that in several laboratory measurements, the measured bottom velocities seem to agree very well with the magnitude of the wave-induced streaming velocity, but not in

direction. The direction of the measured bottom velocity in many return flow experiments is offshore, not onshore as a streaming velocity argument would suggest (see Chapter 6).

Stive & Wind (1986) chose to adopt a different boundary condition in the application of Eq. (2.4). The authors truncate the domain at the wave trough level and argue that since the imbalance that drives the return flow is focused in the trough-to-crest region, it is more appropriate to specify the trough-level shear stress, along with the specification of the flow rate, rather than the bottom velocity. The details of the velocity at the seabed, which is a product of the solution and is generally non-zero, are not discussed.

Svendsen et al. (1987) revisited the original development of Svendsen (1984b) to focus on the matching of the bottom boundary layer velocity and shear stress to the near-bottom velocity and shear stress in the body of the fluid. This matching produces a much smaller eddy viscosity in the boundary layer, where a zero velocity at the bottom is required. In a related effort, Putrevu and Svendsen (1993) extended the analysis of Svendsen et al. (1987) to the shoaling region and showed improvement in the agreement with experimental data by including a streaming velocity effect in the wave induced bottom boundary layer.

Cox and Kobayashi (1997, 1998) used detailed measurements of the return flow both in the boundary layer and in the body of the fluid to develop a logarithmic expression for the velocity in the boundary layer. This solution was matched to a parabolic description of the velocity in the body of the fluid. The authors also demonstrate that a quadratic friction equation with a fitted friction factor was able to reasonably predict the resultant time-dependent bottom shear stress. The authors compare their developments to laboratory data as well as field data (see Section 2.4, Return Flow Measurements, below).

### 2.3 Turbulent Eddy Viscosity

The turbulent eddy viscosity,  $\epsilon$ , is the diffusive mechanism in the present model. In order to produce accurate simulations of the return flow, it is obviously necessary to assign a value to the turbulent eddy viscosity. It will be shown in this work that the application of a spatially variable turbulent eddy viscosity, particularly in the vertical direction, produces significant improvement in the agreement between model simulations and measured data. In this section a review of available literature regarding the selection of eddy viscosity values is presented for both spatially uniform and variable cases. To begin, the determination of an appropriate value to use in the uniform eddy viscosity case is pursued.

The eddy viscosity is a property of the flow situation, which makes its determination difficult. In reviewing the substantial amount of available literature, an attempt is made to bracket the possible range of eddy viscosity values to apply in the numerical model. Furthermore, an effort is made to find a physical basis for applying spatially variable eddy viscosity values. Given this uncertainty, the possible variations in eddy viscosity, both in a spatially uniform and spatially varying scheme, are investigated.

Hansen and Svendsen (1984) present a 1-D analytic expression for the return flow in which the eddy viscosity varies exponentially in the vertical direction to represent the decay of turbulence from the surface down through the water column. The authors produce expressions  $\epsilon$  of between  $0.005ch$  and  $0.01ch$ , where  $c$  is the wave celerity and  $h$  is the local water depth. A typical laboratory breaking wave condition of 0.2 m water depth translates to eddy viscosity values in the range of  $\epsilon = 0.001$  to  $0.003 \text{ m}^2/\text{s}$ , assuming shallow water conditions. Although the authors discuss only laboratory waves, application of the above expressions to field conditions ( $\sim 1$  m water depth), produces values in the range  $\epsilon = 0.016$

to  $0.031 \text{ m}^2/\text{s}$ . It is noted that by assuming shallow water conditions ( $c = (gh)^{1/2}$ ) in these expressions, the horizontal variation in eddy viscosity would be expected to depend on  $h^{3/2}$ .

Stive and Wind (1986) discuss the values of  $\epsilon$  used in both the Hansen and Svendsen (1984) experiments and their own laboratory measurements. The authors compute the value of the depth-uniform eddy viscosity at each cross-shore measuring profile from the collected data. For the experiments of Hansen and Svendsen (1984), Stive and Wind report  $\epsilon$  values of between  $0.0017$  and  $0.0008 \text{ m}^2/\text{s}$  in surf zone water depths ranging between  $14.5 \text{ cm}$  and  $8.6 \text{ cm}$ , respectively. For their own experiments, Stive and Wind report depth-uniform eddy viscosity values of between  $0.0026$  to  $0.0005 \text{ m}^2/\text{s}$  in surf zone water depths ranging between  $18.5$  to  $7.7 \text{ cm}$  respectively. Stive and Wind discuss an analytic approach to determining an appropriate value of  $\epsilon$  using an analogy to the eddy viscosity in wake flows. The resulting expression,  $\epsilon = 10^{-2}ch$ , is similar to that proposed by Hansen and Svendsen (1984). Stive and Wind do not report any information regarding the vertical variation of the eddy viscosity.

Svendsen et al. (1987) discuss the matching of the velocity profile in the bottom boundary layer, in which eddy viscosity values are hypothesized to be significantly lower, to the velocity profile in the body of the fluid. Using the original data reported by Hansen and Svendsen (1984), Svendsen et al. propose values of  $\epsilon$  in the body of the fluid of between approximately  $0.001$  and  $0.003 \text{ m}^2/\text{s}$  for surf zone water depths between  $14.5 \text{ cm}$  and  $8.6 \text{ cm}$ , respectively, in the laboratory. Svendsen et al. discuss the likelihood that the eddy viscosity in the bottom boundary layer may be as much as  $10^3$  times smaller than the appropriate value in the body of the fluid.

Haines and Sallenger (1994) discuss the application of horizontally variable eddy viscosity fields in field data from Duck, North Carolina. The authors relate the horizontal

variation in the eddy viscosity to the dissipation of the turbulent bore formed by wave breaking. The eddy viscosity is at its maximum value just landward of the first break point (on the seaward face of the bar). The value decreases rapidly following breaking, reaching a minimum equilibrium value before rising slightly at the shore break region. The magnitudes of the surface eddy viscosity in the cross shore were determined from fitting the measured field data at each horizontal measuring location. Inspection of the data presented by Haines and Sallenger also indicate a strong dependence of the eddy viscosity on  $h^{3/2}$ . The range of fitted values of  $\epsilon$  found by the authors for this particular field experiment range between 0.0055 and 0.075 m<sup>2</sup>/s. The authors employ a vertically-uniform eddy viscosity at each horizontal location.

Reid (1957) describes the mean horizontal velocity profile in bounded and unbounded channels subjected to surface wind stresses. By linking linearly increasing mixing length descriptions of the turbulent shear stress from the surface and bottom boundaries, a parabolic description of the mixing length is found. Using this relationship in combination with a linear shear stress distribution in the vertical, Reid developed non-dimensional equations describing the velocity profile under a wide range of surface and bottom stress conditions. The two pertinent equations are:

$$\tau(z) = \rho L^2 \left| \frac{du}{dz} \right| \frac{du}{dz} \quad (2.7)$$

$$L(z) = \frac{k_o}{D} (z + z_o)(D + z_1 - z) \quad (2.8)$$

where  $\tau$  is the shear stress whose value at the bottom is described by a quadratic friction expression,  $L$  is the mixing length for turbulent flow,  $k_o$  is von Karman's dimensionless constant (= 0.40),  $D$  is the water depth, and  $z_o$  and  $z_1$  are characteristic bottom and surface

roughness scales, respectively. Reid related the bottom shear stress to that of the surface shear stress by the coefficient,  $m$  (generally,  $|m| < 1$  in the example presented by Reid).

Reid (1957) provides one of the only analytic means of validating the numerical model for flows with non-uniform eddy viscosity. The mixing length,  $L$ , and the turbulent eddy viscosity (used in the numerical model) can be related as follows:

$$\epsilon = L^2 \left| \frac{\partial u}{\partial z} \right| \quad (2.9)$$

The variation in the mixing length over depth and hence the eddy viscosity is explained in Figure 2.1. In the figure, the analogy between the present situation and open channel flow is studied. In the upper three cases, there is zero shear stress and no generation of turbulence at the surface. In the first plot, the assumption of a depth uniform shear stress (an incorrect but occasionally made assumption) and a linearly increasing mixing length from the bottom leads to a linearly increasing eddy viscosity value from the bottom upward via Eq. (2.9). It is noted that the use of a linearly increasing mixing length argument is approximated from the Prandtl development of mixing length above a flat surface in a semi-infinite fluid.

In the second plot of Figure 2.1, a linear distribution for the shear stress is applied in which the shear stress varies linearly from the bottom value to zero at the surface. In this instance the eddy viscosity produced is parabolic, with a maximum at mid-depth. In the third plot, a parabolic distribution of the mixing length is applied, assuming that the mixing length is limited at both boundaries (i.e., no longer a semi-infinite fluid approximation). In this case the resultant eddy viscosity curve resembles a higher order behavior, with a maximum that is shifted toward the bottom where the turbulence is being generated. The fourth plot in Figure 2.1 is the situation modeled by Reid (1957) where turbulence is

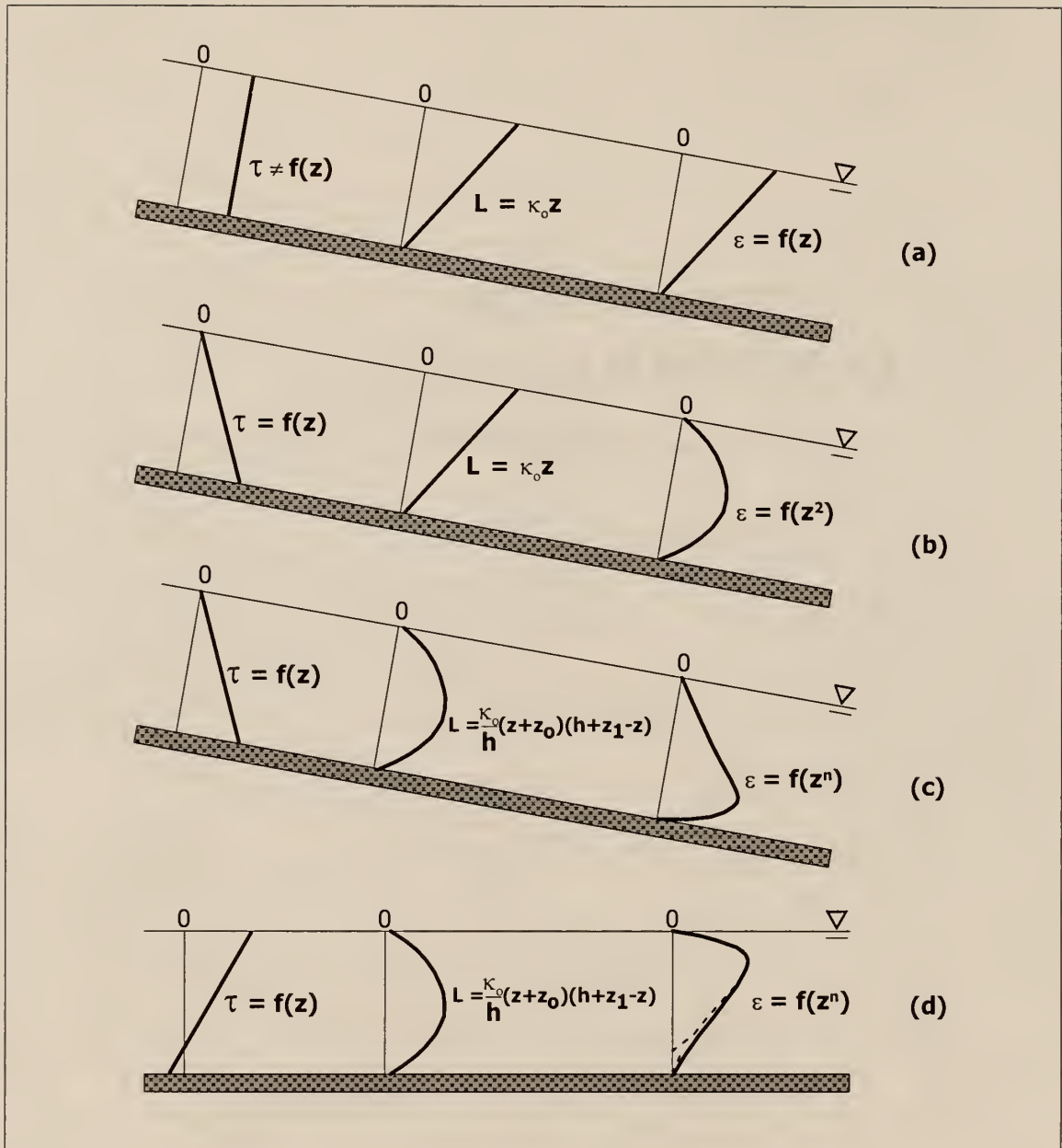


Figure 2.1 Illustration of the effect of the quadratic mixing length expression employed by Reid (1957). The analogy to gravity-driven open channel flow is drawn to illustrate the different distributions of eddy viscosity that are produced under different assumptions for the distribution of shear stress and mixing length. The bottom figure depicts the situation applicable to the present model. The assumption of uniform shear stress shown in plot (a) is incorrect but is shown for comparison.

generated at both boundaries, and the turbulence generated at the surface by the wind stress is much greater than the turbulence generated by the stress at the bottom.

The fourth example in Figure 2.1 is analogous to the present flow situation, in which the surface stress generated by breaking waves is believed to be much greater than the oppositely-directed bottom stress generated by the return flow. This distribution of the shear stress, sketched in the fourth and final plot in Figure 2.1, produces a similar higher order variation in the eddy viscosity as seen in the third plot, with the exception that the maximum value of the eddy viscosity occurs closer to the surface, where the majority of the turbulence is introduced from the breaking waves. This shift of the curve can also be deduced from Eq. (2.8) in that the roughness scale at the surface due to the breaking waves is expected to be much greater than the roughness scale along the bottom. Börekçi (1982) discussed the profile shape produced by the Reid mixing length model and investigated the role of the roughness scales,  $z_0$  and  $z_l$ , in Eq. (2.8). Börekçi applied the wave height as an upper limit on the surface roughness scale and plotted the resultant profiles.

The vertical variation of  $\epsilon$  sketched in Figure 2.1d is a maximum a short distance from the surface (approximately 0.2 or 0.3h below the Mean Water Level). The value of the eddy viscosity quickly decreases to a much lower value at the bottom, perhaps as much as  $10^2$  or  $10^3$  times lower than the surface value (Svendsen et al., 1987). The significantly lower value of eddy viscosity near the seabed acts to allow the fluid to essentially “slip” over the bottom, acting much like a thin wave/current bottom boundary layer solution. In the present model, no mathematics is incorporated to simulate a bottom boundary layer. Thus only the vertical variation in the eddy viscosity can produce this phenomenon in the model. The variation in  $\epsilon$  also serves to produce much more uniform profiles in the body of the fluid when compared to the spatially uniform case.

The vertical variation in eddy viscosity can in some ways be inferred from measurements of turbulent kinetic energy. Stive (1984) presents vertical profiles of turbulent energy under breaking waves in the laboratory. These profiles exhibit a shape similar to the vertical variation in  $\epsilon$  found from Reid (1957). The data of Stive (1984) indicated a peak value of turbulent kinetic energy occurring just below the Mean Water Surface. Ting and Kirby (1994) present similar profiles of turbulent kinetic energy from laboratory measurements.

In the horizontal, substitution of Eq. (2.7) into Eq. (2.9) produces a dependence of  $\epsilon$  on  $L^{3/2}$  (the shear stress,  $\tau$ , varies linearly in the vertical). Since the length,  $L$ , is dependent on the local water depth,  $h$ , the eddy viscosity is expected to depend on  $h^{3/2}$  as well. This is consistent with the findings of Stive and Wind (1986) and Svendsen et al. (1987). This is also the general finding when the eddy viscosity is considered in terms of Froude scaling. Given the Froude scaling time dependence of  $L^{1/2}$ , the eddy viscosity, which has dimensions of  $[L^2/T]$ , would be expected to vary as  $L^{3/2}$ . Use of the depth as a length scale is then an obvious choice.

Inspection of data regarding the variation of  $\epsilon$  in the vertical and horizontal leads to several conclusions. The eddy viscosity appears to be strongly related to the water depth, which can be considered a scale for the turbulent mixing length. Reid (1957) presented a parabolic mixing length argument in which the mixing length reached its maximum at mid-depth. Translation of this mixing length produces a vertical variation in  $\epsilon$  that depends on the shear stress at the boundaries and varies to a higher order, with the peak value occurring well above mid-depth. For simplicity in fitting, and due to the uncertainty in the predicted value near the region of zero shear stress, a third order polynomial is fit to the Reid profile to investigate the vertical variation in  $\epsilon$ .

The horizontal variation in  $\epsilon$  appears to be related to  $h^{3/2}$ , among other factors. Various researchers have proposed values for the eddy viscosity at a particular depth that take the form  $Bch$ , where  $B$  is a constant, typically between 0.005 and 0.01. The overall magnitude of the eddy viscosity may be estimated from this simple expression. Using typical values, assuming a laboratory depth of 0.1 m produces a typical eddy viscosity value of  $0.001 \text{ m}^2/\text{s}$ . Similarly, applying a field depth of 1.0 m in the expression yields a value of  $\epsilon = 0.03 \text{ m}^2/\text{s}$ . Haines and Sallenger (1994) proposed a horizontal variation in eddy viscosity (depth-uniform) based on turbulent bore dissipation. Their hypothesis was borne out through field measurements.

## 2.4 Return Flow Measurements

A significant amount of data exist that describe the return flow under waves. This section provides a introduction to the existing data and highlights the experimental data that will be used in the present discussion to test the numerical model. Russell and Osorio (1958) presented some of the first laboratory measurements of mean velocity profiles, which were aimed primarily at investigating wave induced drift profiles over horizontal bottoms and submerged bars. Drift profiles were measured in a Lagrangian manner by timing neutrally buoyant particles over fixed distances.

More recent laboratory measurements of return flow profiles begin with the work of Stive (1980), who collected velocity measurements under monochromatic, spilling waves breaking on a smooth concrete slope of 1:40. Velocity profiles were measured by Laser Doppler Anemometry (LDA) at a spacing of approximately 1 m across the profile and included profiles seaward of, at, and landward of the break point. Stive focused on the profiles well landward of the break point in the organized inner surf zone region.

Nadaoka and Kondoh (1982) present laboratory LDA velocity measurements of return flows under spilling and plunging breakers measured at seven profiling stations. The waves were monochromatic, breaking on a smooth wooden slope of 1:20. Okayasu and Katayama (1992) present both monochromatic and irregular wave cases for waves breaking on plane and barred planar laboratory beaches. Both beach profiles were constructed of smooth planking of 1:20 slope. The barred-beach case consisted of a bar with 1:20 slopes on both sides. No monochromatic waves were tested on the barred beach.

Ting and Kirby (1994) present velocity profile measurements for monochromatic, spilling waves breaking on a smooth laboratory slope of 1:35. Cox and Kobayashi (1997) present similar data collected in the same wave tank used by Ting and Kirby for monochromatic, spilling waves breaking on an artificially roughened slope of 1:35.

One set of data are simulated with the numerical model to study the return flow profile over a moveable bed profile in the laboratory. Roelvink and Reniers (1995) present return flow data from several experiments conducted as part of the Delta Flume Experiments conducted at the Delft Hydraulics facility in the Netherlands. At least 11 velocity profiles were collected for each experiment. Specific cases from these experiments will be investigated and compared to the numerical model results. Field data from Duck, North Carolina, will also be applied. Smith et al. (1992) present velocity measurements from the DELILAH series of field experiments.

Four plane bed laboratory experiments will be simulated in detail in the present work for purposes of model comparison. The periodic wave, plane slope experiment of Nadaoka and Kondoh (1982), the random wave, barred slope experiment of Okayasu and Katayama (1992), and the periodic wave, plane slope experiments of Ting and Kirby (1994) and Cox and Kobayashi (1997) will be simulated in the numerical model. The Delta Flume

movable bed experiment will be investigated for cases of random waves over (relatively) fixed but irregularly shaped profiles (Roelvink and Reniers, 1995). Lastly, the DELILAH Duck field data set of Smith et al. (1992) will be simulated to study field conditions. These six data sets were chosen primarily for their density of mean velocity measurements across the entire profile.

Some experimental data in the literature were collected under reasonably similar conditions. In these cases the differences and similarities in the results is investigated. Figure 2.2 presents portions of the data collected by Ting and Kirby (1994) and Cox and Kobayashi (1997). Both data were collected in the same tank under similar wave conditions with the exception of a smooth bottom (Ting and Kirby) versus roughened bottom. Inspection of the two experiments reveals that the two cases produced very similar profiles overall, both in shape and magnitude, with the exception of the second profile of Ting and Kirby. Some slight differences in the shape of the individual profiles is observed.

While the data of Ting & Kirby do not extend into the bottom boundary layer, as do the data of Cox and Kobayashi, it is clear that if the older dataset extended through the boundary layer the agreement (at least visually) would improve. The agreement between these experiments is discussed only in terms of overall or visual similarity due primarily to the discrepancies in measuring locations. The numerical model will simulate these two experiments (and others). In these simulations a more quantitative measure will be applied to determine what model parameters and boundary conditions are ‘better’ or ‘worse.’

The agreement between the simulations and the experiments, or between the simulations themselves, is the indicator of what input conditions produce the best answers. The laboratory data certainly have various degrees of error that affect the result. This is particularly true close to the surface, where the data collection techniques (such as LDA)

are affected by aeration and dropout of the signal above the trough level. Although these data do exhibit some scatter and some individual problems, the quality of the return flow data available in the literature is generally considered quite good and is used to validate the present model.

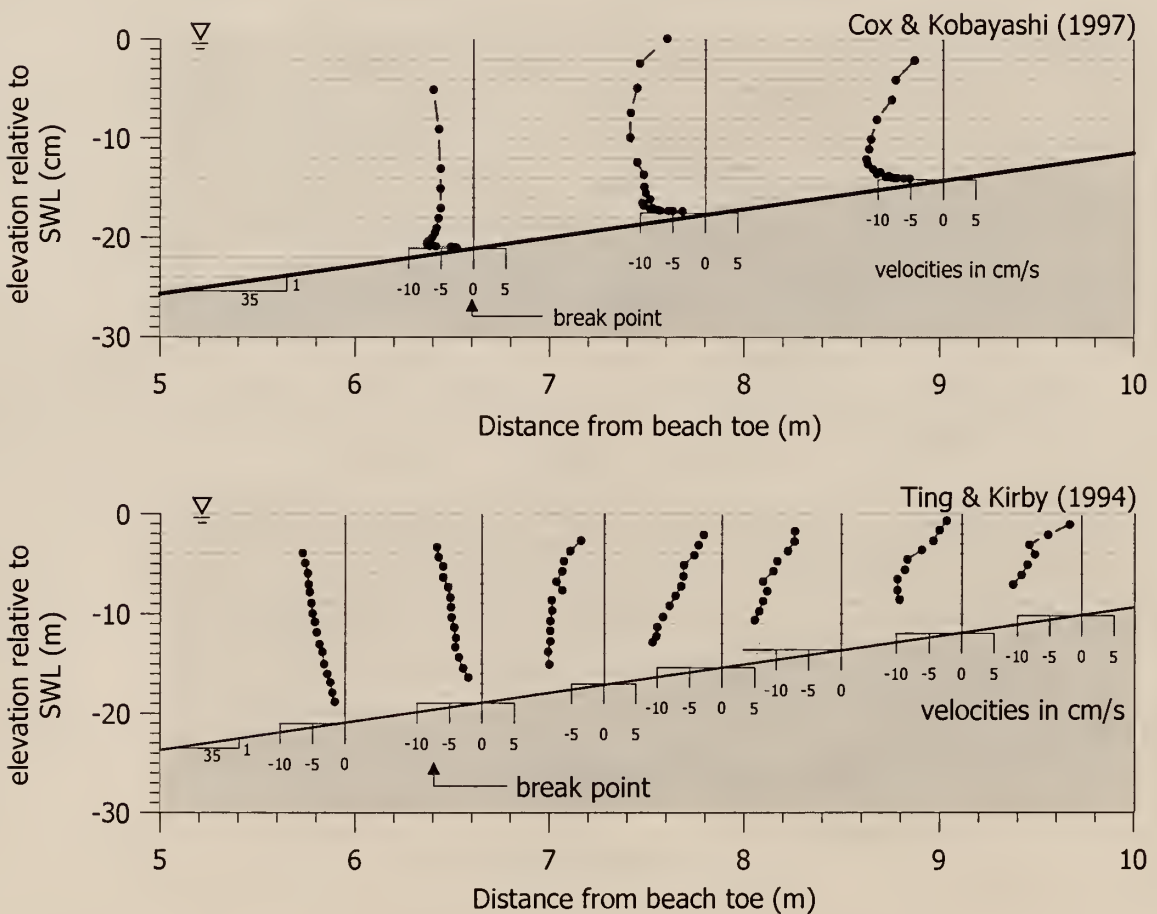


Figure 2.2 Comparison of mean horizontal velocity profiles as reported by Cox and Kobayashi (1997) and Ting and Kirby (1994). These two datasets were collected under very similar conditions in the same wave tank. The primary difference in the experiments is the bottom surface conditions (roughened versus smooth bottom). The wave conditions in the Cox and Kobayashi experiments includes a 2.2 s wave period (periodic waves) with a 17.1 cm breaking wave height over a rough bottom. The Ting and Kirby data set used a 2.0 s wave period and had a breaking wave height of 16.3 cm over a smooth bottom. Both conditions are classified as spilling breakers. Not all profile lines are shown.

## CHAPTER 3

### DERIVATION OF GOVERNING EQUATION AND NUMERICAL MODEL DEVELOPMENT

This chapter presents the derivation of the governing equation and its subsequent discretization for the present numerical model of the return flow in the surf zone. Developments for both one-dimensional (1-D) and two-dimensional (2-D) versions of the model are presented (both options are contained in the same program). For the 2-D model, the governing equation is modified to transform the arbitrary domain based on a real beach profile shape to a rectangular, orthogonal domain for solution. Details of the transformation are provided. The performance of the model depends strongly on the selection of boundary conditions. The range of boundary conditions to be applied is discussed at length in Chapter 4. The derivation of the governing equation and its discretization are quite lengthy, particularly for the 2-D case. The full discretization, including a listing of all coefficients used, is contained in Appendix A. A complete listing of the computer code written in FORTRAN90 is found in Appendix B.

The modeled flow field extends vertically from the mean water surface to the seabed and horizontally from the shoreline out well beyond the surf zone. The governing equation is obtained through cross-differentiating the two-dimensional Navier-Stokes equations for turbulent flow (e.g. the Reynolds equations). The resulting third-order partial differential equation (PDE) in terms of velocity is then recast in terms of the stream function, ultimately producing a fourth-order PDE that retains the generalization of time

dependence and a non-uniform eddy viscosity field. This turbulent eddy viscosity,  $\epsilon$ , is considered a variable quantity in both the cross-shore ( $x$ ) and vertical ( $z$ ) directions.

This development, simplified by the assumption of uniform eddy viscosity and steady state, produces the well-known biharmonic equation. The biharmonic equation can also describe creeping flows of constant molecular viscosity. In the present application the addition of time dependence and variable eddy viscosity significantly alters the governing equation, making analytic solutions obtainable for only the simplest of geometries and viscosity fields and thus prompting a numerical approach to the problem.

### 3.1 Derivation of Governing Equation

To begin, consider the two-dimensional equations of motion given in Equations (3.1) and (3.2) and defined as shown in Figure 3.1. Dally (1980), among others, showed that by time averaging Eqs. (3.1) and (3.2) over a long period, neglecting the acceleration terms on the left hand side of the equations, and cross-differentiating the equations, the biharmonic equation ( $\nabla^4 \psi = 0$ ) for the mean flow can be obtained by assuming uniform viscosity (Dally simply replaced the molecular viscosity with the eddy viscosity).

$$\frac{\partial u}{\partial t} + \frac{\partial u^2}{\partial x} + \frac{\partial uw}{\partial z} = -\frac{1}{\rho} \frac{\partial p}{\partial x} + \frac{1}{\rho} \left( \frac{\partial \tau_{xx}}{\partial x} + \frac{\partial \tau_{zz}}{\partial z} \right) \quad (3.1)$$

$$\frac{\partial w}{\partial t} + \frac{\partial uw}{\partial x} + \frac{\partial w^2}{\partial z} = -\frac{1}{\rho} \frac{\partial p}{\partial z} - g_z + \frac{1}{\rho} \left( \frac{\partial \tau_{xz}}{\partial x} + \frac{\partial \tau_{zz}}{\partial z} \right) \quad (3.2)$$

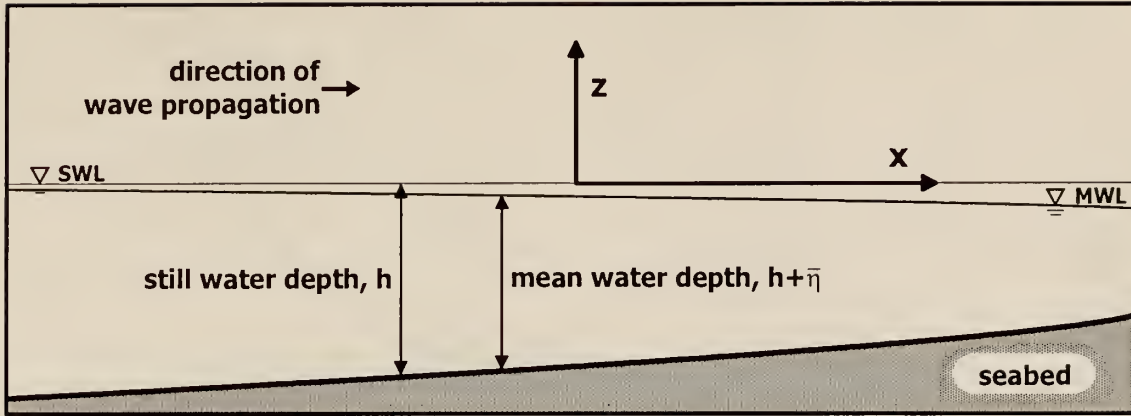


Figure 3.1 Definition sketch for model development (setdown of the MWL shown).

The shear stress terms in Eqs. (3.1) and (3.2) are defined as follows:

$$\tau_{zx} = \tau_{xz} = \rho v \left( \frac{\partial u}{\partial z} + \frac{\partial w}{\partial x} \right) \quad (3.3)$$

$$\tau_{xx} = 2\rho v \left( \frac{\partial u}{\partial x} \right) \quad (3.4)$$

$$\tau_{zz} = 2\rho v \left( \frac{\partial w}{\partial z} \right) \quad (3.5)$$

Dally (1980) derived the biharmonic equation by neglecting acceleration terms, directly substituting the eddy viscosity for the molecular viscosity in Eqs. (3.3) through (3.5) and cross-differentiating the time average of Eqs. (3.1) and (3.2). This approach produces the same PDE, but is somewhat misleading because the contribution to the mean flow field from the turbulent eddy viscosity arises from the nonlinear advective acceleration terms in Eqs. (3.1) and (3.2), the terms that Dally considered negligible. A more rigorous approach, applying the classic Reynolds equations for turbulent flow, traces the introduction of the turbulent eddy viscosity into the problem and provides a clearer picture

of the individual components that contribute to the variation of the eddy viscosity across the surf zone. The reader is referred to Schlichting (1968) for more information regarding the Reynolds equations.

The derivation of the Reynolds equations for turbulent flow from the Navier-Stokes equations (Eqs. (3.1) and (3.2)) requires the decomposition of the velocity terms  $u$  and  $w$  into steady and fluctuating components:

$$u = U + \tilde{u} + u' \quad w = W + \tilde{w} + w' \quad (3.6)$$

where  $U$  and  $W$  represent the mean flow components in the horizontal and vertical directions, respectively,  $\tilde{u}$  and  $\tilde{w}$  represent the oscillating wave orbital motions, and  $u'$  and  $w'$  represent the fluctuating turbulent components of the flow. Substitution of these decompositions into Eqs. (3.1) and (3.2) and subsequent time averaging (denoted by the overbar) over a representative wave period, such as the peak or modal period, yields:

$$\begin{aligned} & \frac{\partial \overline{(U+\tilde{u}+u')}}{\partial t} + \frac{\partial}{\partial x} [\overline{U^2} + \overline{2U\tilde{u}} + \overline{2Uu'} + \overline{2\tilde{u}u'} + \overline{\tilde{u}^2} + \overline{u'^2}] \\ & + \frac{\partial}{\partial z} [\overline{UW} + \overline{U\tilde{w}} + \overline{Uw'} + \overline{\tilde{u}W} + \overline{u'W} + \overline{\tilde{u}\tilde{w}} + \overline{\tilde{u}w'} + \overline{u'\tilde{w}} + \overline{u'w'}] \\ & = -\frac{1}{\rho} \frac{\partial \overline{p}}{\partial x} + \frac{\partial}{\partial x} [2v \frac{\partial}{\partial x} \overline{(U+\tilde{u}+u')}] \\ & + \frac{\partial}{\partial z} [v(\frac{\partial}{\partial z} \overline{(U+\tilde{u}+u')}) + \frac{\partial}{\partial x} \overline{(W+\tilde{w}+w')}] \end{aligned} \quad (3.7)$$

$$\begin{aligned} & \frac{\partial \overline{(W+\tilde{w}+w')}}{\partial t} + \frac{\partial}{\partial x} [\overline{WU} + \overline{W\tilde{u}} + \overline{Wu'} + \overline{\tilde{u}W} + \overline{u'W} + \overline{\tilde{u}\tilde{w}} + \overline{\tilde{u}w'} + \overline{u'\tilde{w}} + \overline{u'w'}] \\ & + \frac{\partial}{\partial z} [\overline{W^2} + \overline{2W\tilde{w}} + \overline{2Ww'} + \overline{2\tilde{w}w'} + \overline{\tilde{w}^2} + \overline{w'^2}] = g - \frac{1}{\rho} \frac{\partial \overline{p}}{\partial z} \\ & + \frac{\partial}{\partial x} [v(\frac{\partial}{\partial z} \overline{(U+\tilde{u}+u')}) + \frac{\partial}{\partial x} \overline{(W+\tilde{w}+w')}] + \frac{\partial}{\partial z} [2v \frac{\partial}{\partial z} \overline{(W+\tilde{w}+w')}] \end{aligned} \quad (3.8)$$

Many of the product terms in Eqs. (3.7) and (3.8) time average to zero. Following the classic eddy viscosity model first introduced by Boussinesq, some of the nonlinear terms are related to the mean flow as “apparent” shear stresses (denoted by the primes), which are similar in form to the viscous shear stresses in Eqs. (3.3) through (3.5):

$$\tau'_{zz} = \tau'_{xz} = -\rho \overline{u'w'} - \rho \overline{\tilde{u}\tilde{w}} - \rho \overline{\tilde{u}w'} - \rho \overline{u'\tilde{w}} = \rho \epsilon \left( \frac{\partial U}{\partial z} + \frac{\partial W}{\partial x} \right) \quad (3.9)$$

$$\tau'_{xx} = -\rho \overline{u'^2} - \rho \overline{\tilde{u}^2} - 2\rho \overline{\tilde{u}u'} = 2\rho \epsilon \left( \frac{\partial U}{\partial x} \right) \quad (3.10)$$

$$\tau'_{zz} = -\rho \overline{w'^2} - \rho \overline{\tilde{w}^2} - 2\rho \overline{\tilde{w}w'} = 2\rho \epsilon \left( \frac{\partial W}{\partial z} \right) \quad (3.11)$$

These definitions of the apparent shear stresses differ slightly from the classic definitions due to the inclusion of the wave orbital motion terms. Careful inspection of Eqs. (3.9) through (3.11) indicates which terms have been treated as zero after time averaging and which terms have been retained in Eqs (3.12) and (3.13). From Eq. (3.7) the last three components of the x-gradient term have been retained, along with the last four components of the z-gradient term (Eq. (3.12)). From Eq. (3.8) the last four components of the x-gradient term and the last three components of the z-gradient term have been retained (Eq. (3.13)). The remaining components have been taken as zero after time averaging. This assumption neglects the acceleration of the mean flow (terms such as the time average of  $U^2$ ) and seems reasonable in the inner surf zone, and even more reasonable outside the surf zone. In the outer surf zone, or transition region, this assumption is more suspect, but for present purposes these terms are neglected.

The terms retained in Eqs. (3.9) through (3.11) represent various contributions to the apparent stress from turbulence and wave motion. The first terms retained, those containing only  $u'$  and/or  $w'$ , represent the classic Reynolds normal and shear stresses in turbulent flow. The terms involving only  $\tilde{u}$  and/or  $\tilde{w}$  represent wave shear and normal stresses (the reader will note from the discussion in Chapter 2 that the gradient in time averaged values of  $\tilde{u}^2$  and  $\tilde{w}^2$  represent the radiation stress (Longuet-Higgins and Stewart, 1962)). In the present development, no details of wave induced flows are included and these terms are incorporated into the turbulent eddy viscosity representation.

The non-linear terms may or may not be significant in various parts of the surf zone. Inside the surf zone, it is assumed that the turbulent Reynolds shear stresses are the primary source of turbulent diffusion, generated by the breaking waves. Outside the surf zone, the importance of the Reynolds stresses is unclear and the wave shear stresses may play a greater role. These terms were investigated by Rivero and Arcilla (1995), who demonstrated that the time-average of quantities such as  $\tilde{u}\tilde{w}$  is not zero for waves shoaling on sloping beds. The magnitude of these wave stresses is not well known, however, their inclusion in the model provides a plausible mechanism for applying turbulent diffusion seaward of the break point.

The cross product terms, such as the time average of  $u'\tilde{w}$ , represent the possible stresses arising from the transport of turbulence by the wave orbital motion. Again, the importance of these terms relative to the Reynolds stresses is unclear, but they are included in the apparent shear stress terms for completeness. It is important to realize that quantifying the eddy viscosity is a difficult task, given that  $\epsilon$  is both a property of the fluid and the flow. However, the need to quantify each of the nonlinear terms in Eqs. (3.7) and (3.8) is relieved by grouping them into the eddy viscosity form of Eqs. (3.9) through (3.11).

Substituting the apparent stresses with the viscous shear stresses into Eqs. (3.7) and (3.8) and dropping the terms that equal zero after time averaging over a representative wave period produces the Reynolds equations for the mean flow:

$$\begin{aligned}\frac{\partial U}{\partial t} &= -\frac{1}{\rho} \frac{\partial \bar{p}}{\partial x} + \frac{1}{\rho} \frac{\partial}{\partial x} \left[ \rho v \frac{\partial U}{\partial x} + 2\rho\epsilon \frac{\partial U}{\partial x} \right] \\ &\quad + \frac{1}{\rho} \frac{\partial}{\partial z} \left[ \rho v \frac{\partial U}{\partial z} + \rho\epsilon \left( \frac{\partial U}{\partial z} + \frac{\partial W}{\partial x} \right) \right]\end{aligned}\tag{3.12}$$

$$\begin{aligned}\frac{\partial W}{\partial t} &= g - \frac{1}{\rho} \frac{\partial \bar{p}}{\partial z} + \frac{1}{\rho} \frac{\partial}{\partial x} \left[ \rho v \frac{\partial W}{\partial x} + \rho\epsilon \left( \frac{\partial U}{\partial z} + \frac{\partial W}{\partial x} \right) \right] \\ &\quad + \frac{1}{\rho} \frac{\partial}{\partial z} \left[ \rho v \frac{\partial W}{\partial z} + 2\rho\epsilon \frac{\partial W}{\partial z} \right]\end{aligned}\tag{3.13}$$

In general, the viscous terms in Eqs. (3.12) and (3.13) are much smaller than the turbulent eddy viscosity terms ( $\nu \ll \epsilon$ ). These terms will be neglected. Cross-differentiation of the two equations produces the following third order PDE, in which the pressure terms have canceled and  $g$  is assumed to be invariant in  $x$ :

$$\begin{aligned}\frac{\partial}{\partial t} \left( \frac{\partial U}{\partial z} - \frac{\partial W}{\partial x} \right) &= \frac{\partial^2 (2\epsilon \frac{\partial U}{\partial x})}{\partial x \partial z} - \frac{\partial^2 (\epsilon \frac{\partial U}{\partial z})}{\partial z^2} + \frac{\partial^2 (\epsilon \frac{\partial W}{\partial x})}{\partial z^2} \\ &\quad - \frac{\partial^2 (\epsilon \frac{\partial U}{\partial z})}{\partial x^2} + \frac{\partial^2 (\epsilon \frac{\partial W}{\partial x})}{\partial x^2} - \frac{\partial^2 (2\epsilon \frac{\partial W}{\partial z})}{\partial x \partial z}\end{aligned}\tag{3.14}$$

A stream function notation is adopted for the mean flow such that:

$$U = -\frac{\partial \Psi}{\partial z} \quad W = \frac{\partial \Psi}{\partial x}\tag{3.15}$$

which modifies Eq. (3.14) to read:

$$\begin{aligned}
 -\frac{\partial}{\partial t} \left( \frac{\partial^2 \psi}{\partial z^2} + \frac{\partial^2 \psi}{\partial x^2} \right) &= -\frac{\partial^2 (2\epsilon \frac{\partial^2 \psi}{\partial x \partial z})}{\partial x \partial z} - \frac{\partial^2 (\epsilon \frac{\partial^2 \psi}{\partial z^2})}{\partial z^2} + \frac{\partial^2 (\epsilon \frac{\partial^2 \psi}{\partial x^2})}{\partial z^2} \\
 &\quad + \frac{\partial^2 (\epsilon \frac{\partial^2 \psi}{\partial z^2})}{\partial x^2} - \frac{\partial^2 (\epsilon \frac{\partial^2 \psi}{\partial x^2})}{\partial x^2} - \frac{\partial^2 (2\epsilon \frac{\partial^2 \psi}{\partial x \partial z})}{\partial x \partial z}
 \end{aligned} \tag{3.16}$$

It is recognized that Equation (3.16) is very similar to the equation describing the transport of vorticity due to turbulent diffusion. The term on the left hand side of Eq. (3.16) is the time derivative of the Laplacian of  $\psi$ , which is equal to  $-\omega$ , where  $\omega$  represents the vorticity in the fluid ( $\nabla^2 \psi = -\omega$ ).

The application of the 2-D model will be presented in terms of uniform and non-uniform eddy viscosity. With uniform eddy viscosity, Eq (3.16) is simplified (subscript notation for all derivatives is adopted at this point):

$$(\Psi_{xx} + \Psi_{zz})_t = \epsilon (\Psi_{xxxx} + 2\Psi_{xx}\Psi_{zz} + \Psi_{zzzz}) \tag{3.17}$$

and the additional assumption of steady flow (over a long period) produces the biharmonic equation:

$$\Psi_{xxxx} + 2\Psi_{xx}\Psi_{zz} + \Psi_{zzzz} = 0 \tag{3.18}$$

As mentioned, Equation (3.18) is commonly known as the biharmonic equation, and can be used to describe the creeping flow of viscous fluids. While the analogy to creeping flow

is not particularly relevant, the steady state version of the equation developed herein is identical to the biharmonic equation if the turbulent eddy viscosity is uniform, thus the few existing analytical solutions for creeping flow situations can be used to test the present model in simple geometries.

Dally (1980) presents an analytic series solution to Eq. (3.18) and attempts to model the horizontal fluid momentum resulting from a surface shear stress applied over a finite length. The results of the analysis by Dally, while limited, provide the impetus for the development of the present approach to return flow modeling. One distinct advantage of this approach is that cross-differentiation has removed the necessity to describe the pressure variation in the flow. Inclusion of a spatially variable eddy viscosity field and the numerical solution provides the opportunity to model the return flow more realistically.

The partial derivatives in Eq. (3.16) are expanded, maintaining that  $\epsilon = \epsilon(x,z)$ . Eq. (3.19) represents the partial differential equation to be modeled in the  $x-z$  domain:

$$\begin{aligned} \Psi_{ztt} + \Psi_{xxt} &= \epsilon \Psi_{xxxx} + 2\epsilon \Psi_{xxzz} + \epsilon \Psi_{zzzz} \\ &+ 2\epsilon_x \Psi_{xxx} + 2\epsilon_z \Psi_{xxz} + 2\epsilon_x \Psi_{xzz} + 2\epsilon_z \Psi_{zzz} \\ &+ (\epsilon_{xx} - \epsilon_{zz}) \Psi_{xx} + 4\epsilon_{xz} \Psi_{xz} + (\epsilon_{zz} - \epsilon_{xx}) \Psi_{zz} \end{aligned} \quad (3.19)$$

### 3.2 Development of One-Dimensional Model

For a simple investigation of the vertical variation of the horizontal velocity in the return flow profile, Eq. (3.19) is simplified and solved numerically. The 1-D partial differential equation in  $z$  is:

$$\Psi_{ztt} = \epsilon \Psi_{zzzz} + 2\epsilon_z \Psi_{zzz} + \epsilon_{zz} \Psi_{zz} \quad (3.20)$$

Eq. (3.19) is discretized using central difference approximations for the spatial gradients in the body of the model domain (to second order in  $\Delta z$ ). The time derivative is modeled as a forward difference approximation, and is represented in a variable, semi-implicit fashion by the inclusion of the time-weighting term,  $\theta$ . The model domain is illustrated in Figure 3.2. The fourth-order derivative in  $z$  yields five terms after discretization; upon collection of all  $\psi_j$  terms, the following finite difference equation results, involving five different points in the domain at two successive times, where  $n$  is the time axis ( $n$  is the time at the previous time step,  $n+1$  is at the new time step). In the 1-D model the vertical origin is taken at the seabed.

$$\begin{aligned}
 & [\psi_{j-1} - 2\psi_j + \psi_{j+1}]^{n+1} = \\
 & \theta \frac{\Delta t}{(\Delta z)^2} [(\epsilon_j - \Delta z \epsilon_{z_j}) \psi_{j-2} + (-4\epsilon_j + 2\Delta z \epsilon_{z_j} + (\Delta z)^2 \epsilon_{zz_j}) \psi_{j-1} \\
 & + (6\epsilon_j - 2(\Delta z)^2 \epsilon_{zz_j}) \psi_j + (-4\epsilon_j - 2\Delta z \epsilon_{z_j} + (\Delta z)^2 \epsilon_{zz_j}) \psi_{j+1} + (\epsilon_j - \Delta z \epsilon_{z_j}) \psi_{j+2}]^{n+1} \\
 & + (1-\theta) \frac{\Delta t}{(\Delta z)^2} [(\epsilon_j - \Delta z \epsilon_{z_j}) \psi_{j-2} + (-4\epsilon_j + 2\Delta z \epsilon_{z_j} + (\Delta z)^2 \epsilon_{zz_j}) \psi_{j-1} \\
 & + (6\epsilon_j - 2(\Delta z)^2 \epsilon_{zz_j}) \psi_j + (-4\epsilon_j - 2\Delta z \epsilon_{z_j} + (\Delta z)^2 \epsilon_{zz_j}) \psi_{j+1} + (\epsilon_j - \Delta z \epsilon_{z_j}) \psi_{j+2}]^n \\
 & + [\psi_{j-1} - 2\psi_j + \psi_{j+1}]^n
 \end{aligned} \tag{3.21}$$

The value of  $\theta$  can be modified to run the model in a fully implicit fashion ( $\theta=1$ ), a fully explicit fashion ( $\theta=0$ ), or any intermediate value. Setting  $\theta=0.5$  is equivalent to using the well known scheme introduced by Crank and Nicholson (1947). The variable implicitness is included to alleviate the time step restrictions of the process modeled, which is similar to modeling the diffusion of vorticity. In a fully explicit scheme, the time step is limited to the following value:

$$\Delta t = \frac{(\Delta z)^2}{2\epsilon} \tag{3.22}$$

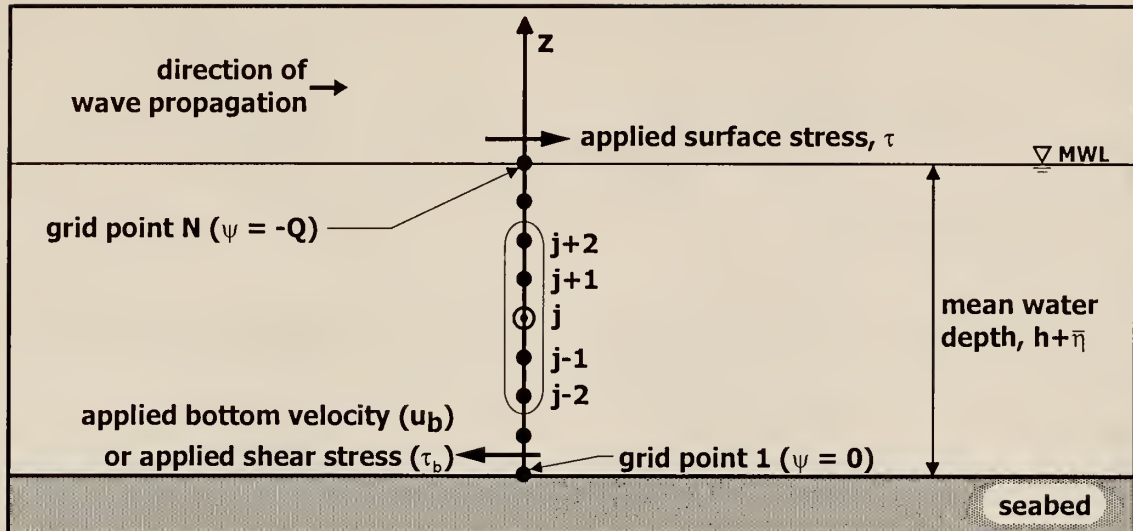


Figure 3.2 Definition sketch for one-dimensional model. The figure illustrates the four applied boundary conditions and five-point solution cell.

which is quite restrictive, resulting in long run times in a 2-D model. The use of a semi-implicit or fully implicit scheme with  $\theta > 0.5$  allows for a much larger time step to be employed, one closer to the order of the physical forcing mechanism in the model, with unconditional stability and convergence (Smith, 1985). It does not, however, guarantee convergence to the correct answer for any time step value. In the present case, the physical time step is controlled by the eddy viscosity, not the wave period. The appropriate choice of time step is discussed in the model validation portion of this work (Chapter 5).

It is noted that higher values of  $\theta$  introduce artificial numerical diffusion (smoothing) into the modeling process. For this reason the value of  $\theta$  is kept at approximately 0.5 to gain the benefit of the relaxed time step requirement but not introduce excessive numerical diffusion. Since it is not the goal of this work to exercise the details of numerical modeling, the reader is referred to any number of numerical modeling texts, such as Hoffman (1989) and Smith (1985). In the models,  $\theta$  is set to 0.51, and the model is exercised at a range of time steps to assure consistency in the final answers.

### 3.2.1 Boundary Conditions for One-Dimensional Model

Application of Eq. (3.21) requires the specification of four boundary conditions (Figure 3.2). As with any numerical model, the selection and implementation of the proper boundary conditions represents a substantial fraction of the modeling task. Recent literature regarding return flow modeling is dominated by the discussion of the proper choice of boundary conditions, and the present model is no exception. The detailed selection of boundary condition values is found in Chapter 4, and the mechanics of applying the boundary conditions in the model are found in Appendix A. The boundary conditions applied herein are those described by Longuet-Higgins (1953) for establishing shear stress, velocity, and stream function value conditions at the boundaries.

In the 1-D model, four boundary conditions and one initial condition are required to produce the desired vertical profile of the stream function. Two of the boundary conditions are simply the specification of the value of the stream function at the seabed and at the Mean Water Level (MWL). The difference in these two conditions dictates the flow rate through the model domain, thus assuring that flow is conserved based on the computed volumetric transport,  $Q$ , of the wave being modeled. Generally, the value of  $\psi$  is set to zero at the seabed and the surface value is specified as  $\psi = -Q$ , where  $Q$  is the forward volumetric transport of the wave and  $-Q$  is the flowrate through the model domain (this results in positive  $\psi$  values, generally producing offshore return flows based on Eq. 3.15).

The third condition is the application of a surface shear stress caused by the passage of the waves. Outside the surf zone this stress may be the result of the gradient in wave height due to shoaling, while inside the surf zone the shear stress is created by the wave height gradient caused by breaking. In terms of  $\psi$ , the shear stress condition is equivalent to a second-derivative condition at the surface. The final boundary condition is applied at

the seabed and the option is given of specifying either the tangential bottom velocity or tangential shear stress condition. The bottom velocity is specified by the first derivative of  $\psi$  with respect to  $z$ .

The initial condition for the model is generally that of a quiescent condition, or “cold start,” where the values of  $\psi$  in the body of the domain are set to zero. The surface boundary conditions then provide the driving force to the problem. As an alternative, an initial estimate of the vertical profile can be provided, either from an assumed profile or from the results of another simulation. This would provide a “hot start” to the model and lead to a steady-state solution in fewer time steps. A steady state solution in the 1-D model is quickly determined and provision of a “hot-start” condition is not needed. In the time-dependent 2-D cases, a good initial estimate is beneficial.

### 3.2.2 Solution Scheme for One-Dimensional Model

The stream function values across the model domain at the  $n+1$  time step are solved simultaneously after creating a 5-band diagonal matrix of  $N-2$  equations using Eq. (3.21). Because the values of  $\psi$  at the surface and bottom are given by the boundary conditions, the matrix and vectors have the dimension  $N-2$ . The boundary conditions are input directly to the matrices and vectors. The program employs two subroutines from the Numerical Recipes suite of routines (Press et al., 1986). The first routine (BANDEC) performs a lower-upper (LU) decomposition on the matrix. These matrices are then sent to the second subroutine (BANBKS) which performs a back substitution operation to solve for the vector of  $\psi$  values. In the 1-D model, only one performance of each routine is required at each time step. Other routines are available to perform the same operations, such as the IMSL routine LSARB.

In time-dependent simulations, the values of the stream function at each point are averaged over many waves to produce the final mean stream function profile, such as to simulate the return flow produced by a random wave field. Intermediate values of the solutions are stored in order to observe the time scales at which the profile evolves due to changes in the input wave parameters. The computer program proceeds to process the values of stream function to produce as output a list of the horizontal velocity and the shear stress, both as the mean value and at any desired intermediate time steps. An example of the model output for uniform eddy viscosity and monochromatic waves is shown in Figure 3.3 for input values matching those used in the return flow discussion of Dean (1995). The computer program is provided in Appendix B.

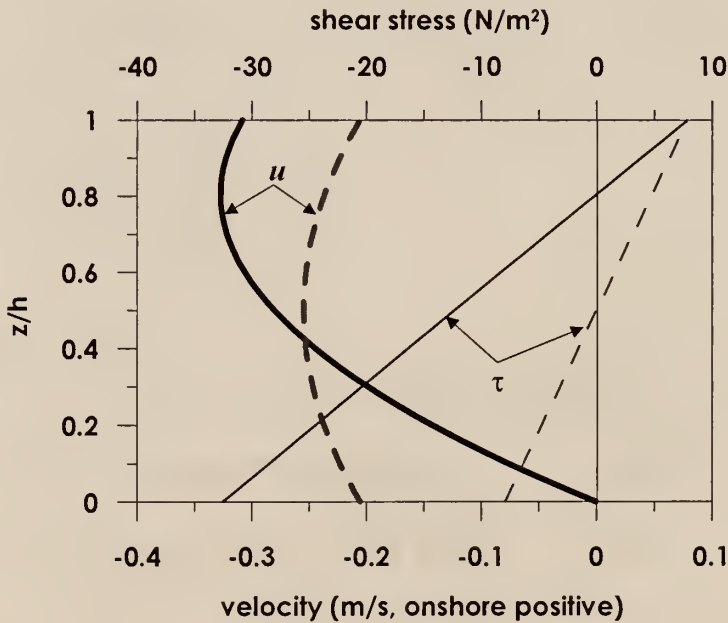


Figure 3.3 Example output from one-dimensional return flow model. The solid lines present the velocity and shear stress distributions assuming a zero bottom velocity boundary condition. The broken lines present the velocity and shear stress distributions assuming a bottom shear stress boundary condition defined to be equal in magnitude and opposite in sign of the applied surface stress ( $m = -1.0$ ). Input values for these examples were chosen to match those used by Dean, 1995, and the zero velocity boundary condition case matches Dean's example ( $H = 0.78$  m,  $h = 1.0$  m,  $\epsilon = 0.04$  m $^2$ /s,  $\tau_s = 7.9$  m $^2$ /s).

### 3.3 Development of Two-Dimensional Return Flow Model

Building on the 1-D model, Eq. (3.19) is revisited and applied in the 2-DV nearshore region. The same boundary conditions used in the 1-D model apply to the 2-D model, with the addition of four more boundary conditions in the horizontal direction, i.e. sidewall boundary conditions. Since Eq. (3.19) is written for the physical,  $x$ - $z$  coordinate system, a coordinate stretching scheme is implemented to allow for the modeling of arbitrary beach profiles. This coordinate stretching simply non-dimensionalizes the vertical coordinate, but lengthens the derivation substantially. For clarity, only the pertinent equations are given in this chapter. Appendix A contains the full development.

#### 3.3.1 Transformation of the Partial Differential Equation

Figure 3.4 illustrates the procedure used to transform the physical geometry of the nearshore region into an orthogonal computational domain. Following Hoffman (1989) the vertical coordinate is non-dimensionalized by the local water depth (Eq. (3.23)). This simple grid-stretching technique allows for the modeling of any profile (Figure 3.4). As contrasted to the 1-D model, the 2-D model will take as the vertical origin the Still Water Level to maintain a horizontal datum since setup and setdown effects will be included, thus grid point #1 corresponds to the surface and grid point  $\#N_j$  applies to the seabed.

$$\eta = z/h \quad (3.23)$$

Transformation of Eq. (3.19) from the  $x$ - $z$  domain to the  $\xi$ - $\eta$  domain simply involves repeated applications of the chain rule for derivatives, as demonstrated below:

$$\frac{\partial \Psi}{\partial z} = \frac{\partial \xi}{\partial z} \frac{\partial \Psi}{\partial \xi} + \frac{\partial \eta}{\partial z} \frac{\partial \Psi}{\partial \eta} \quad (3.24)$$

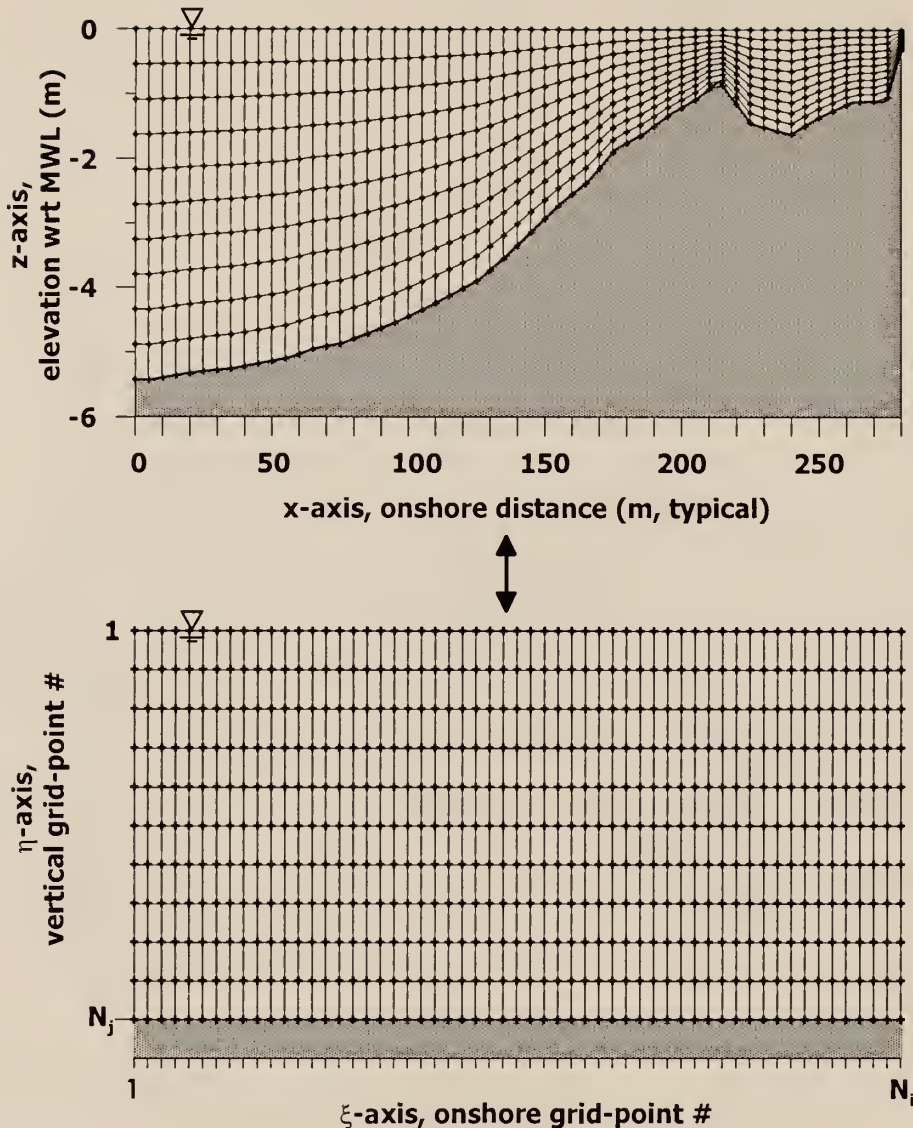


Figure 3.4 Definition sketch of coordinate transformation between the physical,  $x$ - $z$ , domain and the computational,  $\xi$ - $\eta$ , domain.

The approach throughout this derivation will be to separate the time-dependent terms from those that comprise the steady state solution. This produces several more terms and coefficients but makes the operation of the model much clearer. Each term in  $\psi$  in Eq. (3.19) is expanded; including the eddy viscosity terms. Carrying the chain rule through the fourth-order PDE produces additional lower order derivatives of  $\psi$  due to the coordinate

transformation required. The transformed PDE from Eq. (3.19) is:

$$\begin{aligned} [B1\psi_{\xi\xi} + B2\psi_{\xi\eta} + B3\psi_{\eta\eta} + B4\psi_\xi + B5\psi_\eta]_t &= \\ A1\psi_{\xi\xi\xi\xi} + A2\psi_{\xi\xi\xi\eta} + A3\psi_{\xi\xi\eta\eta} + A4\psi_{\xi\eta\eta\eta} + A5\psi_{\eta\eta\eta\eta} \\ + A6\psi_{\xi\xi\xi} + A7\psi_{\xi\xi\eta} + A8\psi_{\xi\eta\eta} + A9\psi_{\eta\eta\eta} \\ + A10\psi_{\xi\xi} + A11\psi_{\xi\eta} + A12\psi_{\eta\eta} + A13\psi_\xi + A14\psi_\eta \end{aligned} \quad (3.25)$$

where the left hand side represents the time dependent terms and the right hand side represents the steady state solution. Each of the 19 coefficients in Eq. (3.25) contains the transformation details of each derivative. As an example, one of the more lengthy coefficients is given below; all the coefficients are defined in Appendix A. The values of  $\epsilon_x$ ,  $\epsilon_z$ ,  $\epsilon_{xx}$ ,  $\epsilon_{zz}$ , and  $\epsilon_{xz}$  that appear in the coefficients of Eq. (3.25) also must be expanded to account for the coordinate transformation via Eqs. (3.23) and (3.24). The value of coefficient A8 from Eq. (3.24) is given to demonstrate the number of terms involved:

$$\begin{aligned} A8 = [ & \epsilon(12\xi_x\eta_x\eta_{xx} + 6\xi_{xx}\eta_x^2 + 2\xi_{xx}\eta_z^2 + 4\xi_x\eta_x\eta_{zz} + 8\xi_x\eta_z\eta_{xz} \\ & + 8\xi_{xz}\eta_x\eta_z + 8\xi_z\eta_x\eta_{xz} + 4\xi_z\eta_{xx}\eta_z + 2\xi_{zz}\eta_x^2 + 6\xi_{zz}\eta_z^2 + 12\xi_z\eta_z\eta_{zz}) \\ & + \epsilon_x(6\xi_x\eta_x^2 + 2\xi_x\eta_z^2 + 4\xi_z\eta_x\eta_z) + \epsilon_z(4\xi_x\eta_x\eta_z + 2\xi_z\eta_x^2 + 6\xi_z\eta_z^2) ] \end{aligned} \quad (3.26)$$

### 3.3.2 Discretization of the Two-Dimensional PDE

Eq. (3.25) is now discretized for the numerical solution of  $\psi$  on the interior points of the grid (recall that the values of the stream function along the edges are specified as boundary conditions, as in the 1-D model). Figure 3.5 compares the discretized solution cell for the  $x$ - $z$  domain versus the solution cell for the transformed  $\xi$ - $\eta$  domain. The transformation process adds an additional eight points to the finite-difference equation.

Eq. (3.25) is discretized using central difference spatial approximations of  $\psi$  with a forward difference approximation in time. As in the 1-D model, the equation includes

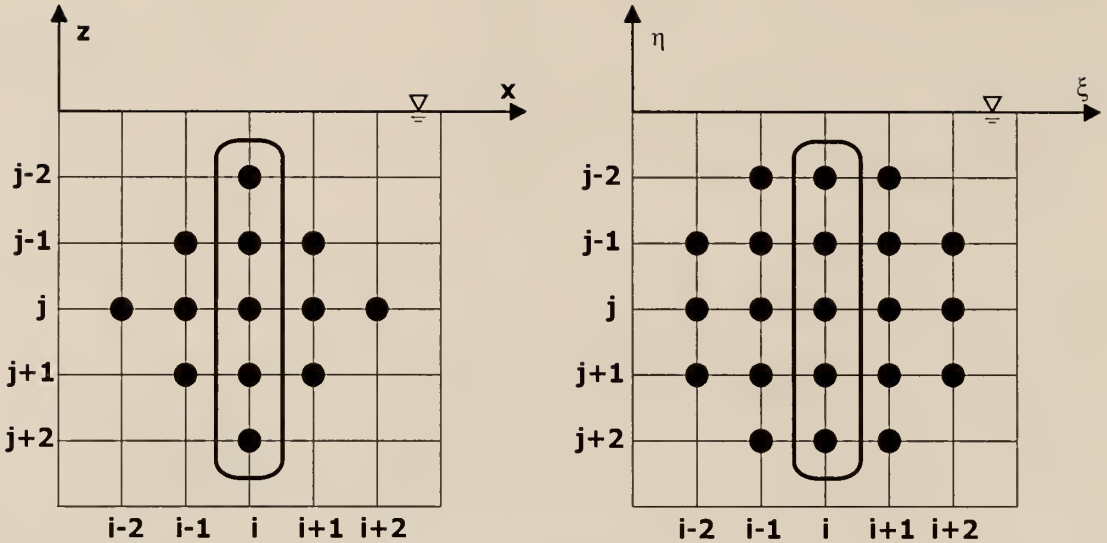


Figure 3.5 Solution cells for the fourth-order finite difference equation in the  $x$ - $z$  domain and the transformed  $\xi$ - $\eta$  domain. The five circled points on column  $i$  represent the solution points in the set of simultaneous equations. Row  $j=1$  corresponds to the surface row.

a variable degree of implicitness in the solution, represented by the value of  $\theta$ . Again, efforts are made to separate those terms arising from the time derivative from those arising from the spatial derivatives. In a somewhat schematic way, the equation is discretized as follows:

$$[\text{time dep. terms}]^{n+1} - [\text{time dep. terms}]^n = \theta \Delta t [\text{s.s. solution terms}]^{n+1} + (1-\theta) \Delta t [\text{s.s. solution terms}]^n \quad (3.27)$$

In Eq. (3.27) the time dependent terms on the left hand side are the discretized forms of the left hand side of Eq. (3.25), while the steady state (s.s.) solution terms are the discretized forms of the right hand side of Eq. (3.25). The full, discretized equation is

given by Eq. (3.28). As written, Eq. (3.28) would produce 21 solution points at the  $n+1$  time step, as opposed to the previous five points in the 1-D model. This presents a problem in establishing a spatially consistent and still manageable matrix of coefficients to solve for simultaneously. This problem is relieved by moving any points that do not reside on the  $i^{th}$  column to the right hand side and solving the system of equations iteratively at each time step (refer to Figure 3.5). Appendix A contains the definitions and rationale behind the assignment of coefficients. A typical steady-state coefficient, corresponding to the  $[j,i]$  point in the solution cell in Eq. (3.28), is presented in Eq. (3.29):

$$\begin{aligned}
& [ DR1\psi_{j-1, i-1} + DR2\psi_{j, i-1} + DR3\psi_{j+1, i-1} \\
& \quad + DL1\psi_{j-1, i} + DL2\psi_{j, i} + DL3\psi_{j+1, i} \\
& \quad + DR4\psi_{j-1, i+1} + DR5\psi_{j, i+1} + DR6\psi_{j+1, i+1} ]^{n+1} \\
& - [ DR1\psi_{j-1, i-1} + DR2\psi_{j, i-1} + DR3\psi_{j+1, i-1} \\
& \quad + DL1\psi_{j-1, i} + DL2\psi_{j, i} + DL3\psi_{j+1, i} \\
& \quad + DR4\psi_{j-1, i+1} + DR5\psi_{j, i+1} + DR6\psi_{j+1, i+1} ]^n \\
& = \theta \Delta t [ CR1\psi_{j-1, i-2} + CR2\psi_{j, i-2} + CR3\psi_{j+1, i-2} \\
& \quad + CR4\psi_{j-2, i-1} + CR5\psi_{j-1, i-1} + CR6\psi_{j, i-1} + CR7\psi_{j+1, i-1} + CR8\psi_{j+2, i-1} \quad (3.28) \\
& \quad + CL1\psi_{j-2, i} + CL2\psi_{j-1, i} + CL3\psi_{j, i} + CL1\psi_{j+1, i} + CL5\psi_{j+2, i} \\
& \quad + CR9\psi_{j-2, i+1} + CR10\psi_{j-1, i+1} + CR11\psi_{j, i+1} + CR12\psi_{j+1, i+1} + CR13\psi_{j+2, i+1} \\
& \quad + CR14\psi_{j-1, i+2} + CR15\psi_{j, i+2} + CR16\psi_{j+1, i+2} ]^{n+1} \\
& \quad + (1-\theta)\Delta t [ CRI\psi_{j-1, i-2} + CR2\psi_{j, i-2} + CR3\psi_{j+1, i-2} \\
& \quad + CR4\psi_{j-2, i-1} + CR5\psi_{j-1, i-1} + CR6\psi_{j, i-1} + CR7\psi_{j+1, i-1} + CR8\psi_{j+2, i-1} \\
& \quad + CL1\psi_{j-2, i} + CL2\psi_{j-1, i} + CL3\psi_{j, i} + CL1\psi_{j+1, i} + CL5\psi_{j+2, i} \\
& \quad + CR9\psi_{j-2, i+1} + CR10\psi_{j-1, i+1} + CR11\psi_{j, i+1} + CR12\psi_{j+1, i+1} + CR13\psi_{j+2, i+1} \\
& \quad + CR14\psi_{j-1, i+2} + CR15\psi_{j, i+2} + CR16\psi_{j+1, i+2} ]^n
\end{aligned}$$

$$CL3 = [ \frac{6A1(\Delta\eta)^4}{(\Delta\xi)^4} + \frac{4A3(\Delta\eta)^2}{(\Delta\xi)^2} + 6A5 - 2A10\frac{(\Delta\eta)^4}{(\Delta\xi)^2} - 2A12(\Delta\eta)^2 ] \quad (3.29)$$

### 3.3.3 Boundary Conditions for Two-Dimensional Model

For the two-dimensional model, the boundary conditions are essentially the same as in the one-dimensional case. The value of the stream function along the boundaries is specified, occupying four of the eight boundary conditions needed. Along the bottom and side boundaries,  $\psi$  is generally set to zero, although inflow or outflow could be specified in the model by changing the value of  $\psi$  from one grid point to the next (refer to Eq. (3.15)). The value of  $\psi$  along the surface is specified as before by the modeling of the wave transformation across the surf zone. At each grid point the value of the volumetric transport created by the wave passage is used to establish  $\psi$  at the surface.

The remaining two boundary conditions at the seabed and the surface are also applied in a fashion similar to the 1-D model case. The two remaining conditions along the sidewall are specified as velocity conditions, with the velocity generally set to zero. However, in the cases of both velocity and shear stress specifications, the transformation of coordinates used to achieve a rectangular model domain complicates their application.

As an example, to specify the tangential bottom velocity along a sloping bottom, the continuity equation must be invoked, along with the chain rule to translate the sloping bottom to the rectangular solution domain:

$$U - Wh_x = -\Psi_z - \Psi_x h_x = U_b \sqrt{h_x^2 + 1} \quad (3.30)$$

which when transformed, discretized and solved for the outlying point just below the seabed produces:

$$\begin{aligned} \Psi_{j+2,i} &= -(U_b)_i \sqrt{h_x^2 + 1} \left( \frac{2\Delta\eta}{h_x \eta_x + \eta_z} \right) - \frac{h_x \xi_x + \xi_z \Delta\eta}{h_x \eta_x + \eta_z \Delta\xi} \Psi_{j+1,i+1} \\ &\quad + \frac{h_x \xi_x + \xi_z \Delta\eta}{h_x \eta_x + \eta_z \Delta\xi} \Psi_{j+1,i-1} + \Psi_{j,i} \end{aligned} \quad (3.31)$$

As the reader might imagine, the construction of a proper boundary condition that involves a second derivative of  $\psi$  is substantially more involved. Further difficulties arise at the corners of the model domain, where two separate boundary conditions share common points in the domain that must be solved for simultaneously. The reader is referred to Appendix A for the full development of the boundary conditions in the transformed coordinate system.

### 3.3.4 Solution Scheme for Two-Dimensional Model

The solution scheme for the 2-D model is similar to that used in the 1-D case. A simultaneous set of  $N_i - 2$  equations is solved for the interior values of  $\psi$  at each vertical section (Figure 3.5). The same subroutines used in the 1-D model are employed to solve the system of equations (BANDEC and BANBKS, Press et al., 1986). This process is swept horizontally from the offshore boundary to the shoreline for each time step.

As discussed previously, the method only solves for the five points on the  $i^{th}$  column at the  $n+1$  time step. In the complete formulation, there would be 21 points to solve for (Eq. (3.28)). This presents difficulties in creating a spatially consistent coefficient matrix. As a concession, the off-column points, those with  $R$  in their coefficient labels, are moved to the right hand side of the equation and their respective  $\psi$  values are treated as known. The points moved from the solution side to the known side are then updated in a series of iterations for each time step. This entails tracking three different values of  $\psi$  at each point in the domain, the old value, the new intermediate value (assumed to be known from the previous iteration at each time step), and the newly solved-for value at each iteration.

The passage of waves across the profile represents the driving force in the model and is entirely described by the boundary conditions (no knowledge of the effect of waves

was incorporated in the derivation of the governing equation other than time averaging). The model begins by determining the set-up and set-down of the MWL and the wave height change across the profile for a chosen typical wave height, providing the initial surface boundary condition (the height used is generally either the root-mean-square (RMS) wave height or the significant wave height, adjusted with an appropriate factor). The model runs through a series of time steps comprising the duration of each wave period (generally the modal period for irregular waves), computing the flow field at each step.

The model then changes the surface boundary conditions based on the next randomly chosen wave height, and runs through the same number of time steps. The change in the value of  $\psi$  at the surface is assumed to occur over a single time step. This is clearly erroneous, however, no data were found to describe the lag in flow rate in a surf zone of changing wave conditions. Obviously the narrower the surf zone width the faster the return flow rate will adjust to a change in condition. This is thought to be especially true in a laboratory setting, where the adjustment in set-up and return flow is rapid.

The set-up and set-down remain fixed throughout the run, thus there is no grid adjustment or wetting and drying of cells in the model. The model continually updates the average value of the stream function at each point in the model and periodically can record the instantaneous values in order to study the time evolution of the flow field. At each time step, the model compares the updated flow field to the previous flow field after each iteration and considers the maximum change in the value of  $\psi$  as a cutoff criteria. Figure 3.6 illustrates the operational steps of the numerical model. Validation of the numerical model operation is discussed in Chapter 5.

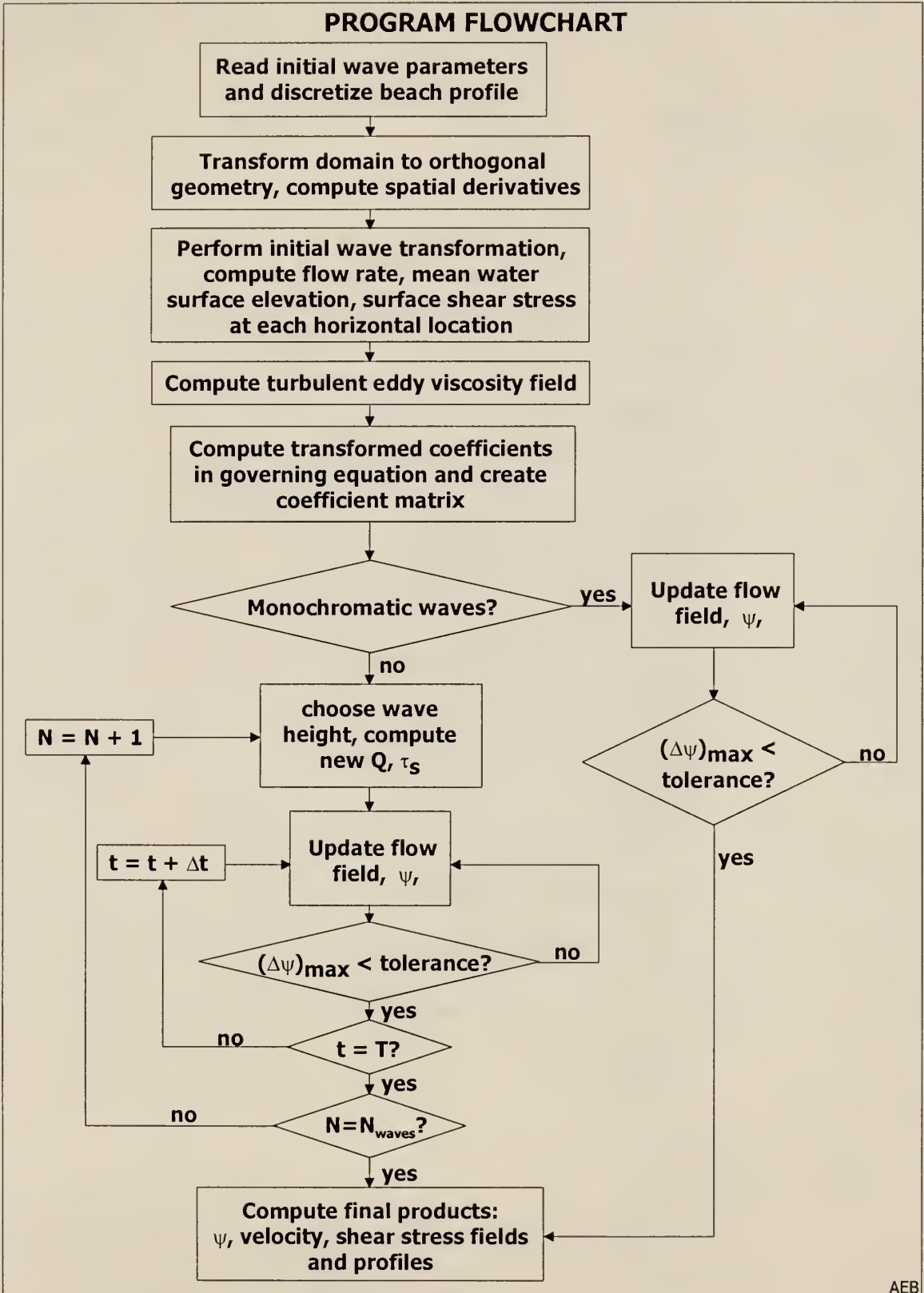


Figure 3.6 Flowchart for two-dimensional numerical model.

## CHAPTER 4

### BOUNDARY CONDITIONS AND TRANSITION REGION TREATMENT

This chapter describes the selection of boundary conditions for use in both the one-dimensional and two-dimensional models. As with any return flow model, the successful prediction of the mean flow field requires careful selection of these conditions. In the present model, this issue is increasingly important, since the use of the fourth order PDE in  $\psi$  requires the application of four boundary conditions in each direction, as opposed to the customary two conditions applied in the simpler equation for  $U$ . Chapter 2 introduced the literature regarding the development of return flow models and their boundary conditions, and Appendix A details the mechanics of applying the conditions in the numerical model.

In this chapter, the options and resultant values applied for each boundary condition are discussed. In many cases, there is more than one option available for each condition. These options will be presented herein and the merits of each will be demonstrated in following chapters. Further, the chosen values are expected to differ significantly between the region seaward of the break point and the surf zone. The applicable mechanisms and equations employed to determine the conditions will also differ. The difficulty of matching conditions across the entire profile arises in most models of the return flow. The details of how a wave transforms in shape, transport, and momentum across the transition region between the break point and the beginning of the inner surf zone, is an area of active

interest. Herein, two methods are applied to smoothly connect the region seaward of the break point to the inner surf zone while maintaining conservation of momentum.

#### 4.1 Wave Height Transformation

In order to determine the two surface boundary conditions it is necessary to describe the wave height across the entire beach profile. This description includes the shoaling region from the offshore boundary to the first break point, the breaker zone, and any intermediate wave reformation and secondary breaker zones within the surf zone.

To begin, the wave height at the offshore boundary is determined. This height can be given directly if known, or the corresponding offshore wave height can be given. In either case, the wave height at breaking, if known, is matched by adjusting the input wave condition. The wave period is provided by the user. In the offshore region, the wave is marched across the model grid toward the shoreline until breaking is achieved, as determined by a user-supplied breaking criteria (such as  $\kappa = H_b/h = 0.8$ ). The waves are shoaled using Stream Function Wave Theory (SFWT, Dean, 1974). This selection was made in order to produce steeper gradients in the wave height near breaking, which provided better overall agreement with the laboratory measurements discussed in this study. Furthermore, the non-linear stream function theory was chosen over linear shoaling because it better approximates the wave profile in the shoaling region, producing narrower waves with higher peaks and flatter troughs (and ultimately lower and more realistic values of volumetric transport and radiation stress,  $S_{xx}$ ).

Stream function theory is a numerical theory, and does not produce simple analytic expressions for shoaling calculations. For this reason, the graphs and lookup tables produced by Dean (1974) were digitized into an interpolation table in the numerical model

to provide the necessary shoaling information. Figure 4.1 provides a reproduction of the stream function shoaling table of Dean (1974) for the case of normally incident waves, as would be the case for this 2-D investigation.

Inside the surf zone, the wave transformation model of Dally et al. (1985) is employed to describe the wave breaking and possible reformation process in the surf zone. This model compares the difference between the local wave energy flux and the stable wave energy flux that would exist at that local water depth. Similar to the well-known constant criteria to describe wave breaking, Dally et al. employ an empirical constant,  $\Gamma'$ , to provide a stable wave criteria, where  $\Gamma'$  is the ratio of the stable wave height to the local

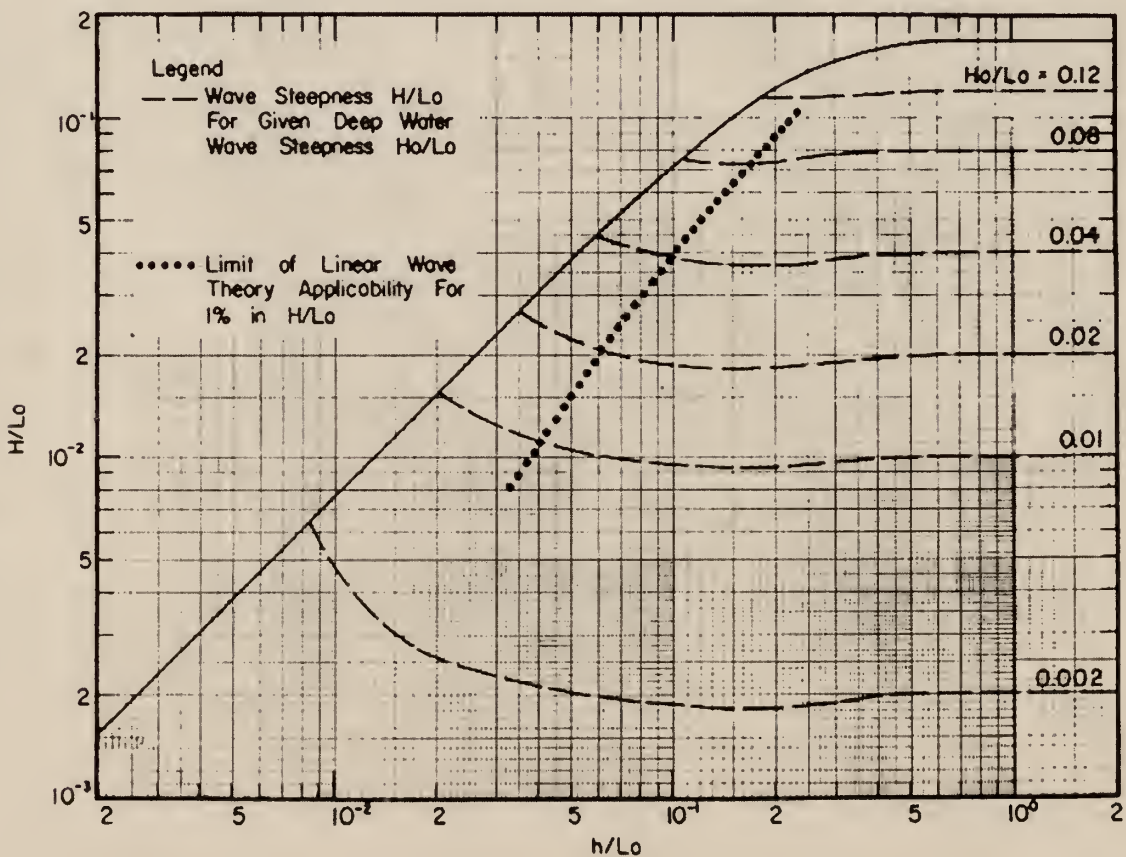


Figure 4.1 Stream function wave theory shoaling table for normally incident waves.  
Figure reproduced from Dean (1974).

water depth. The resultant equation to describe the change in wave height is:

$$\partial \frac{[H^2(h)^{1/2}]}{\partial x} = -\frac{K}{h}[H^2(h)^{1/2} - \Gamma^2(h)^{5/2}] \quad (4.1)$$

where  $h$  represents the mean water depth and  $K$  is a dimensionless decay coefficient. In the present model Eq. (4.1) is solved numerically to accommodate arbitrary beach profile shapes, beginning at the first break point as determined from the offshore shoaling routine. The model marches the finite difference version of Eq. (4.1) across the surf zone, breaking the waves, reforming them, and rebreaking them.

Dally et al. provide best-fit values for the stable wave criteria,  $\Gamma$ , and the dimensionless decay coefficient,  $K$ , of approximately 0.4 and 0.15, respectively, for beach slopes milder than 1/20. For steeper slopes, the authors recommend that  $K$  be set to 0.2. The authors note that this ambiguity in the choice of  $K$  presents some unwanted empiricism into the model overall, but more definitive data to determine its value is not available.

By employing the wave height transformation model of Dally et al. (1985), more realistic wave height profiles can be reproduced, including examples with barred beach profiles, where wave reformation and secondary breaking occurs. A comparison of wave height profiles for two laboratory cases, one on a planar beach and one on a barred beach (Okayasu and Katayama, 1992), is shown in Figure 4.2.

One primary advantage of using the Dally et al. model is that it better describes the sudden decrease in wave height that occurs immediately upon breaking, whereas a simpler model, based only on a depth limiting criteria, would predict a more gentle decrease in wave height. The sharp gradient in wave height following breaking leads directly to increased values of surface shear stress, which will be shown to noticeably affect the shape

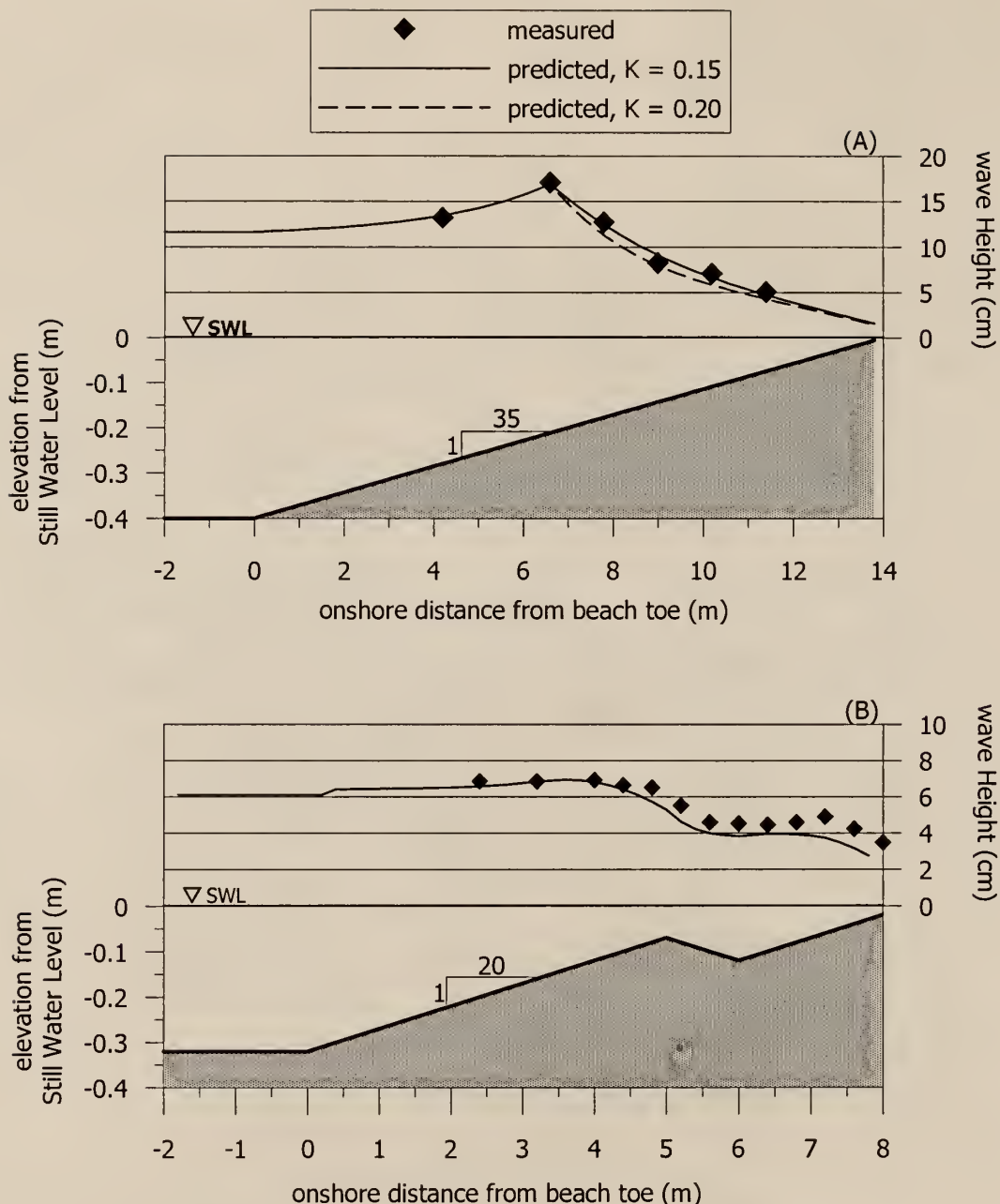


Figure 4.2 Demonstration of wave transformation model for two laboratory studies. The upper plot (A) compares the measured wave height transformation from the experiments of Cox & Kobayashi (1997) for a planar beach of 1/35 slope and a period of  $T = 2.2$  s. The lower plot (B) illustrates the predicted transformation for the random wave spectrum (the RMS value is plotted) used by Okayasu & Katayama (1992) for a barred profile of 1/20 slope. The period in the lower plot was 1.14 s. Seaward of the break point, Stream Function Wave Theory is used for wave height transformation, whereas landward of the first break point, the model of Dally et al. (1985) is employed.

of the return flow profile. In the barred-beach example of Figure 4.2, the model is able to characterize the reformation and rebreaking of the wave following the trough.

In the lower plot of Figure 4.2, the random wave spectrum used by Okayasu and Katayama (1992) was modeled by running individual waves over the profile at a period equal to the spectral peak (1.14 s). The time-dependent feature of the model is applied to produce the average flow field over a large number of randomly chosen waves. The model assumes that the wave height distribution is described by a Rayleigh distribution. The Rayleigh distribution is integrated to produce a cumulative distribution function that varies from zero to one. A random number generator is then applied to select the series of waves to model. Typically, 300 waves are run to produce an average flow field. The first few waves are neglected to avoid averaging “spin-up” conditions into the flow field.

The use of the stream function to model the return flow implicitly includes the effects of pressure. While the pressure terms were eliminated by cross-differentiation, their effect is still represented in the physical problem. The effect of pressure is manifest in a change in the water surface slope, thus resulting in setup or setdown. To accommodate this in the model, the setup and setdown are calculated at each column and the depth is adjusted accordingly. The values of setup and setdown are calculated from linear theory. Setdown, calculated from the offshore boundary to the first break point, is determined as follows:

$$\bar{\eta}_{\text{offshore}} = -\frac{H^2 k}{8 \sinh(2k)} \quad (4.2)$$

where  $k$  represents the wave number ( $2\pi/L$ ). The setup is found from a depth-limited wave height criteria starting from the knowledge of the setdown at the breakpoint:

$$\bar{\eta}_{\text{onshore}} \approx \bar{\eta}_{\text{break}} + 0.186(h_{\text{break}} - h) \quad (4.3)$$

#### 4.2 Determination of Return Flow Rate (Selection of $\psi$ at the Surface)

The first two boundary conditions to be determined govern the flow rate through each vertical section. This rate,  $Q$ , represents the depth-integrated return flow and is equal in magnitude to the wave-induced volumetric transport, or Stokes Drift, directed onshore (and assumed to exist above the model domain). In this way, the combination of the flow through the vertical section of the model domain and the flow assumed to pass above each vertical section sum to zero, thus conserving volume in the surf zone. Determination of the volumetric flow rate at each point across the model domain begins with the prediction of the wave height transformation, described in the previous section.

The flow rate establishes the difference between the value of the stream function at the bed and at the surface (recall the definition of the stream function from Eq. (3.15)). For convenience, the value of the stream function at the bed is arbitrarily set to zero, thus making  $\psi_{surface} = -Q$ . Outside the surf zone, two choices are presented. The first option is to apply linear theory to the value of the volumetric flow rate. Linear wave theory predicts the transport to be:

$$Q = -\frac{E}{\rho C} \quad (4.4)$$

where  $E$  is the wave energy ( $= \frac{1}{8}\rho g H^2$ ) and  $C$  is the wave celerity ( $= \sqrt{gh}$ ) in shallow water (Dean and Dalrymple, 1991). An alternative selection would be to choose the volumetric flow rate that results from a higher order wave theory, such as SFWT. The development of the solution for  $Q$  based on SFWT is quite lengthy and no simple analytic expression is available, therefore the value of  $Q$  chosen is determined from the lookup tables presented by Dean (1974).

To compare, for a wave condition of  $H = 0.78$  m,  $T = 8$  s, and  $h = 1.0$  m, linear wave theory (Eq. 4.4) predicts a return flow value of  $0.238 \text{ m}^3/\text{s}$  per meter of crest width (this example is the same example previously presented from Dean, 1995). Stream function theory, on the other hand, predicts a much smaller value of  $Q$  in this case,  $0.073 \text{ m}^3/\text{s}/\text{m}$ . In this particular example the difference in predicted values is quite extreme (the stream function value is only 30% of the linear value). In general the stream function values will be lower, owing to the nature of the wave profile predicted, which is much narrower and more peaked than the sinusoidal form predicted by linear theory.

The decision to choose either the linear theory or SFWT is based on the nature of the wave height transformation from offshore up to breaking. In general, linear shoaling produces smaller wave heights at breaking relative to SFWT, and the gradient in wave height over a differential distance is likewise less. Overall comparison of the two theories to the laboratory measurements of return flow investigated herein (Chapter 6), both in wave height profile and return flow magnitude, suggests that SFWT provides better agreement across the range of experiments. Thus SFWT is coded into the numerical model as the theory used to shoal waves from the offshore boundary to the first break point.

Inside the surf zone, several options are available. The wave transformation model provides the wave height at each cross shore position. From that wave height, linear theory and SFWT can be applied directly for  $Q$ . The appropriateness of using these theories by themselves (i.e., with no consideration given for transition region or roller effects) is somewhat suspect. For comparison and for use with a roller model, these theories will be applied to determine their agreement with measurements.

An alternative theory is to adopt a wave height profile resembling a sawtooth, then develop the expression for  $Q$  in the same way the linear value is obtained. In the surf zone,

the shallow water assumption is applied, in which the horizontal velocity is assumed to be uniform over depth and given by:

$$\tilde{u} = \eta \sqrt{\frac{g}{h}} \quad (4.5)$$

where  $\eta$  in this case represents the instantaneous elevation of the water surface (the wave height profile). Integration of Eq. (4.5) from the seabed to the water surface and subsequent time averaging produces the volumetric transport based on the time average of the square of  $\eta$ , just as linear theory predicts. However, for a sawtooth wave, the sinusoidal water surface profile is replaced by a linear profile given by:

$$\eta = H \frac{x}{L} \quad (-L/2 < x < L/2) \quad (4.6)$$

which when squared and averaged between  $-L/2$  and  $L/2$  produces a value of  $Q$  that is 2/3 the value of  $Q$  predicted by linear theory.

Some investigators report that inside the surf-zone the value of the volumetric transport from linear theory is lower than the actual transport due to an additional contribution from the volume contained in the surface roller fronting the broken wave crest (Svendsen, 1984a, and Stive & Wind, 1986). Stive and Wind, 1986, report the increased value of volumetric transport as:

$$Q = -\frac{1}{10}(g/h)^{1/2}H(h + \bar{\eta}) \quad (4.7)$$

While the representation of Stive and Wind is intended to better typify a bore-like wave profile in the surf zone, for the example conditions discussed above, the predicted value of  $Q$  is  $0.250 \text{ m}^3/\text{s}/\text{m}$ , which is not substantially larger than the linear value (roughly 5%).

At this stage there are now four options for predicting the value of  $Q$  inside the surf zone. If the same example conditions are applied in the surf zone, the range of  $Q$  now varies from the SFWT value ( $0.073 \text{ m}^3/\text{s}/\text{m}$ ) to the value predicted by Stive & Wind (1986),  $0.250 \text{ m}^3/\text{s}/\text{m}$ . The sawtooth wave theory predicts a rate of  $0.159 \text{ m}^3/\text{s}$  per meter of crest width. Lacking further information to refine the estimate, the range of options will be examined, both to produce the best fit to the measured data, and to compare the validity of each. It will be shown in a later section that the prediction of the transport value plays a very important role in the prediction of the return flow and is one of the primary objectives in simulating the flows in the transition region.

Dally and Brown (1995) present a wave surface roller model that combines SFWT and a surface roller to predict the momentum flux and volumetric transport throughout the surf zone. SFWT is applied to describe the properties of the organized wave motion that persists after breaking. The surface roller component begins to grow after initial breaking and increases the predicted volumetric transport as well as the momentum flux (or radiation stress). The use of SFWT inside the surf zone allows that portion of the description of the parameters to vary smoothly from offshore to onshore. The roller contributions grow smoothly from the break point and then diminish in the inner surf zone.

Definition of Phase Speed. In all the theories applied herein, the wave theory used does not include the effect of the return flow on the wave transformation. This is known as the first definition of phase speed. The SFWT tables presented by Dean (1974) assume that the wave is propagating without lateral boundaries, so that no external or return flow

affects the wave field. Inclusion of the effect of the return flow on the wave transformation, known as the second definition of phase speed, would entail the reformulation of the SFWT to include the effect, a procedure described by Dalrymple and Dean (1975) for uniform currents. This was not included in the present work, where waves propagate over a varying current. The effect of the return flow on the wave transformation is expected to be of secondary importance relative to the application of the various boundary conditions discussed herein. As a check, the wave celerity,  $C$ , (first definition of phase speed) associated with an 8 s linear wave in 1.0 m shallow water is 3.1 m/s. The expected depth averaged return flow magnitude for such a wave is roughly 0.24 m/s, less than 8% of the wave celerity. The ratio of  $U/C$  alters the apparent period of the wave and thus adjusts the predicted volumetric flow rate and radiation stress.

#### 4.3 Specification of the Surface Shear Stress Due to Waves

The third boundary condition to be specified is the mean surface shear stress caused by the passage of the waves. This stress, while actually a force distributed between the trough to crest region of the waves, is modeled as a concentrated stress acting at MWL, as described by Dally, 1980. The force arises from the gradient in wave momentum flux between the trough and the crest. Referring to Figure 1.2, the momentum flux in this region accounts for one-third of the total momentum flux (via linear theory), and is generally of greater magnitude than the force due to the uniform pressure gradient. The surface stress is applied in the numerical model as a second-derivative boundary condition in  $\psi$ .

$$\tau_s = -\rho \frac{\partial}{\partial z} \left( \epsilon_s \frac{\partial \Psi}{\partial z} \right) \quad (4.8)$$

The value of the mean surface stress,  $\tau_s$ , is found from the gradient in the wave-induced radiation stress in the trough-to-crest region, denoted  $S_{xx,I}$ . In shallow water, linear theory produces  $S_{xx,I} = E/2$  (Dean & Dalrymple, 1991), which leads to the following equation for the applied surface stress outside the surf zone:

$$\tau_s \approx -\frac{\partial(E/2)}{\partial x} = -\frac{1}{16}\rho g \frac{\partial H^2}{\partial x} = \frac{E}{4(h+\bar{\eta})} \frac{\partial h}{\partial x} \quad (4.9)$$

For a negative bottom slope (decreasing water depth in the positive  $x$ , onshore, direction), Eq. (4.9) produces an offshore directed stress at the surface. Inside the surf zone, where waves are breaking and decaying in height,  $\tau_s$  is found by assuming that the wave height is related to the local water depth by a constant (i.e.  $H = \kappa h$ ). With  $S_{xx,I}$  equal to  $E/2$ ,  $\tau_s$  is assumed to be:

$$\tau_s \approx -\frac{1}{16}\rho g \kappa^2 \frac{\partial h^2}{\partial x} = -\frac{E}{(h+\bar{\eta})} \frac{\partial h}{\partial x} \quad (4.10)$$

which produces an onshore shear stress at the surface when the bottom slope is negative.

As with the flow rate, researchers have suggested that the additional volume of water carried forward by the surface roller contributes an additional stress to the water surface. Svendsen (1984a) suggests an alternate representation for  $\tau_s$ :

$$\tau_s \approx -\left(\frac{1}{16} + \frac{A_r h}{H^2 L}\right)\rho g \frac{\partial H^2}{\partial x} \quad (4.11)$$

The second term in parentheses in Eq. (4.11) represents the effect of the surface roller, whose cross sectional area is  $A_r$  ( $\approx 0.9H^2$ ) (Svendsen, 1984a). The application of Eq. (4.11)

compared to Eq. (4.12) generally applies a greater stress to the water column. The surface roller model of Dally and Brown (1995) also produces the radiation stress at each point across the domain. From that description, the gradient can be computed to determine the surface shear stress. Lacking better information on the division of the radiation stress between the trough-to-crest region and the body of the fluid in non-linear waves, it is assumed that one-third of the computed radiation stress from this and every other model applied represents the surface shear stress.

It will be shown that the presence of a surface shear stress in most surf zone conditions drives the peak of the offshore return flow to a lower point in the water column and reduces the offshore directed return flow near the surface. In some instances it may cause the opportunity for flow reversal in the upper portion of the water column (onshore). The measurement of surface shear stress due to breaking waves is extremely difficult; information on this subject is inferred from velocity measurements but is affected by the aerated nature of the surf zone, particularly in the upper portions of the water column.

#### 4.4 Specification of Bottom & Sidewall Tangential Boundary Conditions

The final boundary condition to be specified is the tangential condition along the bottom and sidewalls. Here the options are to assign a velocity or a shear stress condition. Generally, the model domain is established such that the offshore boundary is well offshore of the break point. At that position, the mean velocities in both directions are assumed to be very small, thus the tangential condition along the sidewalls is chosen to be a zero-velocity (no-slip) condition. It is noted that there is little data to support applying any other condition. At the onshore boundary, the domain has been extended nearly into the swash zone; assignment of a vertical no-slip condition at this point is considered reasonable.

Along the bottom, the modeled PDE does not expressly consider the presence of a bottom boundary layer, induced by the oscillatory motion of the waves and/or by the return flow. Given that fact, it may be desirable to specify the bottom velocity as either zero or that velocity corresponding to the velocity at the edge of the boundary layer. For generality in the model, the 1-D model bottom velocity boundary condition is specified as follows:

$$U_b = -\left(\frac{\partial \Psi}{\partial z}\right)_b \quad (4.12)$$

As mentioned, the basis for selection of a bottom velocity boundary condition other than zero is fairly limited. It would seem appealing to apply the velocity at the edge of the boundary layer, also known as the streaming velocity, at this stage (Longuet-Higgins, 1953). The streaming velocity is given by:

$$U_\infty = \frac{3}{16} \frac{H^2 \sigma k}{\sinh^2 kh} \quad (4.13)$$

where  $\sigma = 2\pi/T$ , with  $T$  being the wave period. However, it will be shown in following chapters that very little data exist to support an onshore directed velocity at the bottom. This is particularly true in the surf zone, where strong offshore directed bottom velocities are frequently measured. Hansen and Svendsen, 1984, noted that although the direction was incorrect, the magnitude of the bottom velocity predicted by Eq. 4.13 provided good agreement with experimental data. Hansen and Svendsen provided no supporting hypothesis for reversing the direction of this velocity.

It is equally easy to apply a zero velocity condition in Eq. (4.12), and much more defensible since it is required that the velocity ultimately go to zero at the bottom through

some boundary layer. The difficulty in using a zero velocity at the bottom is that the mathematics of the governing PDE are not intended to describe a boundary layer, and in the case of uniform eddy viscosity the resultant velocity profile is parabolic and pinned at zero at the bed. This condition does not always correspond well with measurements, as will be shown in a later chapter. It is possible that applying an adjusted eddy viscosity value at the bottom, in which the eddy viscosity is significantly reduced, may alleviate the strict condition at the bottom, making the resultant velocity profile appear to “slip” over the bottom. A variable eddy viscosity, however, introduces an entirely different set of challenges; these will be discussed in a subsequent chapter.

The other alternative considered is the specification of the bottom shear stress at each vertical section. Eq. (4.14) provides this condition, in which the mean bottom shear stress has been defined as a fraction,  $m$ , of the mean surface shear stress following the work of Reid (1957). The generality of a varying eddy viscosity in the numerical model has been respected:

$$\tau_b = m \tau_s = -\rho \frac{\partial}{\partial z} (\epsilon_b \frac{\partial \Psi}{\partial z}) \quad (4.14)$$

For the case of surface stress along a bounded channel, such as in the present beach profile situation, the quantity  $m$  is generally negative, indicating the bottom stress is directed opposite to the surface stress, as might be expected inside the surf zone for the mean flow in the absence of wind. Reid (1957) discusses the value of  $m$  for steady, wind-driven flows in bounded channels. Applying the example conditions from Dean (1995) ( $Q = 0.238 \text{ m}^3/\text{s}/\text{m}$ ,  $\tau_s = 7.9 \text{ N/m}^2$ , and  $h = 1 \text{ m}$ ), the ratio of bottom to surface shear stress is predicted to be approximately 0.09 to 0.16, depending on the choice of roughness height

(reference Reid, 1957, Figure 11 and Figure 12). It is interesting to note that the shear stress value given by Dean for the surface shear stress due to momentum transfer from breaking waves ( $7.9 \text{ N/m}^2$ ) corresponds roughly to the stress generated by winds just reaching hurricane force ( $>121 \text{ km/h}$ , per Reid (1957)). This illustrates the strong effect breaking waves have on the surf zone flow.

Reid (1957) developed expressions for the velocity profiles in channels due to applied wind stresses by applying the quadratic friction law:

$$\tau_b = \rho \frac{f}{8} |U_{ave}| U_{ave} \quad (4.15)$$

where  $f$  is the Darcy-Weisbach friction factor and  $U_{ave}$  is the depth-averaged value of the return flow. Applying Eq. (3.46) to Dean's example yields a friction factor of roughly 0.1, which approaches the upper limit for friction factors applied in open-channel and pipe flows.

Diegaard et al. (1991) measured the mean and time-varying shear stress under regular waves breaking on a 1:30 beach slope. Few details are given regarding the wave height transformation; the wave height information provided is listed as regular waves of 10 to 13 cm height (presumably on the horizontal portion of the wave tank or at the toe) and 1.5 to 3.0 s period, similar in scale to the experiments discussed above. The authors present data indicating mean bottom shear stresses of 1 to 2  $\text{N/m}^2$  for spilling breakers, and up to 3  $\text{N/m}^2$  for plunging breakers. The breaker heights are not presented, however, using crude assumptions and basic linear theory, Eq. (4.10) would predict a surface shear stress of roughly 3.8  $\text{N/m}^2$ , producing a ratio of stresses of between 0.26 and 0.53 for the spilling breakers. SFWT would produce a higher wave height and a higher shear stress, but a lower

volumetric transport and hence net return flow rate, leading to lower values of the ratio of bottom to surface shear stress.

Overall, the surface shear stress due to breaking waves is expected to be substantially higher than the resultant mean bottom shear stress, perhaps by as much as ten times (per Reid, 1957). It is noted, however, that the return flow may exist in the absence of a significant surface shear stress, such as in the region just seaward of breaking. In those areas, the ratio of the mean bottom to surface shear stress may be greater than one, or may have no physical meaning (as in the case of zero surface shear stress). The analogy is drawn to open channel flow on a gently sloping surface, where the bottom shear stress is non-zero, but the surface shear stress is zero. In application to the model, the existing literature suggest that in the surf zone, where the return flow is driven by breaking waves, the mean bottom shear stress is not expected to exceed 0.3 to 0.5 times the surface shear stress. Those values are believed to be the extreme, high estimate, and an estimate of 0.1 or less may in fact be more appropriate. Again, however, guidance as to the selection of the mean bottom shear stress or the ratio of stresses is limited.

#### 4.5 Matching Conditions Across the Transition Region

The present model is driven from the surface boundary conditions where shoaling and breaking waves exert stresses on the water surface and transport mass onshore which must be returned offshore through the model domain. Techniques for applying these boundary conditions are numerous, as demonstrated in the previous sections. Most of these techniques, however, do not consider the continuity in certain wave properties, such as radiation stress, across the entire profile. For example, the model of Svendsen, 1984a, begins at the end of the transition region, some distance landward of where breaking is

initiated. The expressions developed for radiation stress and mass transport result in large discontinuities at the break point when linked to the corresponding offshore descriptions of these properties.

Discontinuities in the mass transport are not as great a concern as are discontinuities in momentum. The surface roller represents an additional volume of water that can be simply recirculated within the surf zone. This volume of water could originate from outside the surf zone at the beginning of a wave event or from alongshore. Regardless, the fact that there is a recirculating volume of water that does not leave the surf zone is not problematic so long as conservation of mass (volume) is achieved at each vertical section.

The increase in momentum represented by the surface roller does present continuity problems, however. Just prior to breaking, there is a certain amount of momentum in the wave available to be transferred into the surf zone. This momentum must be distributed across the surf zone. Generally this momentum is transferred to the water column via the gradient in radiation stress seen in the decreasing wave height due to breaking. This is principally manifest in the surface shear stress and set up of the MWL in the surf zone. Depending on the representation used to describe this surface shear stress (which is determined in practice by the reduction in wave height across the surf zone), integration of these shear stresses from the shoreline seaward to the break point may result in a total required momentum input to the surf zone that is greater than the momentum input determined from the seaward side (i.e. from SFWT).

Figure 4.3 illustrates this problem and one simple solution adopted to span the transition region and maintain continuity of momentum. The figure plots the value of several wave quantities computed across the surf zone. The data set of Ting and Kirby is chosen to demonstrate the problem. In the upper plot, the variation in wave height across

the surf zone is shown. SFWT is linked at the break point to the wave breaking model of Dally et al. (1985). This variation is, by default, fairly smooth and does not exhibit any substantial discontinuities (except for the cusp at the break point itself).

The second plot in Figure 4.3 illustrates the variation in radiation stress across the surf zone, dependent on the choice of description used. At the break point, the decision must be made as to which theory to apply to describe the necessary properties. The plot shows the discontinuity that arises from any choice of theory (sawtooth, linear, or surface roller). The surface roller approximation produces the greatest discrepancy. A similar discontinuity at the break point is seen in the third plot of the volumetric transport.

There is no mechanism to generate the additional radiation stress, thus the switch in theories presents a problem with conservation of momentum. This problem, the transition region problem, arises in any return flow model, generally because the majority of data collected in the surf zone exhibit integral wave properties that are greater than predicted by higher order wave theories, such as SFWT. Svendsen (1984a) noted this discrepancy in the volumetric transport measured at vertical sections in laboratory surf zones and was prompted to develop the surface roller theory. Svendsen, however, did not discuss the issue of conservation of momentum from the break point landward.

One ad hoc approach to this dilemma is to determine the distance required for the radiation stress to return to the level of the radiation stress just offshore of the break point. This distance may be considered to be the length of the transition region. In application to the periodic wave experiments discussed in this work, this distance is on the order of 6 to 11 water depths at breaking. This appears to be in reasonable agreement with the measurements and discussion of transition lengths (e.g. Nadaoka and Kondoh, 1982). Svendsen (1984a) describes how breaking waves experience a transition region in which

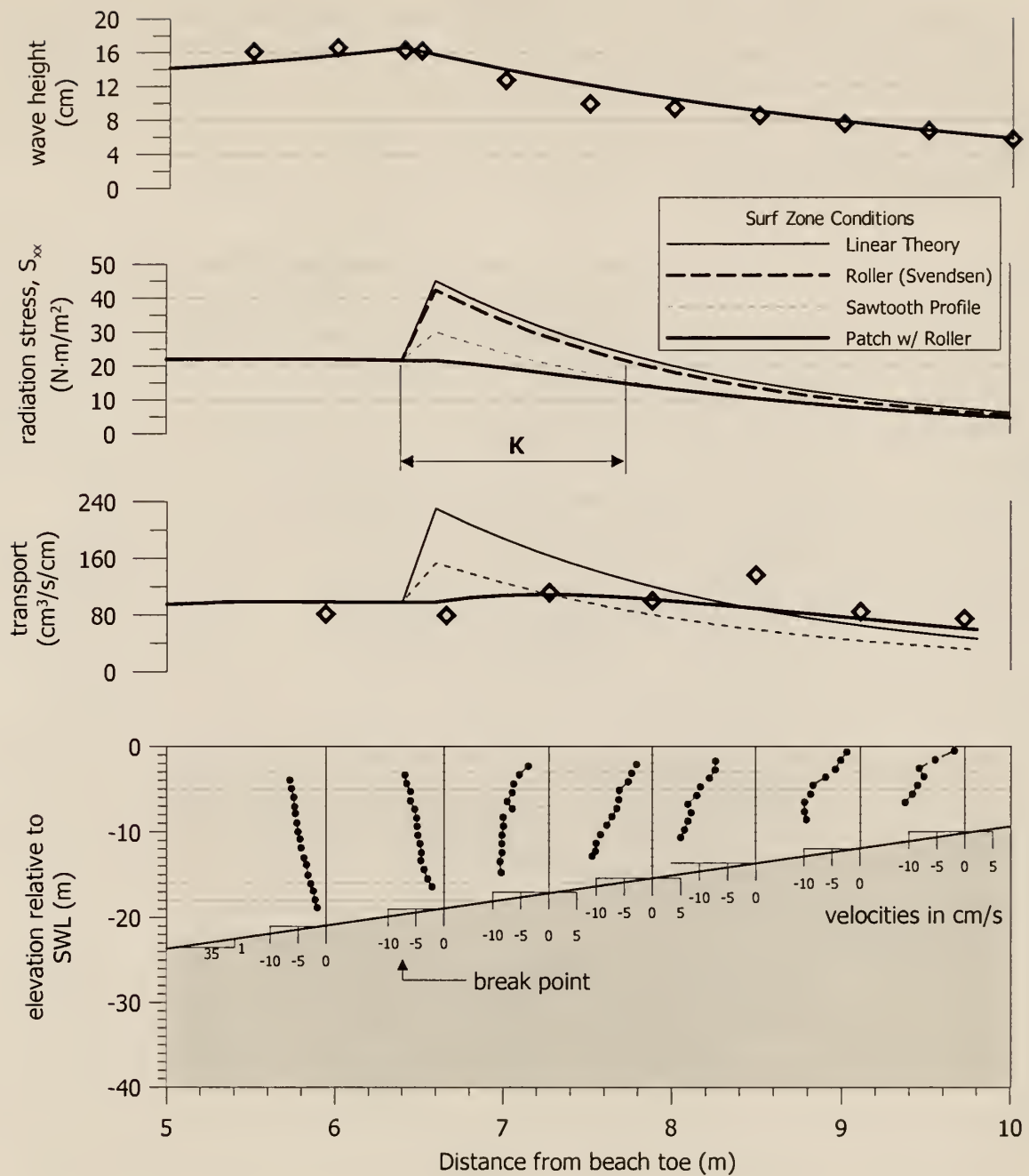


Figure 4.3 Demonstration of the treatment of the transition region in the simulation of the data set of Ting & Kirby (1994). The expressions for radiation stress inside and outside the surf zone are investigated to determine the length necessary for the surf zone value to match the incident value seaward of breaking. This distance is used as a folding length to patch the offshore descriptions of radiation stress and volumetric transport to the inshore descriptions.

the wave is reshaped from a nearly breaking, steep, asymmetric shape just offshore of the break point to a fully developed turbulent bore. Laboratory data cited by Svendsen indicate that in this region there is little momentum loss, as evidenced by the lack of setup of the water surface. Given the lack of momentum loss, the technique of matching the radiation stresses and then patching the offshore description to the onshore description gains some degree of merit.

The offshore and onshore descriptions are patched together in the following fashion. The distance across the transition region is determined by inspecting the radiation stress determined from the surf zone theory for the point where the radiation stress matches the radiation stress just seaward of the break point (b.p.). This distance,  $K$ , is then used to patch the two descriptions of radiation stress such that the stress varies consistently from the break point shoreward. The patching process is demonstrated in Eq. (4.16):

$$(S_{xx})_i = (S_{xx})_{i,inner} - ((S_{xx})_{b.p.+1,inner} - (S_{xx})_{b.p.,stream\ function})e^{-\frac{x}{K}} \quad (4.16)$$

where the values denoted by *inner* could be determined from any theory, such as linear wave theory or a surface roller approximation.

Similarly, the offshore and onshore values of the volumetric transport,  $Q$ , are patched to produce a consistent variation. The variation in  $Q$  is shown in the third plot of Figure 4.3. The transition distance from the radiation stress plot produces a slight increase in the transport just landward of breaking, but still reduces the predicted value of  $Q$  substantially compared to the unpatched case. Inspection of the measured values of  $Q$  indicates that the maximum value of transport occurs some distance landward of the published break point (the velocity profiles were extrapolated to the bottom and to the

MWL). Published literature suggest that in this region the wave is reforming itself into the surface roller form described by Svendsen, while only transferring a small amount of momentum to the water column. The patch described herein reproduces this phenomenon. Using the patched description of the radiation stress, the surface shear stress can be computed and thus varies smoothly across the profile as well.

Further evidence of the transition region is seen by inspection of the velocity profile immediately landward of breaking in Figure 4.3. This profile suggests that the strong return flow profile characteristic of inner surf zone areas is not present. In fact the profile at the break point exhibits a shape typical of offshore velocity profiles. It is apparent from the plot of volumetric transport that the use of the higher value of transport (e.g. from linear or surface roller expressions) would lead to a significant overestimate in the transport value. The merged curve reproduces the measured transport values quite well, with the exception of the fifth profile ( $x \sim 8.5$  m). No explanation for the transport measured at that station is provided. A coefficient could be introduced to modify the characteristic distance,  $K$ , applied in Eq. (4.16), however, no guidance for such a coefficient exists, except for a fitting to existing data, which would introduce an unwanted degree of empiricism.

Dally and Brown (1995) present a surface roller model in which the dissipation of wave energy is assumed to be derived from the shear at the interface between the organized wave form (predicted by SFWT) and the turbulent surface roller fronting the wave. The dissipation is represented by contributions from both the organized wave motion and the roller, which first grows in size then dissipates across the surf zone. The initial growth of the roller limits the decrease in total radiation stress, and provides a plausible means of increasing the volumetric transport landward of the break point. Dally and Brown provide expressions for the momentum flux and the volumetric flux of the roller. The volume flux

of the roller is then added to the volume flux of the organized wave form and thus produces somewhat higher predicted values of transport across the transition region.

In this work, all simulations incorporate some attempt to patch the offshore region to the inner surf zone by providing a treatment of the transition region. This is accomplished either through the characteristic patch-length approach or through application of the Dally and Brown (1995) roller model. In the first instance, the characteristic length will be determined from linear and sawtooth theories as well as the roller model of Svendsen (1984a).

## CHAPTER 5

### MODEL TESTING & VALIDATION

Before proceeding to the modeling of actual surf zone flows, the model will be applied in simple flow situations for which analytical solutions exist in order to validate its performance. While the inclusion of an arbitrary domain geometry and a spatially variable eddy viscosity field precludes an analytic solution to the full problem, certain solutions are available for simpler cases, such as simple one-dimensional flows and two-dimensional flows of uniform eddy viscosity and horizontal bottom geometry. Using these simple examples, the models may be tested and validated to develop confidence in the results produced from the more complicated simulations.

This chapter presents test cases designed to demonstrate the proper performance of the numerical model developed in Chapter 3. The steady-state 1-D simulations are compared to solutions of horizontal flows subject to various boundary conditions. The time-dependent 1-D flow field is compared to solutions of the diffusion equation, a second-order, time dependent PDE in terms of the horizontal velocity,  $U$ . The present, governing fourth-order equation in  $\psi$  is essentially equivalent to the equation describing the diffusion of vorticity, and solutions in  $\psi$  should produce equivalent solutions in  $U$  when converted. This is quite advantageous, since solutions to the time dependent fourth-order equation, even in one dimension, are difficult to obtain for the desired boundary conditions.

For the 2-D case, obtaining an analytic solution for any time-dependent flow in any geometry has proven difficult. In light of this problem, the steady-state problem is

investigated. Solutions for the steady state problem in two dimensions follow those solutions of the biharmonic equation. A Fourier series solution is developed to compare to the results of the numerical model. Additionally, for extremely simple flow situations, vertical sections taken well away from sidewall boundaries and areas of spatial gradients in the horizontal are expected to behave very similarly to the one-dimensional solutions.

## 5.1 One-Dimensional Analytic Solutions

### 5.1.1 Steady-State Simulations

To begin, an analytic solution to the steady, one-dimensional, fourth-order equation in  $\psi$  is found. The PDE is:

$$\Psi_{zzzz} = 0 \quad (5.1)$$

Solutions of the form  $\psi = e^{kz}$  are sought. Application of this form to Eq. (5.1) yields four repeated roots ( $=0$ ), resulting in the following general solution:

$$\Psi = Az^3 + Bz^2 + Cz + D \quad (5.2)$$

The boundary conditions to be investigated are illustrated in Figure 5.1 and are listed as:

$$\Psi(0) = \Psi(h) = 0 \quad \Psi_z(0) = 0 \quad \Psi_{zz}(h) = -\frac{\tau}{\rho\epsilon} \quad (5.3)$$

Application of the four boundary conditions in Eq. (5.3) results in the following equation for the steady state, analytic solution:

$$\Psi_{(1-D \text{ s.s.})} = -\frac{\tau'}{4h}z^3 + \frac{\tau'}{4}z^2 = \frac{\tau'h^2}{4}(\frac{z}{h})^2(1-\frac{z}{h}) \quad (5.4)$$

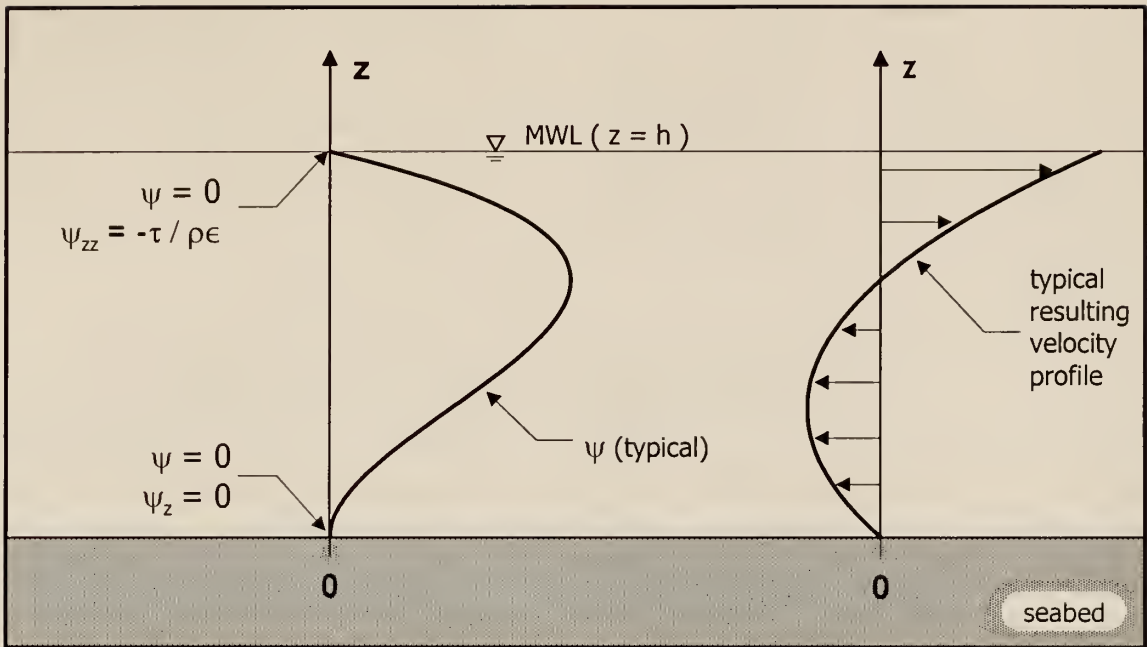


Figure 5.1 Definition sketch of one-dimensional problem. The four boundary conditions are shown along with typical profiles of  $\psi$  and the resulting velocity distribution. Note that the schematic velocity profile results in zero net flow through the vertical section, consistent with the applied boundary conditions of  $\psi(0) = \psi(h) = 0$ .

where  $\tau' = \tau/\rho\epsilon$  and the origin is taken at the seabed. This solution, when converted to the corresponding horizontal velocity,  $U$ , produces the profile of Dally (1980) and Dean (1995) described in Chapter 2 (Equation (2.5)). Figure 5.2 plots the results of the simulation under the conditions in Eq. (5.3) for the example values of Dean (1995). The plot shows the near-perfect agreement of the simulation with the analytic solution in this simple example.

In Figure 5.2, the resulting velocity and shear stress profiles demonstrate the parabolic and linear shapes, respectively, that one would expect from taking successive derivatives of Eq. (5.4). This example was chosen to produce no net flow through the vertical section. In the surf-zone, this situation could be replaced by some non-zero flow value, such as the wave-induced volumetric transport, simply by adjusting the surface boundary condition in Eq. (5.3) to the desired value, e.g.  $\psi(h) = -Q$ .

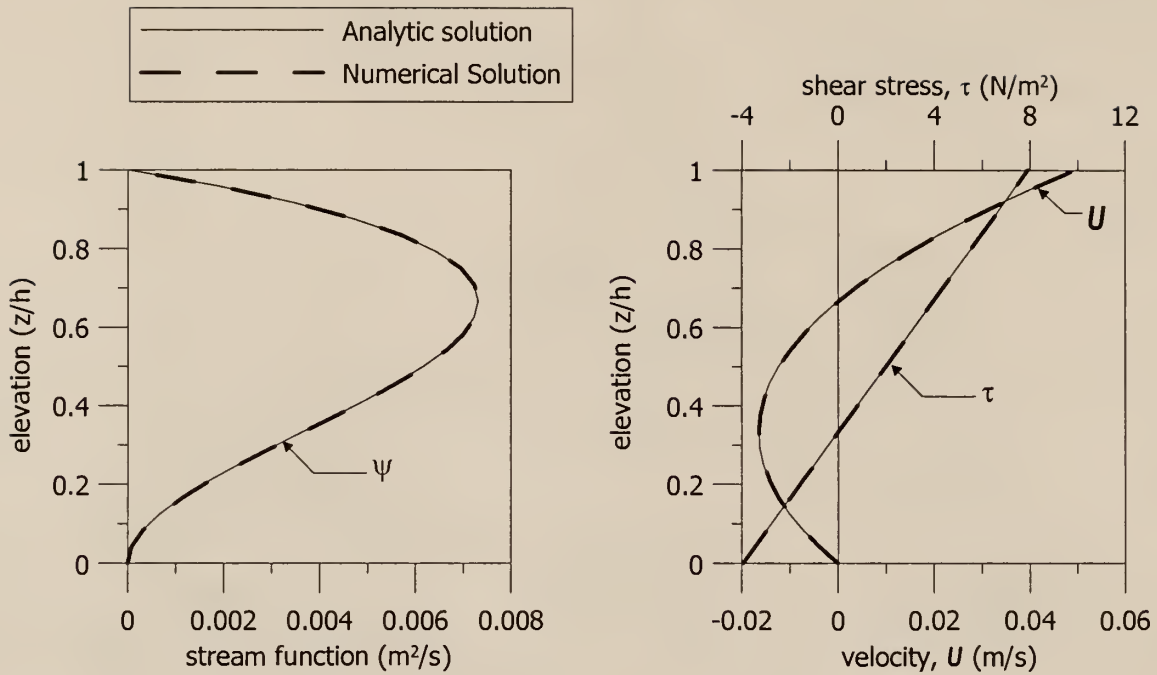


Figure 5.2 Comparison of 1-D numerical model to analytic solution for steady-state conditions. The chosen example simulates flow in a bounded channel driven only by a surface shear stress. The example conditions are similar to those given in Dean (1995) ( $\tau = 7.9 \text{ N/m}^2$ ,  $\epsilon = 0.04 \text{ m}^2/\text{s}$ ,  $Q = 0.0$ ).

### 5.1.2 Variable Eddy Viscosity Simulations - Steady State

Reid (1957) presented velocity and shear stress profiles in a bounded channel (i.e.,  $Q = 0$ ) subject to a surface stress using a quadratic expression for mixing length and hence turbulent diffusion. As discussed in Chapter 2, Reid combined a parabolic description of the turbulent mixing length,  $L$ , to the quadratic friction law to determine the resultant linear shear stress profile. The description of the mixing length employs coefficients describing the relative roughness of the bed and the water surface (Eq. (2.8)). As discussed in previous chapters, limited experimental results are provided to guide the selection of these characteristic lengths and the ratio of the bottom and surface shear stresses.

To demonstrate the ability of the numerical model to properly accommodate variable eddy viscosity fields, the case of zero net flow was simulated. The results of the simulation are illustrated in Figure 5.3. The example of Reid is non-dimensionalized by the surface shear velocity ( $\sqrt{(\tau_s/\rho)}$ ), therefore, the surface shear stress applied in the previous example by Dean (1995) is employed to present the results in dimensional units. For the case of  $m = \tau_b/\tau_s < 0$ , the model employs two different expressions, joined at the elevation where the return flow value is a maximum (the point where the shear stress is zero,  $\partial U/\partial z = 0$ ). Figure 5.3 also plots the profile predicted by Reid (1957). The profile produced is much more uniform in the middle of the domain, suggestive of the turbulent flow present. The resulting parabolic mixing length produced in this example is shown in the first lower plot (b).

Using the relationship between mixing length and eddy viscosity presented by Eq.(2.9), the eddy viscosity distribution suggested by the example in Figure 5.3 is plotted in Figure 5.3(c). The difficulty of the use of two equations to fit the profile, along with the indeterminate value of  $\epsilon$  that results where  $\partial U/\partial z = 0$ , is apparent in the plot near the bottom. An exact fit of  $\epsilon$  predicted from the method of Reid creates sharp gradients in the derivatives of the eddy viscosity distribution that do not allow solution in the numerical model. To reproduce the Reid velocity profile, the distribution of  $\epsilon$  was fit to a smooth third-order polynomial as shown in Figure 5.3(c). The velocity profile produced by the numerical model is in very good agreement with the analytical approach of Reid (1957).

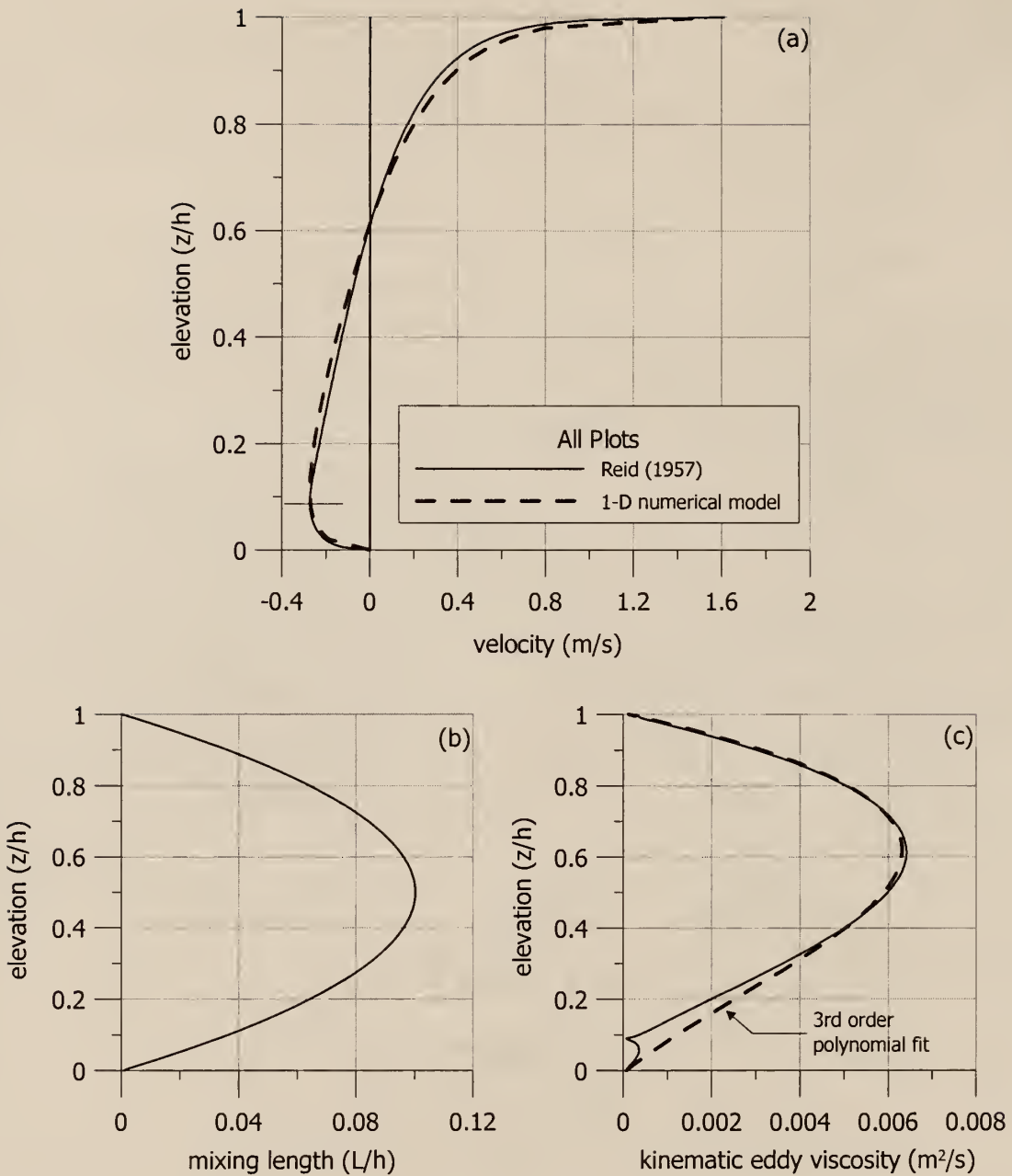


Figure 5.3 Comparison of 1-D numerical model results to those of Reid (1957) for the case of  $Q = 0$ . The upper plot depicts the analytic and numerical solutions to the horizontal velocity profile (a). Reid employs a parabolic mixing length theory (b). In order to reproduce the predicted eddy viscosity seen in plot (c), it was necessary to fit the predicted curve as a 3<sup>rd</sup> order polynomial. The difficulty in fitting the predicted eddy viscosity from Reid is apparent in plot (c), where the two expressions used by Reid are fit at the point in the profile where  $\partial U / \partial z = 0$ , thus producing an indeterminate condition.

Note that the eddy viscosity distribution predicted from Reid (1957) peaks at a depth approximately equal to 0.6 times the local water depth. In surf zone flows, it is expected that this peak may be shifted further toward the surface. In laboratory experiments with spilling breakers, Ting and Kirby (1994) present the measured vertical distribution of the time-mean horizontal turbulent velocity. These distributions exhibit a similar shape to the eddy viscosity distribution shown in Figure 5.3, however the peak of the mean turbulent velocity measured in the laboratory under breaking waves appears to be as high as 0.7 to 0.8 times the local water depth. Stive (1984) presents similar distributions of turbulent intensity under breaking waves in which the peak value is shifted toward the surface.

### 5.1.3 Time-Dependent Simulation

The ability of the model to reproduce time-dependent behavior is now investigated. In this instance the one-dimensional equation in  $\psi$  becomes:

$$\Psi_{zzi} = \epsilon \Psi_{zzzz} \quad (5.5)$$

where for simplicity the eddy viscosity has been assumed uniform. The boundary conditions of Eq. (5.3) are retained along with an initial condition of quiescence ( $\psi(z, 0) = 0$ ). In the time dependent case, analytical solutions to the fourth order PDE of Eq. (5.5) were unobtainable, however, it is recognized that in terms of velocity,  $U$ , the model should reproduce results from simulations of the second-order diffusion equation:

$$\frac{\partial U}{\partial t} = \epsilon \frac{\partial^2 U}{\partial z^2} \quad (5.6)$$

Solutions to Eq. (5.6), typically Fourier sine series solutions given the finite physical domain, are readily obtainable. Carslaw and Jaeger (1986), provide two solutions that can be superimposed to produce the time-dependent version of the steady-state example presented in Figure 5.2. To begin, the solution for the horizontal velocity profile that develops from a fixed bottom velocity ( $=0$ ) and a specified surface shear stress,  $\tau$ , is found:

$$U_1 = -\frac{\tau}{\rho\epsilon} z + \frac{8h}{\pi^2 \rho\epsilon} \sum_{n=0}^{\infty} \frac{(-1)^n}{(2n+1)^2} \sin\left(\frac{(2n+1)\pi}{2h} z\right) e^{-\epsilon\left[\frac{(2n+1)\pi}{4h}\right]^2 t} \quad (5.7)$$

with boundary and initial conditions:

$$U_1(z,0) = 0 \quad U_1(0,t) = 0 \quad U_{1z}(h,t) = \frac{\tau}{\rho\epsilon} \quad (5.8)$$

The second solution needed is similar to the solution that results from modeling the diffusion of heat within a slender rod with internal heat generation. The PDE in this case is:

$$\frac{\partial U}{\partial t} = \epsilon \frac{\partial^2 U}{\partial z^2} - A(z,t) \quad (5.9)$$

In the present physical problem, the additional term,  $A$ , represents the combination of the pressure and momentum flux gradients, which would result in the slope of the water surface. One solution to Eq. (5.9), for the case of a uniform forcing term,  $A_o$ , is:

$$U_2 = \frac{-A_o h^2}{2} \left[ 1 - \frac{z^2}{h^2} - \frac{32}{\pi^3} \sum_{n=0}^{\infty} \frac{(-1)^n}{(2n+1)^3} \cos\left(\frac{(2n+1)\pi}{2h} z\right) e^{-\epsilon\left[\frac{(2n+1)\pi}{4h}\right]^2 t} \right] \quad (5.10)$$

subject to the conditions:

$$U_2(z,0) = 0 \quad U_2(0,t) = 0 \quad U_2(2h,t) = 0 \quad (5.11)$$

Note that in the formulation for  $U_2$  by Carslaw and Jaeger, symmetry has been employed to solve the equation in the domain  $0 \leq z \leq 2h$ , thus producing a situation in which the shear stress at the surface ( $z = h$ ) is zero. The superposition of the two solutions,  $U_1$  and  $U_2$ , between  $0 \leq z \leq h$  results in the desired value of shear stress at the surface ( $z = h$ ).

The first solution, Eq. (5.7), applies to the case of zero internal forcing ( $A = 0$ ), such as the case of wind blowing across an unbounded channel. Application of Eq. (5.10) then constrains the solution to achieve the desired flow rate. In Eq. (5.7), the flow rate at infinite time is dictated by the shear stress, which controls the slope of the velocity profile. At infinite time the velocity profile would be linear with a slope of  $\tau_s/\rho\epsilon$  and the corresponding  $Q$  would be  $\tau_s h^2/(2\rho\epsilon)$  per unit channel width (see Figure 5.4).

The 1-D simulation is compared with solutions from Eqs. (5.7) and (5.10) in Figure 5.4, where the constant term  $A_o$  in Eq. (5.10) is adjusted at each time,  $t$ , to produce the desired flow rate through the section. The pressure gradient that produces the desired  $Q$  must change with time. In keeping with the previous example, the case to be investigated will be the “spin-up to” and spin-down from ” cases of the example in Figure 5.2.

Figure 5.4 plots the results of the simulation to bring the initially quiescent domain to the steady-state condition seen in Figure 5.2. The figure plots the two separate solutions from Eqs. (5.7) and (5.10) at  $t = 1$  s. For reference the steady state result of each solution and their sum is shown. The numerical result at the corresponding time agrees extremely well with the analytic solution in this case. The numerical model is run with a time step of 0.1 s and a spatial resolution of 1/24th the water depth,  $h$  ( $h = 1$  m in this example).

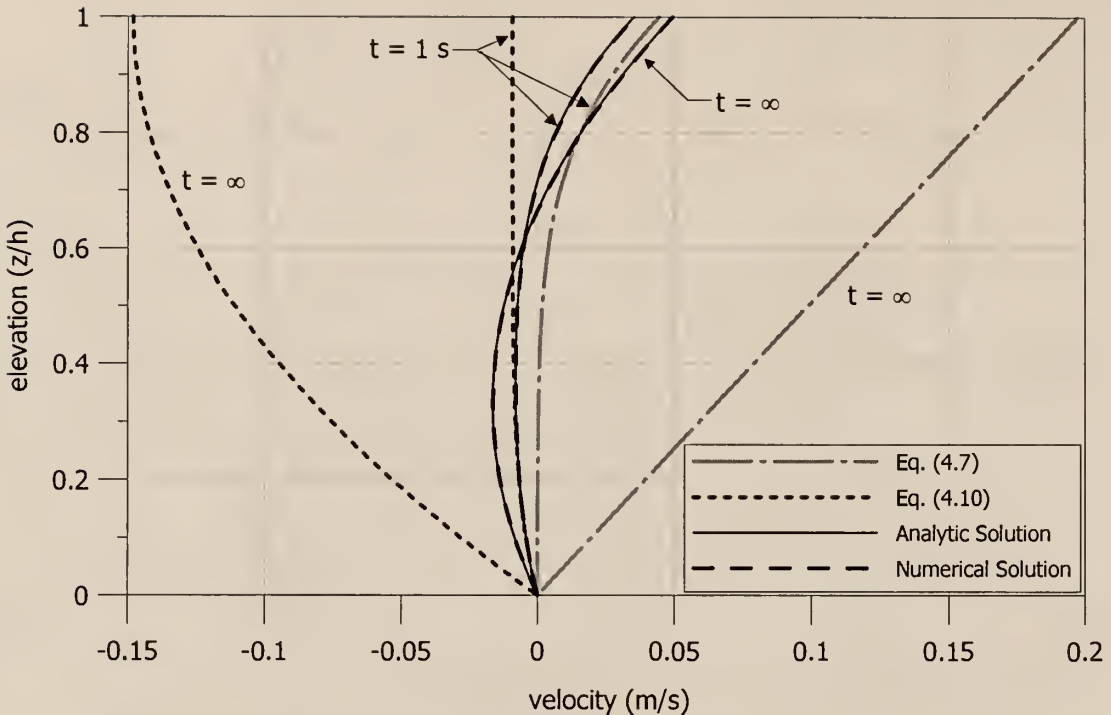


Figure 5.4 Comparison of numerical model results to superimposed analytic solutions to the diffusion equation. The figure plots the individual contributions from the surface shear stress term, Eq. (5.7), and the pressure gradient, Eq. (5.10) at time  $t = 1$  s and  $t = \infty$  ( $Q = 0.0$ ,  $\tau_s = 7.9$  N/m<sup>2</sup>,  $\epsilon = 0.04$  m<sup>2</sup>/s ).

As discussed, the generation of the results in Figure 5.4 necessitated the temporal adjustment of the pressure gradient in Eq. (5.10). Figure 5.5 indicates the time history of the value of the pressure gradient. Figure 5.5 indicates that the pressure gradient increases quickly and asymptotically from zero to its steady state value. The need to adjust the pressure gradient again raises an important issue in modeling the time-dependent return flow. Herein, the model is assumed to adjust immediately to changes in the applied boundary conditions describing the flow rate balance. Obviously there is some lag associated with the adjustment of the flow rate in the surf zone. Little data exist to describe the time dependent nature of  $Q$ , and hence the appropriate time dependent description of the flow rate in Eq. (5.10). This area would benefit from additional research.

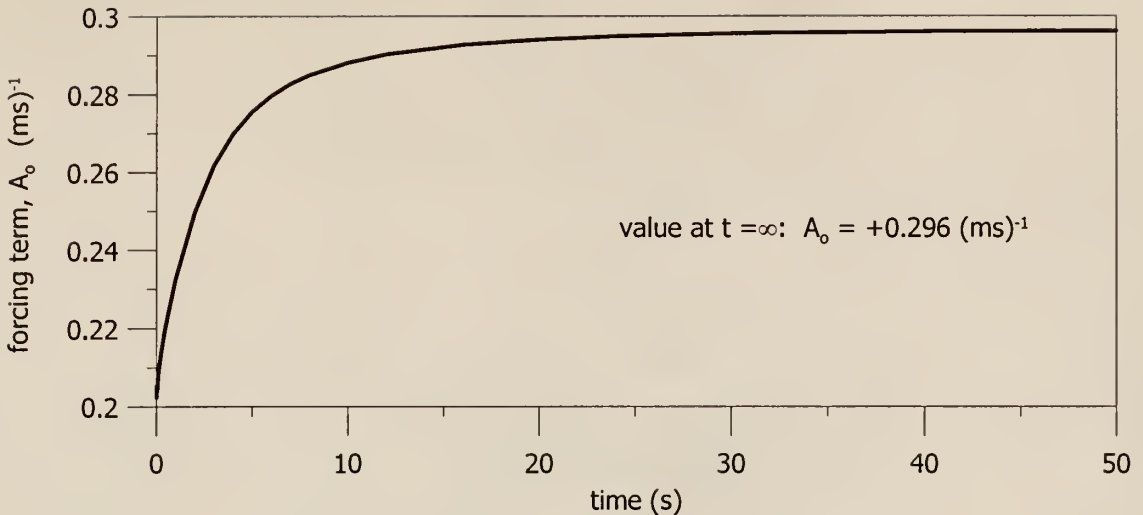


Figure 5.5 Time history of the forcing term,  $A$ , in Eq. (5.10). The forcing term is composed of the pressure and momentum flux gradients. While the forcing term in Eq. (5.10) is considered a constant in the solution, it is adjusted at each time step to impose a no-flow condition in the simulation.

In testing the ability of the numerical model to “spin-up” and “spin down” from the steady-state case, a dependence on the time step was observed. Figure 5.6 illustrates this problem. The figure illustrates three separate runs of the numerical model under the same conditions but with different time steps. For the larger time steps, errors in the velocity profile develop close to the water surface where the second order boundary condition must be satisfied. The numerical model is run semi-implicitly with a time weighting greater than 0.5 toward the implicit case in order to alleviate the strict requirement of the time step needed to achieve stability and convergence (see Chapter 3). The use of the semi-implicit formulation with  $\theta > 0.5$  assures stability and convergence, however, it does not assure that the model will converge to the desired answer (e.g. Abbott, 1979).

In Figure 5.6 it is noticed that difficulties arise for time steps greater than approximately 0.2 s. This time step, however, still represents a ten-fold improvement over

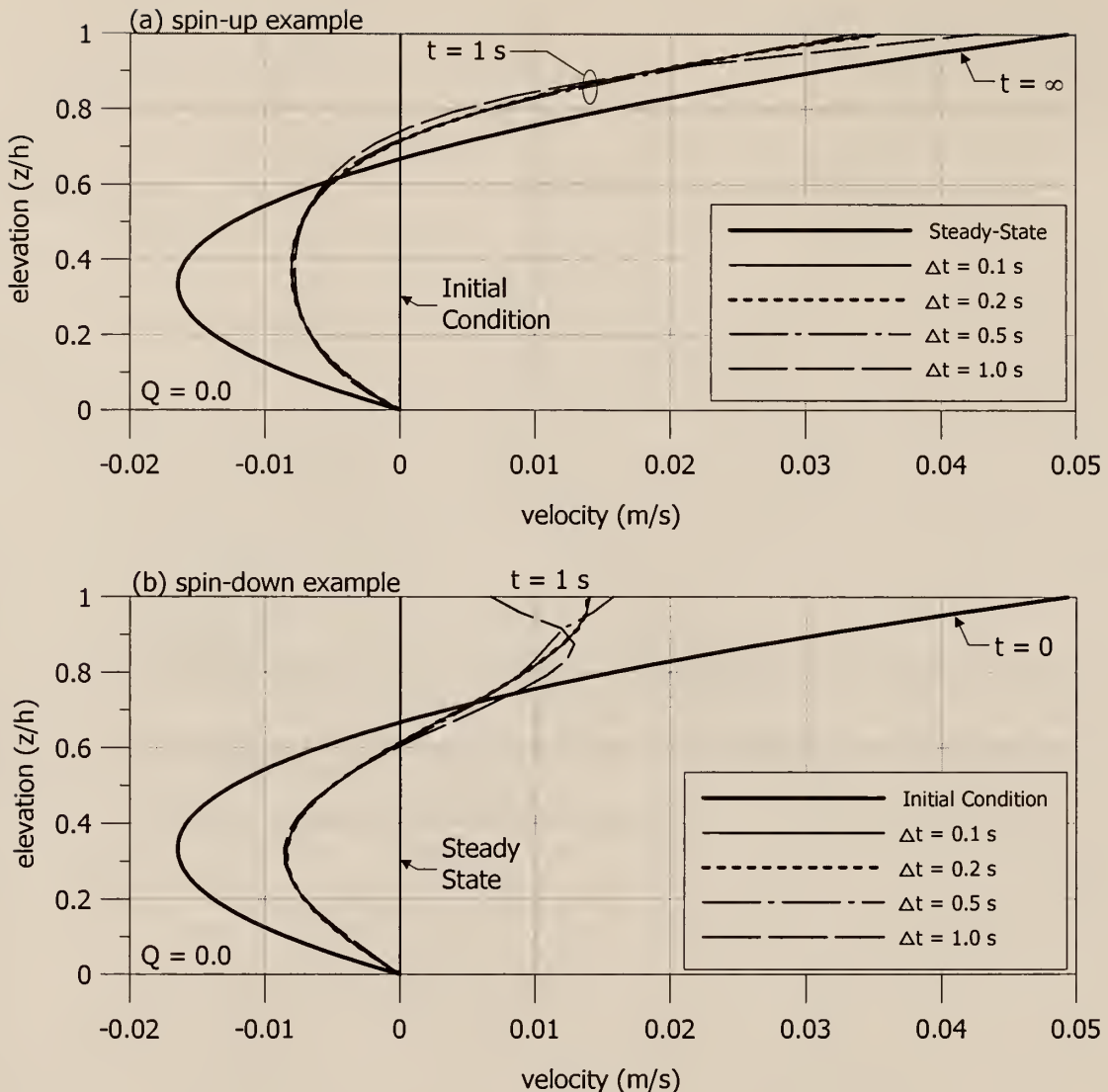


Figure 5.6 Investigation of time step dependence on the one-dimensional semi-implicit numerical model. The model illustrates that for higher time steps, errors develop in the velocity profile. The time step dictated by the fully explicit criteria controlled by the eddy viscosity and the spatial resolution is 0.02 s. The errors arise for time steps greater than 0.2 seconds in this example, and are seen in both the spin-up and spin down examples ( $\tau = 7.9 \text{ N/m}^2$ ,  $\epsilon = 0.04 \text{ m}^2/\text{s}$ ,  $Q = 0.0$ ).

the limiting time step in the fully-explicit case, 0.02 s. This example, that of a “spin-up” and “spin-down,” represents an extreme situation for modeling of surf-zone flows. In the actual simulation of the surf-zone, the “spin-up” period would be neglected in the time-

averaging of the velocity profiles. However, the actual simulations do require the model to compute the velocity profiles that result from changing some of the input boundary conditions. Both the value of  $Q$  and the value of the surface shear stress,  $\tau_s$ , will be updated on a time scale of several seconds, roughly equivalent to the passage of a wave. The use of an excessively large time step could produce an anomalous answer at any given time step in the simulation. While small errors in the answers at each time step would be expected to affect the long-term average, the overall effect is likely to be minimal when averaged over several hundred waves.

## 5.2 Two-Dimensional Model Validation

The 2-D model will now be compared to simple flow cases to validate its performance. Attempts to solve the 1-D, time-dependent fourth-order PDE analytically proved to be unfruitful (a proper representation of  $\psi$  was unobtainable for a series solution, and the resulting integral form from a Laplace Transform approach was untractable from an analytic standpoint). Given the difficulty with the 1-D solution, a 2-D analytic solution to the time-dependent problem was not sought. It is noted that for simple horizontal bottom geometries the numerical solutions away from the lateral boundaries and areas of horizontal gradients may be compared to the 1-D time-dependent solutions presented in the previous section. With that in mind, simple 2-D flows will be investigated that involve similar input conditions to the examples presented previously.

### 5.2.1 Comparisons to One-Dimensional Results

The first example shown is a comparison of the steady-state solution generated by the 2-D numerical model for the case of a constant and uniform unit surface shear stress

over a long tank with a horizontal bottom. The numerical results near the center of the tank are compared to the 1-D analytic solution (Eq. (5.4)). Figure 5.7 plots the results of this comparison. For completeness, and to check the sidewall boundary conditions, simulations are produced with the stress applied in both directions to check for symmetry. The results in Figure 5.7 indicate that the 2-D model reproduces the expected 1-D answer away from the sidewall (as indicated by the overlapping contours of  $\psi$ ) and accounts for the presence of the sidewall equally well in either direction of the applied stress. The 1-D analytic solution is the same at each vertical section (note that the 1-D solution was not applied at the sidewalls; the vertical contours of the 1-D solution immediately adjacent to the sidewalls are simply an artifice of the plotting program). No anomalies are witnessed in the corners, indicating the corner boundary condition code is properly applied.

### 5.2.2 Comparison to Analytic Series Solution

Derivation. For the simple steady-state case of a rectangular, flat-bottomed domain, a solution to the biharmonic equation can be found. The equation is:

$$\frac{\partial^4 \psi}{\partial x^4} + 2 \frac{\partial^4 \psi}{\partial x^2 \partial z^2} + \frac{\partial^4 \psi}{\partial z^4} = 0 \quad (5.12)$$

subject to the boundary conditions:

$$\begin{aligned} \psi(x, -h) &= \psi(0, z) = \psi(L, z) = 0 \\ \psi_z(x, -h) &= \psi_x(0, z) = \psi_x(L, z) = 0 \\ \psi(x, 0) &= -Q(x) \\ \psi_{zz}(x, 0) &= -\frac{\tau_s}{\rho \epsilon} = 0 \end{aligned} \quad (5.13)$$

A solution of the following separable form is sought:

$$\psi = f(z)e^{i\alpha x} \quad (5.14)$$

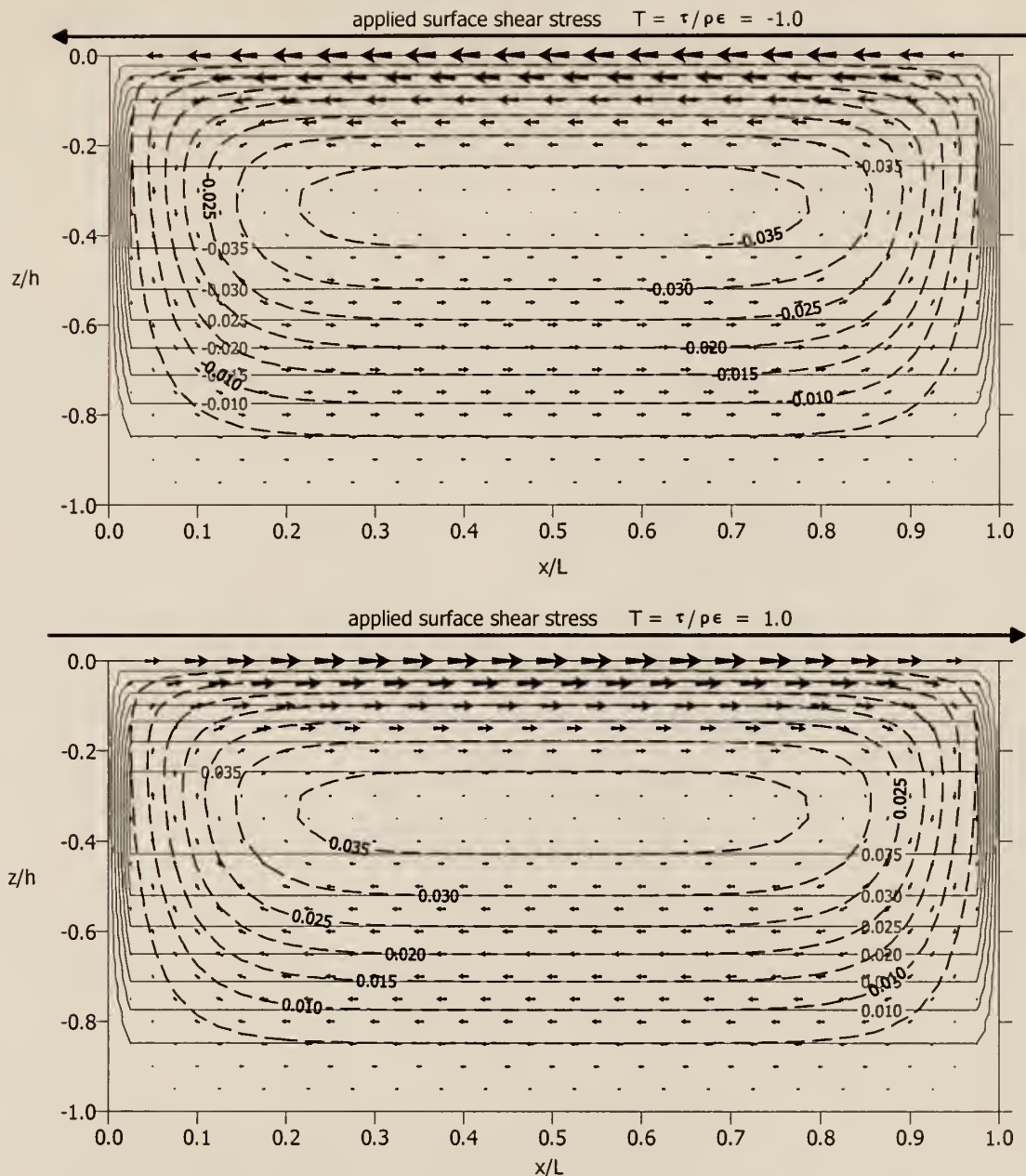


Figure 5.7 Comparison of 2-D numerical model to 1-D analytical results of Eq. (5.4) computed at each vertical section. The 2-D model properly reproduces the analytic results near the center of the tank where there are no horizontal gradients (as indicated by the overlapping contours of the stream function). Additionally, the 2-D numerical model properly accommodates the sidewall conditions where the sidewall velocity equals zero. The applied surface shear stress is simulated in both directions to test for symmetry and to identify any possible corner boundary condition problems. None are observed.

Substitution of Eq. (5.14) into Eq. (5.12) yields the following fourth-order ODE:

$$f_{zzzz} - 2\alpha^2 f_{zz} + \alpha^4 f = 0 \quad (5.15)$$

as shown by Dally, 1980, among others, which has the following form of solution:

$$f = C_1 \sinh(\alpha z) + C_2 \cosh(\alpha z) + C_3 z \sinh(\alpha z) + C_4 z \cosh(\alpha z) \quad (5.16)$$

A series representation for  $\psi$  is now sought:

$$\psi(x, z) = \sum_{j=1}^J [C_{j,1} \sinh(\alpha_j z) + C_{j,2} \cosh(\alpha_j z) + C_{j,3} z \sinh(\alpha_j z) + C_{j,4} z \cosh(\alpha_j z)] e^{i\alpha_j x} \quad (5.17)$$

where  $J$  is the total number of terms used to describe the forcing function (composed of wave numbers,  $\alpha_j$ ). The reader will recognize the form of Eq. (5.17) as the form of an inverse Fourier Transform. The coefficients,  $C_{j,1-4}$ , may be solved for as a set of simultaneous equations as follows:

$$a_{j,m,n} C_{j,m} = b_{j,n} \quad (m=1,4 \quad n=1,4) \quad (5.18)$$

recognizing that each coefficient,  $C$ , has a real and imaginary component. The  $a$  and  $b$  values are determined from the surface and bottom boundary conditions. Application of the boundary conditions creates the set of simultaneous equations that appear in Eq. (5.18):

$$\begin{aligned} B.C. \ 1: \quad & \psi(x, -h) = 0 \\ -C_1 \sinh(\alpha h) + C_2 \cosh(\alpha h) + C_3 h \sinh(\alpha h) - C_4 h \cosh(\alpha h) & = 0 = b_{j,1} \end{aligned} \quad (5.19)$$

$$\begin{aligned} B.C. \ 2: \quad & -\psi_z(x, -h) = U = 0 \\ -C_1 \alpha \cosh(\alpha h) + C_2 \alpha \sinh(\alpha h) & = 0 = b_{j,2} \\ + C_3 [\sinh(\alpha h) + \alpha h \cosh(\alpha h)] - C_4 [\cosh(\alpha h) + \alpha h \sinh(\alpha h)] & = 0 \end{aligned} \quad (5.20)$$

$$\begin{aligned} \text{B.C. 3: } \quad \psi(x,0) &= -Q(x) \\ C_2 &= -\sum_{j=1}^J Q e^{-i\alpha x} = b_{j,3} \end{aligned} \quad (5.21)$$

$$\begin{aligned} \text{B.C. 4: } \quad \psi_{zz}(x,0) &= -\frac{\tau(x)}{\rho\epsilon} \\ C_2\alpha^2 + 2C_3\alpha &= -\sum_{j=1}^J \frac{\tau(x)}{\rho\epsilon} e^{-i\alpha x} = b_{j,4} \end{aligned} \quad (5.22)$$

It is recognized from Eqs. (5.21) and (5.22) that the coefficients  $b_{j,3}$  and  $b_{j,4}$  are simply the Fourier Transforms of the surface boundary condition applied. In this example, the domain is chosen to be  $2^N$  points across so that the smallest wave number corresponds to the length of the domain and the remainder of the wave numbers are multiples of that value in order to take advantage of Fast Fourier Transform techniques.

The method is applied by solving for the  $C$  coefficients described in Eqs. (5.18) through (5.22) for each wave number to be included in the series summation. These  $C$  values are then used in the inverse Fourier Transform equation seen in Eq. (5.17) (again, usually applied as an inverse Fast Fourier Transform). Eq. (5.17) is applied at each desired elevation to obtain the value of  $\psi$  at each horizontal position at a given elevation.

It is noted that the four additional boundary conditions are satisfied in this solution by the nature of the function of  $x$  in Eq. (5.14). By representing the surface conditions as sinusoidal functions whose smallest wave number is defined by the length of the domain (e.g. the tank length), the sidewalls become vertical lines of symmetry, thus satisfying the no-flow, no-slip conditions specified in Eq. (5.13).

Application. The results from the 2-D numerical model are compared to the analytic solution just derived for the simple case of a varying sinusoidal transport. This case demonstrates the effect of changing the value of  $\psi$  across the surf zone, which creates inflow and outflow at the surface, much like what would be expected in an actual surf zone. Figure 5.8 plots the results of this simulation. It is seen that the numerical and analytical solutions agree quite well at all locations, and the numerical model is able to reproduce the inflows and outflows at the surface necessary to model the return flow in the surf zone from the MWL to the seabed.

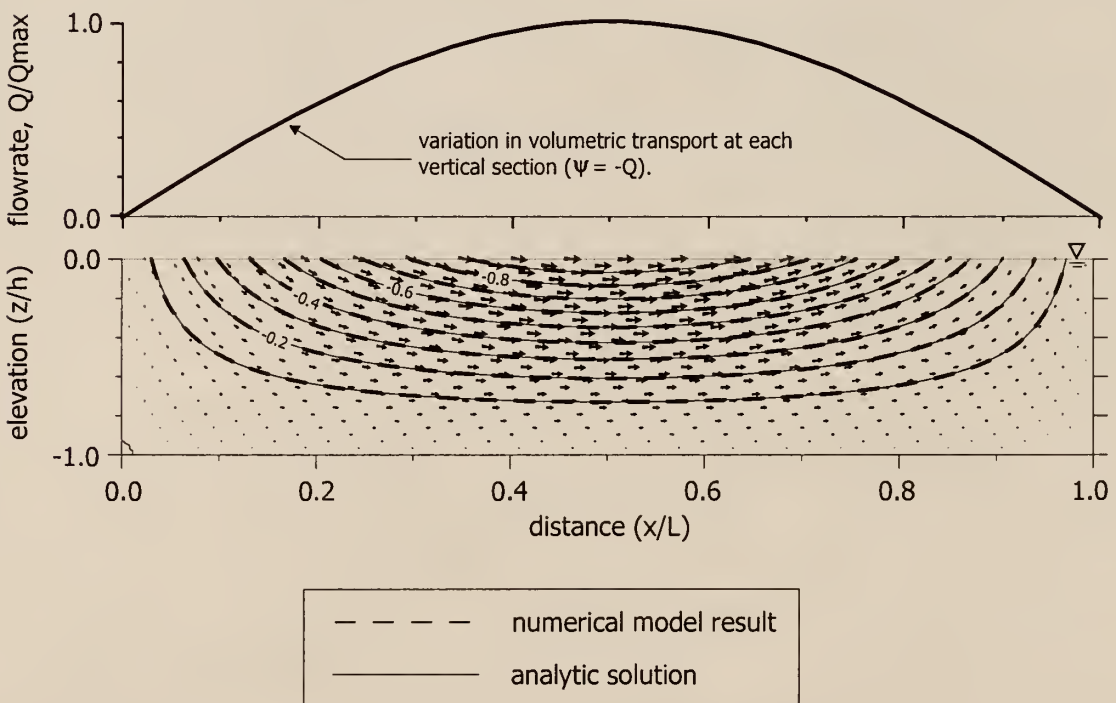


Figure 5.8 Comparison of numerical model results to Fourier series solution (Eq. (5.17)). The numerical model accurately reproduces the streamlines for the sinusoidally varying surface boundary condition applied. The variation in the value of  $\psi$  across the surface produces inflow and outflow at the surface, as shown.

## CHAPTER 6

### COMPARISON OF NUMERICAL MODEL TO EXPERIMENTAL DATA

In this chapter, the model is applied to simulate numerous return flow experiments in laboratory and field settings. Simulations are conducted over a range of boundary conditions and parameters to determine a combination of values that produces the best overall agreement for the available experimental data. The performance of the model at any one measured velocity profile is expressed in terms of the Root-Mean-Square error ( $E_{RMS}$ ) of the vertical structure of the horizontal velocity profile. The RMS error thus describes not only the prediction of the mean, depth averaged velocity (or flow rate), but also the ability to predict the *shape* of the profile. To compare the results of various experiments, the RMS error is normalized and denoted as  $\beta$ . The distribution of  $\beta$  across the profile and the average value of  $\beta$  for a particular simulation are compared to other simulations to identify which combination of parameters best suits the processes involved.

The range of parameters is extensive. Herein an attempt is made to describe the range of effects of the possible combinations of parameters. Table 6.1 lists the parameters to be investigated in the simulations, along with a brief description of the source or range of values to be applied for each parameter. Six experiments will be simulated using the two-dimensional numerical model: four laboratory experiments with fixed beds, one laboratory experiment with a moveable bed, and one field experiment. The results presented in this chapter stem from over 190 simulations.

Table 6.1 Parameters to be Investigated/Adjusted in Numerical Model for Comparison to Experimental Data.

Parameter	Derivation of Value
Volumetric Flow Rate, $Q$	Linear Wave Theory Sawtooth Approximation Stream Function Wave Theory Svendsen (1984a) Surface Roller Approximation Dally and Brown (1995) Surface Roller Approximation
Surface Shear Stress, $\tau_s$	Linear Wave Theory Sawtooth Approximation Stream Function Wave Theory Svendsen (1984a) Surface Roller Approximation Dally and Brown (1995) Surface Roller Approximation
Bottom Boundary Condition	Bottom Velocity, $U_b$ (= zero) or Bottom Shear Stress, $\tau_b$ (= zero)
Eddy Viscosity, $\epsilon$	uniform, horizontal, horizontal/vertical variation

Note: Seaward of first break point, Stream Function Wave Theory (SFWT) (Dean, 1974) is used to determine  $Q$  and  $\tau_s$ .

### 6.1 Introduction of Model Output and RMS Errors

To compare the results of the various simulations to the experimental data, two indices are computed. The first is simply the RMS error in the vertical structure of the horizontal velocity at each measured profile line in a particular data set. In order to fairly compare the performance of the model from one data set to another, a normalized root mean square error is introduced.

To illustrate these indices, one simulation from the numerical model is presented in Figure 6.1, simulating the laboratory data of Cox and Kobayashi (1997). The figure presents the contours of the stream function,  $\psi$ , along with the predicted velocity vectors calculated from  $\psi$  using Eq. (3.15). The wave height profile and the Mean Water Surface (MWS), including set-down and set-up effects, are also presented. Figure 6.2 depicts the comparison of vertical profiles of mean horizontal velocity for this experiment.

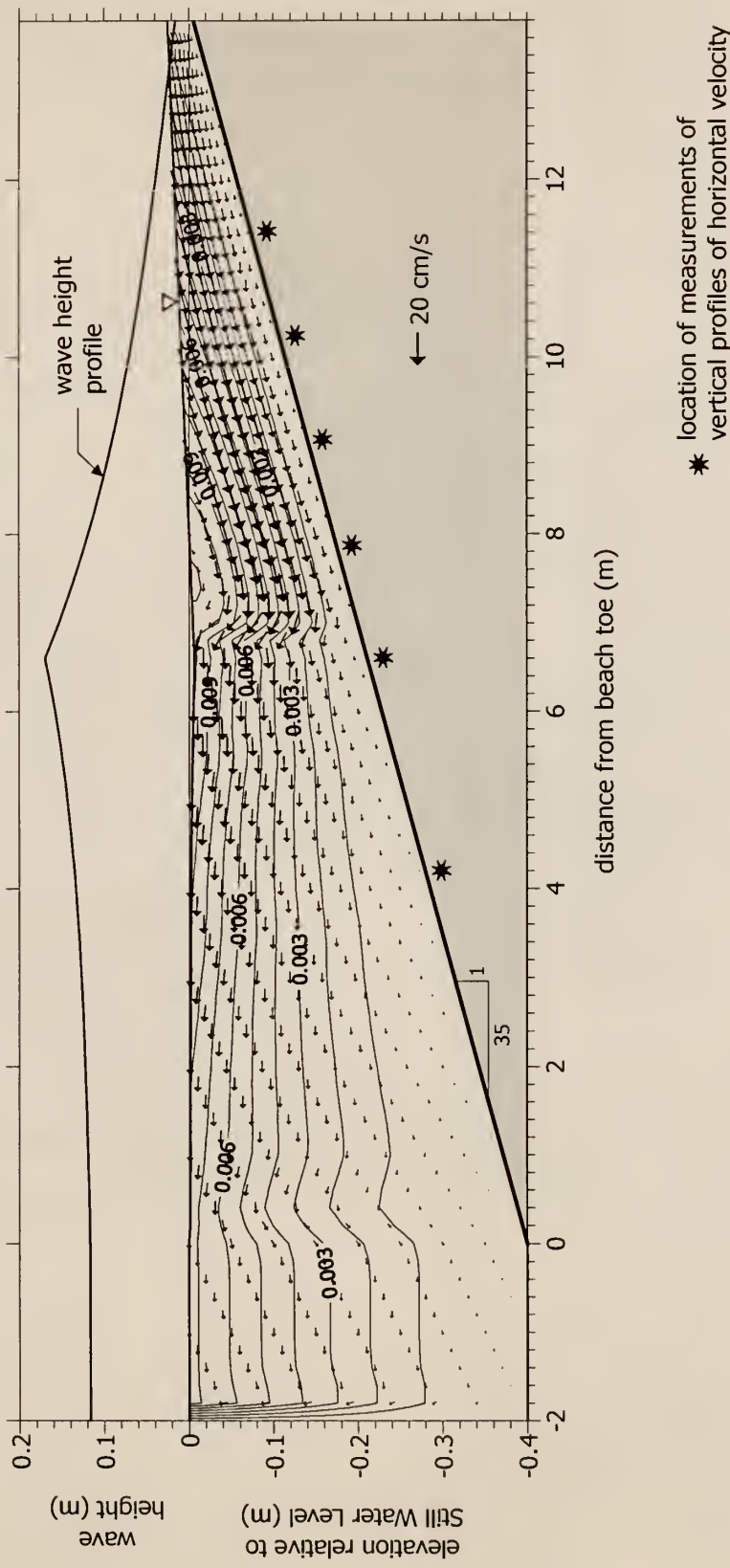


Figure 6.1 Example contour and velocity vector plot of laboratory experiments by Cox and Kobayashi (1997). The contours are lines of constant  $\psi$  (streamlines). The size of the velocity vectors indicates the magnitude of the velocity of the flow. The wave height profile and set-up and set-down of the water surface are indicated in the plot. Conditions for this experiment are listed in the following figure (Figure 6.2). The parameters for the simulation include a no-slip bottom boundary condition and flow rate and surface shear stress conditions inside the surf zone dictated by a surface roller approximation (Svendsen, 1984a). The offshore conditions are patched into the inner surf zone conditions by the characteristic length determined from the radiation stress profile.

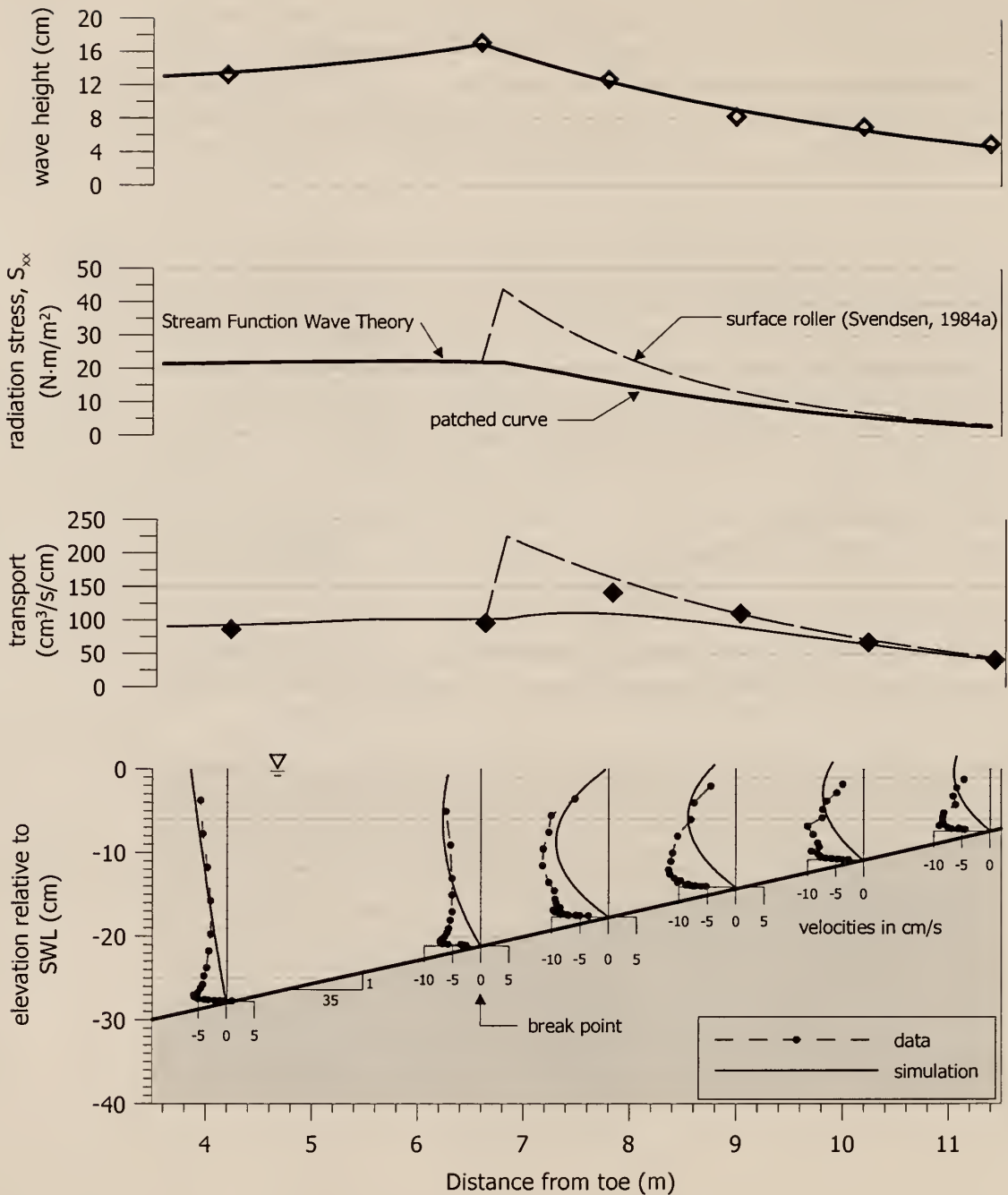


Figure 6.2 Example of cross shore variation in wave height, radiation stress, volumetric transport, and vertical profiles of horizontal velocity for the experiments of Cox and Kobayashi (1997). The breaking wave height is 17.1 cm and the wave period is 2.2 s. In this simulation the offshore description is patched with the inner surf zone description computed from a surface roller approximation (Svendsen, 1984a) by matching the radiation stress across the transition region. The turbulent eddy viscosity is held uniform in this simulation at  $\epsilon = 0.001 \text{ m}^2/\text{s}$ .

In the simulations presented in Figures 6.1 and 6.2, the parameters used include the surface roller approximation of Svendsen (1984a) for the volumetric transport and the surface shear stress boundary conditions. The no-slip bottom boundary condition is chosen and the eddy viscosity is held uniform at  $0.001 \text{ m}^2/\text{s}$ .

Inspection of Figure 6.1 illustrates one benefit of the present 2-D numerical model. The use of the stream function provides the horizontal and vertical velocity field throughout the domain. The changing volumetric transport of the wave as it traverses the profile is evident in the streamlines that intersect the MWS. The sudden change in the flow field that results from the breaking wave is also readily apparent. The sharp decreasing gradient in wave height that occurs at breaking begins to produce an injection of fluid through the MWS, and also applies a strong onshore-directed surface shear stress. The vertical sections landward of breaking experience weaker offshore flows near the water surface, with correspondingly stronger offshore flows near the bottom.

Figure 6.2 shows the change in wave height, radiation stress, volumetric transport, and horizontal velocity profile seaward and landward of the break point. Seaward of the break point, the measured profiles are more uniform, landward of the break point the profiles exhibit a more parabolic shape, with the peak offshore return flow shifted toward the bottom (this is a general observation of most return flow profiles). The data collected by Cox and Kobayashi (1997) include measurements in the bottom boundary layer over the rough bed. The measured values near the bed indicate an overshoot of the velocity in the boundary layer relative to the velocity in the body of the fluid above the boundary layer. In Figure 6.2, the parameters chosen obviously do not reproduce this phenomenon since the bottom velocity was set to zero and the eddy viscosity was held uniform. The predicted volumetric transport is also underestimated in the transition region ( $x \sim 6.6 \text{ to } 8.0 \text{ m}$ ).

While the choice of parameters used to generate the predictions shown in Figures 6.1 and 6.2 may not be the best possible, the general behavior is reproduced. The error in vertical structure between the measured and predicted profiles can be quantified by computing  $E_{RMS}$  and  $\beta$ . The sum of the square of the errors is normalized by the sum of the squares of the measured values alone (over the vertical range). The resulting ratio produces a statistical index that describes the degree of agreement between the prediction and the measurements, where lower values indicate better agreement:

$$\beta = \sqrt{\frac{\sum (U_{pred} - U_{meas})^2}{\sum (U_{meas})^2}} \quad (6.1)$$

The value of  $\beta$  will be shown to depend strongly on the prediction of the flow rate, but it also is affected by the shape of the profile which is dictated by other boundary conditions. The value of  $\beta$  may vary from zero to values greater than 1.0. It is recognized, however, that it requires zero predictive ability to produce a value of  $\beta = 1.0$ . Assuming the predicted velocity across the profile is zero everywhere, a  $\beta$  value of 1.0 is obtained. Values of  $\beta$  closer to 0.0 are desired. The RMS error is defined as follows:

$$E_{RMS} = \sqrt{\frac{1}{N} \sum (U_{pred} - U_{meas})^2} \quad (6.2)$$

To compute  $E_{RMS}$  and  $\beta$ , the measured and simulated profiles were interpolated to a fine, uniform, resolution to avoid over-weighting the value of areas of dense measurements, such as in the boundary layer of the Cox and Kobayashi experiment. The resolution is chosen such that all available measured data are used. Table 6.2 lists the

resulting values of  $E_{RMS}$  and  $\beta$  for the six stations shown in Figure 6.2. The table indicates that most profile lines were not well predicted, with percent errors of 45% or more along five of the six measured profile lines. The best agreement was found at Station #3 where the model predicted the measured velocities to within 34%.

Table 6.2 Errors in Example Simulation Shown In Figures 6.1 and 6.2 for Cox and Kobayashi (1997) Laboratory Experiment.

Measuring Station	$E_{RMS}$ (cm/s)	$\beta$
1 (offshore)	1.8	0.486
2	2.4	0.450
3	3.6	0.360
4	4.7	0.496
5	3.9	0.510
6 (onshore)	3.9	0.568

For the example simulation shown, three choices of parameters strongly affect the value of  $\beta$ . The underestimation of the flow rate, particularly at Stations #3 and #4, creates a substantial degree of error. Additionally, the choice of a zero bottom velocity coupled with the uniform eddy viscosity field produces substantial errors in the prediction of the flow field in most of the profiles in this simulation, particularly in the inner surf zone and near the bottom where the bottom boundary layer is clearly present. A zero bottom shear stress condition, or a spatially varying eddy viscosity field, such as one based on the mixing length model of Reid (1957), will be shown to generate improved results, forcing the peak of the return flow curves closer to the seabed and creating more uniform profiles.

Table 6.3 lists the experimental data sets simulated in the present work and their conditions. Four laboratory experiments using planar slopes, one of which is barred, are studied. One of the four experiments applied random waves, the other three applied periodic (monochromatic) waves. One movable bed laboratory experiment was simulated, in which random waves were run on an approximately stable but irregularly shaped beach profile. One field experiment was simulated in the model, which applied random waves.

Table 6.3 Conditions for Return Flow Measurements Simulated by Numerical Model.

Experiment	Condition	Wave Height (cm)	Period, s	Beach Slope
Cox & Kobayashi, 1997	Lab, rough bed	17.1 (breaking)	2.2 (periodic)	1:35
Ting & Kirby, 1994	Lab, smooth bed	16.3 (breaking)	2.0 (periodic)	1:35
Nadaoka & Kondoh, 1982	Lab, smooth bed	21.1 (breaking)	1.32 (periodic)	1:20
Okayasu & Katayama, 1992	Lab, smooth, barred bed	10.6 ( $H_s$ , incident)	1.14 ( $T_p$ )	1:20 (all slopes)
Roelvink & Reniers, 1995	Lab, rough, movable bed	94 ( $H_s$ , incident)	4.8 ( $T_p$ )	1:50
Smith et al. 1992	Field	76 ( $H_s$ , incident)	9.7 ( $T_p$ )	1:22

It is noted that the use or non-use of a transition region treatment is not considered as a parameter. While some simulations may demonstrate better agreement without the momentum conservation consideration (such as in Figure 6.2), it is not physically appropriate to leave the conservation issue unresolved. Where needed, the momentum conservation patch between the offshore region and the inner surf zone will be applied. The radiation stress ( $S_{xx}$ ) patch is applied to three different descriptions of the surf zone

flow. In accordance with Dally and Brown (1995), the organized wave flow will be described using stream function wave theory in combination with their roller model. It will be shown that the transition region length is not necessarily properly modeled by either model. Further discussion on the transition region is found in Chapter 7.

To further demonstrate the  $S_{xx}$  patch technique, two simulations of the Ting and Kirby (1994) data set were performed, one with the patch and one without. The two simulations illustrate that the patch improves the agreement of the profiles immediately landward of breaking over the non-patched case because the development of the volumetric transport due to the surface roller is better modeled (Figure 6.3). The overall agreement of the surf zone profiles benefits from the reduced shear stress predicted from the patched  $S_{xx}$  curve, which exhibits a milder slope, and thus smaller surface shear stresses. In Figure 6.2, the simulation of the Cox and Kobayashi data set does not benefit from using the patch. However, Cox and Kobayashi did not collect measurements immediately landward of breaking. It is hypothesized that immediately landward of breaking, most unpatched inner surf zone descriptions would overestimate the transport and velocity in this region.

Figure 6.4 compares the  $S_{xx}$  patch method to the model of Dally and Brown (1995) for the data of Ting and Kirby (1994). The no-slip bottom boundary condition is applied along with a uniform eddy viscosity field. The Dally and Brown model is applied using a value of  $\beta_D = 0.15$ , determined from calibration against published return flow experiments such as Nadaoka and Kondoh (1982) and modified from their originally published value of 0.10. Duncan (1981) found  $\beta_D$  values of between 0.17 and 0.25 for surface rollers generated by towed hydrofoils. The Dally and Brown model provides a slight increase in the predicted values of  $S_{xx}$  and transport. The increased transport improves the agreement of the measured velocity profiles, as does the milder slope of the  $S_{xx}$  curve.

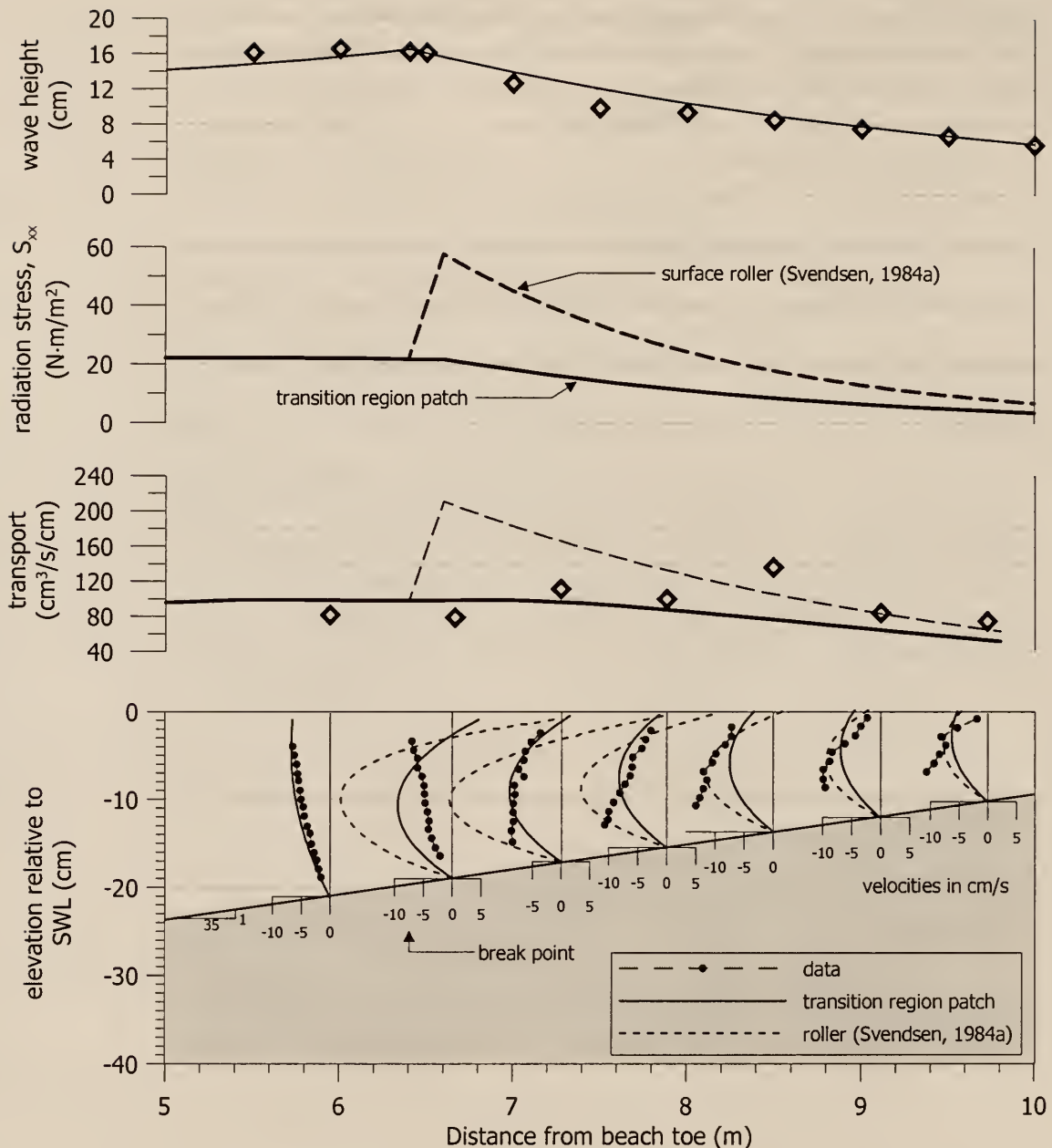


Figure 6.3 Comparison of cross shore variation in wave height, radiation stress, volumetric transport, and vertical profiles of horizontal velocity for the experiments of Ting and Kirby (1994) ( $\epsilon = 0.001 \text{ m}^2/\text{s}$ ). In these two simulations, the effect of merging the offshore description of wave characteristics with the inner surf zone description (computed from a surface roller approximation in this case) is illustrated. The merging technique improves the prediction by more accurately reproducing the measured return flow rate at each measuring station in the transition region (approximately  $x \sim 6.6$  to  $8.6$  m), and by reducing the applied surface shear stress, as evidenced by the milder slope of the patched radiation stress curve.

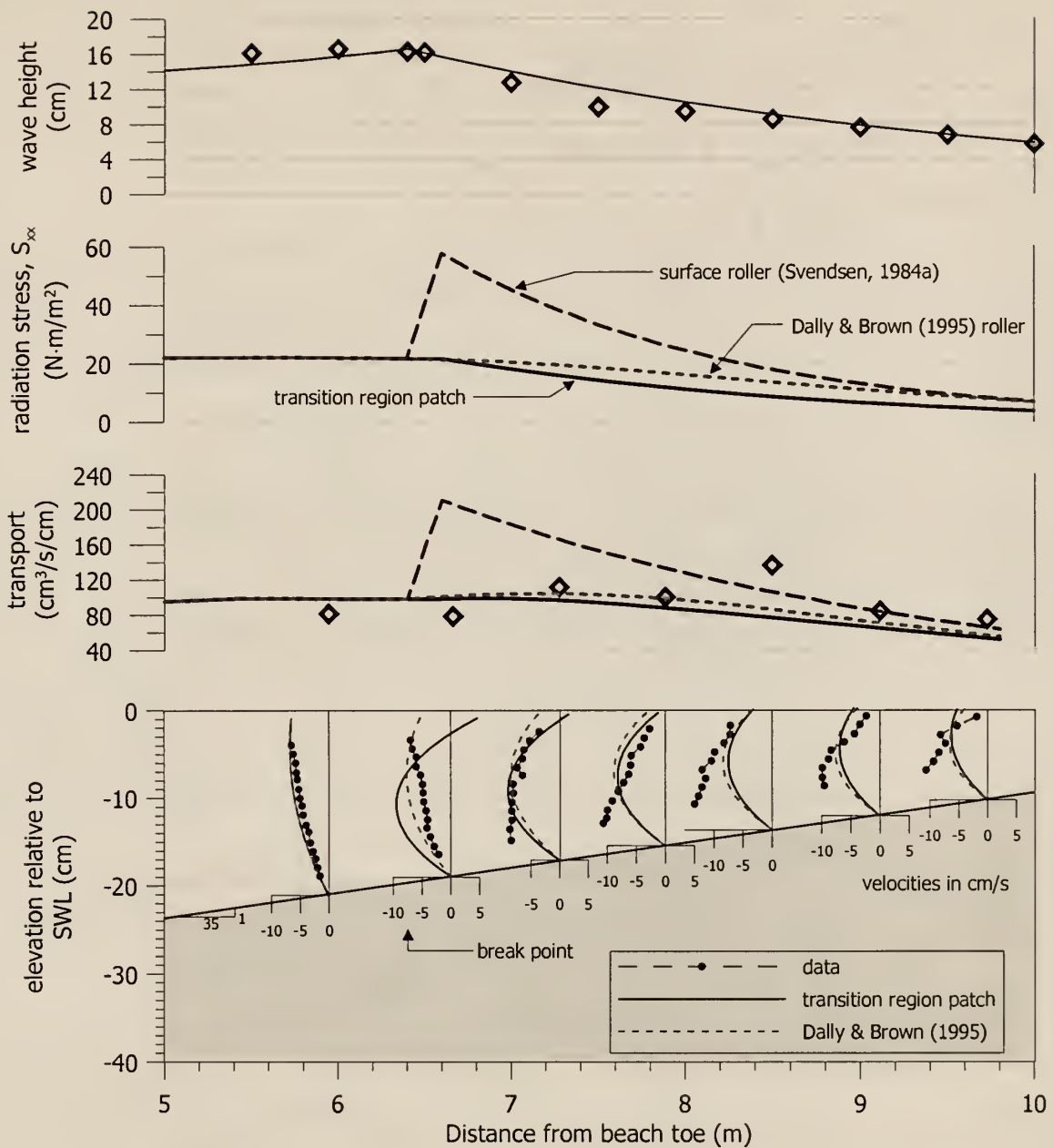


Figure 6.4 Comparison of present radiation stress transition region patch to the wave surface roller model of Dally and Brown (1995) for the data set of Ting and Kirby (1994) ( $\epsilon = 0.001 \text{ m}^2/\text{s}$ ). Both models conserve momentum across the profile from the offshore region to the inner surf zone. The Dally and Brown model predicts higher values of radiation stress and transport in the transition region, but lower surface shear stress due to the milder slope of the radiation stress curve. The increased predicted transport in the transition region improves the agreement with the data, as shown in the third and fourth plots. The plots of the Dally and Brown model apply a  $\beta_D$  value of 0.15, higher than the value in their published work (Dally, personal communication).

Having introduced the products that the model generates and the index to be used in determining the level of disparity between the measured and predicted flow fields, the array of parameters available for boundary conditions are now tested to attempt to draw some conclusions about which boundary conditions produce the best simulation. Each of the available experimental data sets will be simulated using a similar matrix of input parameters. In this way, common performance features will be revealed.

## 6.2 Simulation of Cox and Kobayashi (1997) Experiments

Figure 6.5 compares 20 simulations of the Cox and Kobayashi (1997) experiments outlined in Table 6.3. The simulations are based on the parameters listed in Table 6.1. The upper plots apply a no-slip bottom velocity boundary condition while the lower plots apply a zero shear stress bottom boundary condition. All 20 simulations apply a uniform eddy viscosity; the plots on the left hand side apply a value of  $\epsilon = 0.001 \text{ m}^2/\text{s}$  and the plots on the right hand side apply a value of  $\epsilon = 0.01 \text{ m}^2/\text{s}$ . The plots compare  $\beta$  across the profile at the six stations reported. Where necessary the inner surf zone flow descriptions are patched with SFWT in the offshore region. The Dally and Brown (1995) roller model incorporates SFWT with the roller, and thus does not require patching.

In Figure 6.5, the parameter that affects the overall agreement the most is the prediction of the volumetric flow rate. The patched roller approximation of Svendsen (1984a) and the Dally and Brown (1995) roller model produce the highest value of transport at each profile, which appears to produce the greatest level of agreement with the measured data in each plot. The choice of zero shear stress as a bottom boundary condition also produces improved overall agreement. For either bottom condition, the lower eddy viscosity values produce lower (better) values of  $\beta$ .

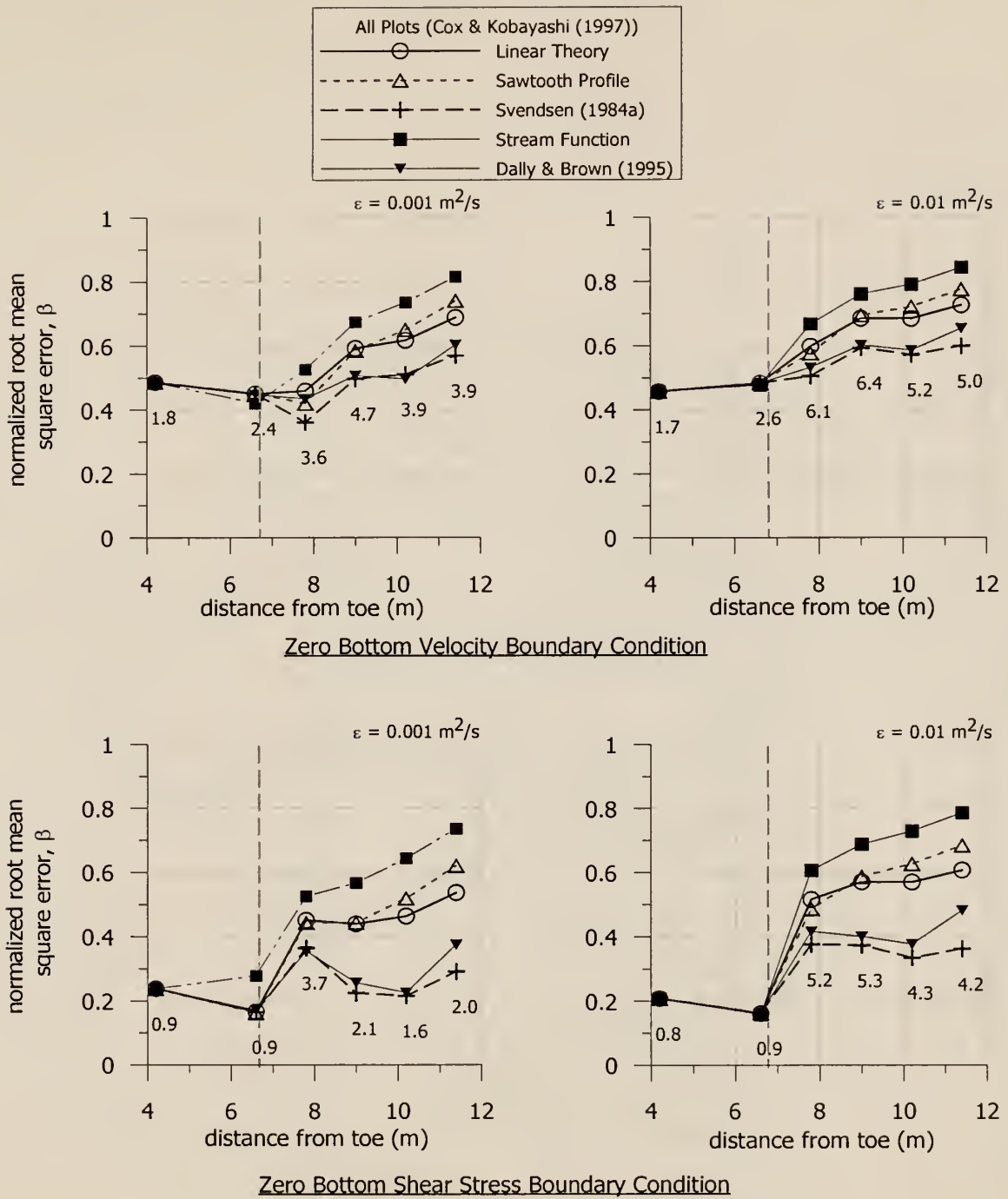


Figure 6.5 Comparison of simulations of the data set of Cox and Kobayashi (1997). The plots compare the normalized RMS error,  $\beta$ , for two different eddy viscosity values and two different bottom boundary conditions. The RMS error is given in cm/s at each measuring line for the theory that provides the best agreement (the surface roller approximation). In each case the eddy viscosity is held uniform over the entire domain. The mean measured velocity at each station is found by dividing the RMS error by the corresponding  $\beta$  value. The vertical dashed lines indicate the break point location.

The improved agreement shown in the lower plots of Figure 6.5 compared to the upper plots stems from the combination of a spatially uniform eddy viscosity field and a no-slip bottom boundary condition. This combination clearly does not simulate any boundary layer behavior, whereas the zero bottom shear stress condition does. It will be shown that a vertically varying eddy viscosity field improves the agreement when applying a no-slip bottom condition.

In Figure 6.5, for the no-slip bottom boundary condition, at both values of  $\epsilon$ , agreement to within only 40 to 60% is achieved, at best. The corresponding RMS errors in velocity for the best simulation in each plot are listed in the figure. The zero bottom shear stress boundary condition provides improved agreement, matching the measured velocity profiles to within approximately 20 to 40% for the Svendsen surface roller case.

Figure 6.6 plots the wave height, radiation stress, volumetric transport, and velocity profiles for the lower eddy viscosity value ( $\epsilon = 0.001 \text{ m}^2/\text{s}$ ) in Figure 6.5. The velocity profiles corresponding to the Svendsen (1984a) surface roller simulations for the no-slip and zero bottom shear stress conditions are plotted. The effect of each of the inner surf zone experiments is evident. SFWT used alone predicts the lowest values of radiation stress and volumetric transport, whereas the surface roller models predict the highest values. Consistent with Figure 6.5, the surface roller models more closely simulate the measured value of volumetric transport and thus produce better agreement with the measured velocity profiles.

In Figure 6.5, the zero bottom shear stress condition provides improved agreement at most measuring lines because it better simulates the behavior of the flow just outside of the bottom boundary layer (evident in the measured data). Inspection of the measured results (Figure 6.6) suggest that perhaps a bottom shear stress condition in which the shear

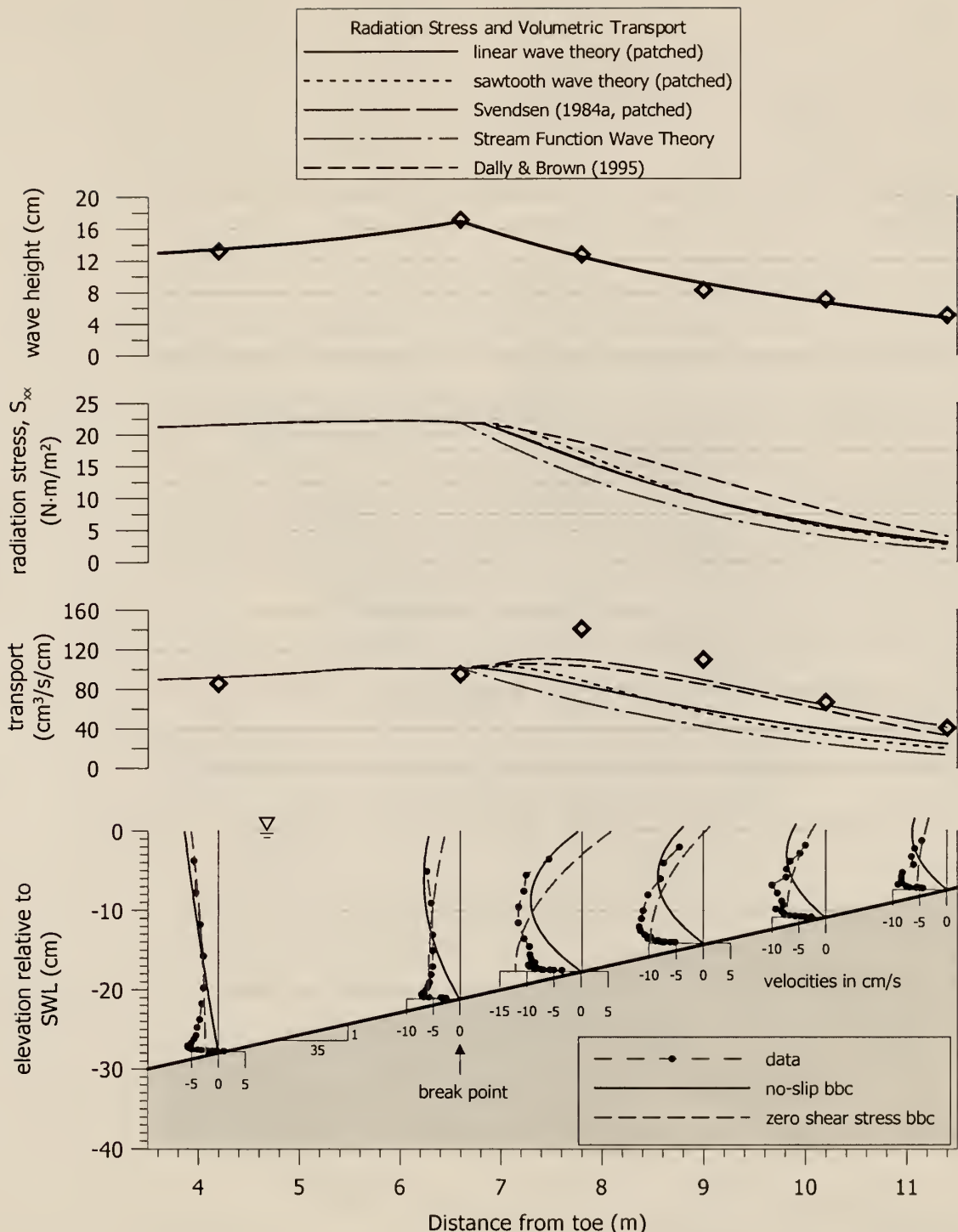


Figure 6.6 Comparison of predicted radiation stress and volumetric transport for the experiments of Cox and Kobayashi (1997). The five curves in each of the second and third frames illustrate the prediction of  $S_{xx}$  and  $Q$  for the five different surf zone descriptions listed. The velocity profiles predicted for the no-slip and zero shear stress bottom boundary conditions are plotted in the last frame and correspond to the patched Svendsen (1984a) surface roller approximation with a uniform value of  $\epsilon = 0.001 \text{ m}^2/\text{s}$ .

is small, but finite, would improve the agreement further. As discussed in the literature review and elsewhere, the knowledge of bottom shear stress values is limited.

To attempt to improve the simulations, a horizontally-varying eddy viscosity is introduced in the model. The value of  $\epsilon$  at each horizontal position is found from:

$$\epsilon = 0.01h\sqrt{gh} \quad (6.3)$$

as suggested by Stive and Wind (1986) with the simplifying assumption of shallow water. In the present simulation, with depths reaching 0.4 m, the values of  $\epsilon$  range from 0.0079 m<sup>2</sup>/s in 0.4 m water depth to approximately 0.0003 m<sup>2</sup>/s in 0.05 m water depth.

It must be recognized that detailed knowledge of the value of the turbulent eddy viscosity is difficult to obtain, yet its value is extremely important in predicting the shape of the undertow profile. This is evidenced by the plots of Figures 6.5 and 6.6, in which the surface shear stress is determined from an external theory (e.g. linear, surface roller, etc.) and the eddy viscosity is constant for the simulations of each theory in each plot. The application of the surface shear stress boundary condition to the determination of  $\psi$ , however, is dependent on the value of the turbulent eddy viscosity at the surface. An increase in  $\epsilon$  results in a milder slope of the velocity profile at the water surface and hence a more uniform velocity profile overall.

A further attempt to refine the simulation is the application of a vertically varying eddy viscosity separately or in conjunction with the horizontal variation. As discussed in Chapters 2 and 5, the mixing length hypothesis of Reid (1957) is applied to determine the vertical variation in eddy viscosity caused by a surface applied shear stress. In the present example, the surface stress is much larger than the bottom stress, resulting in an eddy viscosity distribution whose peak is strongly shifted upward toward the surface and which

diminishes sharply near the bottom. In the present work, a similarity profile is applied at each vertical section in which the value of  $\epsilon$  at the surface is either constant across the surface or is found from Eq. (6.3). The shape of this profile can be seen in the discussions in Chapter 2 and Chapter 5. The peak value is located at approximately 70% of the water depth (from the bottom) and is taken to be twice the value at the surface. The value at the bottom is taken to be 1/100th the surface value, in keeping with the findings of Svendsen et al. (1987), among others. The low value of  $\epsilon$  near the bottom mimics a boundary layer without mathematically including such a feature.

Figure 6.7 plots the results of 12 additional simulations, two each of the horizontally-varying but depth-uniform eddy viscosity case, two each of the vertically-varying eddy viscosity case, and two each of the horizontally- *and* vertically-varying eddy viscosity case. The surf zone descriptions are those of the patched surface roller of Svendsen (1984a) and the roller model of Dally and Brown (1995). The distributions of  $\beta$  are plotted against the same two surf zone descriptions applying a uniform value of  $\epsilon = 0.001 \text{ m}^2/\text{s}$ . Both the no-slip and zero bottom shear stress cases are shown. Example velocity profiles from the profile at Station #4 are shown in Figure 6.8 and Figure 6.9 to illustrate the differences between the various combinations of parameters.

For the no-slip bottom boundary condition, Figure 6.7 indicates that the inclusion of a horizontally varying eddy viscosity by itself provides only a marginal level of improvement over the uniform case. The no-slip condition and the depth-uniform  $\epsilon$  prevent the model from reasonably approximating the steep gradient near the bottom (where a thin boundary layer clearly exists). Inclusion of the vertically-varying eddy viscosity, however, significantly improves the agreement between the simulation and the measurements. The vertically-varying eddy viscosity lowers the  $\beta$  values by nearly half

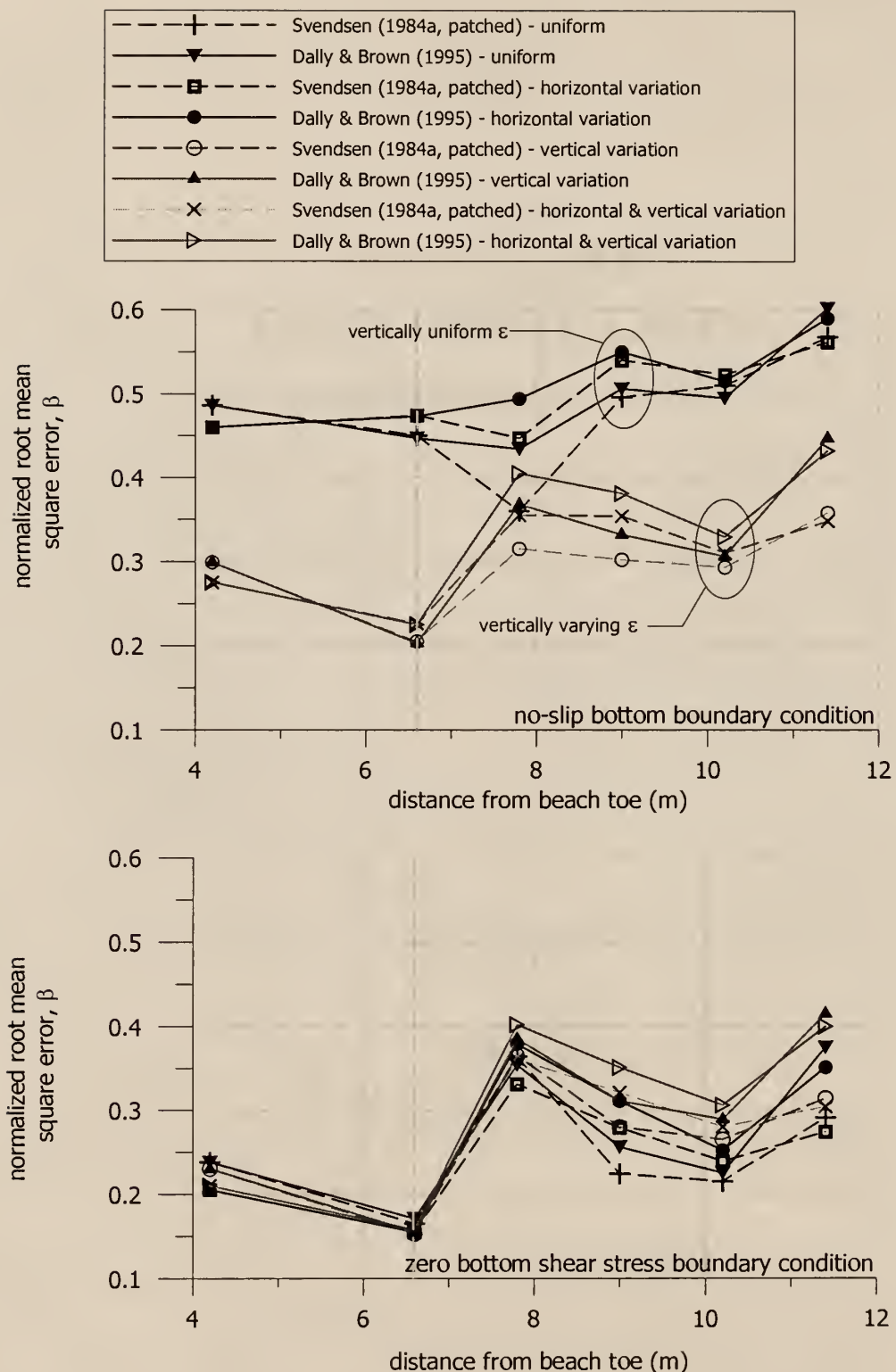


Figure 6.7 Comparison of normalized RMS errors,  $\beta$ , for the experiment of Cox and Kobayashi (1997) employing spatially variable eddy viscosity fields. The roller models of Svendsen (1984a, patched) and Dally and Brown (1995) are used for the comparison.

at most stations, to within 25 to 35% error. The reasons for this improvement are illustrated in Figure 6.8, where the four simulations using the patched Svendsen model are compared to the measured horizontal velocity profile at Station #4. While the transport is underestimated in all four simulations, the comparison of the four simulated velocity profiles at Station #4 indicates that the two depth-uniform cases cannot match the measurements near the bottom, whereas the significant decrease in eddy viscosity near the bottom of the depth-varying eddy viscosity case allows the fluid to “slip” over the bottom and simulate the presence of a boundary layer.

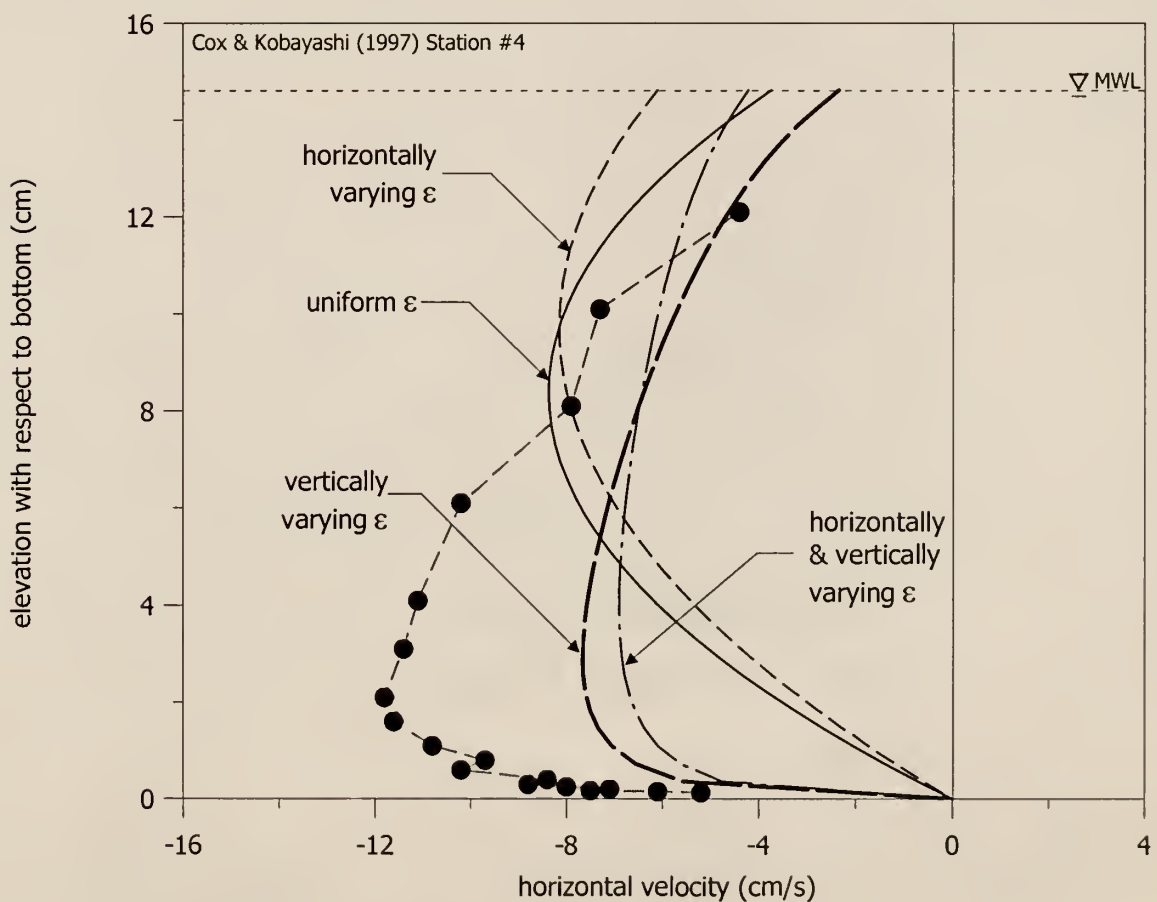


Figure 6.8 Comparison of vertical profiles of horizontal velocity at Station #4 of the Cox and Kobayashi (1997) data set. The plot illustrates the significant improvement in the agreement by including a vertically varying eddy viscosity field with a no-slip bottom boundary condition.

In contrast, application of a variable eddy viscosity field and a zero bottom shear stress boundary condition yields minimal improvement (Figure 6.7). The horizontally varying eddy viscosity field provides only minor improvement in the offshore region, and degrades the agreement in the surf zone. The same applies to the vertical variation of  $\epsilon$ . Figure 6.9 illustrates how the zero bottom stress essentially moves the bottom boundary from the bed to the top of the boundary layer, where the shear stress is assumed to be zero. A vertically varying  $\epsilon$  also provides no improvement since it allows the effect of the surface shear stress to diminish before reaching the bottom. The profile is more uniform throughout the body of the domain, and the agreement at some elevations decreases.

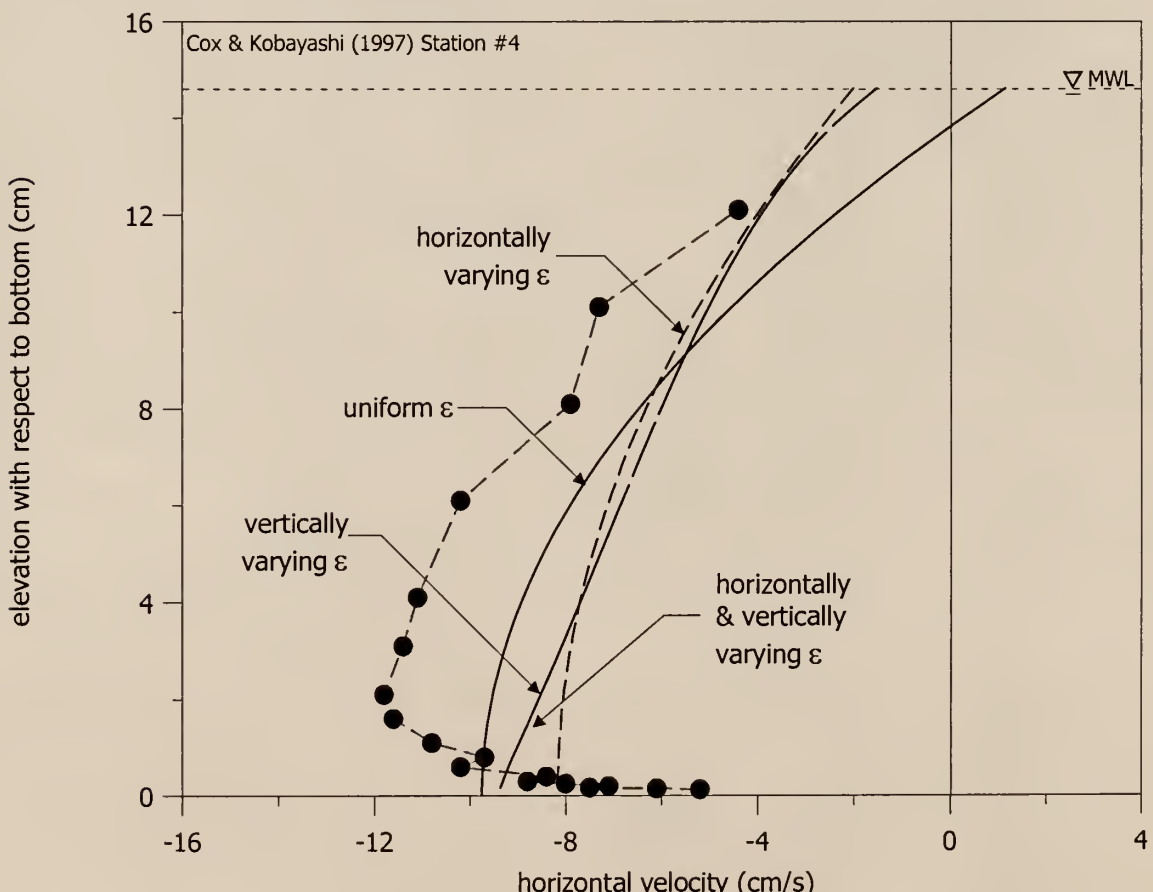


Figure 6.9 Comparison of vertical profiles of horizontal velocity at Station #4 of the Cox and Kobayashi (1997) data set for a zero bottom shear stress boundary condition.

Inspection of Figure 6.7 suggests that the data set of Cox and Kobayashi are best simulated by applying a uniform eddy viscosity field and a zero bottom shear stress condition with a surface roller model (patched if necessary). Another combination, that of a vertically varying eddy viscosity field with a no-slip bottom boundary condition, yields results slightly worse, although it may be argued that the physical processes are better modeled by the latter arrangement. The appropriate boundary condition and eddy viscosity model may be based on the resultant shear stress profiles, as discussed in Chapter 7.

Figure 6.10 illustrates the flow field predicted by the model for the conditions depicted in Figure 6.8. The figure shows the low level of activity in the offshore region and the sudden transition of the flow field following breaking. Figure 6.11 plots the velocity profiles shown in Figure 6.10 against the measured profiles of Cox and Kobayashi. The

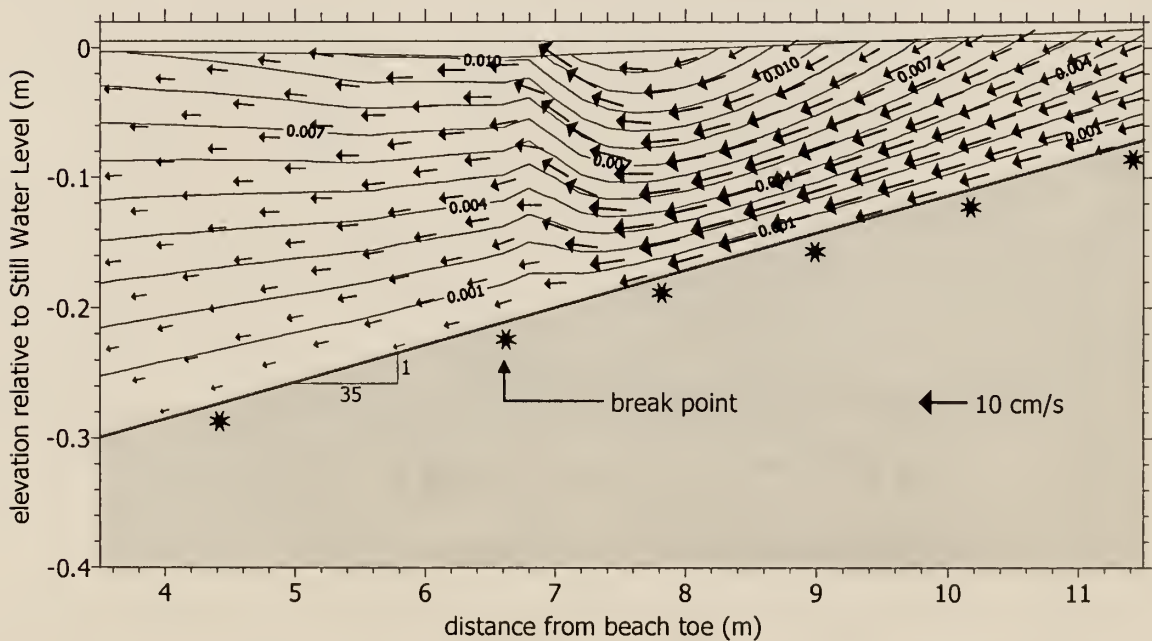


Figure 6.10 Predicted flow field for the data set of Cox and Kobayashi (1997). The simulation includes a vertically varying eddy viscosity field and applies the Svendsen (1984a, patched) surface roller model with a no-slip bottom boundary condition. The contours are lines of constant  $\psi$ . The size and orientation of vectors indicates the velocity field.

no-slip bottom boundary condition and the vertically varying eddy viscosity field accurately reproduce the magnitude and shape of the measured profiles. The profiles do indicate areas where the volumetric flow rate is not adequately modeled.

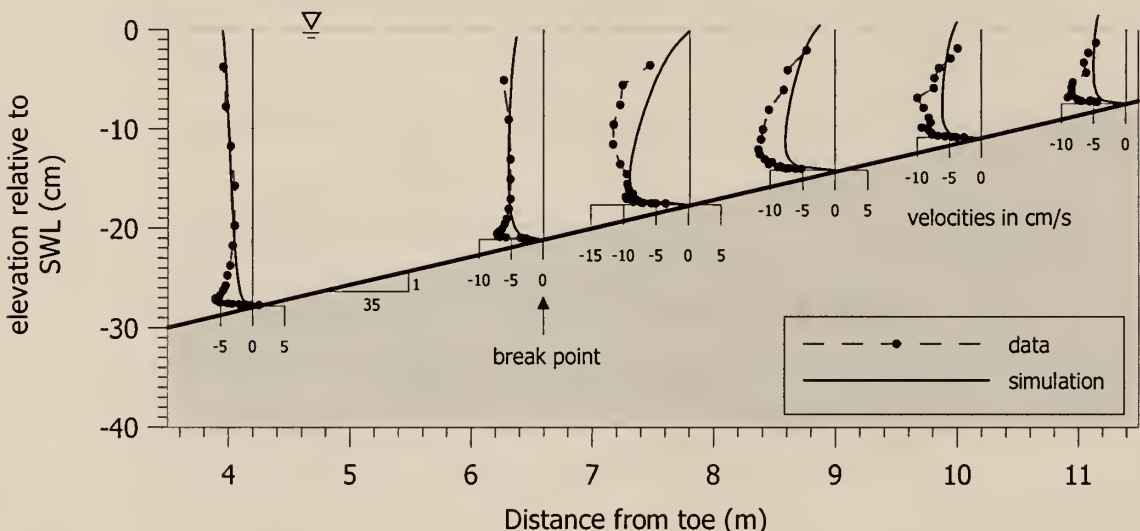


Figure 6.11 Velocity profiles corresponding to the flow field in Figure 6.10 predicted for the data set of Cox and Kobayashi (1997). The simulation includes a vertically varying eddy viscosity field and applies the Svendsen (1984a, patched) roller model.

### 6.3 Simulation of Ting and Kirby (1994) Experiments

The same 32 simulations were performed for the experiments of Ting and Kirby (1994). Figure 6.12 plots the  $\beta$  values for 20 simulations in which the eddy viscosity is held uniform over the model domain. Two values of  $\epsilon$  were investigated,  $0.001 \text{ m}^2/\text{s}$  and  $0.01 \text{ m}^2/\text{s}$ , and two different boundary conditions were applied, no-slip and zero shear stress. All simulations satisfy the conservation of momentum across the profile.

As in the previous simulations of the Cox and Kobayashi data set, the surface roller models appear to produce the best overall agreement, primarily due to the increased value

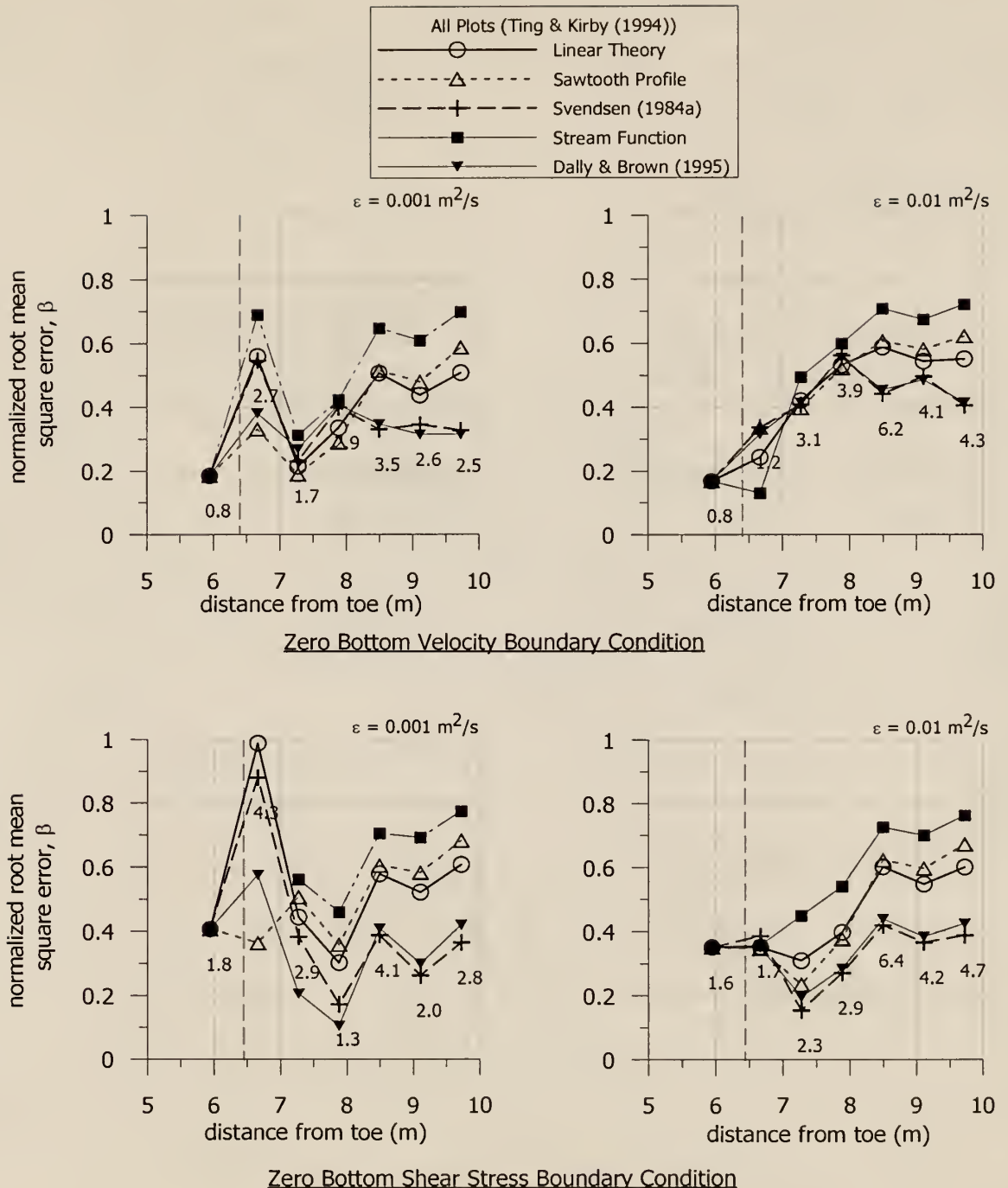


Figure 6.12 Comparison of simulations for the data set of Ting and Kirby (1994). The plots compare the normalized RMS error,  $\beta$ , for two different eddy viscosity values and two different bottom boundary conditions. Typical values of the RMS error at each station are given in cm/s. In each case the eddy viscosity is held uniform over the entire domain. The mean measured velocity at each station is found by dividing the RMS error by the corresponding  $\beta$  value. The vertical dashed line indicates the break point location.

of transport predicted by these models. The choice of a zero bottom shear stress appears to provide slightly better results, although there is considerably more scatter in the results than in the previous experiment. It is noted that in this experiment, a profile of horizontal velocity was measured immediately landward of the break point. At this point, the profile resembles an offshore return flow profile as opposed to a surf zone profile. This profile lies at the seaward end of the transition region (Figure 6.13).

Figure 6.13 compares the two choices of bottom boundary conditions for the patched Svendsen roller model. The comparison of the predicted radiation stress and volumetric transport for the Ting and Kirby (1994) experiments are also plotted. The results shown are quite similar to the results in Figure 6.6 from the previous experiment. Inspection of the radiation stress and transport curves in Figure 6.13 indicate the improved agreement achieved from the surface roller models. The patched Svendsen roller model produces the highest transport prediction and surface shear stress (seen in the slope of the radiation stress curve).

One significant difference in the Ting and Kirby experiments compared to the Cox and Kobayashi experiments is the lack of measurements close to the bed. Without these data points, the behavior of the velocity profile close to the bed is lost, a fact which reduces the basis for identifying appropriate bottom boundary conditions. The zero bottom shear stress simulation produces much better agreement with the measured data, but if the complete profile were available (down to the bed) the agreement would certainly decrease. It is hypothesized, however, that the profile must resemble the Cox and Kobayashi data set near the bed to some degree.

Figure 6.14 presents the results of simulations performed with spatially variable eddy viscosity fields. These simulations follow the same test pattern as in the previous

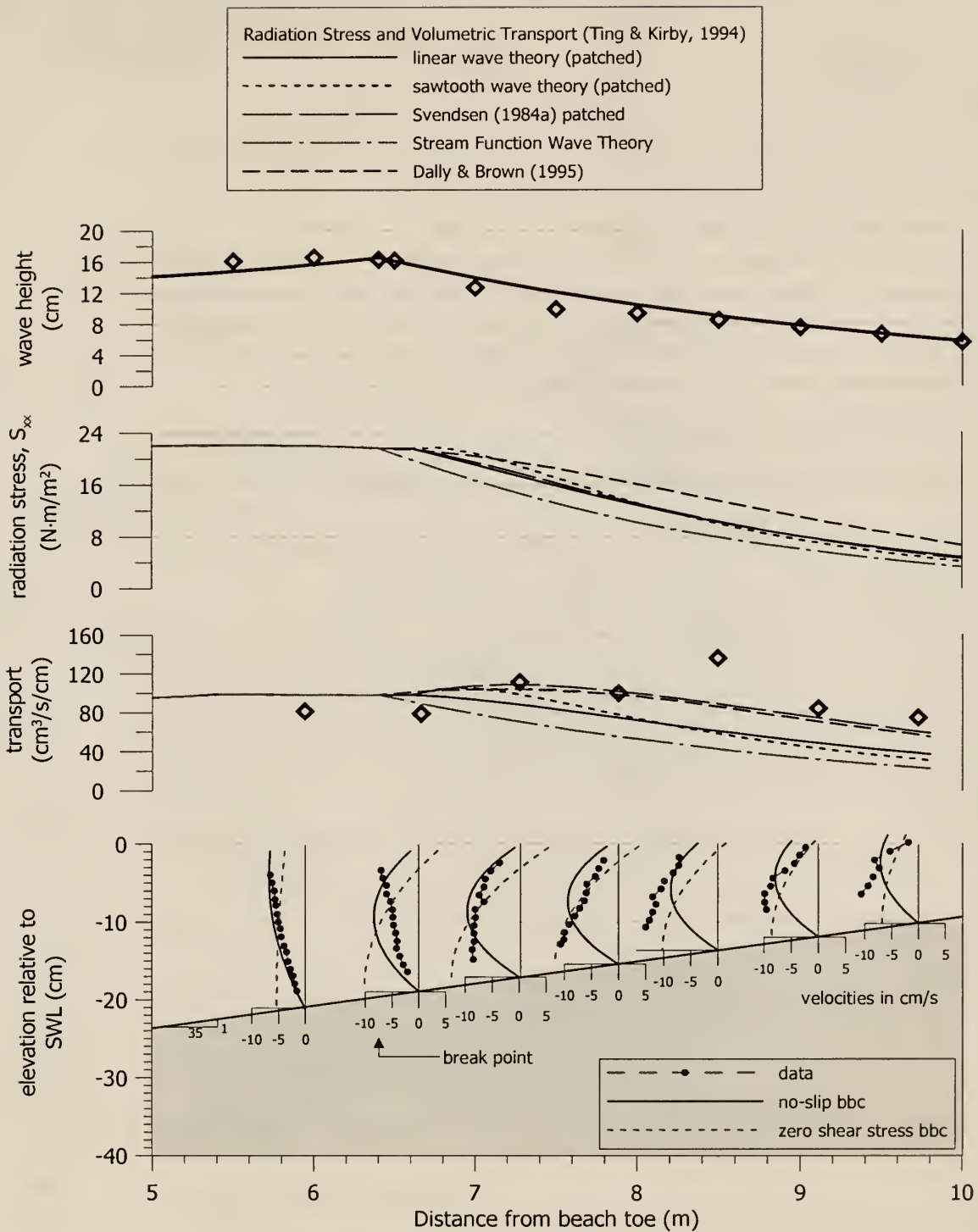


Figure 6.13 Comparison of predicted radiation stress and volumetric transport for the experiments of Ting and Kirby (1994). The five curves in each of the second and third frames illustrate the prediction of  $S_{xx}$  and  $Q$  for the five different surf zone descriptions listed. The velocity profiles predicted for the no-slip and zero shear stress bottom boundary conditions are plotted in the lower frame and correspond to the patched Svendsen (1984a) surface roller approximation with a uniform value of  $\epsilon = 0.001 \text{ m}^2/\text{s}$ .

cases. The scatter in these data prevent as clear a conclusion from being drawn. Overall, however, the behavior is similar to the previous experiment. For the no-slip bottom boundary condition, the inclusion of a vertically varying  $\epsilon$  produces improved agreement at most stations. The inclusion of a horizontal variation again has little effect. For the zero bottom shear stress case, the use of any spatially variable eddy viscosity field produces little improvement.

One interesting feature that relates to the difference in offshore and surf zone return flow profiles can be illustrated by comparing Figures 6.8 and 6.9 from the previous experiments to Figures 6.15 and 6.16 from the Ting and Kirby experiment. Figure 6.8 and 6.9 plot simulations of a surf zone profile, whereas Figures 6.15 and 6.16 present simulations of an offshore profile. In Figure 6.15, the measured profile is compared to the various descriptions of the eddy viscosity field. Offshore of the break point, the measured profile is much more linear and suggests that an offshore stress is being applied at the surface. This would arise from a shoaling wave with increasing radiation stress shoreward. Referring back to Figure 6.13, the radiation stress in these simulations is predicted to be essentially constant although the wave continues to shoal and grow in height. This is a particular feature of the Stream Function Wave Theory, and is discussed further in Chapter 7.

In Figure 6.15, including a vertically varying eddy viscosity field degrades the agreement with the measurements. Use of a horizontally varying value has little effect, although the general shape of the uniform case curve is maintained. None of the curves reproduce the trend of increasingly offshore directed flow seen in the measurements due to the reason mentioned above.

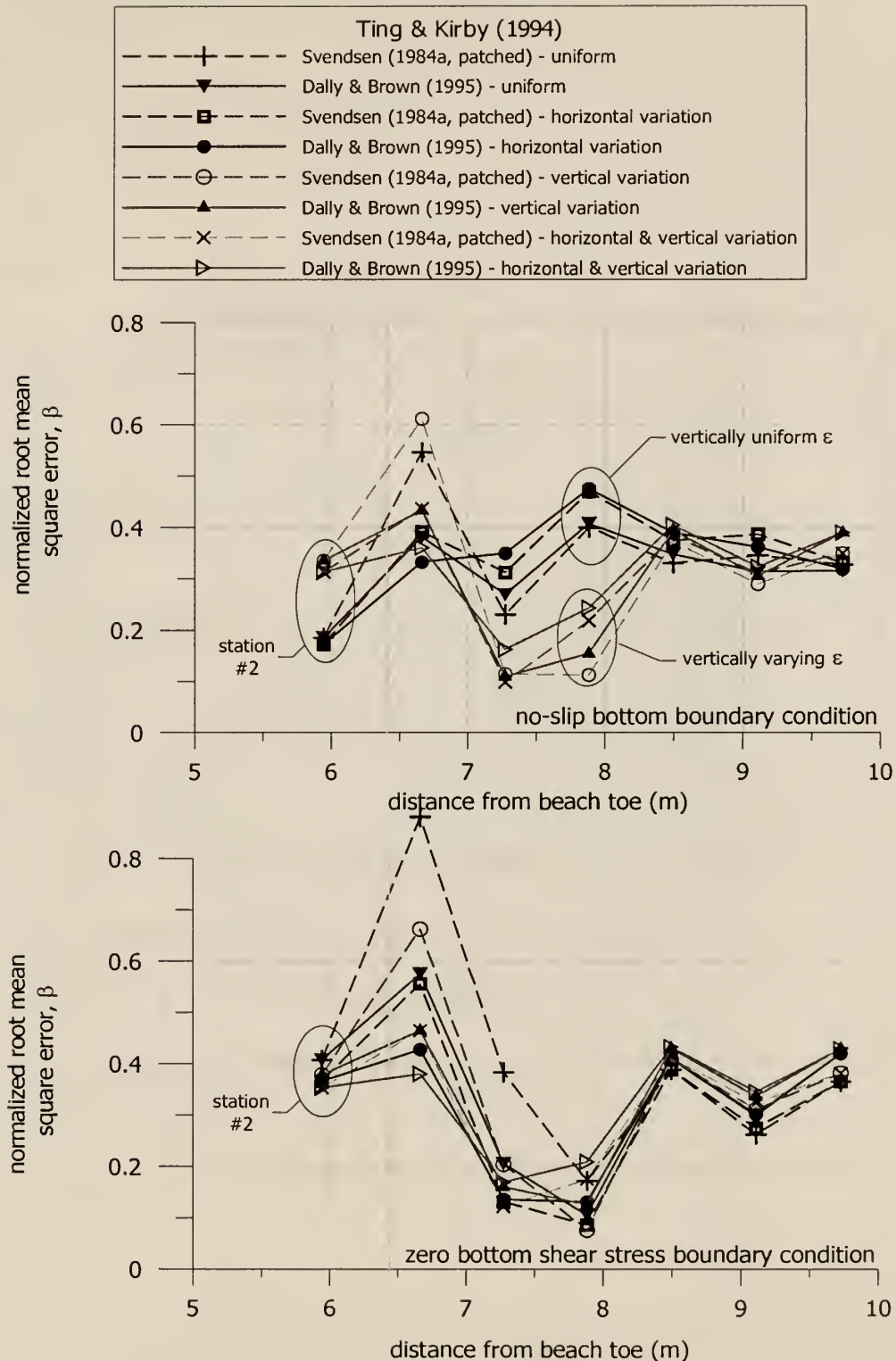


Figure 6.14 Comparison of normalized root-mean-square errors,  $\beta$ , for the experiments of Ting and Kirby (1994) employing spatially variable eddy viscosity fields. The roller models of Svendsen (1984a, patched) and Dally and Brown (1995) are used for the comparison.

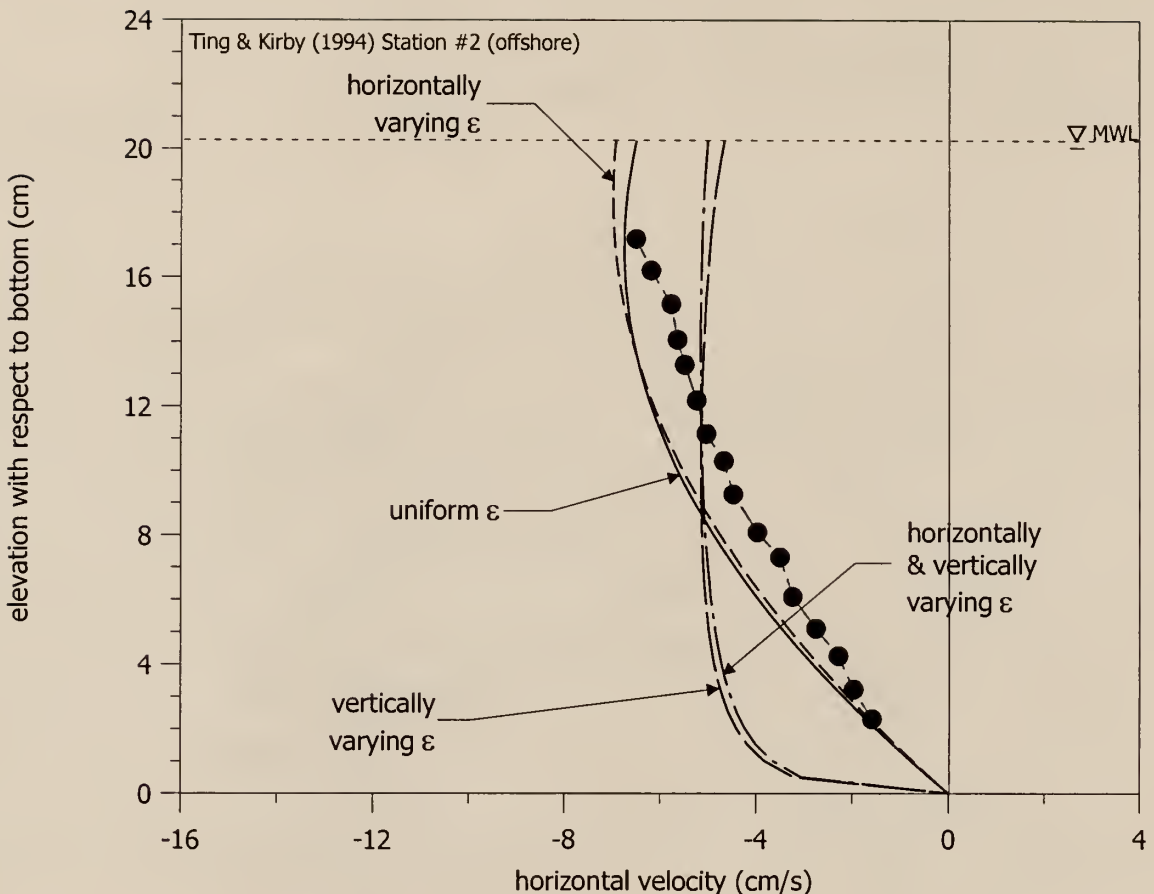


Figure 6.15 Comparison of vertical profiles of horizontal velocity at Station #2 (offshore of the break point) of the Ting and Kirby (1994) data set for a no-slip bottom boundary condition.

In Figure 6.16, the zero bottom shear stress condition appears to be inappropriate regardless of the choice of eddy viscosity distribution. The measurements clearly trend to zero velocity at the bottom and do not indicate a well-defined boundary layer. None of the spatially variable eddy viscosity fields improve the agreement. Comparison of these profiles with the surf zone profiles of Figures 6.8 and 6.9 suggests that a different bottom boundary condition or different description of  $\epsilon$  should be applied inside and outside the surf zone. The difficulty in doing so is the decision of where to switch from an offshore to surf zone description. This is likely related to the treatment of the transition region.

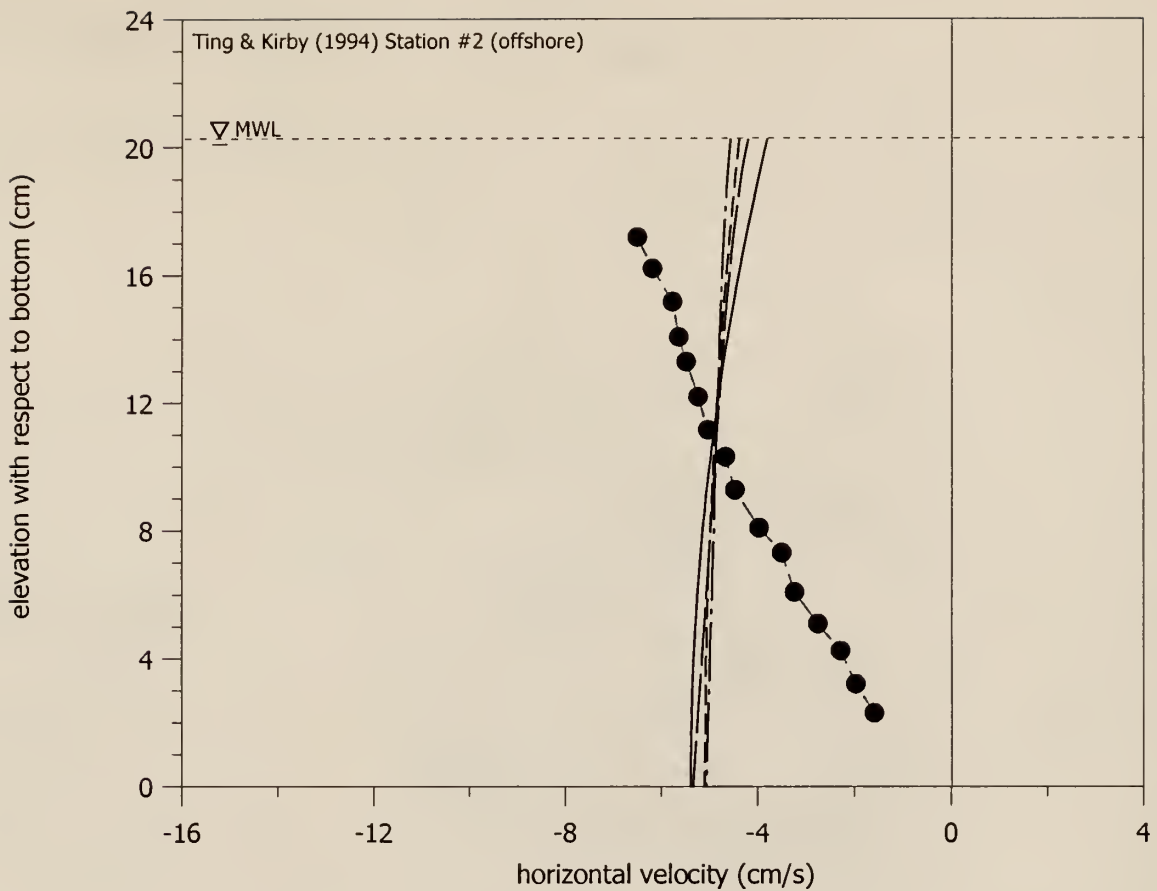


Figure 6.16 Comparison of velocity profiles at Station #2 (offshore of break point) of the Ting and Kirby (1994) data set. In these simulations a zero bottom shear stress condition is applied. The inclusion of any spatially variable eddy viscosity field provides very little change in the agreement over the spatially uniform case.

Inspection of Figure 6.14 suggests that the Ting and Kirby data set is best simulated overall by applying a vertically varying eddy viscosity field and a no slip bottom boundary condition in conjunction with a surface roller model (patched to the offshore in the present case of Svendsen, 1984a). Offshore of the break point, however, this combination does not provide the best agreement. The use of a horizontally varying similarity profile to describe the vertical variation in  $\epsilon$  would improve the agreement, but would require a more sophisticated treatment of the eddy viscosity. Figures 6.17 and 6.18 illustrate the simulated flow field and corresponding velocity profiles for the simulation described above.

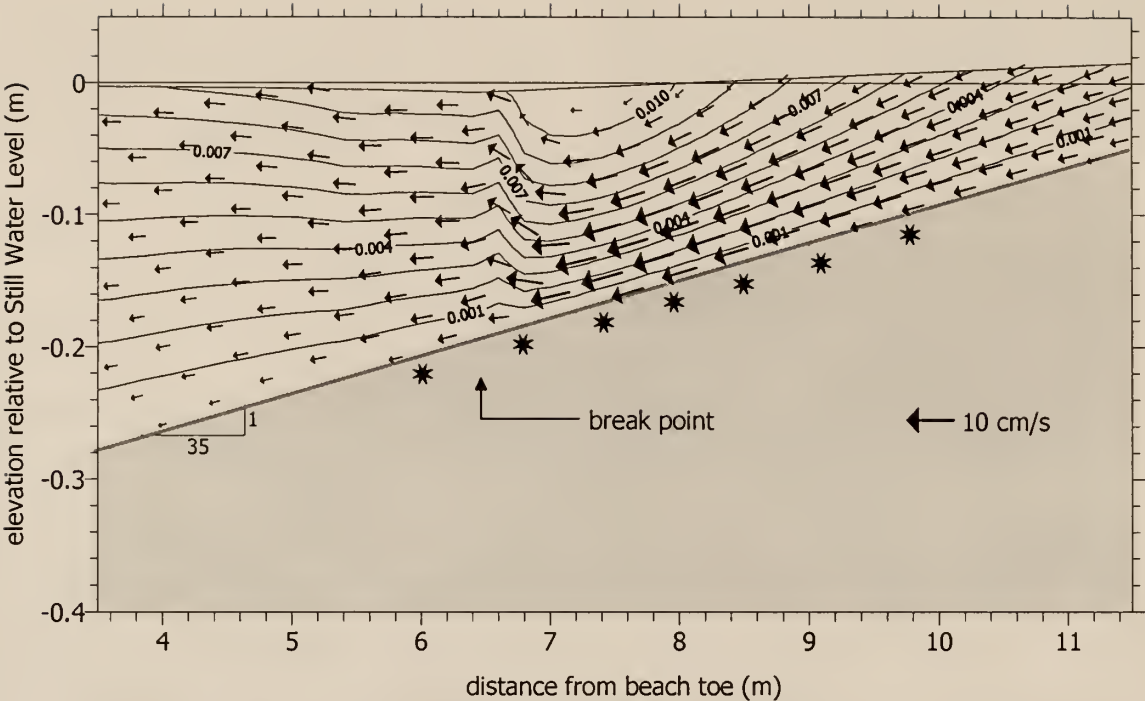


Figure 6.17 Predicted flow field for the data set of Ting and Kirby (1994). The simulation includes a vertically varying eddy viscosity field and applies a patched version of the Svendsen (1984a) surface roller model with a no-slip bottom boundary condition. The contours are lines of constant  $\psi$ . The size and orientation of vectors describes the velocity field.

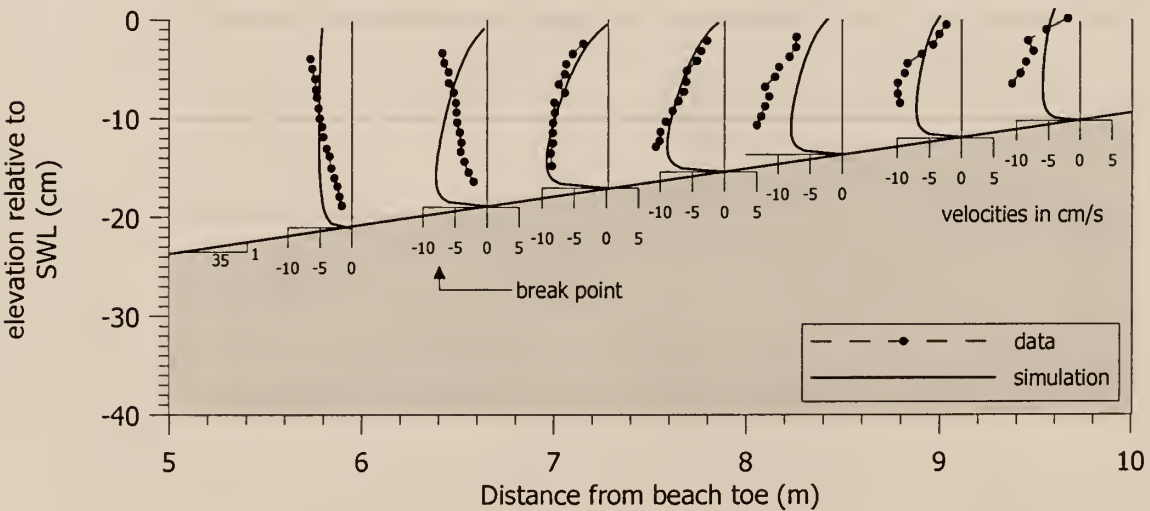


Figure 6.18 Velocity profiles corresponding to the flow field in Figure 6.17 predicted for the data set of Ting and Kirby (1994). The simulation includes a vertically varying eddy viscosity field and applies the Svendsen (1984a, patched) surface roller model.

Inspection of the offshore velocity profiles from both the Ting and Kirby (1994) and Cox and Kobayashi (1997) data sets suggests the presence of an offshore directed surface stress. The linearly increasing offshore mean velocity suggests a finite offshore stress at the surface. In comparison, open-channel gravity driven flows experience zero surface shear stress and hence the slope of the velocity profile is zero at the surface. The *predicted* velocity profiles of Cox and Kobayashi exhibit an offshore surface stress outside the breakpoint, due to the shoaling waves and the resulting increasing radiation stress seaward of the break point.

In the simulation of the Ting and Kirby experiments, the predicted behavior of the radiation stress in the shoaling region does not produce an offshore directed stress; the radiation stress remains constant or decreases slightly prior to breaking. This behavior of the wave properties in the Ting and Kirby experiments prevents the predicted velocity profile from agreeing with the measured profile in shape, even though the transport is reasonably well predicted. SFWT does predict a slight decrease in the non-dimensional integral wave properties (such as transport and momentum flux). If the wave shoals sufficiently, the increase in wave height, which is one of the non-dimensionalizing parameters used in SFWT, more than offsets the decrease in the non-dimensional value and the dimensional value of the integral property increases.

In the Ting and Kirby experiments, and in the Nadaoka and Kondoh experiments to be presented, there are instances where the shoaling wave does not increase in height sufficiently and the dimensional integral properties decrease. A decreasing radiation stress creates an onshore directed shear stress at the surface, which does not agree with the measurements, as shown in Figure 6.18 among others. This difficulty in the behavior of SFWT (and other higher order wave theories) is discussed further in Chapter 7.

#### 6.4 Simulation of Nadaoka and Kondoh (1982) Experiments

Figure 6.19 presents the normalized RMS errors computed from the 20 uniform eddy viscosity simulations of the Nadaoka and Kondoh (1982) experiments (Case 1). The parameters for these simulations are identical to the two previous simulated experiments. In the offshore region, the higher value of  $\epsilon$  produces better agreement with the measurements for both bottom boundary conditions. In the surf zone, the zero bottom shear stress condition generally provides improved agreement compared to the inaccurate combination of a no-slip boundary condition and a vertically uniform eddy viscosity field.

Figure 6.20 plots the wave height, radiation stress, volumetric transport, and velocity profiles corresponding to the no-slip and zero shear stress boundary condition cases at the lower value of  $\epsilon (= 0.001 \text{ m}^2/\text{s})$ . Inspection of the volumetric transport curve suggests once again that the theories that produce the higher values of  $Q$  produce the best agreement with the measurements (e.g., the Dally and Brown roller model and the patched Svendsen model). The velocity profiles predicted by using the Dally and Brown (1995) model are plotted in the last frame.

Inspection of the first two profiles illustrates the on/offshore directed stress problem discussed previously. In this example, the low wave period (1.32 s) precludes a significant amount of shoaling, as seen in the measurements. The resulting radiation stress exhibits a significant negative gradient *prior* to breaking, nearly as great as the decline predicted in the surf zone. This produces an onshore-directed stress in an area where the measurements suggest the stress is offshore. The transport measurements in the offshore region do not change significantly in the shoaling region, and the SFWT wave theory adequately simulates these values but does also exhibit a slight decrease prior to breaking.

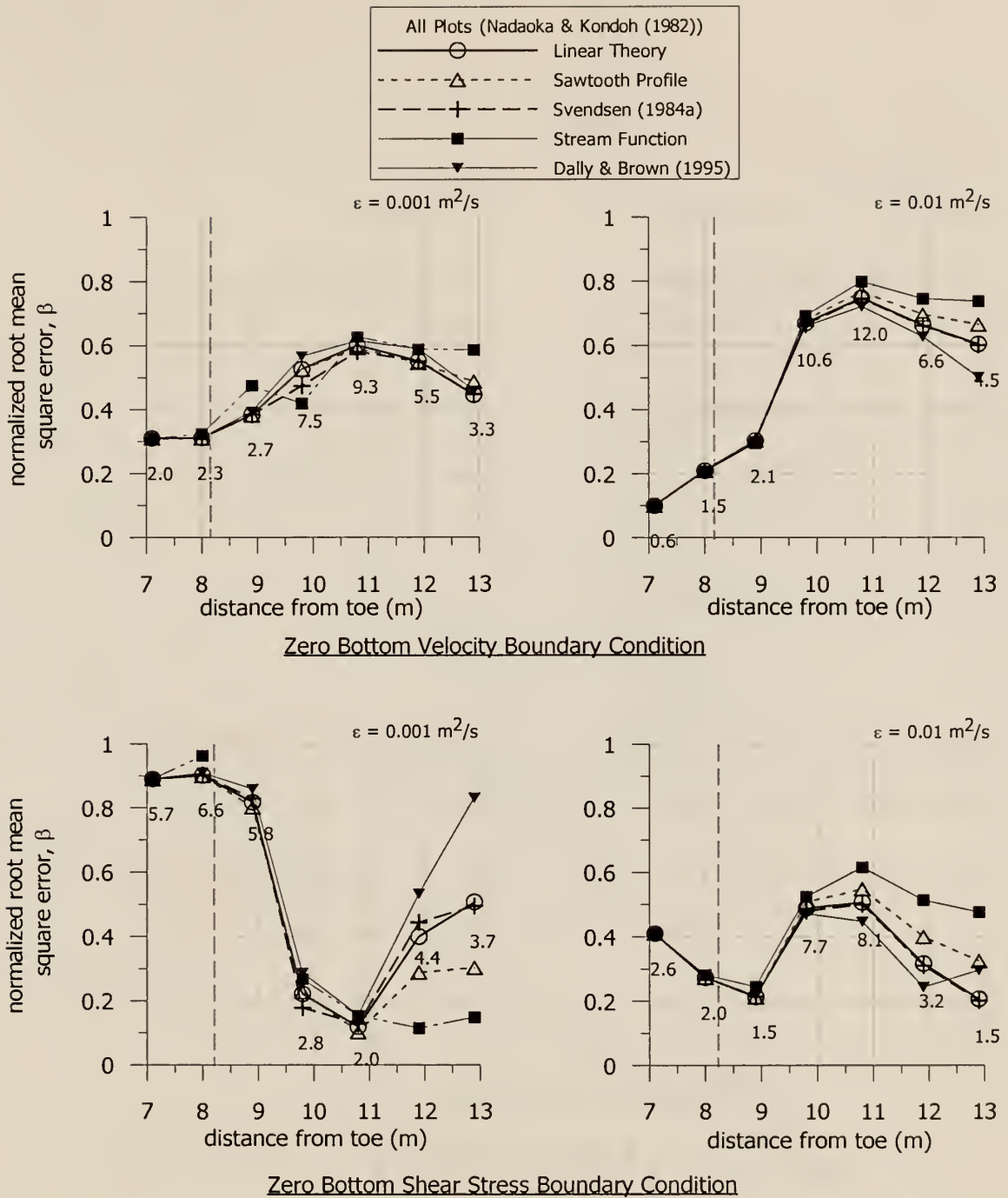


Figure 6.19 Comparison of simulations of the data set of Nadaoka and Kondoh (1982, Case 1). The plots compare the normalized RMS error,  $\beta$ , for two different eddy viscosity values and two different bottom boundary conditions. Typical RMS errors are given in cm/s at each measuring line. In each case the eddy viscosity is held uniform over the entire domain. The mean measured velocity at each station is found by dividing the RMS error by the corresponding  $\beta$  value. The dashed line indicates the break point location.

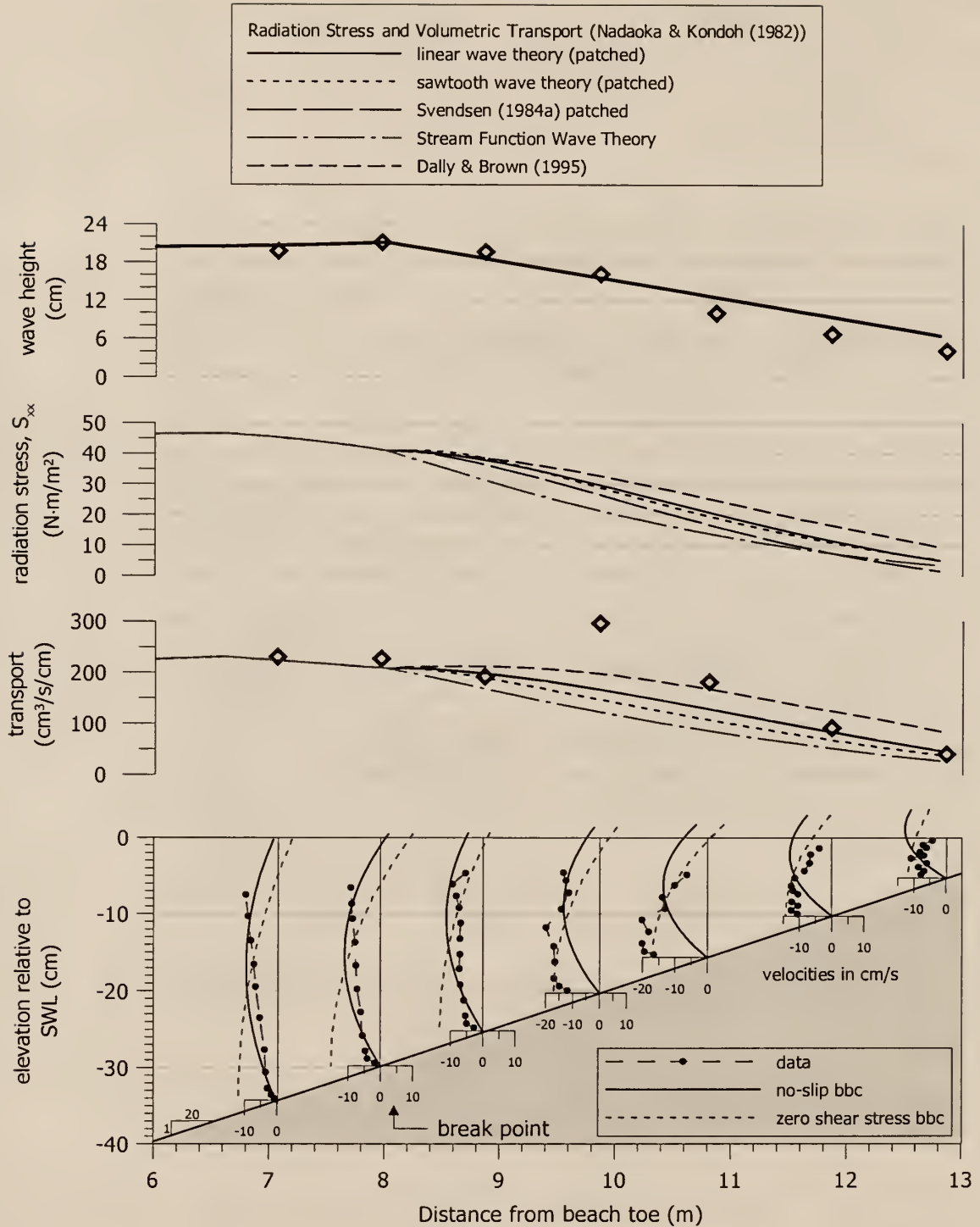


Figure 6.20 Comparison of predicted radiation stress and volumetric transport for the experiments of Nadaoka and Kondoh (1982, Case 1). The five curves in each of the second and third frames illustrate the prediction of  $S_{xx}$  and  $Q$  for the five different surf zone descriptions listed. The velocity profiles predicted for the no-slip and zero shear stress bottom boundary conditions are plotted in the last frame and correspond to the roller model of Dally and Brown (1995) with a uniform value of  $\epsilon = 0.001 \text{ m}^2/\text{s}$ .

As seen in the previous experiments, inclusion of a spatially variable eddy viscosity tends to improve the agreement between the measurements and the simulations, particularly for the no-slip boundary condition cases in the surf zone. Figure 6.21 presents the  $\beta$  values computed from the simulations of the Nadaoka and Kondoh experiments with horizontally and/or vertically variable eddy viscosity fields. Again, the inclusion of the vertical variation in  $\epsilon$  seaward of the break point degrades the prediction in that region, particularly for the zero bottom shear stress case. The horizontal variation, however, results in higher values of the eddy viscosity in the offshore region, producing more uniform values that provide better agreement with the measurements. Horizontal variation in  $\epsilon$  in the surf zone provides little improvement and in some cases increases the slope of the velocity profile excessively, degrading the agreement unless a vertical variation is also applied.

Based on Figure 6.21, the experiments of Nadaoka and Kondoh (1982) are best simulated by applying a zero bottom shear stress condition in conjunction with a horizontally and vertically varying eddy viscosity field. The no-slip condition applied with a vertical variation provides improved agreement as well, and perhaps better describes the processes involved in the flow field at the seabed. In each case, the patched Svendsen model is chosen based on its higher transport values.

Figure 6.22 illustrates the predicted flow field from these two scenarios. The plot illustrates the difficulty in the wave description seen in Figure 6.20 where the radiation stress and volumetric transport decrease prior to breaking. The resulting influx of flow and the onshore shear stress (at  $x = 7$  to  $8$  m) create a different flow pattern than the ones presented in the previous experiments. The strong upflow generated just landward of the break point feeds the roller. Seaward of the break point, the decrease in the radiation stress and the volumetric transport creates an upward directed flow (at approximately  $x = 6$  m).

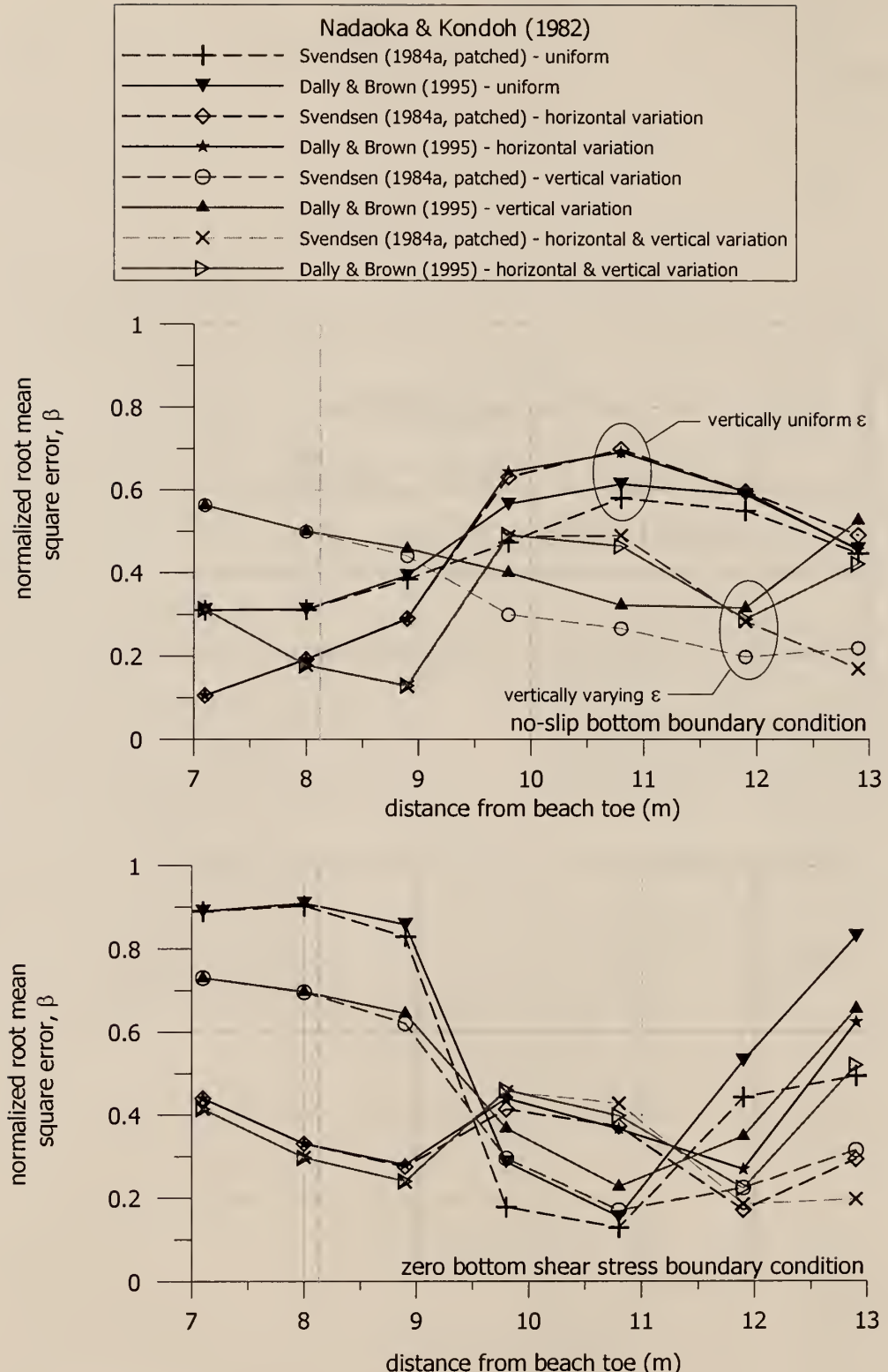


Figure 6.21 Comparison of normalized root-mean-square errors,  $\beta$ , for the experiments of Nadaoka and Kondoh (1982) employing spatially variable eddy viscosity fields. The roller model of Svendsen (1984a, patched) is used for the comparison in Figure 6.22.

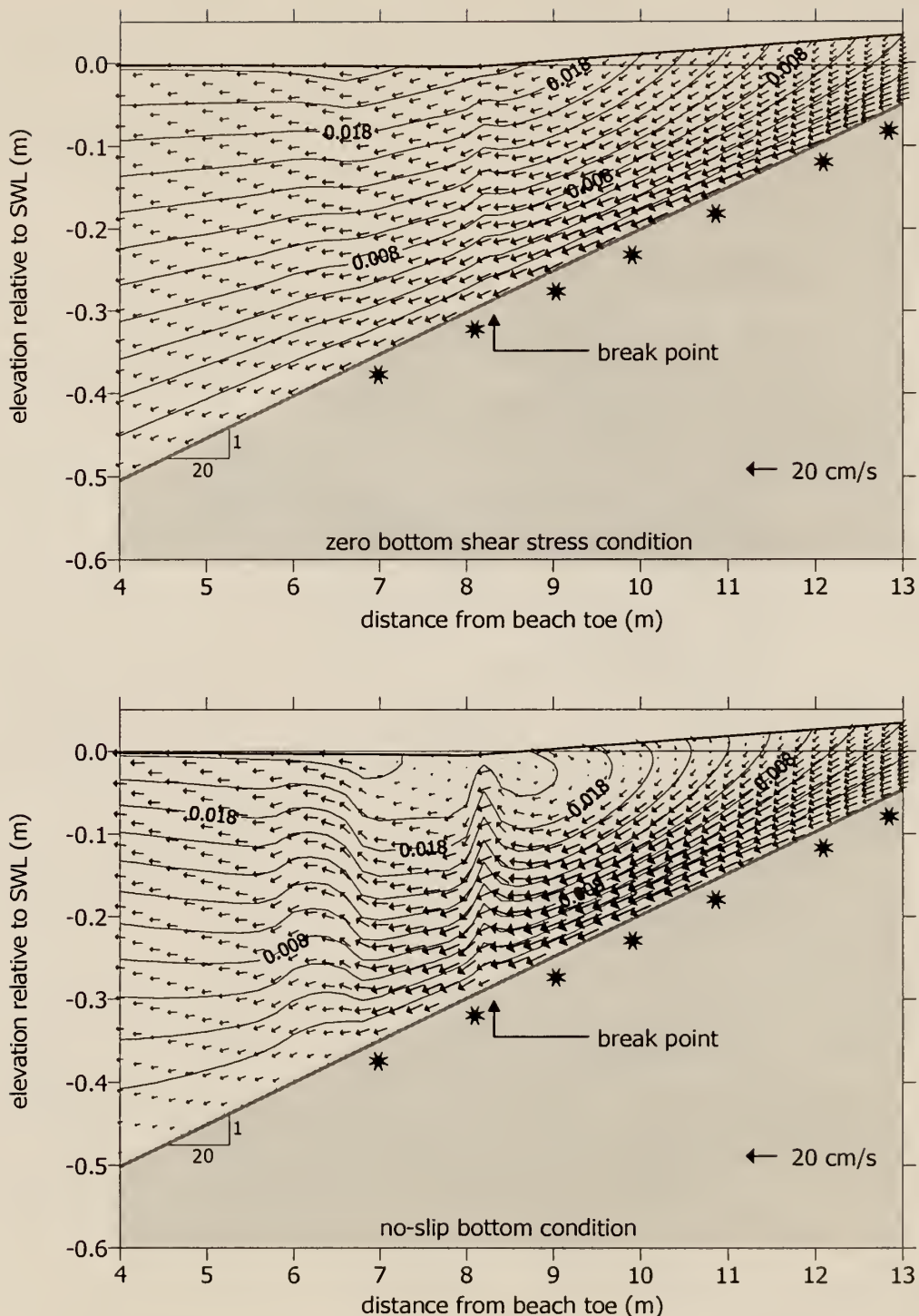


Figure 6.22 Predicted flow fields for the experiments of Nadaoka and Kondoh (1982). The upper plot applies a zero bottom shear stress condition with a vertically and horizontally varying eddy viscosity field. The lower plot applies a no-slip bottom boundary condition with a vertically varying eddy viscosity field. Both simulation apply the roller model of Svendsen (1984a) patched to the offshore region.

Figure 6.23 presents the velocity profiles corresponding to the lower plot of Figure 6.22. The combination of the no-slip bottom boundary condition and the vertically varying eddy viscosity field reproduces the flow behavior at the four inner surf zone profiles. The onshore stress applied at the three outer profiles fails to capture the behavior of the velocity profile in that region although the volumetric transport is well simulated.

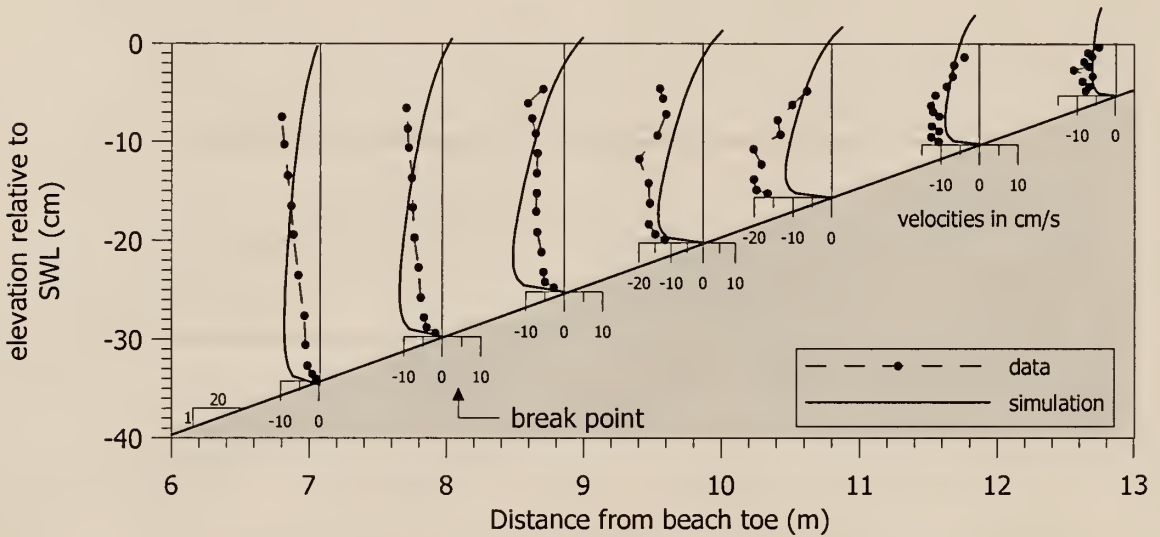


Figure 6.23 Velocity profiles corresponding to the flow field in the lower plot of Figure 6.22 for the data of Nadaoka and Kondoh (1982). The simulation includes a vertically varying eddy viscosity field and applies the Svendsen (1984a, patched) roller model.

## 6.5 Simulation of Okayasu and Katayama (1992) Experiments

In this simulation, random waves are applied in a laboratory setting over a barred smooth profile. As discussed in Chapter 4, random waves are simulated in the model by changing the boundary conditions at a frequency equivalent to the peak period of the wave spectrum. Individual waves, chosen at random based on a Rayleigh distribution, are shoaled and broken across the model domain and the corresponding boundary conditions applied. Rather than simply average the effects of several waves, the model attempts to reproduce the time dependence of the change in boundary conditions.

Figure 6.24 plots the RMS wave height, average radiation stress, and average volumetric transport predicted for the Okayasu and Katayama (1992) experiments. Velocity profiles corresponding to SFWT predictions with no-slip and zero bottom shear stress boundary conditions are plotted in the lower frame. In the simulations, the RMS wave height is reasonably reproduced, but the transport at each measured station is greatly overestimated. This results in large errors in the predicted velocity profiles. In previous experiments the roller models produced the best agreement, primarily due to the prediction of *increased* transport. In the present experiments SFWT provides the lowest transport and closest agreement, but still greatly exceeds the measured transport at several stations.

Comparison of the measured RMS wave height profile seen in the upper frame to the measured value of transport for the first offshore station indicates that the transport is much lower than what is expected for an RMS wave height of roughly 7 cm. From linear wave theory for monochromatic waves, a 7 cm wave would produce a volumetric transport value of roughly  $43 \text{ cm}^3/\text{s}/\text{cm}$ . The measured volumetric transport corresponds to a linear wave height of approximately 3.4 cm. The other five measured values of  $Q$  appear consistently low in comparison to the measured RMS wave height profile and the other experiments/simulations. The cause of the discrepancy between the simulations and the data is not immediately apparent, although the measured  $Q$  values do appear quite low for the reported wave height data.

Figure 6.25 presents the  $\beta$  values for the same 20 simulations presented in prior experiments. The large discrepancy in  $Q$  produces substantial errors in the velocity profile predictions, particularly in the offshore region. The model also appears to poorly predict the velocity profile in the trough of the beach. This may be attributed to the low prediction of  $Q$  or to the reduced gradient in radiation stress predicted by the model.

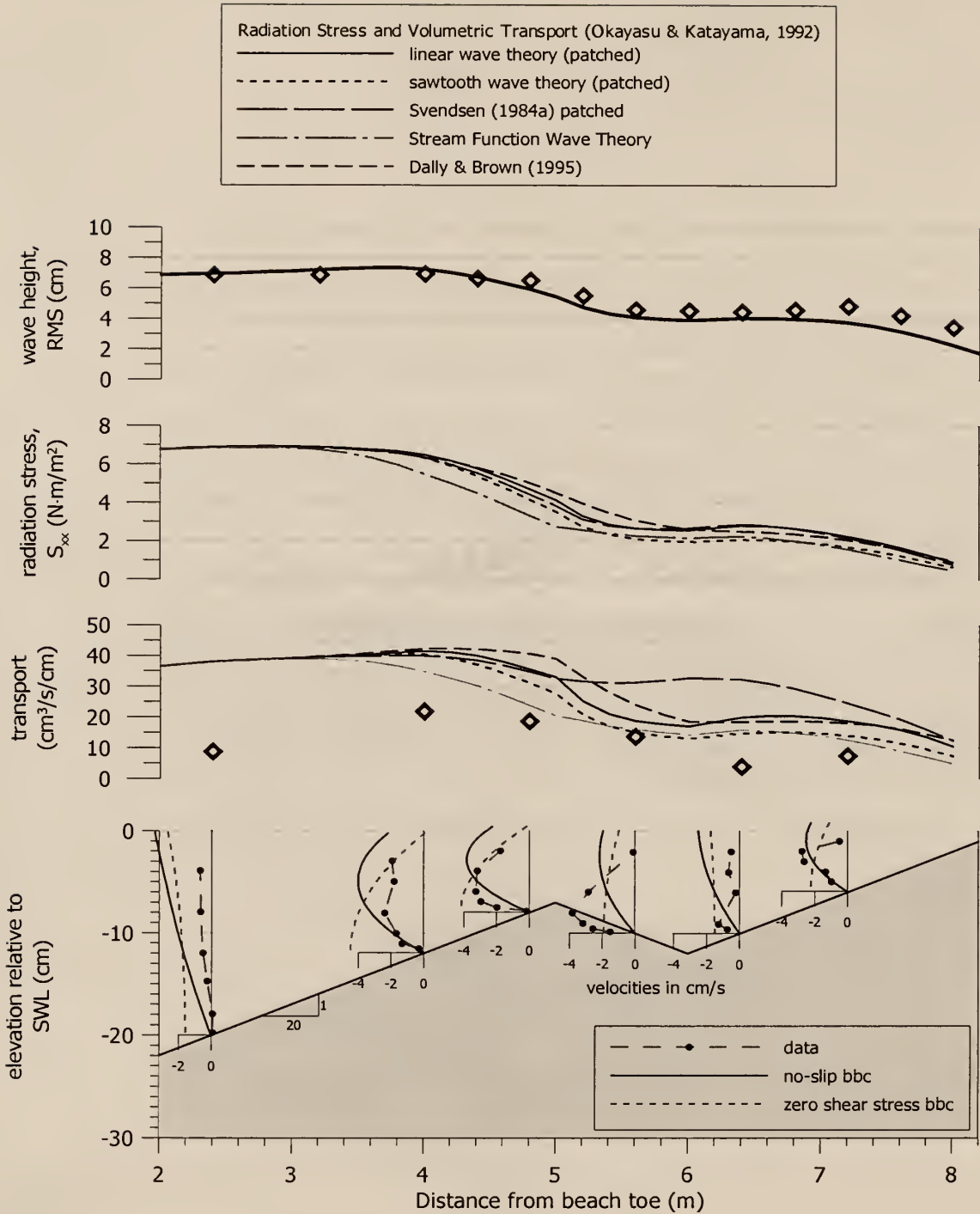


Figure 6.24 Comparison of predicted RMS wave height, radiation stress, volumetric transport for the random wave experiments of Okayasu and Katayama (1992). The five curves in each of the second and third frames illustrate the prediction of  $S_{xx}$  and  $Q$  for the five different surf zone descriptions listed. The velocity profiles predicted for the no-slip and zero shear stress bottom boundary conditions are plotted in the last frame and correspond to the use of SFWT in the surf zone with a uniform value of  $\epsilon = 0.001$  m<sup>2</sup>/s.

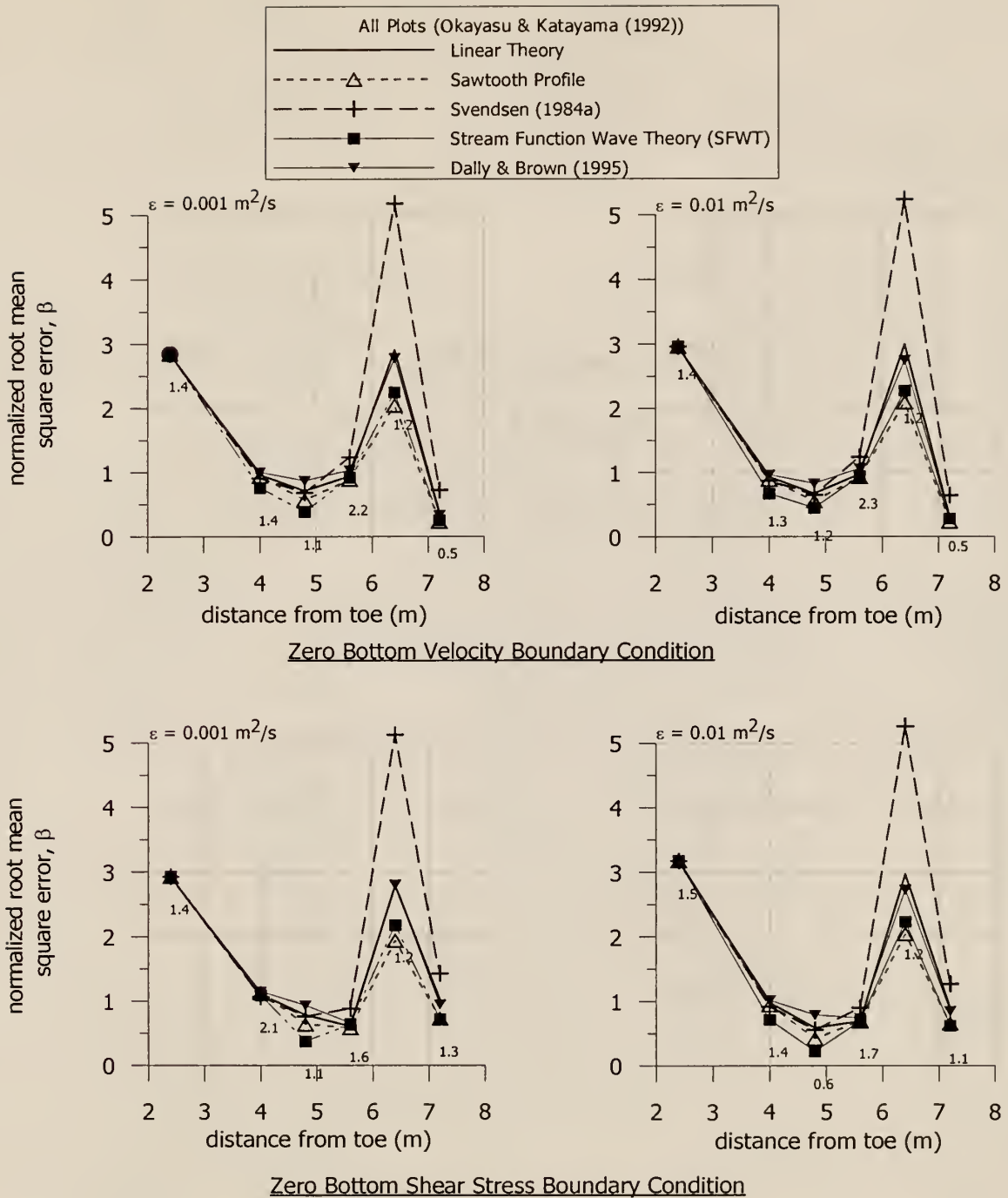


Figure 6.25 Comparison of simulations of the data set of Okayasu and Katayama (1992). The plots compare the normalized RMS error,  $\beta$ , for two different eddy viscosity values and two different bottom boundary conditions. The RMS error is given in cm/s at each measuring line for the theory that provides the best agreement (SFWT in the present case). In each case the eddy viscosity is held uniform over the entire domain. The mean measured velocity at each station is found by dividing the RMS error by the corresponding  $\beta$  value.

While most of the errors in Figure 6.25 exceed 1.0 (the no-skill prediction level), the roller model of Svendsen (1984a) produces the most notable disagreement. In the trough, this model does not predict a sufficient decrease in the volumetric transport as do the other theories. While the wave height is predicted to decrease slightly in the trough, the transport value predicted by Svendsen (Chapter 4) depends also on the square root of the depth, which is obviously increasing immediately landward of the bar crest.

Figure 6.26 presents the  $\beta$  values determined from various spatially variable eddy viscosity fields. In keeping with the results in Figures 6.24 and 6.25, the SFWT results are used in conjunction with vertically and/or horizontally varying eddy viscosity descriptions. The results from applying the Dally and Brown (1995) model are also plotted for comparison. Inspection of the upper plot in Figure 6.26, corresponding to the no-slip boundary condition, indicates that the description of the flow rate is the primary parameter in achieving good agreement with the measurements; no eddy viscosity variation improves the agreement of the Dally & Brown simulations enough to provide better agreement than the SFWT simulations.

Despite the overall poor agreement between the simulations and the data due to the overestimation of the volumetric transport, some general performance features can be discerned from this experiment. As in the previous experiments, the use of a vertically varying eddy viscosity field (with or without a corresponding horizontal variation) does provide some degree of improvement over the spatially uniform case, typically 5 to 10% in some cases. This is seen in the simulation results plotted in the upper frame of Figure 6.26. For both surf zone descriptions, the vertical variation reduces the value of  $\beta$  at most stations. This benefit is not gained in the zero bottom shear stress case, as discussed previously and as shown in the lower plot of Figure 6.26.

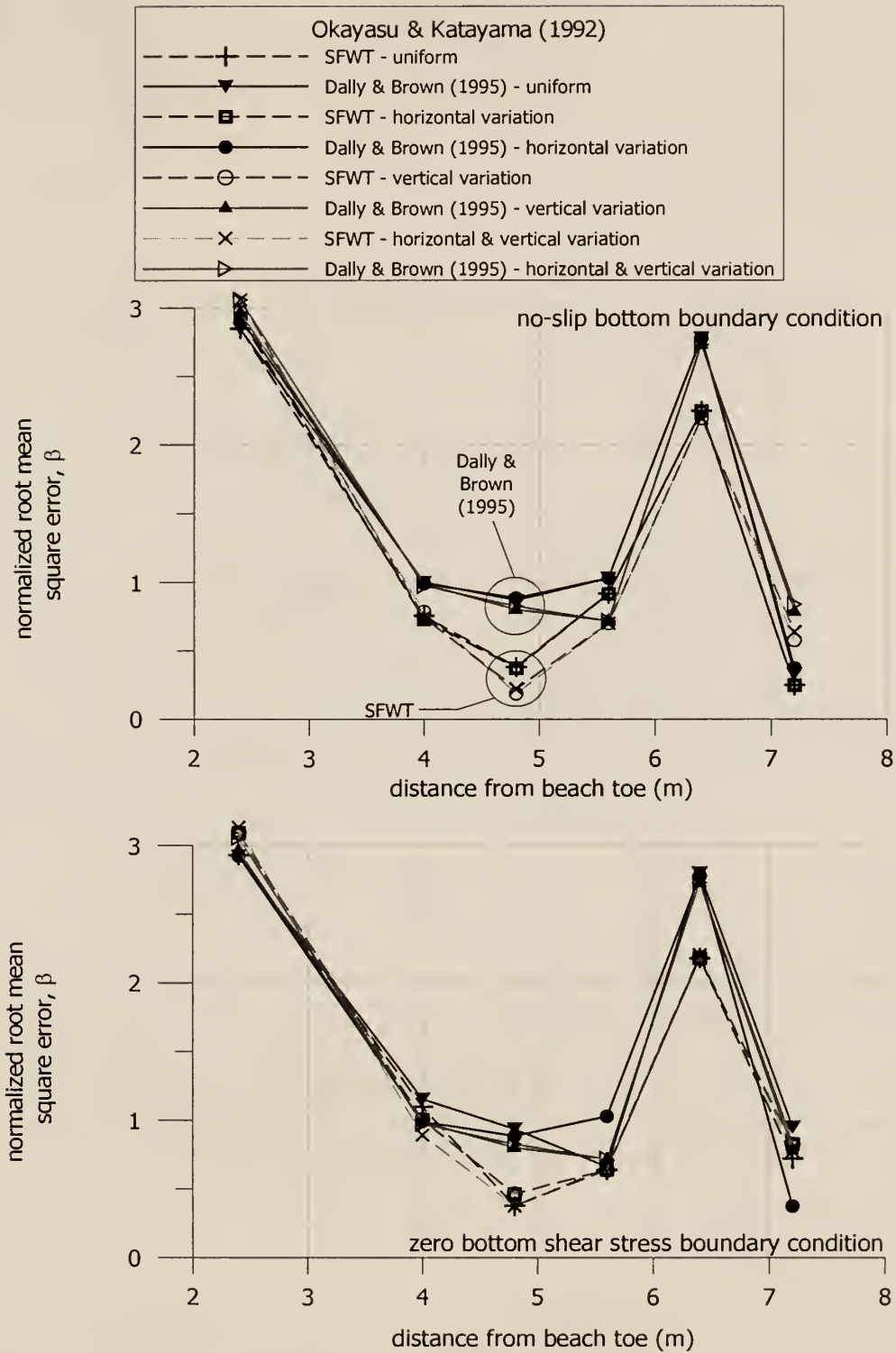


Figure 6.26 Comparison of normalized root-mean-square errors,  $\beta$ , obtained for the experiments of Okayasu and Katayama (1992) by applying spatially variable eddy viscosity fields. Application of SFWT with a vertically varying eddy viscosity field and a no-slip bottom boundary condition provides the lowest overall error, although large overestimations in the volumetric transport produce large errors at Stations #1 and #5.

Figure 6.27 presents the flow field predicted for the Okayasu and Katayama (1992) experiment. The flow field is produced by applying SFWT with a vertically varying eddy viscosity field and a no-slip bottom boundary condition. The calculated Mean Water Surface is evident in the plot, and indicates the varying setup and set-down that is expected to occur over the barred system. The flow field indicates the location of the primary breaker zone seaward of the bar. The flow weakens as the wave reforms following the bar then strengthens slightly as the waves break a second time on the inner surf zone slope.

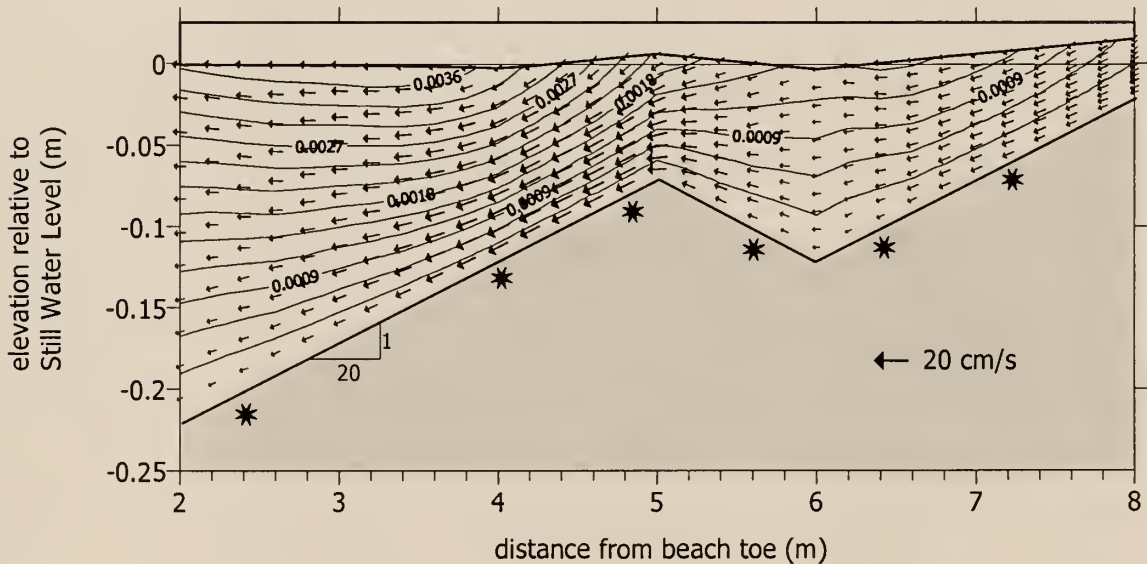


Figure 6.27 Predicted flow field for the experiments of Okayasu and Katayama (1992). SFWT is applied to best match the measured volumetric transport. A vertically varying eddy viscosity field is applied with a no-slip bottom boundary condition.

Of interest is how well the model would reproduce the measured values of velocity by simply applying the RMS wave height in a monochromatic fashion to describe the flow field. Figure 6.28 plots the  $\beta$  values for the flow field plotted in Figure 6.27 along with the simulation found by applying the RMS wave height (7.5 cm) with SFWT in the surf zone, the same vertically varying eddy viscosity field, and the no-slip bottom boundary condition.

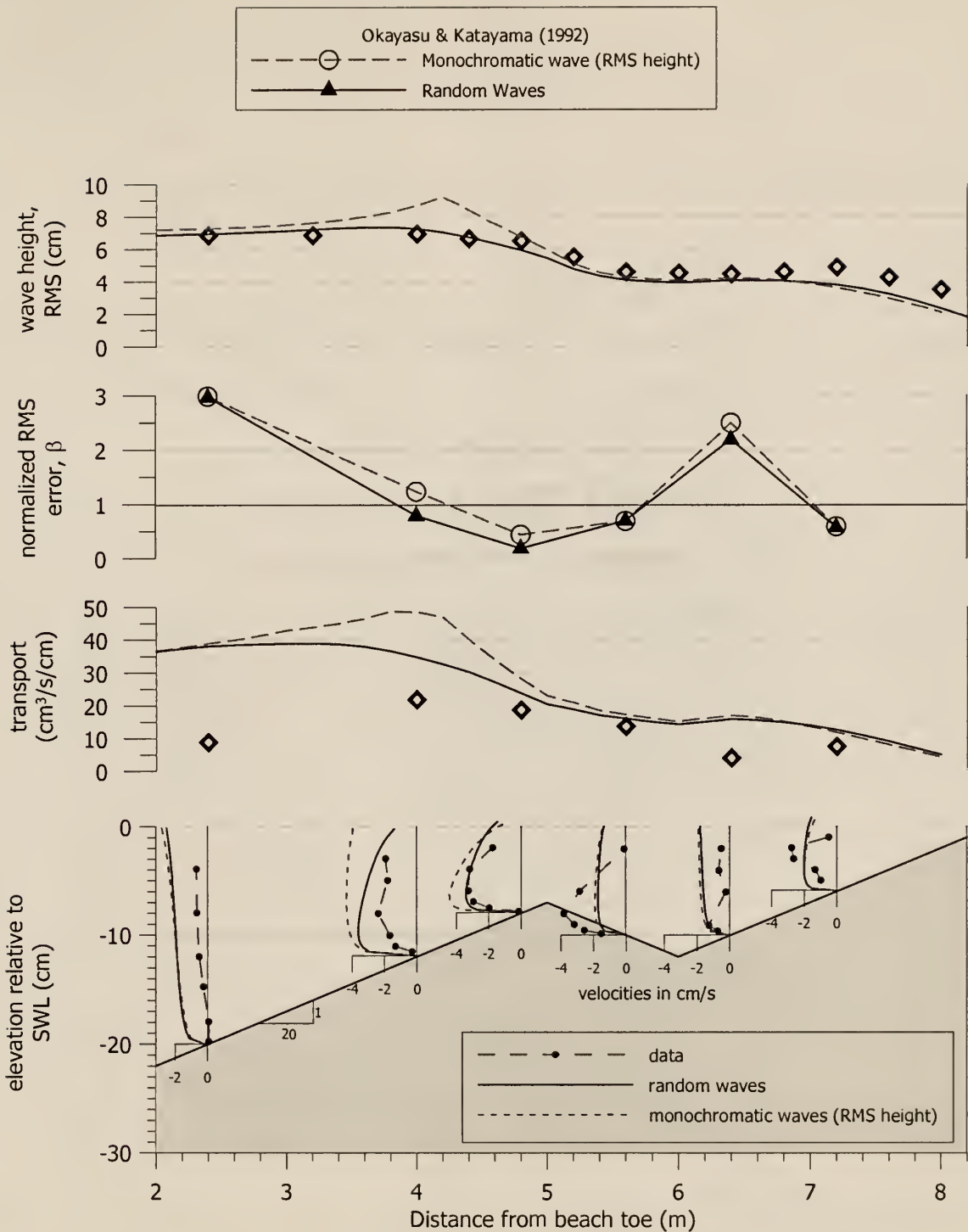


Figure 6.28 Comparison of simulations applying random waves averaged over time and applying a monochromatic wave field of RMS height. The random wave method smooths the flow field due to the variable location of the break point. This produces lower predicted flow rates, particularly in the vicinity of the primary breakpoint, seaward of the bar. Both simulations apply SFWT in the surf zone and apply a vertically varying eddy viscosity field with a no-slip bottom boundary condition.

Figure 6.28 illustrates the smoothing of the predicted wave height profile by the random wave method which provides better agreement with the measured wave data. The variable location of the break point reduces the average wave height in the vicinity of the primary breakpoint, thus producing a lower predicted volumetric flow rate than in the monochromatic case. The normalized RMS errors are plotted in the second frame for these two simulations and show the increasing error associated with using only the RMS wave height as input to the steady, monochromatic version of the model.

Figure 6.28 also indicates the marginally improved agreement with the measured velocity profiles obtained by applying the vertically varying eddy viscosity field. The data do not extend to the bed or up into the water column close to the wave trough in all cases, although several profiles do indicate the presence of the boundary layer. The uniform shape of the velocity profile in the body of the domain improves the agreement over the range of measurements as does the sharp gradient in the velocity near the bed (Figures 6.26 and 6.28). In some instances, such as at Stations #3 and #4, the data suggest that an even lower value of  $\epsilon$  at the surface might further improve the agreement by increasing the slope of the velocity profile at the surface. Lacking a better description for what the value of  $\epsilon$  should be, the trend is noted but no attempt to calibrate the value of  $\epsilon$  is offered.

Inspection of the simulations suggests that the random wave, barred beach laboratory case of Okayasu and Katayama (1992) is not well simulated by the present model. None of the wave theories applied are able to predict the low flow rates shown in the measurements. While it is expected that the flow rate in a random wave case would be lower than the corresponding flow from a monochromatic wave case (as shown in Figure 6.28), the measured flow rate appears to be significantly lower than any theory used herein would predict.

The errors indicate that the primary parameter in modeling the vertical structure of the return flow is the prediction of the flow rate. Inspection of the simulations presented above indicates that the choice of tangential surface and bottom boundary conditions or spatially variable eddy viscosity fields is of secondary importance. For example in Figure 6.28, the value of  $Q$  at Station #1 (offshore) is substantially overestimated, and further modifications to the other boundary conditions or  $\epsilon$  does little to improve the agreement. On the other hand, at Station #3 just seaward of the bar crest, the SFWT reasonably predicts  $Q$ , and the effect of  $\epsilon$  or the bottom conditions can be better appreciated (Figure 6.26). It is noted that applying SFWT alone to describe surf zone properties is not considered to be the most accurate method, but it produces the best agreement in this experiment.

## 6.6 Simulation of Roelvink and Reniers (1995) Experiments

In these experiments, random waves of 94 cm significant height were run over a moveable sand bed in a large wave channel (Roelvink and Reniers, 1995, Case 1A). This case (1A) is one of a larger group of experiments and was chosen from the data set as the one experiment in which the beach profile changed only minimally during the run. Figure 6.29 plots the results of the 20 uniform eddy viscosity cases for the two bottom boundary conditions. These 20 simulations are the same as those conducted in the previous sections.

Inspection of Figure 6.29 immediately indicates that the choice of eddy viscosity in this large flume experiment plays an important role. Whereas in the previous experiments the lower values of  $\epsilon$  produced the best agreement with the data, in this large experiment the eddy viscosity is obviously much greater. The use of the higher eddy viscosity clearly improves the agreement with the data while the lower value of  $\epsilon$  produce  $\beta$  values much greater than 1.0 in most cases. The reason behind the great disparity

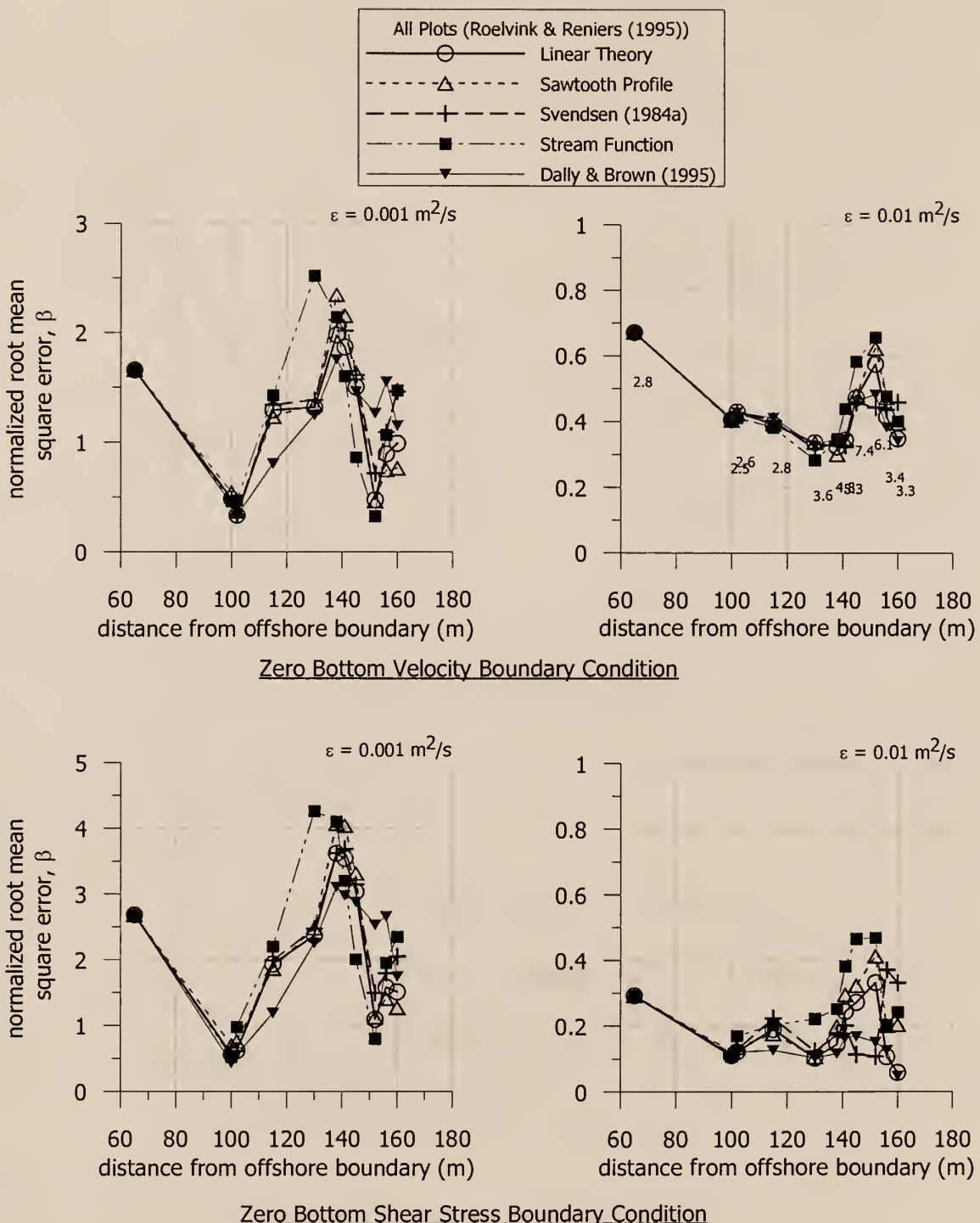


Figure 6.29 Comparison of simulations of the data set of Roelvink and Reniers (1995) from the Delta flume experiments in Delft, The Netherlands. The plots compare the normalized RMS error,  $\beta$ , for two different eddy viscosity values and two different bottom boundary conditions. Note the different vertical scales. Typical RMS errors are given in cm/s at each measuring line. In each case the eddy viscosity is held uniform over the entire domain. The mean measured velocity at each station is found by dividing the RMS error by the corresponding  $\beta$  value.

between the eddy viscosity values is demonstrated in Figure 6.30. For the same applied surface shear stress, the lower values of  $\epsilon$  substantially increase the slope of the velocity profile at the surface, as given by  $\tau/(\rho\epsilon)$ . Since the eddy viscosity field in this example and in the cases of Figure 6.29 is held spatially uniform, the resultant velocity profile must vary as shown in Figure 6.30 in order to satisfy the volumetric flow rate boundary conditions. In the small laboratory experiments presented previously, where the lower values of  $\epsilon$  are more appropriate, the higher values of  $\epsilon$  simply produced more vertically uniform profiles while satisfying the volumetric flow rate requirement.

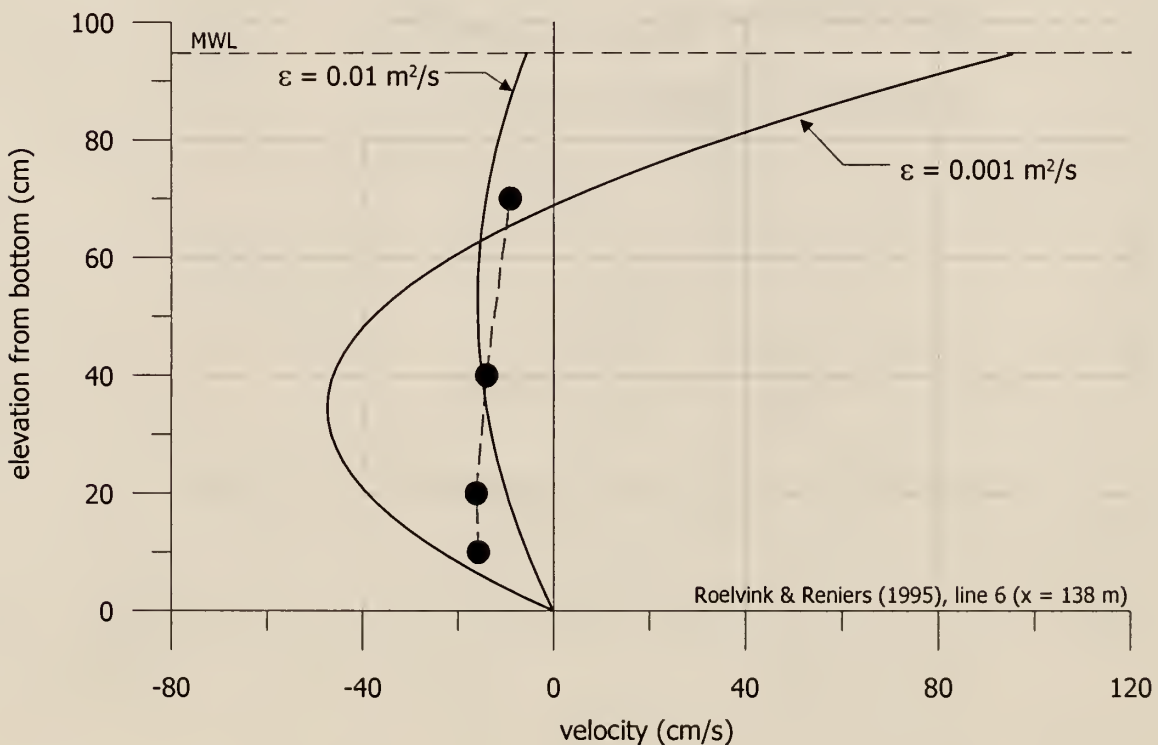


Figure 6.30 Demonstration of the effect of the choice of surface eddy viscosity. In this example, the choice of a lower value of  $\epsilon$  results in a much steeper slope of the velocity profile at the surface (given by  $\tau/(\rho\epsilon)$ ) for the same flow rate. The uniform eddy viscosity field dictates a parabolic profile, which produces significant errors when compared to the data. The higher value of  $\epsilon$  produces a smaller slope of the velocity profile at the surface and better overall agreement with the data.

Figure 6.31 plots the RMS wave height, radiation stress, and volumetric transport predicted by the five surf zone descriptions. Over the mild slope of this experiment, approximately 1:60, the roller models again produce the best agreement with data in terms of the volumetric transport. In this experiment, the roller model of Dally and Brown (1995) appears to best match the volumetric transport data across the entire profile. The velocity profiles plotted in the last frame of Figure 6.32 compare the choice of bottom boundary condition at the higher value of  $\epsilon$  ( $= 0.01 \text{ m}^2/\text{s}$ ).

As seen in the profiles, and in Figure 6.29, for the uniform eddy viscosity field, the zero bottom shear stress boundary condition provides better agreement with the data at most stations. It must be noted that data were collected in the flume at five discrete elevations above the bed with the lowest current meter fixed 10 cm above the bed, thus no boundary layer information is available. The ability of the zero shear stress bottom condition cases to better match the measured data is apparent in the velocity profiles in Figure 6.31. It is hypothesized that these simulations would not produce the best agreement if measurements closer to the bed were available.

In the shallow trough (located roughly between  $x = 142 \text{ m}$  to  $156 \text{ m}$ ) the agreement worsens, although only slightly for the zero bottom shear stress cases. This does not appear to be related to the prediction of the flow rate, as in the previous experiment, but may be a result of an underestimate of the surface shear stress. This would result from the model predicting that, after breaking, waves reach a stable wave height prematurely thus causing an underestimation in the gradient in wave radiation stress across the trough. The predicted RMS wave heights agree well with the measured wave data, which provides little information as to how to improve the prediction in this area.

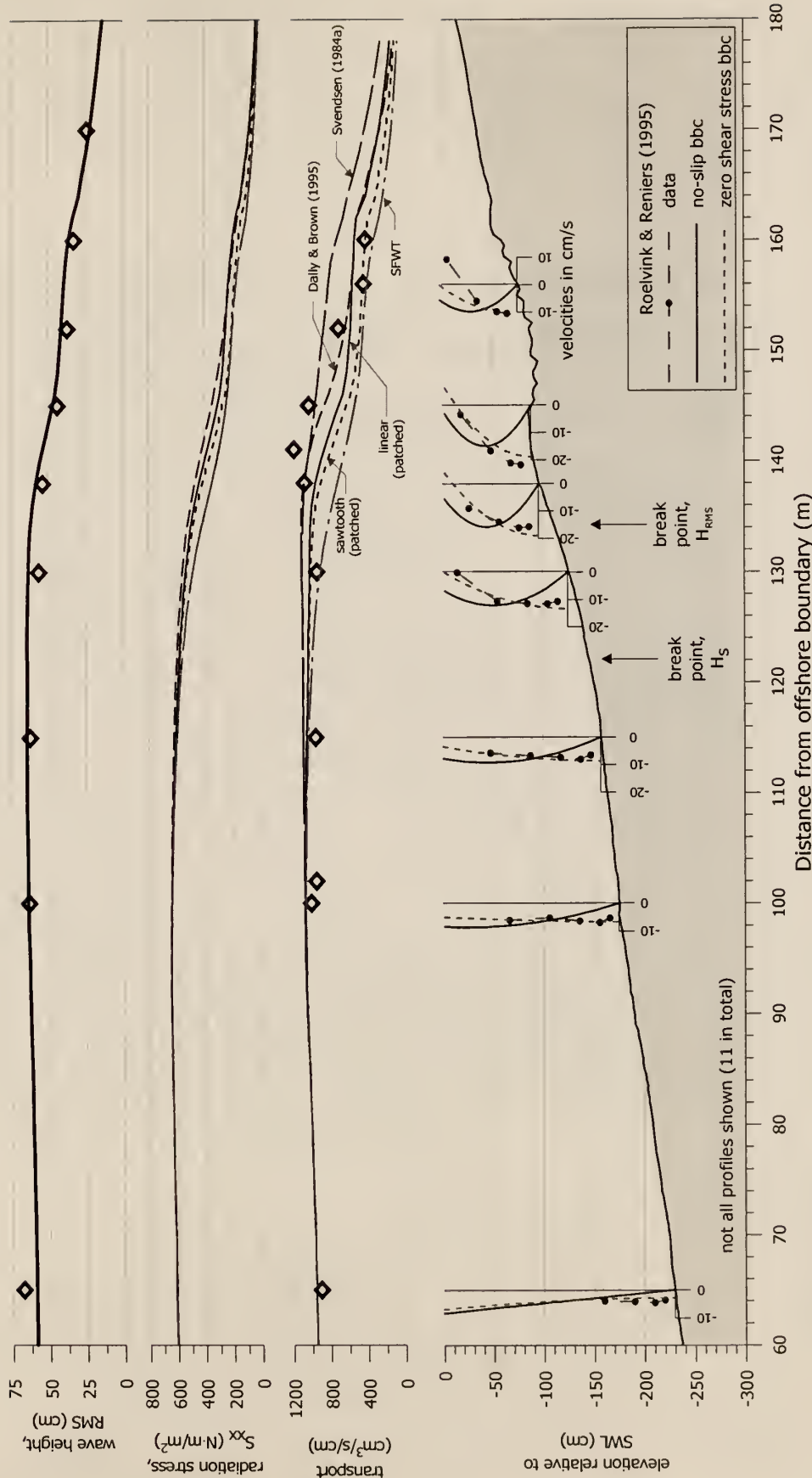


Figure 6.31 Comparison of predicted radiation stress and volumetric transport for the experiments of Roelvink and Reniers (1995). The five curves in each of the second and third frames illustrate the prediction of  $S_{xx}$  and  $Q$  for the five different surf zone descriptions listed. The velocity profiles predicted for the no-slip and zero shear stress bottom boundary conditions are plotted in the last frame and correspond to the roller model of Dally and Brown (1995) with a uniform value of  $\epsilon = 0.01 \text{ m}^2/\text{s}$ .

Figure 6.32 plots the  $\beta$  values determined from an additional 12 simulations that apply spatially variable eddy viscosity fields to the models of Svendsen (1984a) and Dally and Brown (1995). In this case, the spatially variable fields are based on and compared to the uniform eddy viscosity cases applying the higher value of  $\epsilon$  ( $= 0.01 \text{ m}^2/\text{s}$ ). Despite the scatter in the data, for the no-slip bottom boundary condition, the inclusion of a vertically varying eddy viscosity field provides noticeable improvement over the uniform and horizontally varying-only cases, as much as a 30% reduction in error at some stations. For the zero bottom shear stress condition, the trend is less clear although the horizontally varying cases do indicate improved agreement. In all cases, the model again does not perform as well in the shallow trough region.

Figure 6.33 plots the predicted flow field for the Roelvink and Reniers (1995) experiment. The field is simulated using the Dally and Brown (1995) roller model with a vertically varying eddy viscosity field and a no-slip bottom boundary condition. Inspection of Figure 6.32 indicates similar predictive capability between this choice and a zero bottom shear stress case, and it is hypothesized that the no-slip case with a vertical variation in  $\epsilon$  more accurately models the processes at work. As in the previous experiments, the model indicates the significant flows associated with the primary break point, followed by the second break following the trough.

Again the “best” simulation determined from the random wave cases is compared to the simulation of the experiments found by only applying the RMS wave height (66 cm) in the steady-state version of the model. As before, the strong shoaling predicted for the individual wave leads to large overestimations of the flow rate, particularly in the region near the primary break point (Figure 6.34).

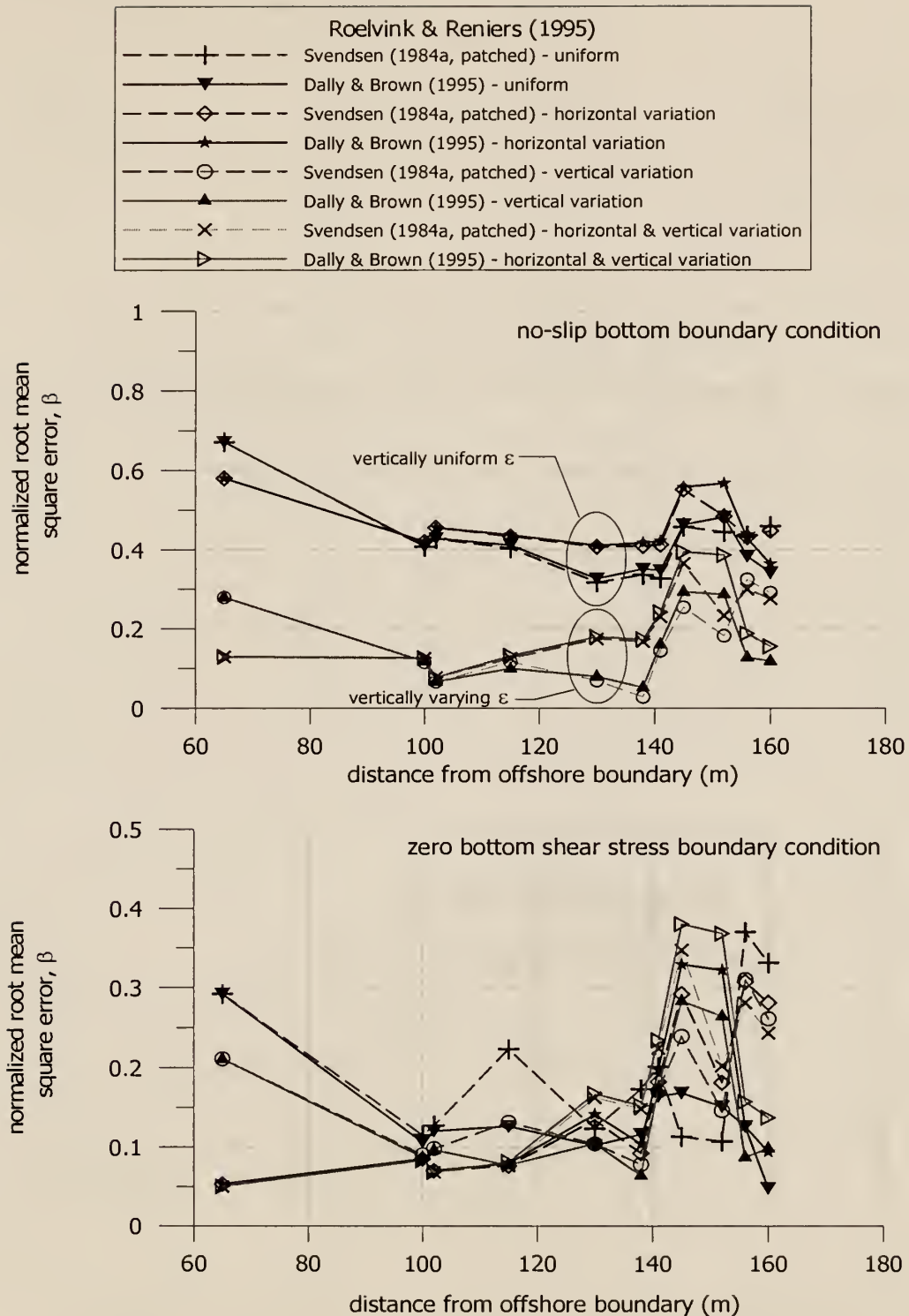


Figure 6.32 Comparison of normalized root-mean-square errors,  $\beta$ , obtained for the experiments of Roelvink and Reniers (1995) by applying spatially variable eddy viscosity fields. Inclusion of a vertical variation in the eddy viscosity produces a significant reduction in the errors computed. All simulations experience difficulty in matching the measured profiles in the trough region ( $x = 145$  to  $155$  m).

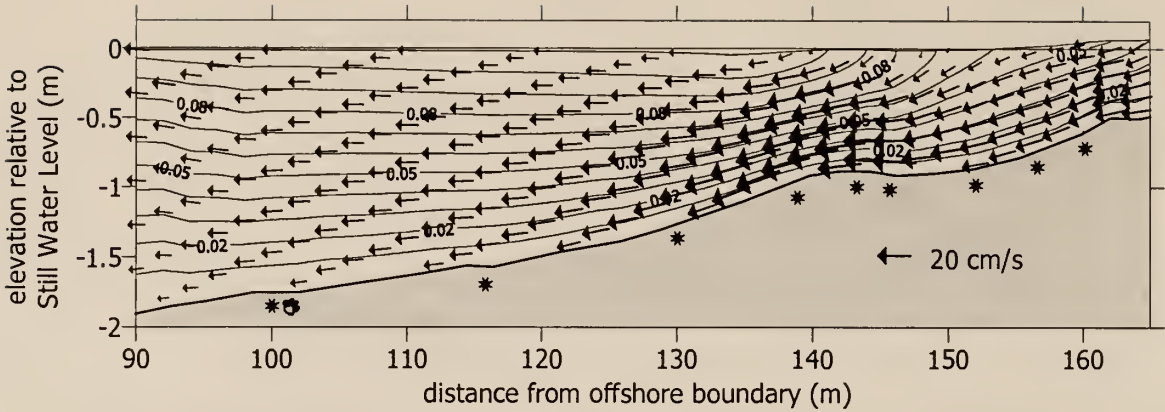


Figure 6.33 Flow field predicted for the experiments of Roelvink and Reniers (1995). The simulation applies the roller model of Dally and Brown (1995) in the surf zone with a no-slip bottom boundary condition and a vertically varying eddy viscosity field.

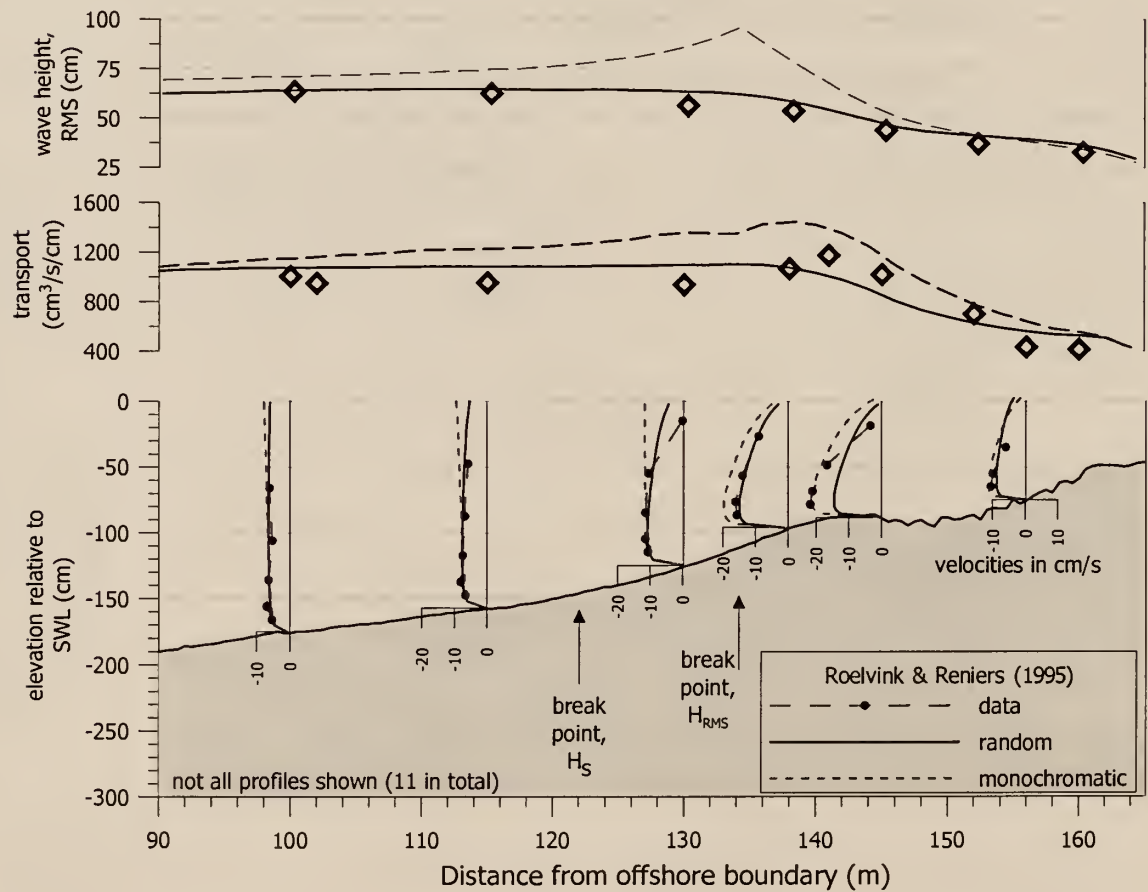


Figure 6.34 Comparison of simulations applying time-averaged random waves versus monochromatic waves of RMS height. Random waves produce a smoother flow field and lower flow rates near the primary breakpoint due to the variable nature of the break point. Both simulations apply the Dally and Brown (1995) model with a vertically varying eddy viscosity field with a no-slip bottom condition.

### 6.7 Simulation of Smith et al. (1992) Experiments

Smith et al. (1992) present return flow field data from Duck, NC, collected as part of the DELILAH Duck series of experiments in October, 1990. The return flow data were collected under a range of sea conditions using a vertical array of five current meters attached to a mobile sled. Depending on the depth of the flow at any given cross-shore location in the barred profile, two to four data points are available below trough level. Smith et al. (1992) present three different sets of return flow data. The one chosen for modeling herein represents the case where waves are approaching the shoreline closest to shore normal, although its angle of approach is 15 degrees from shore normal. It is noted that conditions of truly shore-normal wave approach in the field are rare.

Figure 6.35 presents the normalized RMS errors for the 20 simulations of uniform eddy viscosity fields. For the lower eddy viscosity values, the scatter is considerable and not surprising when the limited number of data points is considered. For both bottom conditions, the higher eddy viscosity values produce better overall agreement, as expected for this field experiment. The one exception is the Svendsen (1984a) roller model. It is not formulated to accommodate barred profiles. As in the previous barred examples (e.g. Okayasu and Katayama (1992)), the Svendsen model predicts increased values of transport in the trough due to the dependence on depth in its formulation.

Overall, the simulations applying higher values of eddy viscosity only reproduce the measured velocity profiles to within 50 to 85%. The RMS errors plotted in Figure 6.35 are fairly large, as much as 24 cm/s. The difficulties associated with modeling this field experiment are further illustrated in Figure 6.36. The figure indicates that the volumetric transport predicted by the model is significantly lower than the measured values seaward of the bar crest. Inside the surf zone, the wave heights and transport are well predicted.

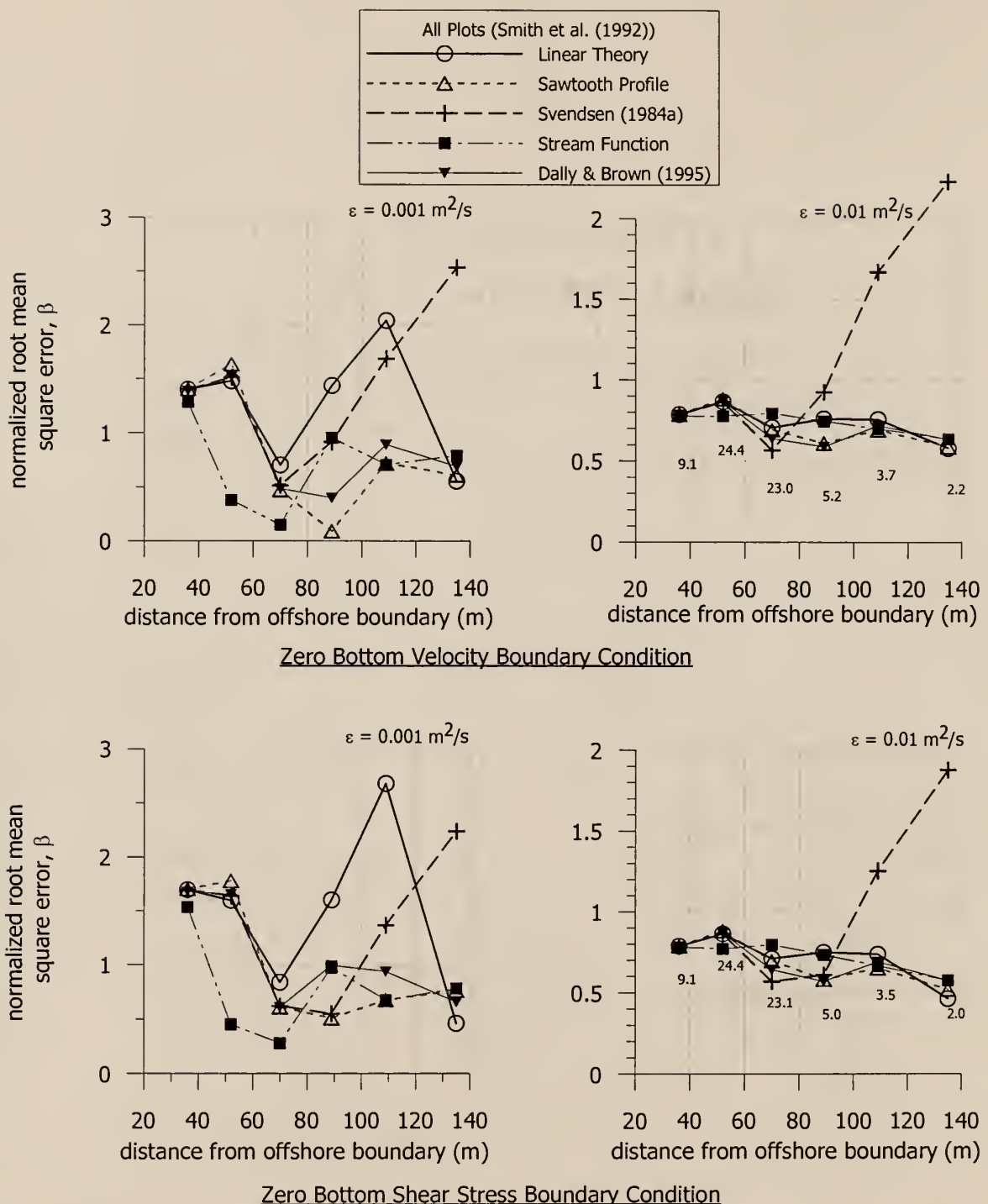


Figure 6.35 Comparison of simulations of the data set of Smith et al. (1992). The plots compare the normalized RMS error,  $\beta$ , for two different eddy viscosity values and two different bottom boundary conditions (note the different vertical scales). A typical RMS error is given in cm/s at each measuring station. In each case the eddy viscosity is held uniform over the entire domain. The mean measured velocity at each station is found by dividing the RMS error by the corresponding  $\beta$  value.

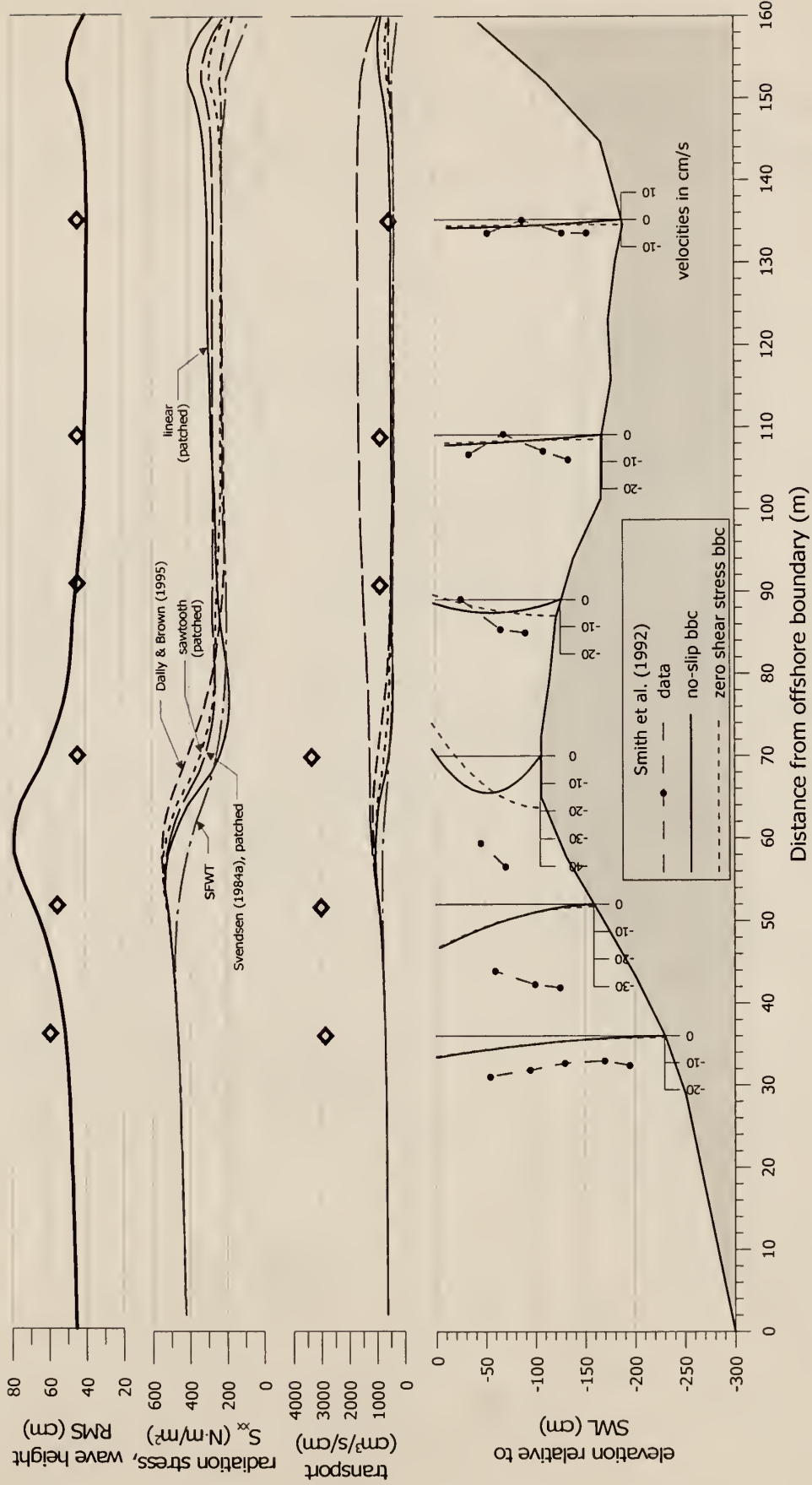


Figure 6.36 Comparison of predicted radiation stress and volumetric transport for the experiments of Smith et al. (1992). The five curves in each of the second and third frames illustrate the prediction of  $S_{xx}$  and  $Q$  for the five different surf zone descriptions listed. The velocity profiles predicted for the no-slip and zero shear stress bottom boundary conditions are plotted in the last frame and correspond to the roller model of Dally and Brown (1995) with a uniform value of  $\epsilon = 0.01 \text{ m}^2/\text{s}$ .

As in the Okayasu and Katayama experiments, the measured wave height information and the measured volumetric transport do not appear to agree. In this instance in the discrepancy is in the opposite direction. The measured waves heights would be expected to produce much *lower* values of transport than reported, whereas in the Okayasu and Katayama experiments the measured wave heights would be expected to produce much higher transport values than reported. For the Smith et al. data, a 1.6 m wave is needed to produce the transport levels measured (assuming monochromatic linear wave theory). The reported RMS wave height for this data set is only 0.54 m. It will be shown that even at its shoaled peak, a monochromatic wave of 0.54 m height does not produce transport levels close to the measured values.

In the present experiment, it is possible that the longshore current may be non-uniform in the longshore direction, producing areas of offshore directed flow separate from the shore normal wave induced return flow. In their work, Smith et al. calibrated their return flow predictions with their data set in order to model the vertical structure of the return flow, thus circumventing this problem. It seems unlikely that any wave theory will predict the magnitude of the flows seen in the offshore stations of Figure 6.36, some of which reach 40 cm/s. Given that difficulty, the present model is incapable of modeling the first three stations of the Smith et al. (1992) data set.

The model is capable of reproducing the inner stations with some success. As shown in Figure 6.35, the RMS errors at these stations is much more reasonable, approaching 50% error. It must be stressed that the error is computed only in the vertical range where measurements exist, which in this case is somewhat limited. The two innermost stations reveal some unusual structure but tend to resemble offshore profiles, or profiles in areas where waves are shoaling rather than breaking. The model generally

captures this behavior although it is obviously not capable of reproducing the measured inflection point. The validity of the measured inflection point is somewhat suspect.

Figure 6.37 presents the normalized errors produced from the simulations that apply spatially variable eddy viscosity fields. Only the results from the Dally and Brown (1995) model simulations are shown. In the figure, the difficulty in the agreement of  $Q$  seaward of the bar crest invalidates any further attempt to improve the prediction. Inside the surf zone, the variation in  $\epsilon$  produces very little improvement, although some decrease in the value of  $\beta$  is seen for the vertically varying cases at the innermost stations.

Figure 6.38 plots the profiles corresponding to the Dally and Brown model with a vertically varying eddy viscosity field and a no-slip bottom boundary condition. In the plot the effect of modeling the flow field with a monochromatic wave of RMS height is also shown. Despite the increased wave height near the primary breakpoint, the transport predicted by the monochromatic wave is still significantly lower than the measured value. Figure 6.38 shows some improvement in the prediction of the shape of the profiles, but still does not agree satisfactorily with the measurements.

In general, the present model does not satisfactorily predict the measurements from the experiments of Smith et al. (1992). The primary difficulty lies in the inability to predict the return flow rate at the three offshore profile stations. This inability may be a problem with the experimental data set in which contributions to the current from sources other than the cross-shore wave induced return flow are included. The measured wave heights do not appear to correspond well to the measured velocity profiles in terms of the volumetric flow rate at each station. Use of the Dally and Brown (1995) roller model with a vertically varying eddy viscosity field provides only a marginal level of improvement. In general the velocity profiles in the surf zone are predicted only to within approximately 55%.

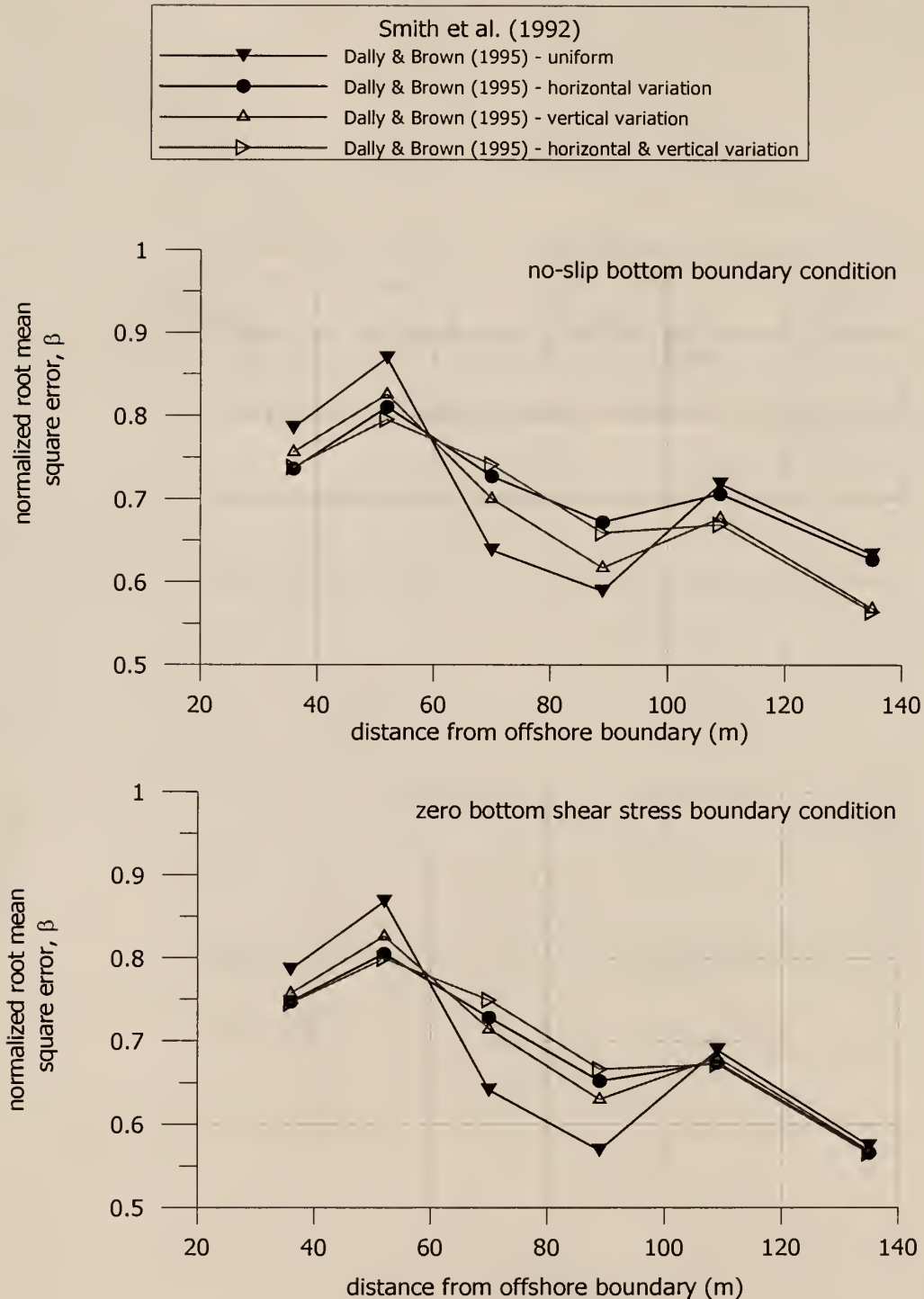


Figure 6.37 Comparison of normalized root-mean-square errors,  $\beta$ , obtained for the experiments of Smith et al. (1992) by applying spatially variable eddy viscosity fields. The Dally and Brown (1995) model with a vertically varying eddy viscosity field applied with a no-slip bottom boundary condition provides only marginal improvement at the inner surf zone stations.

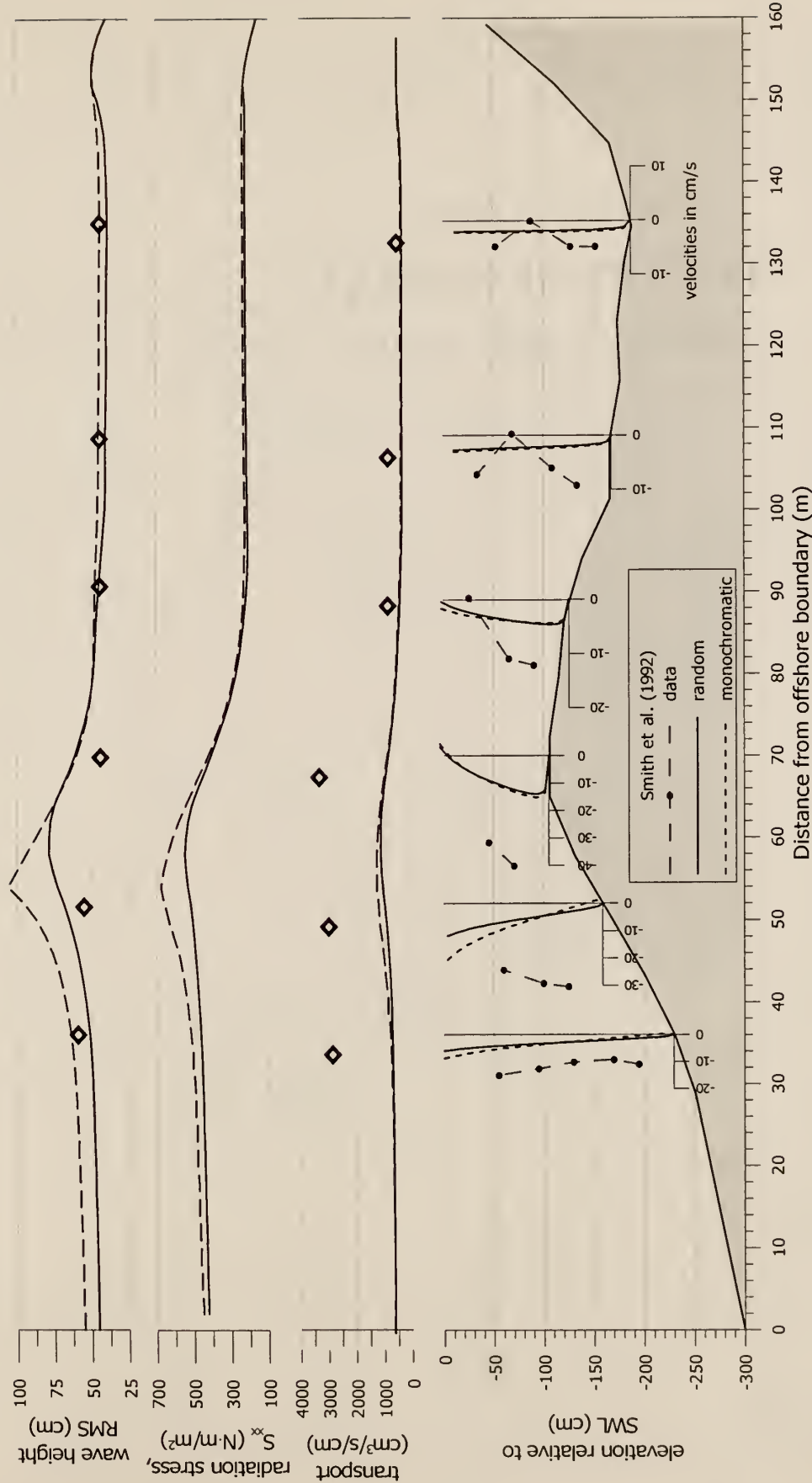


Figure 6.38 Comparison of simulations applying time-averaged random waves versus monochromatic waves of RMS height. Random waves produce a smoother flow field due to the variable location of the break point. This produces lower predicted flow rates, particularly near the primary breakpoint. Both simulations apply the Dally and Brown (1995) model with a vertically varying eddy viscosity field with a no-slip bottom BC. Neither approach simulates the measurements very well.

### 6.8 Comments

Comparison of the model to experimental observations demonstrates that the model is capable of simulating the vertical structure of the return flow. The simulations illustrate the strengths and weaknesses of the model as well as the most important aspects of return flow modeling. The primary factor in correctly simulating the return flow and its vertical structure is the proper prediction of the volumetric return flow rate. This flow rate is determined from the wave-induced mass transport, which is assumed to occur in the landward direction above the modeled domain. This volumetric transport must return seaward through the model domain such that the sum of the two is zero at any vertical section in order to conserve mass.

For most experiments, the model is able to accurately predict the vertical structure and magnitude of the return flow across the surf zone to within at most 25 to 30% error or better. The majority of the simulations indicate that in the surf zone, those descriptions that include a surface roller approximation (Svendsen (1984a) or Dally and Brown (1995)) produce better agreement with measurements, primarily due to the prediction of increased transport levels. In some of the simulations presented herein (2 of 6 experiments), the model does not simulate the measured volumetric transport properly. This leads to substantial errors in the prediction of the velocity profiles and is only marginally improved by altering the other boundary conditions or the eddy viscosity field.

Further improvement is observed when a vertical variation of  $\epsilon$  is applied with a no-slip bottom boundary condition, allowing the profile to mimic a bottom boundary layer and creating more uniform velocity profiles in the body of the flow. Inclusion of a depth-dependent horizontal variation in the eddy viscosity provides very little improvement, as it does not consider the degree of turbulence generated by the breaking waves.

Some of the difficulties encountered in the comparison to the published data are discussed in Chapter 7. In particular, the treatment of the transition region is examined, including a comparison of the model to published data regarding the structure of the vertical mean velocities in the surf zone. Additionally, the behavior of Stream Function Wave Theory in shoaling and breaking waves is discussed further in Chapter 7. The overall implications of the present 2-D stream function return flow model on sediment transport in the surf zone are also presented in the following chapter.

## CHAPTER 7

### IMPLICATIONS FOR CROSS-SHORE SEDIMENT TRANSPORT AND FUTURE STUDY

In this chapter, various aspects of the application of the model are discussed and the implications of the model results for cross-shore sediment transport are investigated. One of the objectives of developing the present model was to create a laterally coupled model (cross-shore direction) in which the effects of the applied stresses would be distributed across the domain in a unified manner in order to avoid large discontinuities in the velocity and shear stresses, particularly near the break point. This feature is sought in order to potentially apply the present hydrodynamic model to a sediment transport module to predict beach profile evolution. Discontinuities in flows and shear stresses lead to unrealistic predictions of erosion or accretion in profile change models, such as the unrealistically large growth of break point bars (Dally, 1980). The behavior of the model across the domain and near the break point is investigated in terms of the distribution of mean bottom shear stress across the profile and the nature of the vertical profiles of velocity and shear stress in the vicinity of the break point. The application of the full two-dimensional model versus the application of individual one-dimensional vertical profile solutions is discussed.

The nature of the velocity and shear stress profiles seaward of the break point is investigated with regard to the possible creation of onshore directed bottom flows caused by equivalent offshore directed surface shear stresses applied by shoaling waves. It is

hypothesized that this mechanism may play a role in onshore directed sediment transport and the formation of shore parallel bars through a conservation of angular momentum argument, as qualitatively described by Dyhr-Nielsen and Sørensen (1970). Many experimental data sets present velocity profiles seaward of the break point that suggest that offshore directed surface stresses are present. Some of these data sets also report onshore directed flows near the seabed. These flows have traditionally been attributed to viscous boundary layer streaming effects, but it is of interest to investigate the possibility of onshore directed flows present even in the absence of a viscous boundary layer argument.

Other aspects of interest include the treatment of the transition region. As discussed in Chapter 4 and presented in Chapter 6, the inner surf zone is separated from the offshore by a region in which breaking waves undergo a transformation of energy and momentum. Very little momentum is lost from the wave/roller system in this region but there is a distinct transfer of momentum from the organized wave motion to the roller. This transfer is the mechanism for conserving momentum across the profile. As discussed previously, many descriptions of inner surf zone flows do not consider the agreement in integral properties of waves (such as volumetric flow rate and momentum). The transition region bridges the gap between these areas and assures conservation of momentum.

The treatment of the transition region is a difficult issue. Herein two approaches have been applied. The first is simply a spatially decaying patch between the offshore and inner surf zone values of radiation stress (momentum flux). The second method is the application of the model of Dally and Brown (1995) in which the details of the growth of the surface roller and the transfer of momentum from the wave motion to the roller are modeled. How well these methods model the transition region is gaged in terms of the visual change in shape of the measured velocity profile and the combined comparison of

the change in volumetric transport across the profile in relation to measured profiles of vertical velocity.

Some difficulties in modeling the return flow are discussed. As seen in Chapter 6, the description of the wave properties, particularly the volumetric transport, is of primary importance in modeling the mean value and vertical structure of the return flow. In some instances the use of Stream Function Wave Theory (SFWT) predicts that the occurrence of the maximum value of some wave properties, such as radiation stress and volumetric transport, does not correspond to the highest wave predicted by the SFWT shoaling method. This produces gradients in properties such as radiation stress that are somewhat counterintuitive (i.e., oppositely directed). The existence of this phenomenon has been noted by previous researchers and is discussed briefly in this chapter. Additionally, the selection of the description of the vertical variation of eddy viscosity is reviewed.

### 7.1 Variation in Predicted Bottom Shear Stress and Shear Stress Profiles

Figure 7.1 presents the variation in mean bottom shear stress predicted for the model experiments of Cox and Kobayashi (1997). The plot includes the results of four simulations intended to demonstrate a range of possible solutions to the flow field. The figure illustrates the significant discontinuity that is created by applying an unpatched surf zone description (the roller of Svendsen (1984a) in this case) to the SFWT in the offshore. At the break point the large discrepancy between the two theories creates a large onshore then offshore value of bottom shear stress progressing onshore across the profile. The large onshore value of shear stress is the result of the 2-D finite difference description of the shear stress. At the break point, the model requires information from adjacent cells to compute the shear stress. These cells contain information computed from the two different

unpatched theories, thus creating the large discontinuity. The direction of the excessively large shear stresses suggests that the flows strongly and unrealistically converge at the break point, a fact that would suggest the formation of a break-point bar but that would also create instability in any sediment transport module applied to this hydrodynamic model.

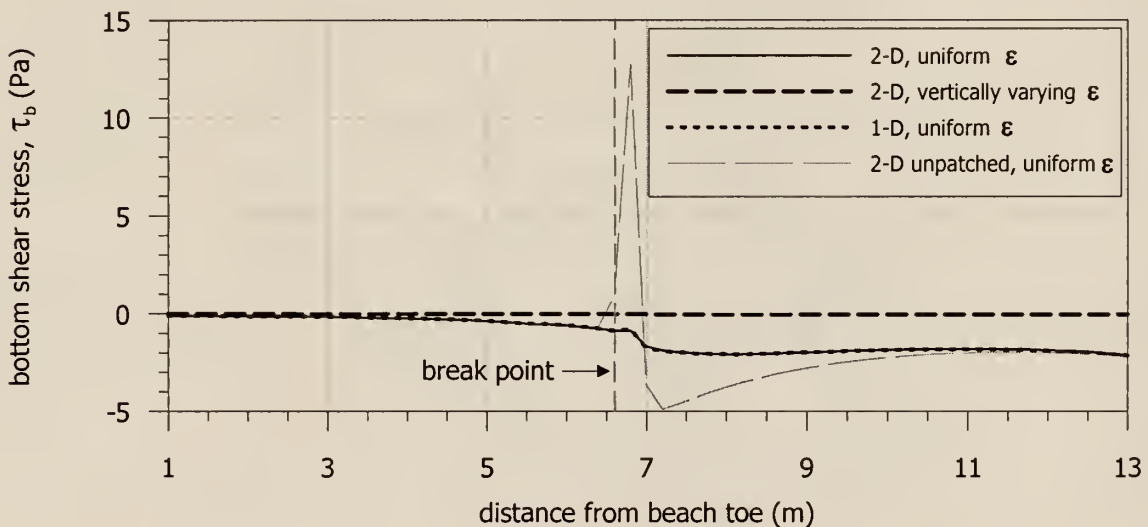


Figure 7.1 Cross-shore variation in mean bottom shear stress for the experiment of Cox and Kobayashi (1997). The figure illustrates the significant discontinuity resulting from applying surf zone and offshore wave theories that do not conserve momentum across the profile. The negligible effect of applying the 1-D vs. 2-D formulations is demonstrated. The effect of applying a vertically varying eddy viscosity field is shown to demonstrate the significant reduction in bottom shear stress predicted.

Figure 7.1 also shows that the benefit of applying the full 2-D solution to compute the bottom shear stress is negligible relative to applying the computationally simpler 1-D model at each vertical section in the domain. In applying the model to the various experiments discussed in Chapter 6, very little difference in the flow fields predicted by the 1-D and 2-D formulations was observed. Only a minimal alteration of the velocity and shear stress profiles along the vertical sections in the immediate vicinity of breaking was

predicted. Inclusion of an appropriately patched description of the boundary conditions further minimizes the differences. While the 1-D formulation cannot guarantee continuity at all locations between two adjacent vertical sections in the model, the differences are quite minor due to the specification of the overall flow through each vertical section via the externally determined boundary conditions. Further, away from the break point region, the boundary conditions vary gently in the cross-shore direction.

An additional simulation plotted in Figure 7.1 illustrates the effect of applying a vertically varying eddy viscosity field, based on the similarity profile discussed in Chapters 2 and 4 and applied in Chapter 6. The significantly lower value of the eddy viscosity was shown to produce improved agreement with velocity measurements in and near the bottom boundary layer. This has the added effect of reducing the shear stress on the bottom significantly in comparison to the uniform eddy viscosity cases. Figure 7.2 plots the cross-shore variation in bottom shear stress for simulations including the vertical variation in  $\epsilon$ . The plot indicates that the unpatched version still generates a large discontinuity near the break point despite the reduced eddy viscosity. Figure 7.2 also demonstrates that while the patch technique described in Chapter 4 does satisfy the conservation of momentum requirement, the method does not create a totally smooth variation in bottom shear stress (and other properties as seen in Chapter 6). The roller model of Dally and Brown (1995), however, does produce a smooth variation in bottom shear stress and other quantities.

While Cox and Kobayashi (1997) do not report mean bottom shear stress values, Cox et al. (1995) present the phase averaged variation in bottom shear stress at the six measuring stations for the same experiment. These stresses vary between approximately -2.0 and +2.0 Pa, and the average value appears to be no more than -0.5 Pa, much less at some stations. These findings are of the same magnitude as the bottom shear stress values

reported by Deigaard et al. (1991) for similar laboratory conditions. At all stations, the average does appear to be negative (offshore directed). The inability to determine the laboratory bottom shear stress more precisely prevents a more definitive determination of the choice of eddy viscosity to apply near the bottom, although the higher value (applied in the uniform case) does appear to produce mean stresses closer to the range of the *maximum* phase averaged values rather than the lower, mean, value.

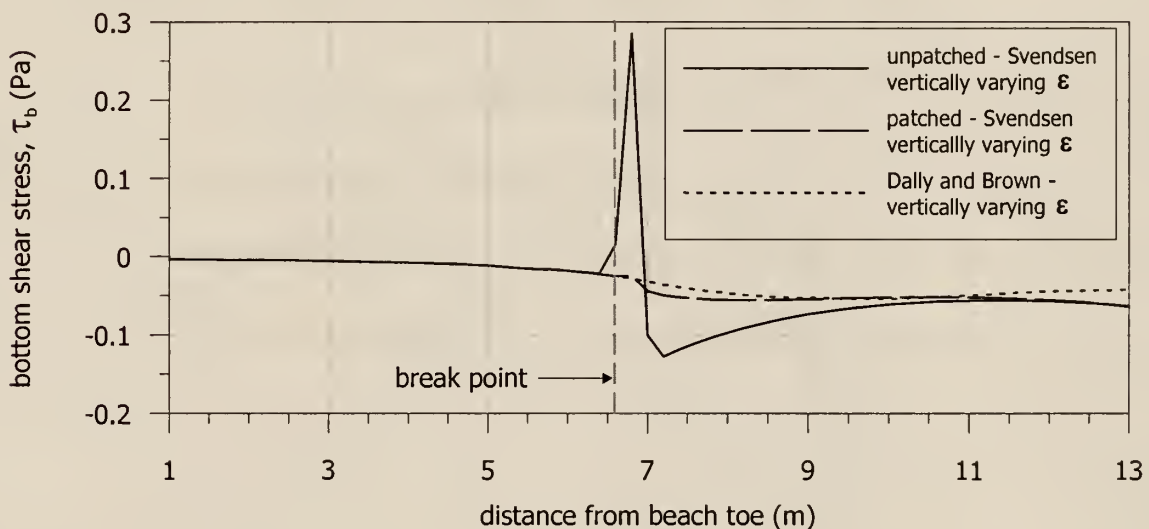


Figure 7.2 Cross-shore variation in mean bottom shear stress for the experiment of Cox and Kobayashi (1997). Each simulation applies a vertically varying eddy viscosity.

Figure 7.3 plots the profiles of horizontal velocity, shear stress, and turbulent eddy viscosity at two locations in the Cox and Kobayashi (1997) experiment. These locations correspond to station #1 (offshore) and station #5 (surf zone). Each figure plots the profiles from simulations applying uniform and vertically varying eddy viscosity fields. The plot illustrates how the variable eddy viscosity alters the shear stress profile, significantly reducing the mean bottom shear stress. The eddy viscosity at the bottom is reduced so much that the model has difficulty in reproducing the expected linear shear stress profile.

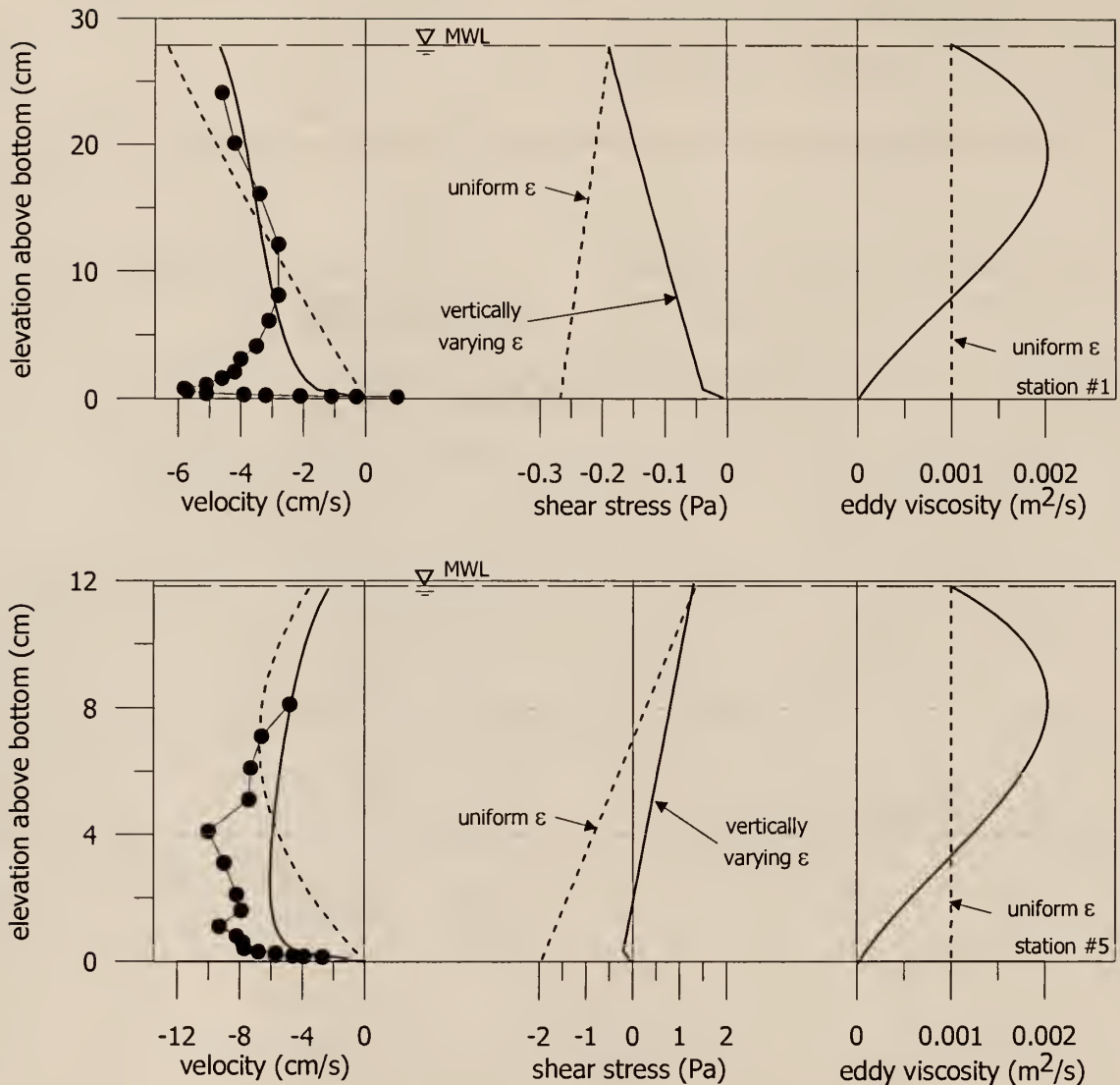


Figure 7.3 Vertical profiles of velocity, shear stress, and eddy viscosity at two measuring stations of the experiment of Cox and Kobayashi (1997).

In the governing equation (Chapter 3), the convective acceleration of the mean flow has been neglected or grouped with the turbulent terms included in the eddy viscosity representation. These acceleration terms could cause the shear stress profile to be non-linear (depending on vertical variation), but in the present development a linear profile is expected. It is hypothesized that the vertical step-size and the significant decrease in  $\epsilon$  at the bottom grid point produce the small error in the shear stress profile seen in the plots.

It is noted that the same vertical distribution of  $\epsilon$  is applied at both the inshore and offshore profiles. Seaward of the break point this vertical distribution has a profound effect on the shear stress profile, altering the slope of the shear stress profile as it significantly reduces the magnitude of the shear stress approaching the bottom. Offshore, this vertical distribution of  $\epsilon$  is no doubt unrealistic, since the mechanism generating the turbulence is completely different in shoaling and breaking waves. The appropriate distribution to apply seaward of the break point is not clear, and the choice of how to vary the vertical distribution in the horizontal direction across the profile is not immediately clear either. This is an area in which further research would certainly improve the predictive capability of the model. Of the two cases, however, the vertically varying  $\epsilon$  case does appear to better simulate the measured velocity distribution at the seaward station (#1).

With regard to bottom shear stress and sediment transport, clearly the description of the wave characteristics must be conservative across the entire profile in order to produce a smooth variation in the bottom shear stress. It is hypothesized that the smooth variation would better reproduce erosional and accretional behavior in beach profile evolution models, better predicting the formation or movement of shore parallel bars. Comparison of the 1-D simulation versus the 2-D simulation indicates very little difference in the two results. While the 2-D formulation guarantees conservation of flow at any location, the differences in the two formulations are minor. The error in conservation is limited due to the specification of the flow rate through each vertical section.

## 7.2 Transition Region Treatment

The treatment of the transition region is discussed in detail in Chapters 4 and 6. Therein it was found that it is clearly necessary to incorporate the conservation of

momentum in describing the wave/boundary conditions across the entire profile. The techniques used to patch the offshore description to the inner surf zone strongly alter the velocity profiles in the transition region primarily through the reduction of the predicted volumetric flow rate. In Chapter 6 it is shown that the velocity profiles inside and outside the surf zone are distinctly different in shape, and that shape gradually changes from one to the other across the surf zone. This provides one means of estimating the horizontal length of the transition region.

It is of interest to investigate the predicted length of the transition region and compare it to the apparent length from the measurements. An additional indicator of the length of the transition region is the distribution of the mean vertical velocity. Some of the experiments presented in Chapter 6 also report vertical velocity measurements. These can be investigated to determine at what point the mean vertical velocity generally changes direction. At the seaward end of the transition region, the vertical velocity is directed upward, indicating the feeding of the surface roller. In the inner surf zone, the flow is directed downward, indicating the decrease in wave height, momentum, and transport.

Nadaoka and Kondoh (1982) report the vertical velocity from their measurements. They also discuss the apparent length of the transition region. Referring to Figure 6.20, Nadaoka and Kondoh state that the transition region extends for approximately 1.9 to 2.9 m (from the break point at station #2 to station #4 or #5). This translates to approximately six to ten equivalent water depths (depth defined at breaking). They base their observation on the distribution of turbulence intensity which appears to reach a maximum in their measurements between stations #4 and #5. The measured volumetric transport also reaches a maximum in this region, after which it begins to decrease. In this region the measured vertical velocities are generally positive.

Figure 7.4 plots the predicted flow field for the experiments of Nadaoka and Kondoh (1982, Case 1, from Figure 6.22). Figure 7.5 compares the simulated and measured *vertical* velocities at the seven stations. Figure 7.4 indicates a narrow region of upward directed flow just landward of the break point. The region lies between stations, and does not agree well with the measurements (Figure 7.5). The predicted variation in volumetric transport across the profile using the Svendsen model (Figure 7.5) predicts little increase in  $Q$  once breaking occurs, hence very little significant upward directed flow is generated. The same holds for the model of Dally and Brown, which does predict a slight increase in the volumetric transport just after the break point, but does not correspond well with the measurements. Overall the predicted transition lengths are far too short.

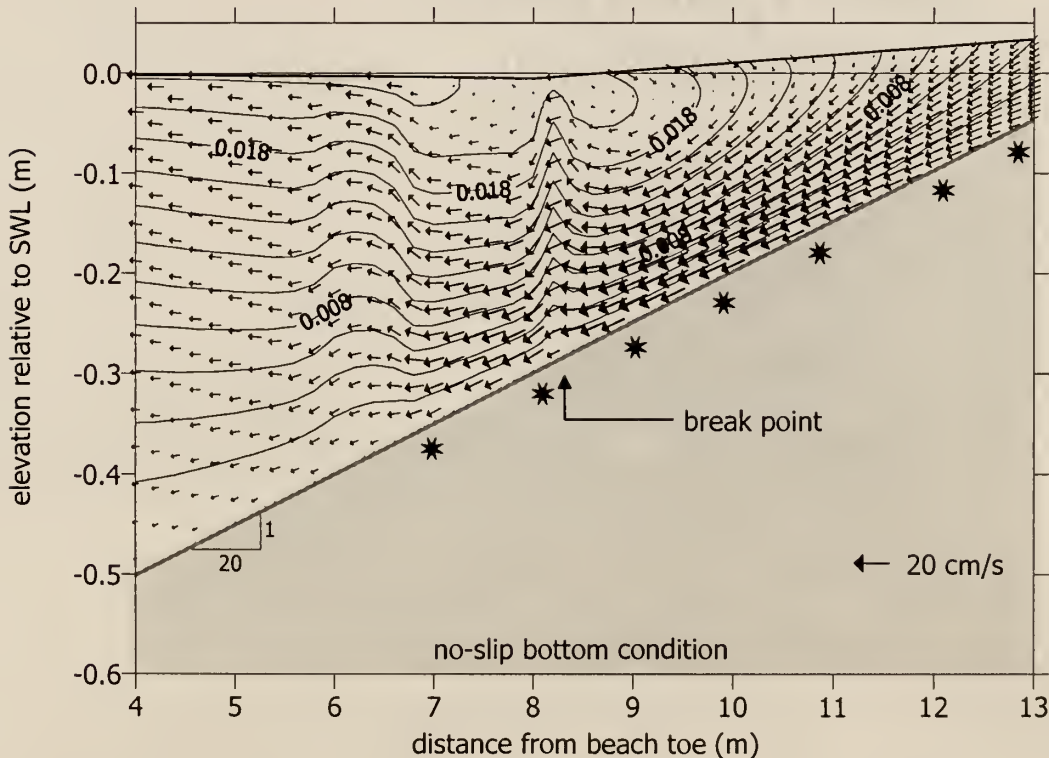


Figure 7.4 Predicted flow field for the experiment of Nadaoka and Kondoh (1982, Case 1). The simulation does predict a narrow region of upward flow landward of the break point that provides input to a surface roller, but the upward flows do not correspond well with the measurements.

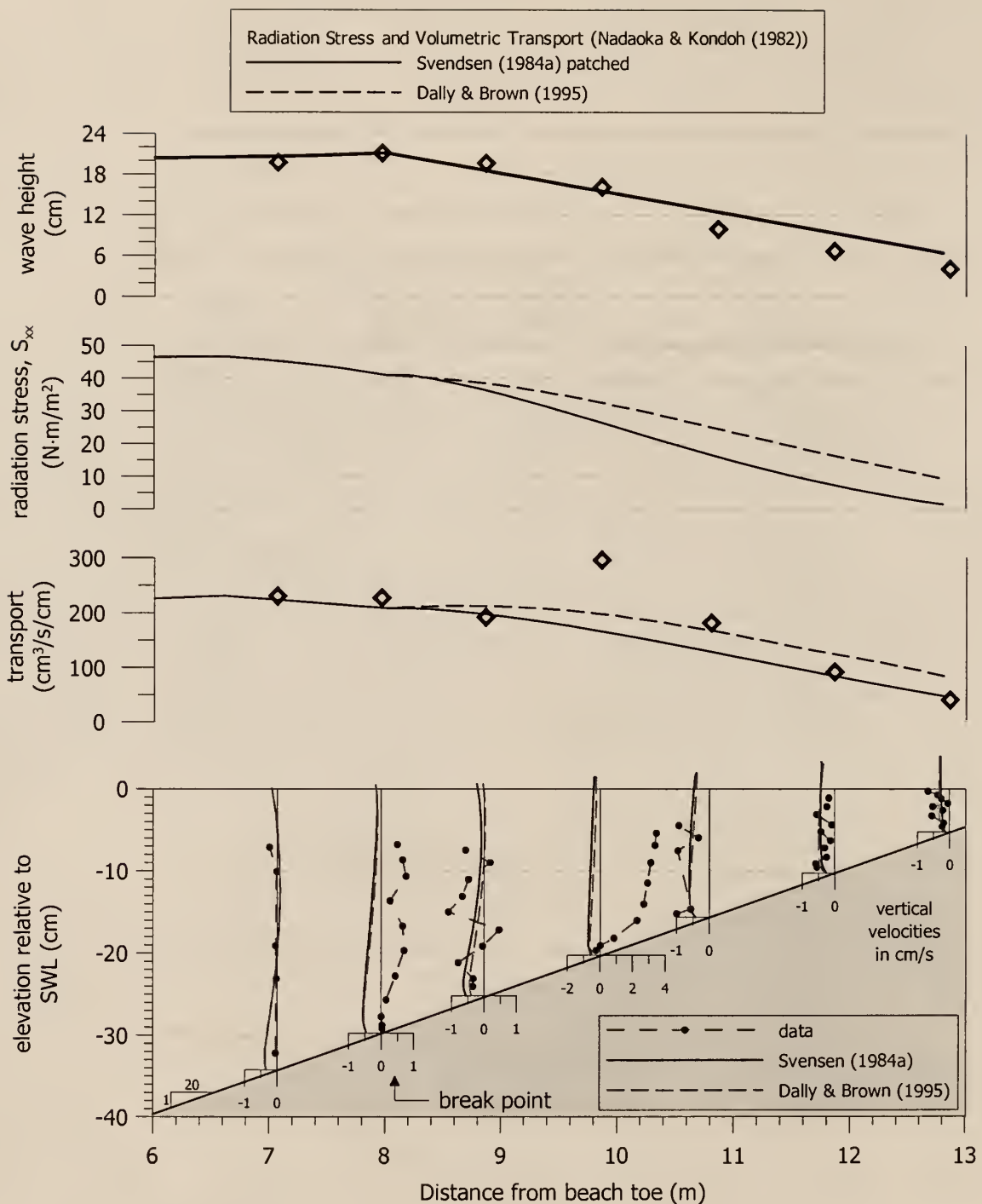


Figure 7.5 Comparison of predicted and measured profiles of vertical velocity for the experiment of Nadaoka and Kondoh (1982, Case 1). The data are compared to simulations applying the models of Svendsen (1984a) and Dally and Brown (1995). A no-slip bottom boundary condition is applied with a vertically varying eddy viscosity field. The lack of a significant predicted increase in the volumetric transport landward of the break point precludes the prediction of any positive (upward) velocities at the measuring stations.

Cox et al. (1995) present vertical mean velocity data for their experiments. The vertical velocity data exhibit a behavior similar to the Nadaoka and Kondoh experiments. The mean flows are directed upward in the region landward of breaking for a distance of at least 11 breaking water depths. Figure 7.6 illustrates the predicted flow field for this experiment, as presented in Chapter 6. Figure 7.7 plots the corresponding predicted vertical velocity profiles against the measured data for the Cox et al (1995)/Cox and Kobayashi (1997) experiment. As shown in Figures 7.6 and 7.7, the region in which flows are directed upward is quite narrow, roughly 4 breaking water depths (as compared to 11 depths from the data). Again none of the models that conserve momentum across the surf zone predict a sufficient increase in volumetric transport over a sufficient distance to create the upward flow present in the data.

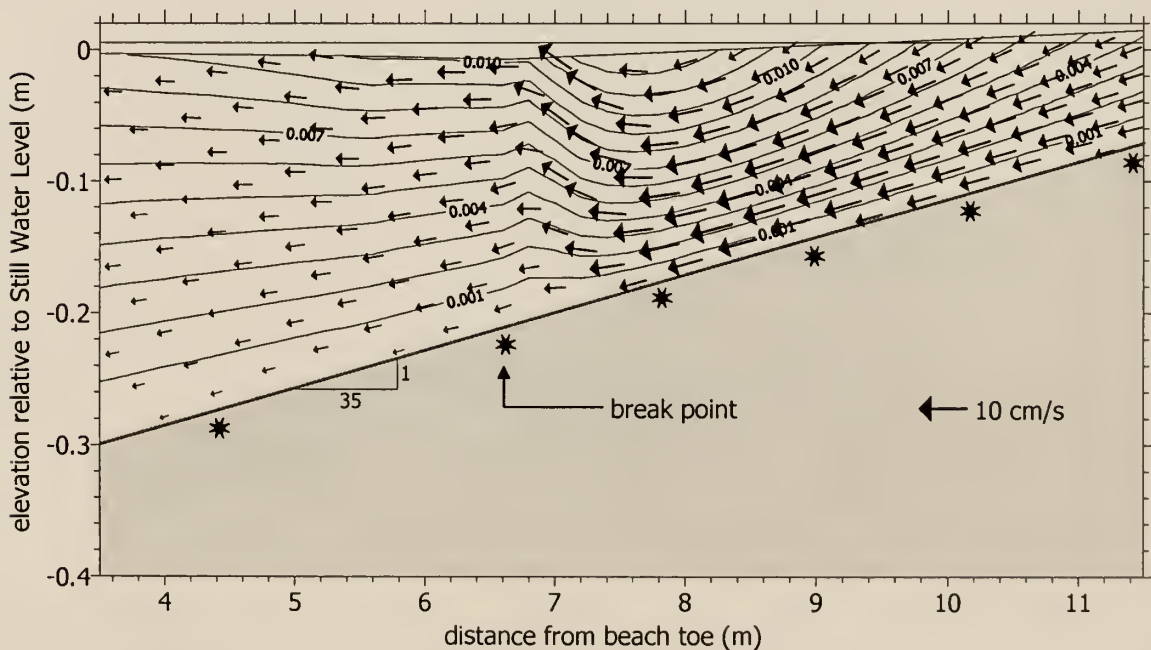


Figure 7.6 Predicted flow field for the experiments of Cox and Kobayashi (1997). The simulation applies a vertically varying eddy viscosity field and a patched version of the Svendsen (1984a) roller model with a no-slip bottom boundary condition. Landward of breaking, the model predicts a narrow region in which the flow is directed upward, suggesting an increasing volumetric transport in the transition region.

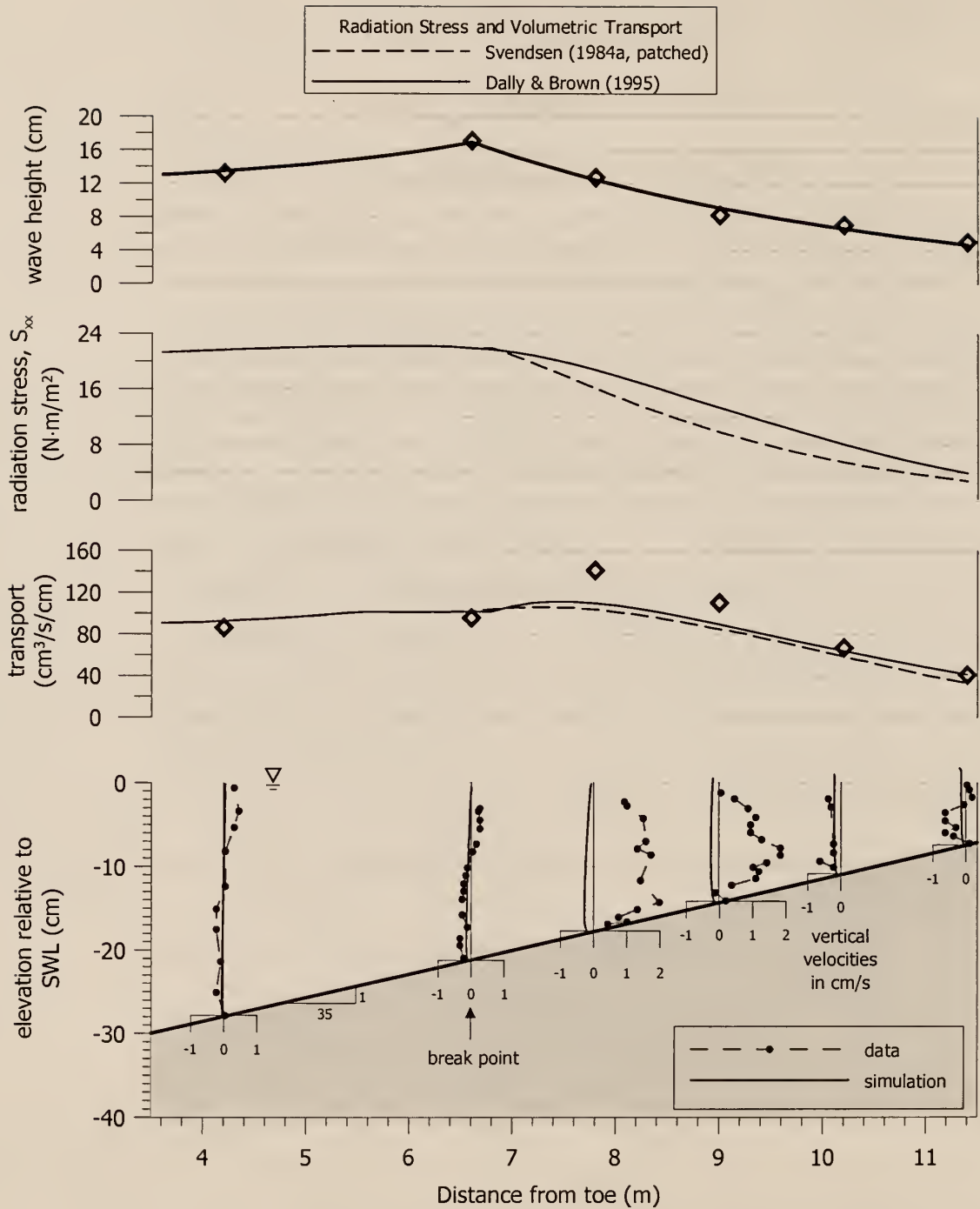


Figure 7.7 Comparison of predicted and measured vertical mean velocities from the experiments of Cox et al. (1995)/Cox and Kobayashi (1997). The predicted profiles apply the Svendsen (1984a) surface roller model with a vertically varying eddy viscosity field and a no-slip bottom boundary condition. The model reasonably predicts the vertical velocities at stations #1, #2, #5, and #6, but fails to predict the upward flows reported at stations #3 and #4.

Comparison of Figures 7.5 and 7.7 suggests that the change in direction of the vertical velocities is not necessarily the best indicator of the extent of the transition region. In Figure 7.7, upward flows are measured in an area where the volumetric transport is decreasing (station #4). Decreasing wave induced transport would suggest that flow is being injected into the domain through the Mean Water Surface, a process that would create downward flows. The difficulty in simulating the mean vertical velocities is compounded by the fact that these velocities result from relatively small differences in large quantities (i.e., the differences in  $Q$  between vertical sections). Nadaoka and Kondoh (1982) describe the transition region length in terms of the turbulent intensity. Cox et al. (1995) present turbulence data as well that roughly defines the transition length.

In the present model, it appears that both roller models applied can predict an increase in the volumetric transport associated with the roller which reasonably simulates the *horizontal* velocities. The prediction in the cross-shore gradient of the transport is not as good, and fails to properly predict the vertical velocity structure just landward of breaking. The model does predict upward mean flows, but the velocity profiles develop too rapidly into inner surf zone shapes and the upward flows are contained in too narrow a region landward of the break point. Interestingly, the distance needed in the patching technique to match the radiation stresses is on the order of the apparent transition lengths in the data (6 to 10 breaking water depths). Once patched to the inner surf zone, however, the prediction of  $Q$  is reasonable but the vertical velocity structure is not well predicted.

### 7.3 Onshore Bottom Stresses and Velocities Seaward of the Break Point

Dyhr-Nielsen and Sørensen (1970) suggest the possibility of onshore directed bottom shear stresses seaward of the break point created by the balance of moments in the

water column due to shoaling waves. They hypothesize that this mechanism results in sediment transport directed toward the break point and that the reverse situation applies inside the surf zone for breaking waves. This suggests that transport from both regions is directed toward the break point, thus promoting the formation of a break point bar. The possibility of this phenomenon is easily investigated in the present model.

In Chapter 6 the predicted cross-shore variation in the radiation stress was presented for six experiments. The gradient in the radiation stress in the trough to crest region of the waves produces the applied surface shear stress. In the results presented in Chapter 6 it was shown that for many of the experiments, the gradient is positive in the shoaling region, thus producing an offshore directed shear stress at the surface. Measurements of the horizontal velocity from several experiments suggests the presence of this offshore directed surface stress (e.g., Figure 7.3, upper frame).

Figure 7.8 presents a schematic that illustrates the effect of an increasingly offshore directed surface shear stress. The figure plots three velocity profiles that have the same value of transport through the vertical section and apply the same uniform eddy viscosity. For zero surface shear stress, the resulting horizontal velocity profile intersects the water surface perpendicularly and decreases consistently to zero based on the no-slip boundary condition. As the surface shear stress is increased, for the same value of  $Q$ , the slope of the velocity profile increases, causing the maximum magnitude of the flow to increase to accommodate the same flow rate. As shown in the figure, it is possible to increase the shear stress to the point that the flow reverses direction to produce the same flow rate. This reversal creates a positive (onshore) velocity and shear stress at the bed, thus promoting onshore transport.

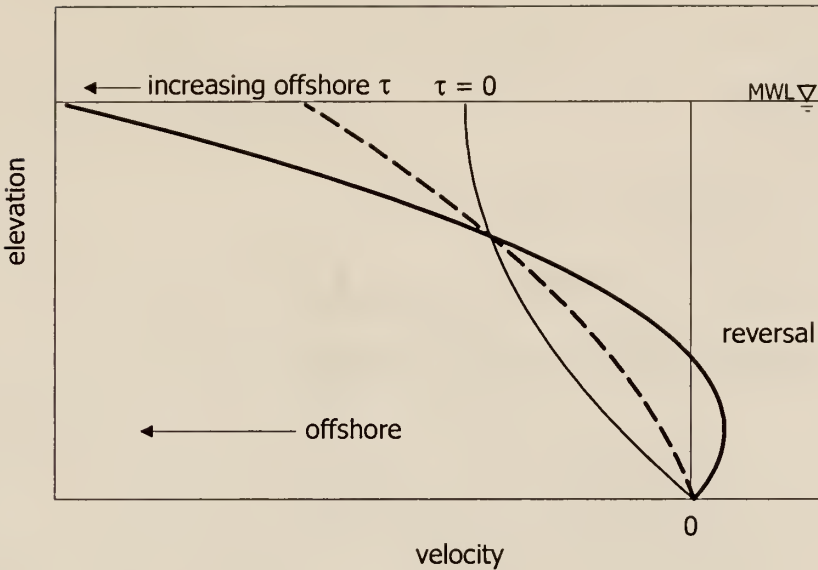


Figure 7.8 Schematic of the effect of increasing the magnitude of the offshore directed shear stress applied in the shoaling region. For fixed volumetric flow rate and uniform eddy viscosity, the increase in shear stress increases the slope of the velocity profile at the water surface, creating greater curvature to the profile and ultimately causing the flow near the bottom to reverse direction (onshore).

An expression for the surface shear stress in the shoaling region was presented in Chapter 4:

$$\tau_s \approx -\frac{\partial(E/2)}{\partial x} = -\frac{1}{16}\rho g \frac{\partial H^2}{\partial x} = \frac{E}{4(h+\bar{\eta})} \frac{\partial h}{\partial x} \quad (7.1)$$

Inspection of Eq. (7.1) indicates that the surface shear stress is dependent on the bottom slope,  $\partial h / \partial x$ . Figure 7.9 plots the predicted flow field in the offshore region of the experiment of Roelvink and Reniers (1995). As the waves shoal over this slope (roughly 1:23), the gradient in wave height, and thus wave radiation stress, is great enough to create a reversal of the flow. This is seen in the plot as the region where the zero streamline departs from the bed. The predicted velocities are very small in this region but are

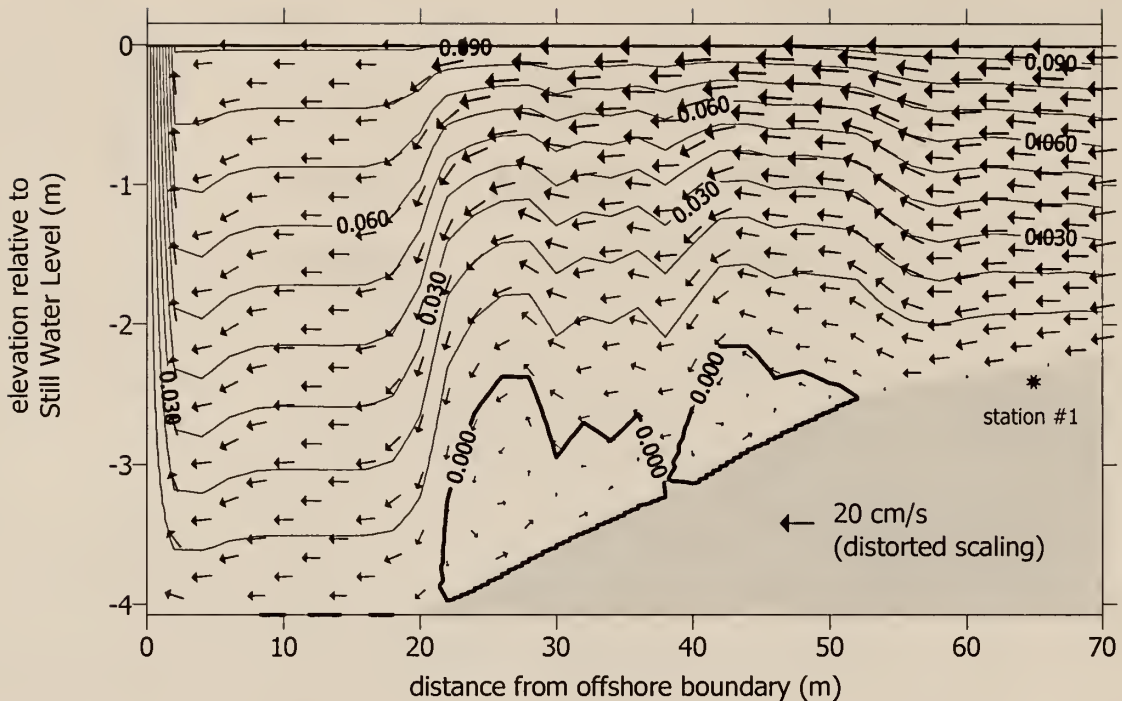


Figure 7.9 Predicted flow field in the offshore region for the experiments of Roelvink and Reniers (1995). The steep slope at the toe of the beach creates a strong gradient in the radiation stress, resulting in an offshore directed surface shear stress strong enough to create a reversal in the flow at the bed. The scale of the velocity vectors is distorted to illustrate the direction of the weak flows at the bed. The reversal is indicated by the location of the zero streamline, which leaves the bed along the steep (1:23) toe slope.

predicted to be directed onshore. To test this phenomenon to assure that the reversal of flow and the separation of the zero streamline is due to this effect and not a pressure-driven separation or numerical problem, the experiment was run without the offshore stress applied. The model does not predict this feature without the offshore directed surface shear stress. Further, the simulation predicts this reversal even when a vertically varying eddy viscosity field is applied.

The potential reversal of flow under shoaling waves would contribute to onshore directed sediment transport in conjunction with the onshore streaming velocity in the boundary layer. The creation of this onshore directed flow or stress can be thought of in

terms of the balance of moments in the water column. Various researchers (Longuet-Higgins, 1980, Brinch-Nielsen and Jonsson (1985)) have investigated the angular momentum in water waves. Brinch-Nielsen and Jonsson (1985) found that it was necessary to include an onshore directed bottom stress in shoaling waves in order to balance the angular momentum equation. The authors note that the difficulty in defining the vertical stresses in the water column obscures the usefulness of the angular momentum description.

The potential onshore directed stress caused by wave shoaling is not the only mechanism for onshore transport. The asymmetry of shoaling waves contributes an onshore directed stress as well. This stress is time dependent, and would not be accounted for in the present, time-averaged model.

#### 7.4 Selection of Wave Theory and Phase Speed Definition

For some of the experiments presented in Chapter 6, it is observed that some of the integral wave properties, most notably the wave radiation stress, reach their maximum value before the wave height is predicted to reach its maximum value. The result of this phenomenon is the reduction in radiation stress just prior to breaking which, as discussed in the previous section, results in the prediction of onshore directed surface shear stresses in areas where measurements suggest the presence of offshore directed shear stresses. To clarify this behavior, the use of the Stream Function Wave Theory and the selection of the first definition of phase speed, in which waves do not propagate over their own adverse return flow current, are discussed.

Figure 7.10 plots the nondimensional values of wave momentum flux (radiation stress) predicted by Stream Function Wave Theory (Dean, 1974). In the plot, waves shoal and increase in height from the lower right edge of the contoured area to the upper left edge

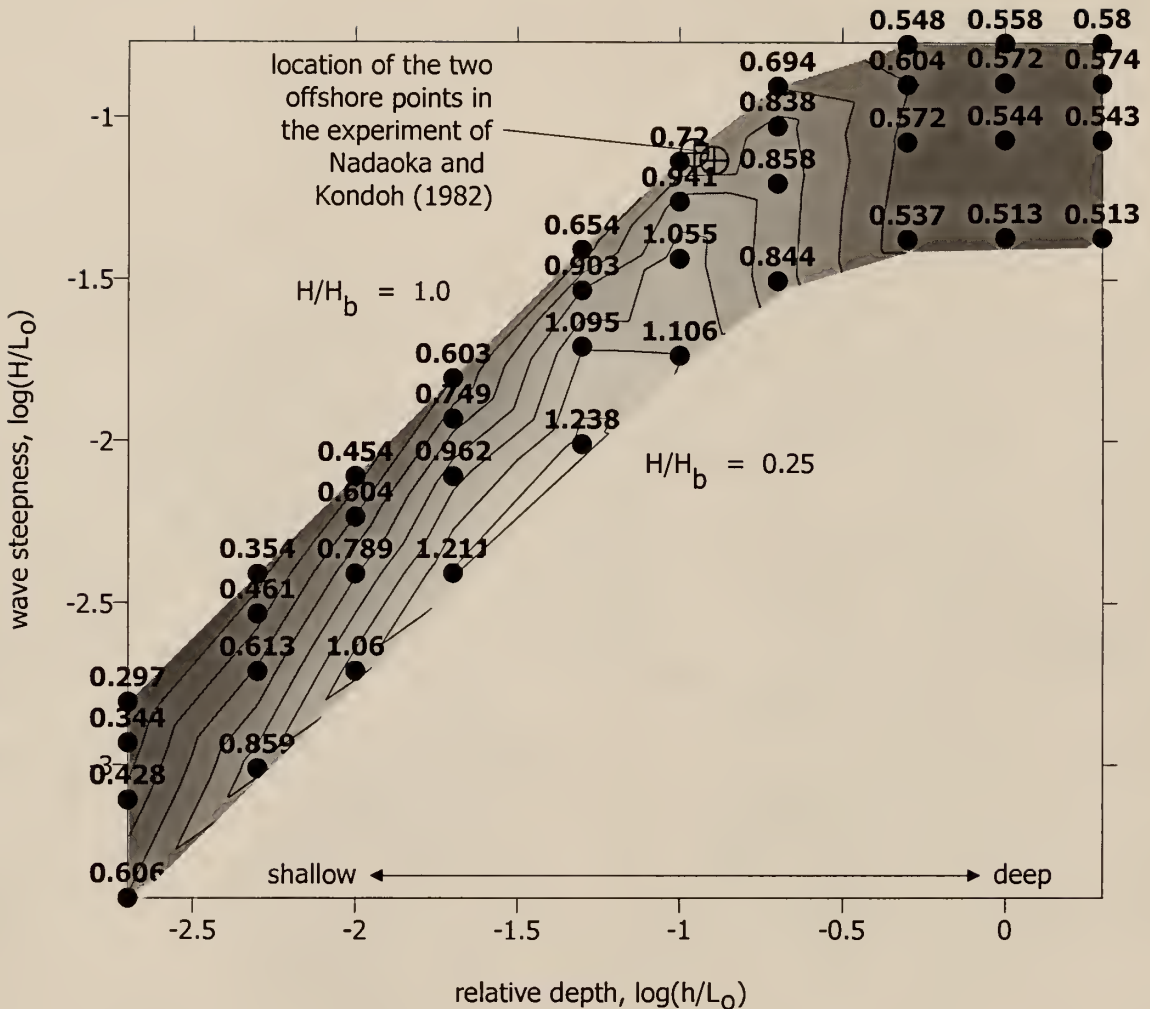


Figure 7.10 Contours of nondimensional wave induced momentum flux (radiation stress) determined from the 40 cases tabulated for Stream Function Wave Theory by Dean (1974). The plot illustrates how the maximum value of nondimensional momentum flux varies with respect to the height of a wave relative to the breaking wave height at the same depth. The maximum value of *nondimensional* momentum flux does not occur at  $H/H_b = 1.0$ .

of the plot, as described by the values of  $H/H_b$ . The contour plot illustrates that the maximum values of the *nondimensional* radiation stress do not occur at the maximum, breaking wave height. The radiation stress predicted from SFWT is nondimensionalized by the corresponding value of wave energy determined from linear theory,  $\rho g H^2/8$ .

In shoaling waves, the increase in wave height is frequently sufficient to overcome the reduction in nondimensional radiation stress so that the dimensional value increases, as would be intuitively expected. In some instances, the shoaling is not sufficient to produce an increase in the predicted dimensional radiation stress, and the value remains constant or actually decreases. The sign of the gradient in radiation stress determines the direction of application of the surface shear stress, and if the gradient is negative, the stress is onshore. Many measurements indicate that this stress is directed offshore.

Several researchers have noted that many integral properties of shoaling waves predicted by higher order theories, such as Stokes higher order theories and SFWT, do not correspond to the highest wave. Cokelet (1977) discussed this phenomenon and noted that the average kinetic energy, momentum, and phase speed in steady waves reach maxima before the wave shoals to its greatest height prior to breaking. Longuet-Higgins (1975) also notes this behavior in the momentum, kinetic and potential energy, and phase speed. Using Fourier wave theory, the model described by Sobey et al. (1987) also demonstrates a small decrease in some integral wave properties prior to breaking in some instances.

The difficulty in the prediction of the gradient of radiation stress might be offset by applying a wave theory that incorporates the effect of the return current. The present model applies SFWT in the offshore region assuming the first definition of phase speed, in which the wave is assumed to propagate over still water. In reality, waves propagate toward shore against the return flow current. A theory that includes the effect of the adverse return current is based on the second definition of phase speed. Since the SFWT applied herein is based on the tables by Dean (1974), the model employs the first definition. The tables would require reformulation to account for the return flow; however, the SFWT can be applied to the case of flow over a uniform current (Dean and Dalrymple, 1975).

Using the model of Sobey et al. (1987) the shoaling behavior of the Cox and Kobayashi (1997), Ting and Kirby (1994), and Nadaoka and Kondoh (1982) experiments was investigated using Fourier wave theory (also a steady wave theory) with and without the return current. The results indicate that without the return current, small decreases in the momentum flux prior to breaking were predicted for all three experiments. With the application of the adverse current, only the Nadaoka and Kondoh experiment indicated an increase in the predicted radiation stress. In that experiment, the radiation stress is then predicted to continue to increase up to the break point, a feature that would improve the prediction of the velocity profiles seaward of the break point in that experiment by reversing the direction of the applied surface shear stress.

The magnitude of the predicted momentum flux is not significantly different, but the change in sign of the gradient obviously affects the agreement with the measurements. Figure 7.11 presents a comparison of the predicted velocity profile at station #1 of the Nadaoka and Kondoh (1982) experiment applying the same surface stress magnitude, but in the opposite direction (stress predicted by present model). Inspection of Figure 7.11 clearly suggests the offshore directed stress is the appropriate choice. The results of the other two experiments using the Fourier wave theory, however, do not support the hypothesis that the difficulty in the radiation stress gradient is related to the phase speed definition.

### 7.5 Selection of Vertical Distribution of Eddy Viscosity

In previous chapters, the vertical variation in eddy viscosity was based on the parabolic mixing length model proposed by Reid (1957), primarily because it provided a plausible means of prescribing the change of  $\epsilon$  over the water column. As shown in

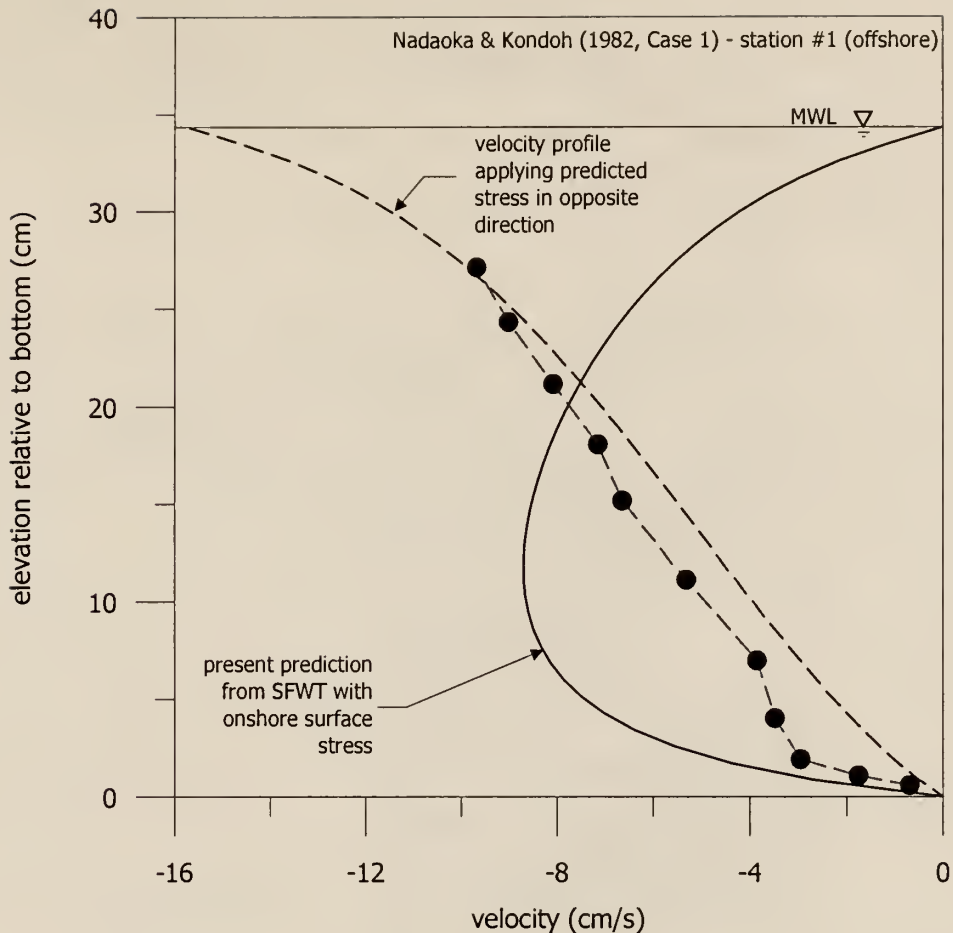


Figure 7.11 Comparison of predicted velocity profiles applying offshore and onshore directed surface stresses. The present model predicts an onshore directed stress due to the decreasing radiation stress predicted. The Fourier wave theory including the effect of wave propagation against the return current predicts an offshore directed shear stress which significantly improves the agreement with the measurement.

Chapter 6, difficulties in predicting the volumetric transport at any given station negated the benefit of properly describing the shape of the predicted velocity profile, but in some instances the measurements suggested that perhaps the Reid method was not appropriate. In this section, the shape of the velocity profile produced by the chosen description of  $\epsilon$  will be investigated. To appreciate the proper choice of the shape of the velocity profile, the requirement of the prediction of  $Q$  will be dropped, rather,  $Q$  will be fit to the measured

velocity profiles over the vertical range of measurements. Only profiles inside the surf zone are discussed; the vertical variation does not provide significant benefit to offshore return flow profiles.

Figure 7.12 plots three similarity profiles for the vertical variation of the eddy viscosity. Each profile assumes that the value of  $\epsilon$  at the surface is given (either through calculation or assumption). The profiles vary from 1.0 at the surface to some small fraction at the bottom. In the Reid model, the eddy viscosity grows from the surface downward and decrease sharply toward the bed, simulating the increase in turbulence thought to exist just below the surface due to the breaking waves. The second profile varies with  $z^{3/2}$ . This choice can be derived from several arguments. From a dimensional standpoint, the eddy viscosity can be shown through Froude number scaling to vary as  $L^{3/2}$ , where  $L$  is some characteristic length. In a somewhat ad hoc application, the Prandtl mixing length theory can be applied and modified to provide the following expression:

$$\epsilon = \kappa(z + z_o) \sqrt{\frac{\tau}{\rho}} \quad (7.2)$$

The shear stress in Eq. (7.2) is intended to describe the uniform shear stress present in wall boundary layers and is intended to describe the variation near the boundary. It is perhaps somewhat fortuitous that the eddy viscosity profile predicted by Eq. (7.2) does produce good agreement with the measured data (better than the Reid model). However, the resulting shape of the  $\epsilon$  profile is quite defensible. The  $z^{3/2}$  profile indicates that the turbulence is a maximum at the surface and decreases quickly from the surface to the bottom. The Reid model assumes that the eddy viscosity must decrease near the upper boundary due to mixing length limitations. Since the present application involves a quasi-

free surface with water particle motion assumed to be occurring in the region above the model domain, this limitation is not absolutely necessary, thus the eddy viscosity maximum could potentially be located at the surface. The linear variation of  $\epsilon$  is simply presented for comparison, no physical rationale is given.

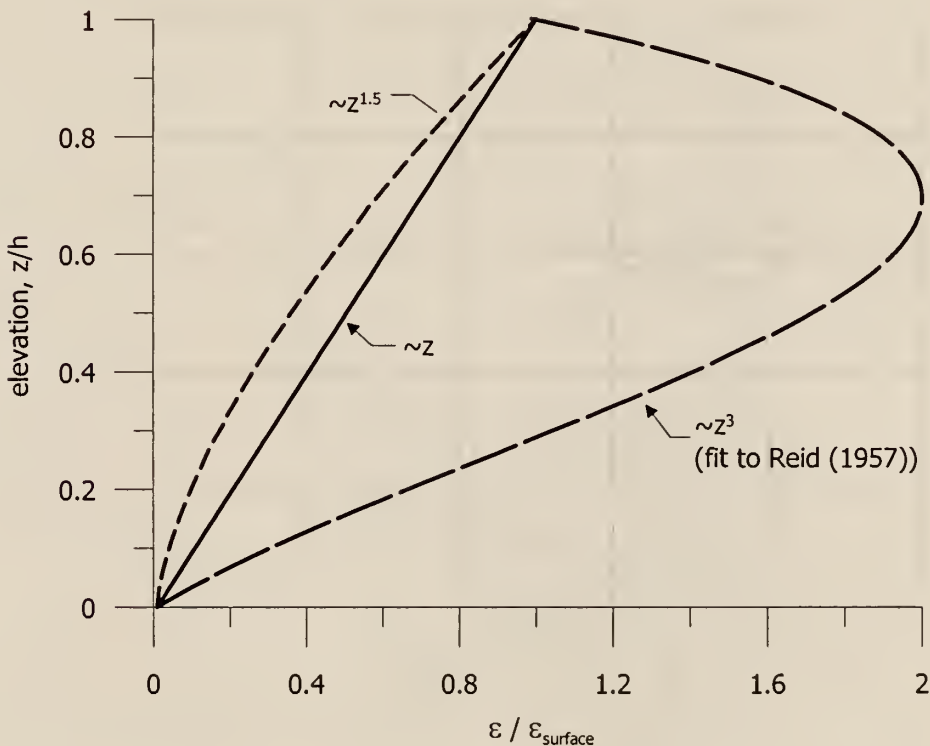


Figure 7.12 Comparison of nondimensionalized vertical distributions of eddy viscosity.

In Figure 7.12, the value of  $\epsilon$  at the bed is set to be 1/100<sup>th</sup> of the value at the surface. This selection is based loosely on the observations of Reid (1957), Svendsen et al. (1987), and the results presented in Chapter 6. Svendsen et al. (1987) report that the appropriate value of  $\epsilon$  at the bed is approximately  $10^{-2}$  to  $10^{-3}$  times the surface value. While this range is still quite wide, it does present some estimate of the appropriate value.

From Eq. (7.2), the value near the bottom could have been determined by applying some surface roughness value. In applying this technique in the model, it was found that the velocity profile is quite sensitive to  $z_o$ , making it difficult to choose one value of  $z_o$  that would apply at all stations in a given simulation. Choosing a fixed fraction  $\epsilon_{surface}$  to apply at the bottom introduces unwanted empiricism into the model, but produces a much more robust predictive capability.

Figure 7.13 plots the results of three simulations applying the distributions seen in Figure 7.12 for Station #5 of the Cox and Kobayashi (1997) experiment. The plot illustrates the differences between the linear and  $z^{3/2}$  variations and the  $z^3$  approximation to the mixing length method of Reid. The differences between the two can be described by inspection of both Figures 7.12 and 7.13. The  $z^3$  method, with an increasing eddy viscosity just below the surface, damps out the application of the surface shear stress quite rapidly, producing a much more uniform velocity distribution in the body of the domain, over predicting the velocity near the surface, and under predicting the velocity near the bottom.

Table 7.1 presents the normalized RMS errors for a series of simulations comparing the linear,  $z^{3/2}$ , and  $z^3$  distributions for the surf zone stations only. The linear and  $z^{3/2}$  cases are tested with bottom values of 1/100th and 1/200th the surface value. Overall, the  $z^{3/2}$  distributions produce slightly better agreement with the data than the linear distribution. Given the uncertainty in the application of the value of  $\epsilon$  at the bed, it is recommended that the conservative value of  $0.01 \epsilon_{surface}$  be applied in the absence of velocity profile data.

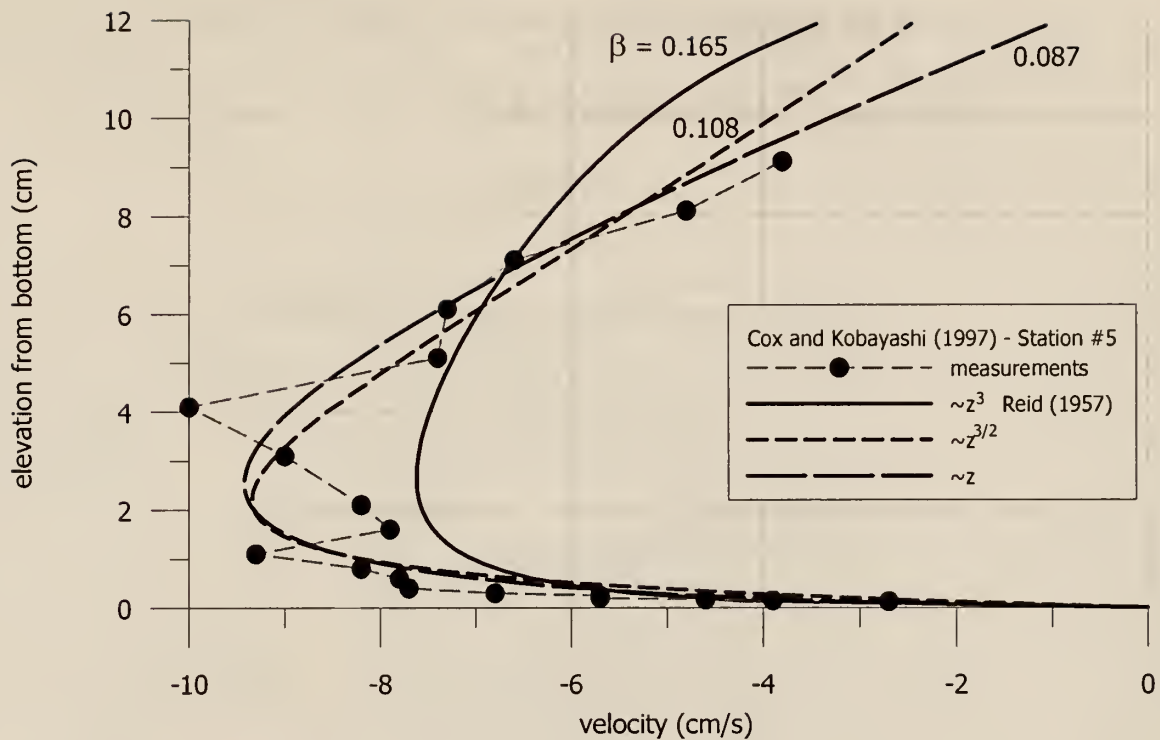


Figure 7.13 Comparison of predicted velocity profiles applying the eddy viscosity distributions plotted in Figure 7.12. The flow rate has been fit to the measured velocity profile in order to isolate the effect of the shape of the predicted profiles.

Table 7.1 Comparison of normalized RMS errors calculated from applying the eddy viscosity distributions in Figure 7.12 for the experiment of Cox and Kobayashi (1997).

Station #	$\epsilon \sim z^3$ $\epsilon_{bed} = 0.01 \epsilon_s$	$\epsilon \sim z^{3/2}$ $\epsilon_{bed} = 0.01 \epsilon_s$	$\epsilon \sim z^{3/2}$ $\epsilon_{bed} = 0.005 \epsilon_s$	$\epsilon \sim z$ $\epsilon_{bed} = 0.01 \epsilon_s$	$\epsilon \sim z$ $\epsilon_{bed} = 0.005 \epsilon_s$
3	0.099	0.144	0.170	0.239	0.283
4	0.129	0.103	0.057	0.101	0.120
5	0.165	0.108	0.108	0.087	0.090
6	0.205	0.121	0.078	0.180	0.138

## CHAPTER 8

### SUMMARY, CONCLUSIONS, AND RECOMMENDATIONS FOR FUTURE WORK

A numerical model is developed to investigate the use of the stream function,  $\psi$ , to model the wave-induced return flow in the nearshore region and to test the application and effects of various wave theories and boundary conditions on the flow. Solution of  $\psi$  produces the velocity in the horizontal and vertical directions, providing a view of the complete flow field in the 2-DV plane. The governing equation, a fourth-order partial differential equation in  $\psi$ , is not specific to wave-induced flows; therefore, the details of the wave forcing are introduced entirely through the boundary conditions. In this way the model provides a convenient platform to evaluate different combinations of applied boundary conditions. The model accommodates monochromatic or random wave fields and arbitrary bottom profiles, allowing the modeling of flows over bar-trough beach profiles or any other irregular profile geometry.

#### 8.1 Summary

The primary motivation for the present work derives from the efforts of Dyhr-Nielsen and Sørensen (1970) and Dally (1980) in studying the hydrodynamics associated with beach profile evolution. This prompted the desire to develop a hydrodynamic model that would accurately describe the nature and direction of flows and shear stresses in the surf zone. In particular, it was of interest to study the differences in these properties inside

and outside the break point to study the possible formation of longshore bars. The choice of the stream function formulation arose from the desire to attempt to clearly define the boundary conditions applied in the nearshore region and describe the complete flow field. The present model was also developed to couple the offshore flow to the onshore flow in a conservative fashion.

The governing equation of the model is the product of the cross-differentiation of the turbulent Reynolds Equations in the 2-DV plane. The cross-differentiation eliminates the pressure gradient terms from the equation, thus removing the need to describe these terms. The formulation applies a turbulent eddy viscosity representation of the turbulent (and wave-induced) shear stresses, and retains the spatial variability of the eddy viscosity in both directions. The mean velocity terms in the cross-differentiated equation are recast in terms of the stream function to produce one equation with one unknown. The governing equation is thus a fourth-order partial differential equation for  $\psi$  with respect to  $x$ ,  $z$ , and  $t$ . The governing equation is then written in a finite difference formulation for numerical solution.

Boundary conditions for the numerical model are determined by the wave transformation across the nearshore region. In the offshore region, Stream Function Wave Theory (Dean, 1974) describes the shoaling process and the variation in volumetric transport and wave radiation stress up to the break point. Upon breaking, the wave transformation model of Dally et al. (1985) is used to describe the wave breaking process and the possible reshoaling and rebreaking of waves in the surf zone. The resulting variation of volumetric transport and radiation stress is described by applying five different wave theories. All theories are applied in a manner that conserves momentum across the entire profile.

The model is compared to six experimental data sets of wave-induced return flow over a range of wave conditions and physical settings. These experiments are simulated with a broad range of combinations of boundary conditions and spatially variable turbulent eddy viscosity fields. The model is evaluated based on its ability to simulate measured vertical profiles of horizontal velocity from the six published studies. The range of simulations demonstrates the various aspects and difficulties of return flow modeling. These issues are investigated in terms of the predicted variation in velocity profiles, shear stress profiles, and the cross-shore variation in bottom shear stress. From these simulations, conclusions about the usefulness of the present formulation for return flow modeling are drawn.

## 8.2 Conclusions

The present numerical model is able to simulate the wave-induced return flow in the nearshore region over arbitrary beach profiles and under monochromatic and random wave fields. The model provides a convenient platform for evaluating different combinations of wave theories and boundary conditions. Based on comparisons of the model to existing data of wave induced return flows, the following conclusions are offered:

- 1) The use of the stream function,  $\psi$ , to simulate the wave-induced return flow provides the distinct advantage of yielding velocity descriptions in both the horizontal and vertical direction, thus presenting a clear description of the entire 2-DV flow field.
- 2) The nature of the governing equation provides a convenient platform for investigating the effect of various boundary conditions and turbulent eddy viscosity fields.
- 3) Simulation of various experiments reveals that the primary parameter in describing the vertical structure of the return flow in the nearshore region is the proper

prediction of the volumetric return flow rate. This rate is determined from the wave-induced mass/volumetric transport. The forward transport is assumed to be returned seaward through the domain of the model such that the combined transport at any vertical section is zero in order to conserve volume (mass). This rate is predicted from various wave theories and, as demonstrated herein, is reasonably well predicted in the offshore region and the inner surf zone, but is not always well predicted in the transition region between the two.

4) Simulation of published return flow experiments reveals that the model is able to predict the vertical structure to within 25 to 30% of the measured values. This predictive capability is strongly dependent on the predicted value of the volumetric transport (Item #3, above). Proper estimates of the transport can produce agreement of the simulations with the measurements of less than 10%. For data sets that include measurements very close to the bed, the addition of a vertically varying eddy viscosity field improves the predictive capability, to within 10 to 15%.

5) Simulation of various experiments indicates the importance of the proper description of the wave transformation across the profile in terms of conservation of momentum. This is demonstrated through inspection of the distribution of bottom shear stresses across the profile and the variation of the vertical profiles of velocity and shear stress, particularly in the vicinity of the break point. A lack of momentum conservation generally leads to large discontinuities in velocity and shear stress near the break point, which is hypothesized to create instabilities upon application of the model to a sediment transport module. Proper modeling of this feature and the treatment of the transition region are important considerations in predicting the flows just landward of the break point.

6) The use of the 2-D version of the model versus the 1-D version was found to have minimal effect on the predicted flow field. While the simpler and quicker 1-D model does not guarantee conservation of mass at any point between two vertical sections, the difficulty is limited due to the specification of the flow rate through each vertical section as a boundary condition. The application of a consistent and conservative wave transformation description (Item #5, above) was found to play a much stronger role in producing a smooth, coupled description of shear stress and velocity across the profile.

7) The application of a spatially variable turbulent eddy viscosity field was found to produce improved agreement with measured velocity profiles. In particular, the application of a vertically varying eddy viscosity,  $\epsilon$ , in the surf zone was found to better simulate those profiles that contain measurements near the bed. The vertical variation, in which  $\epsilon$  decreases significantly near the bottom, produces a better simulation of the bottom boundary layer, in which the velocity increases sharply just above the bed through the bottom boundary layer. The mathematics of a boundary layer are not incorporated in the model, thus the vertical variation in  $\epsilon$  allows the simulation of the boundary layer and improves agreement with measurements near the bed. Away from the bed, applying a distribution with a continually increasing eddy viscosity (such as a  $z^{3/2}$  dependence with  $\epsilon$  greatest at the surface ) or a simulation incorporating a zero shear stress bottom boundary condition were found to produce better agreement with data.

8) The existence of offshore directed surface shear stresses generated by shoaling waves is clearly indicated in the measurements of mean velocity seaward of the break point. The model is able to predict these stresses based on the gradient of radiation stress predicted by the wave transformation module. In some cases, however, the model predicts gradients in radiation stress that are oppositely directed (i.e., decreasing rather than

increasing) from what is expected in shoaling waves. In these instances the model predicts onshore directed surface shear stresses which produce velocity profiles that do not agree well with measurements. This difficulty may be the result of applying a wave theory seaward of the break point that does not consider the presence of the adverse return current and/or the unsteadiness in the rapidly shoaling waves.

9) The model demonstrates the possibility of onshore directed bottom stresses seaward of the breakpoint via the application of an offshore directed surface stress. A strong offshore surface stress can produce an onshore directed shear stress due to the need to conserve mass through the vertical section. This is the mechanism proposed by Dyhr-Nielsen and Sørensen (1970) that may contribute to the formation of longshore bars. This mechanism would act independently of the streaming velocity in the bottom boundary layer. The lack of sufficient measurements near the bed precludes the validation of this hypothesis, but the possibility of its existence is clearly seen in the simulations. The shape of the velocity profiles seaward of the break point suggests that this mechanism is possible.

### 8.3 Recommendations for Future Work

Several features of the present work merit further consideration and can easily be investigated or incorporated into the model for investigation. The model was initially developed from the biharmonic equation consistent with the work of Dally (1980). As such, some terms in the equations of motion were either neglected or grouped into the eddy viscosity representation. It is of interest to revisit the original development and study the effect of explicitly including some of these terms, such as the convective acceleration of the mean flow. This may provide more useful information about the flows in the transition region, where the present model does not provide as accurate a prediction.

In the random wave mode, the model assumes that the boundary conditions and flow rate adjust instantly to the next wave passage. This is obviously unrealistic, although the model does keep track of the history of the flow over the series of applied waves. The application of more smoothly time-dependent boundary conditions may produce information about the time dependence of the flow field at any vertical profile. This would be of interest in erosion/scour modeling during storm events.

The treatment of the turbulent eddy viscosity is an area where improvements may be made. The variation of the eddy viscosity field in the vertical direction is of particular importance. The vertical variation presently applied in the model is shown to reproduce the measurements of horizontal velocity quite well, especially in those data sets that include measurements close to the bed. Offshore, the vertical variation is likely not correctly modeled, since the waves are not breaking and generating turbulence in the same fashion. The horizontal variation in the value of  $\epsilon$  and its vertical variation is one area of further study that would certainly improve the predictive capability of the model.

Attempts were made to model the transition region by an ad hoc patching technique and by the application of a growing surface roller model (Dally and Brown, 1995). These attempts improved the predictive capability of the model while maintaining the conservation of wave integral properties, but neither was seen to simulate the flows in the transition region well, particularly in terms of the predicted volumetric flow rate. Further work in this area would no doubt improve the predictive capability of the model.

With regard to data collection, more information is needed about the variation of the return flow in the region seaward of the break point. In particular, measurements close to the bed (in combination with the entire water column) under a range of conditions would be useful in elucidating the mechanisms that can create onshore directed bottom flows.

## APPENDIX A NUMERICAL MODEL DEVELOPMENT

This appendix presents the discretization of the fourth-order partial differential equation (PDE) used in the present surf zone return flow model. The governing equation is derived from the Reynolds equations in Chapter 3. The discretization procedure for both the 1-D and 2-D descriptions is presented in this appendix. The mechanics of applying the various boundary conditions discussed in the main text are also detailed.

As discussed in the main text, the governing equation includes a time-dependent term and a completely general variable eddy viscosity field. Further complicating the development of the model is the need to simulate flows over profiles of arbitrary shape, including longshore bars. To accomplish this task, a simple grid-stretching technique is employed in which the vertical coordinate is non-dimensionalized by the local water depth (including set-up and set-down effects). This maps the irregular physical geometry into an orthogonal coordinate system in which the governing equation is solved. While the concept of the transformation is quite straightforward, the repeated applications of chain rule derivatives necessary to translate the fourth-order PDE from the physical to the model domain substantially lengthens the derivation.

Figure A.1 illustrates the coordinate frame chosen for the problem. Eq. (A.1) presents the governing partial differential equation, as derived in Chapter 3:

$$\begin{aligned}
 \psi_{ztt} + \psi_{xxt} &= \epsilon\psi_{xxxx} + 2\epsilon\psi_{xxzz} + \epsilon\psi_{zzzz} \\
 &+ 2\epsilon_x\psi_{xxx} + 2\epsilon_z\psi_{xxz} + 2\epsilon_x\psi_{xzz} + 2\epsilon_z\psi_{zzz} \\
 &+ (\epsilon_{xx} - \epsilon_{zz})\psi_{xx} + 4\epsilon_{xz}\psi_{xz} + (\epsilon_{zz} - \epsilon_{xx})\psi_{zz}
 \end{aligned} \tag{A.1}$$

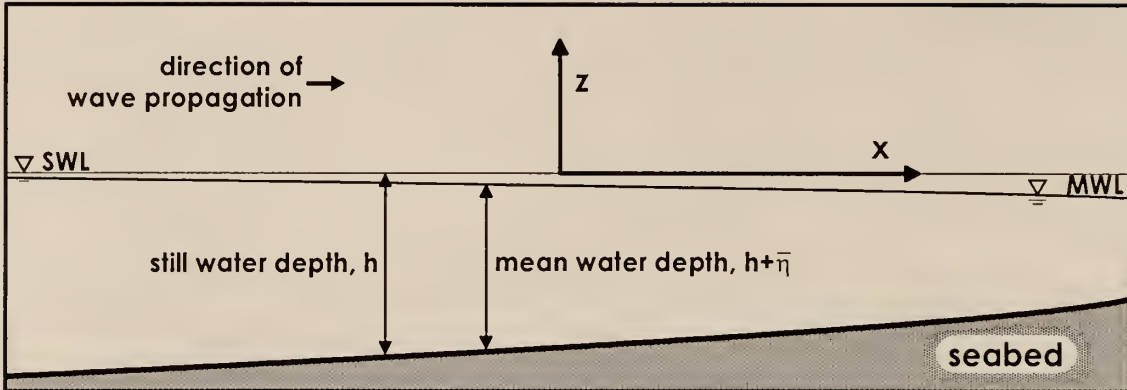


Figure A.1 Definition sketch for model development.

Eq. (A.1) is obtained by cross-differentiation of the Reynold equations for turbulent flow, after time-averaging the equations over a typical wave period. The remaining time dependent term represents the slow change in the return flow arising from changing wave conditions in the model. The Reynolds stress terms and wave normal and shear stresses are grouped together as apparent stresses governed by a turbulent eddy viscosity,  $\epsilon$ . The cross-differentiated equation is then recast in terms of the stream function to produce the final fourth-order PDE.

### A.1 Development of One-Dimensional Model

For a simple investigation of the vertical variation of the horizontal velocity in the return flow profile, Eq. (A.1) is simplified and solved numerically. The 1-D partial differential equation in  $z$  is:

$$\psi_{zzt} = \epsilon \psi_{zzzz} + 2\epsilon_z \psi_{zzz} + \epsilon_{zz} \psi_{zz} \quad (\text{A.2})$$

Eq. (A.2) is discretized using central difference approximations for the spatial gradients in the body of the model domain (to second order in  $\Delta z$ ). The time derivative is modeled as

a forward difference approximation, and is represented in a variable, semi-implicit fashion by the inclusion of the term  $\theta$ . The model domain is illustrated in Figure A.2. The fourth-order derivative in  $z$  yields five terms after discretization; upon collection of all  $\psi_j$  terms, the following finite difference equation results, involving five different points in the domain at two time steps:

$$\begin{aligned}
 & [\psi_{j-1} - 2\psi_j + \psi_{j+1}]^{n+1} = \\
 & \theta \frac{\Delta t}{(\Delta z)^2} [(\epsilon_j - \Delta z \epsilon_{z_j}) \psi_{j-2} + (-4\epsilon_j + 2\Delta z \epsilon_{z_j} + (\Delta z)^2 \epsilon_{zz_j}) \psi_{j-1} \\
 & + (6\epsilon_j - 2(\Delta z)^2 \epsilon_{zz_j}) \psi_j + (-4\epsilon_j - 2\Delta z \epsilon_{z_j} + (\Delta z)^2 \epsilon_{zz_j}) \psi_{j+1} + (\epsilon_j - \Delta z \epsilon_{z_j}) \psi_{j+2}]^{n+1} \\
 & + (1-\theta) \frac{\Delta t}{(\Delta z)^2} [(\epsilon_j - \Delta z \epsilon_{z_j}) \psi_{j-2} + (-4\epsilon_j + 2\Delta z \epsilon_{z_j} + (\Delta z)^2 \epsilon_{zz_j}) \psi_{j-1} \\
 & + (6\epsilon_j - 2(\Delta z)^2 \epsilon_{zz_j}) \psi_j + (-4\epsilon_j - 2\Delta z \epsilon_{z_j} + (\Delta z)^2 \epsilon_{zz_j}) \psi_{j+1} + (\epsilon_j - \Delta z \epsilon_{z_j}) \psi_{j+2}]^n \\
 & + [\psi_{j-1} - 2\psi_j + \psi_{j+1}]^n
 \end{aligned} \tag{A.3}$$

where  $n$  represents the time step in the model ( $n$  is the old time step,  $n+1$  is the new time step).

As discussed in the main text, the value of  $\theta$  can be modified to run the model in a fully implicit fashion ( $\theta=1$ ), a fully explicit fashion ( $\theta=0$ ), or any intermediate value. Setting  $\theta=0.5$  is equivalent to using the well-known scheme introduced by Crank and Nicholson (1947). The variable implicitness is included to relax the time step restrictions of the process modeled, which is similar to modeling the diffusion of vorticity. In a fully explicit scheme, the time step is limited by the following:

$$\Delta t = \frac{(\Delta z)^2}{2\epsilon} \tag{A.4}$$

which is quite restrictive, resulting in extremely long run times in a 2-D model. In the applications,  $\theta$  is set to 0.51, and the model is exercised at a range of time steps to assure consistency in the final answers. In the present case, the time step is dictated by the eddy viscosity, not the wave period. Given that, the time step is typically much less than a wave period (an order of magnitude or more).

### A.1.1 Boundary Conditions for One-Dimensional Model

Application of Eq. (A.3) requires the specification of four boundary conditions (Figure A.2). As with any numerical model, the selection and implementation of the proper boundary conditions represents a substantial fraction of the modeling task. Recent literature regarding return flow modeling is dominated by the discussion of the proper choice of boundary conditions, and the present model is no exception. The selection of boundary condition values is reserved for the main text (Chapter 4), while the mechanics associated with the application of said conditions is described herein.

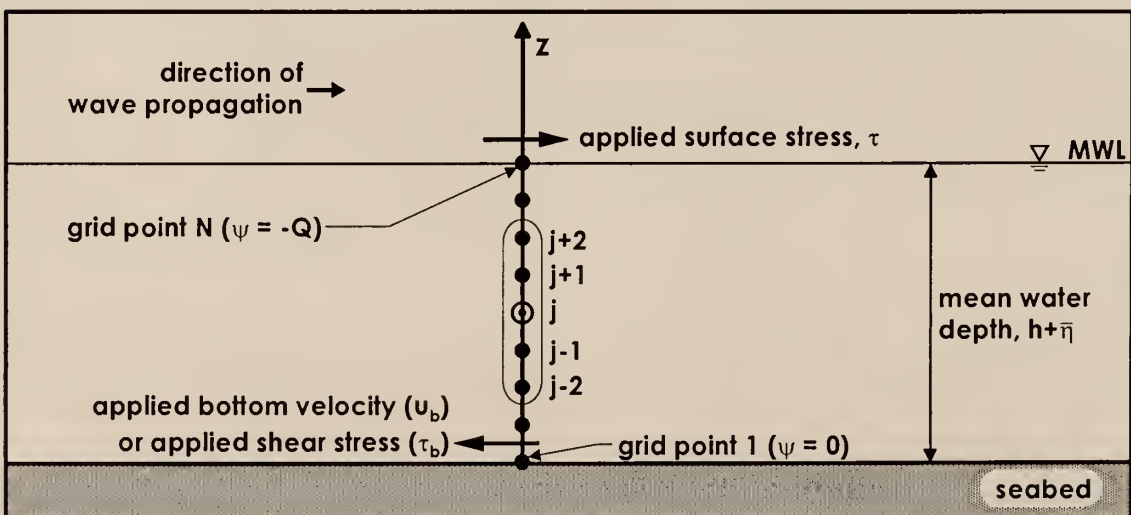


Figure A.2 Definition sketch for one-dimensional model. The figure illustrates the four applied boundary conditions and the 5-point solution cell.

The first two boundary conditions will be the specification of the value of  $\psi$  at the surface and at the bottom. The difference in these two values defines the flow rate through the 1-D model domain. At the bottom,  $\psi$  is set to zero, while  $\psi$  at the mean water surface is set equal to the negative value of the volumetric transport,  $Q$ , through the section.

The time dependency written into the model allows for simple modeling of irregular wave fields. This is accomplished by employing a random number generator that selects wave heights from a cumulative distribution function of wave height. The chosen wave height is then used to determine the boundary conditions that will be applied for the duration of that wave. The period of each wave is taken to be the modal frequency of the modeled spectrum. The wave heights are generally assumed to be Rayleigh distributed. In the case of monochromatic waves, the model can simply be set to repeat the same boundary conditions until the results produced do not change with time.

The third boundary condition to be specified is the mean surface shear stress caused by the passage of the waves. This stress, while actually a force distributed between the trough to crest region of the waves, is modeled as a concentrated stress acting at the mean water level, as described by Dally, 1980 and others. While the surface stress generally results from gradients in the  $x$ -direction, its effect on the one-dimensional model in the  $z$ -direction is included as a second-derivative boundary condition in  $\psi$ :

$$\tau_s = \rho\epsilon \frac{\partial u}{\partial z} = -\rho\epsilon \frac{\partial^2 \psi}{\partial z^2} \quad (\text{A.5})$$

which when discretized becomes:

$$\psi_{N+1} = -\psi_{N-1} + 2\psi_N - \frac{\tau_s}{\rho\epsilon}(\Delta z)^2 \quad (\text{A.6})$$

The fourth boundary condition specifies either the tangential bottom velocity or the tangential bottom stress. The modeled PDE does not expressly consider the presence of a bottom boundary layer, induced by the oscillatory motion of the waves and/or by the return flow. Given that fact, it may be desirable to specify the bottom velocity as either zero or that velocity corresponding to the boundary layer edge velocity. For generality in the model, the 1-D model bottom velocity boundary condition is specified as follows:

$$U_b = -(\Psi_z)_b \quad (\text{A.7})$$

which is discretized and solved for the virtual grid point one row beyond the bottom (see Figure A.2). Taking the bottom as the origin (grid point  $j = 1$ ) with the surface elevation (grid point  $j = N$ ) at  $z = (h + \bar{\eta})$ , the virtual grid point ( $j \sim 0$ ) is solved for:

$$\Psi_0 = 2\Delta z U_b + \Psi_2 \quad (\text{A.8})$$

where  $\Psi_2$  represents the  $j = 2$  grid point in the model domain (Figure A.2).

To specify a bottom shear stress condition, the development given in Eqs. (A.5) and (A.6) is applied at the bottom, and the virtual grid point one row below the bottom is found:

$$\Psi_0 = 2\Psi_1 - \Psi_2 - m \frac{\tau_s}{\rho \epsilon_b} (\Delta z)^2 \quad (\text{A.9})$$

In Eq. (A.9), the bottom shear stress has been defined as a fraction,  $m$ , of the surface shear stress following the work of Reid (1957), and the generality of a varying eddy viscosity in the numerical model has been respected. For the case of surface stress along a bounded channel, similar to the present 2-D beach profile situation, the quantity  $m$  is generally negative, indicating the bottom stress is directed opposite to the surface stress, as might be

expected inside the surf zone for the mean flow. Specification of the value of  $m$  inside and outside the surf zone is discussed in the main text along with the selection of appropriate values for the other boundary conditions.

The initial condition for the model is generally taken as a quiescent condition ( $\psi = 0$  in the body of the fluid). This essential creates a “cold start” requiring some period of spin-up time to achieve consistent dynamic conditions. Conversely, some initial estimate of the stream function profile could be used to “hot start” the model and minimize the spin-up time required. This profile could be the product of a previous model run or simply an estimate of the desired output profile (a linear profile, for example).

### A.1.2 Solution Scheme for One-Dimensional Model

The stream function values across the model domain at the  $n+1$  time step are solved for simultaneously after creating a 5-band diagonal matrix of  $N-2$  equations using Eq. (A.2). The matrix and vectors are of size  $N-2$  because the values of  $\psi$  at the surface and bottom are given by the boundary conditions. The boundary conditions described in the previous section are input directly to the matrices and vectors. The program to model the 1-D return flow distribution employs two subroutines from the Numerical Recipes suite of routines (Press et al. 1986). The first routine (BANDEC) performs a lower-upper (LU) decomposition on the matrix. These matrices are then sent to the second subroutine (BANBKS) which performs a back substitution operation to solve for the vector of  $\psi$  values. In the 1-D model, only one performance of each routine is required at each time step.

The solved values of the stream function at each point are averaged over many waves to produce the final mean stream function profile. Intermediate values of the

solutions are stored in order to observe the time scales at which the profile evolves due to changes in the input wave parameters. The computer program proceeds to process the values of stream function to produce as output a list of the horizontal velocity and the shear stress, both as the mean value and at any desired intermediate time steps. The computer program containing the 1-D and 2-D codes is provided in Appendix B.

## A.2 Development of Two-Dimensional Return Flow Model

Building on the one-dimensional model, Eq. (A.1) is revisited and applied in the 2-DV nearshore region. The same general boundary conditions used in the 1-D model apply to the 2-D model, with the addition of four more boundary conditions in the horizontal direction, i.e. sidewall boundary conditions. Since Eq. (A.1) is written for the orthogonal coordinate system, a coordinate stretching scheme is implemented to allow for modeling of arbitrary beach profiles. This coordinate stretching simply non-dimensionalizes the vertical coordinate, but lengthens the derivation substantially. For completeness, the coordinate transformation and equation discretization are included in this appendix.

### A.2.1 Transformation of the Partial Differential Equation

Figure A.3 depicts the procedure used to transform the physical geometry of the nearshore region into a rectangular, orthogonal computational domain. Following Hoffman (1989) the vertical coordinate is non-dimensionalized by the local water depth (Eq. (A.10)). This grid-stretching technique allows for the modeling of any beach profile (Figure A.3). As opposed to the 1-D case, the 2-D case will take as the vertical origin the Still Water Level to maintain a horizontal datum since set-up and set-down effects will be included; grid point #1 corresponds to the surface and grid point  $N_y$  applies to the seabed.

$$\eta = -z/h \quad (\text{A.10})$$

Transformation of Eq. (A.1) from the  $x$ - $z$  domain to the  $\xi$ - $\eta$  domain simply involves repeated applications of the chain rule for derivatives, as demonstrated below:

$$\frac{\partial \Psi}{\partial z} = \frac{\partial \xi}{\partial z} \frac{\partial \Psi}{\partial \xi} + \frac{\partial \eta}{\partial z} \frac{\partial \Psi}{\partial \eta} \quad (\text{A.11})$$

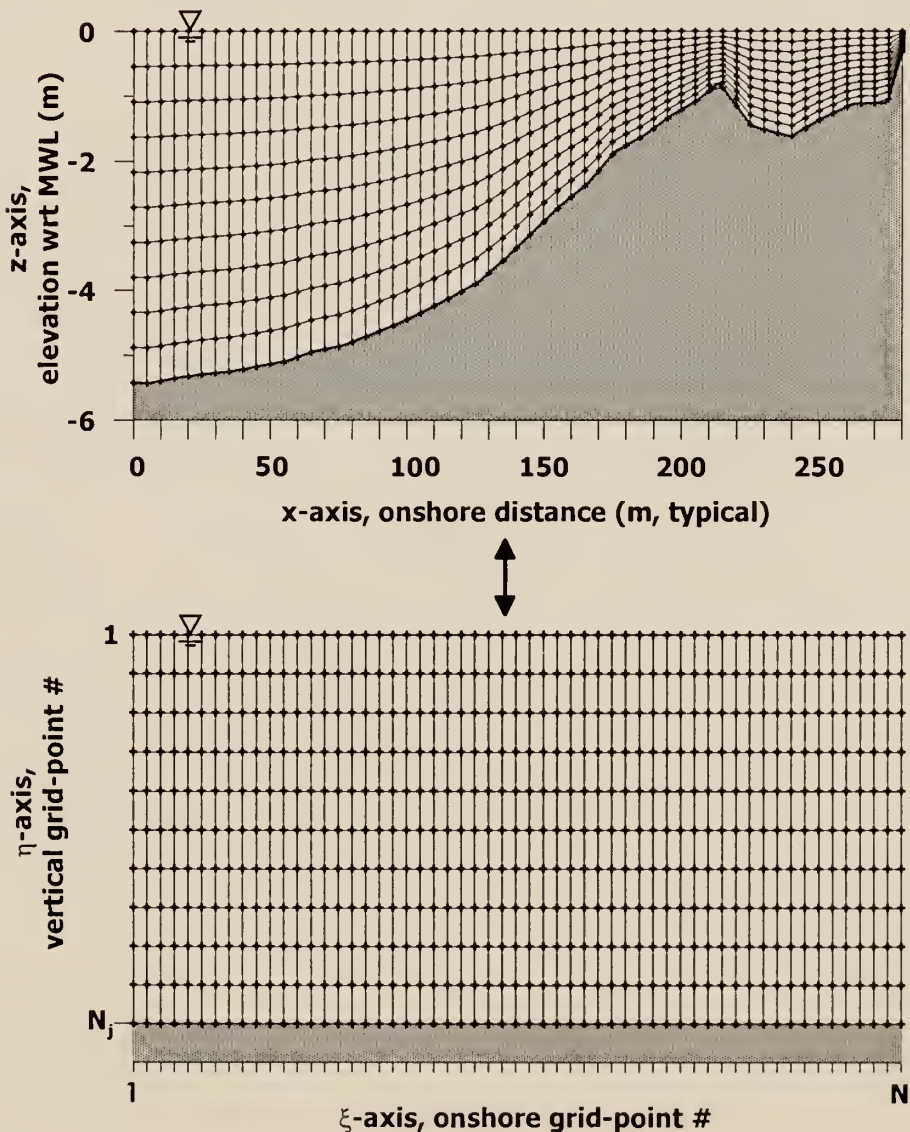


Figure A.3 Definition sketch of coordinate transformation between the physical,  $x$ - $z$ , domain and the computational,  $\xi$ - $\eta$  domain.

The approach in this derivation will be to separate the time dependent terms from the terms that comprise the steady state solution in order to maintain the appearance of the steady state solution in each case modeled. This produces several more terms and coefficients but makes the operation of the model much clearer. Each term in  $\psi$  in Eq. (A.1) is expanded; including the eddy viscosity terms. The transformation and subsequent collection of common terms produces many additional derivatives of  $\psi$  due to the coordinate transformation required. The transformed PDE is:

$$\begin{aligned} [B1\psi_{\xi\xi} + B2\psi_{\xi\eta} + B3\psi_{\eta\eta} + B4\psi_\xi + B5\psi_\eta]_t &= \\ A1\psi_{\xi\xi\xi\xi} + A2\psi_{\xi\xi\xi\eta} + A3\psi_{\xi\xi\eta\eta} + A4\psi_{\xi\eta\eta\eta} + A5\psi_{\eta\eta\eta\eta} \\ + A6\psi_{\xi\xi\xi\xi} + A7\psi_{\xi\xi\eta\eta} + A8\psi_{\xi\eta\eta\eta} + A9\psi_{\eta\eta\eta\eta} \\ + A10\psi_{\xi\xi\xi\xi} + A11\psi_{\xi\xi\eta\eta} + A12\psi_{\eta\eta\eta\eta} + A13\psi_\xi + A14\psi_\eta \end{aligned} \quad (\text{A.12})$$

where the left hand side represents the time dependent terms and the right hand side represents the steady state solution. Each coefficient is defined as follows:

$$A1 = [\epsilon(\xi_x^4 + 2\xi_x^2\xi_z^2 + \xi_z^4)] \quad (\text{A.13})$$

$$A2 = [\epsilon(4\xi_x^3\eta_x + 4\xi_x^2\xi_z\eta_z + 4\xi_x\xi_z^2\eta_x + 4\xi_z^3\eta_z)] \quad (\text{A.14})$$

$$A3 = [\epsilon(6\xi_x^2\eta_x^2 + 2\xi_x^2\eta_z^2 + 8\xi_x\xi_z\eta_x\eta_z + 2\xi_z^2\eta_x^2 + 6\xi_z^2\eta_z^2)] \quad (\text{A.15})$$

$$A4 = [\epsilon(4\xi_x\eta_x^3 + 4\xi_z\eta_x^2\eta_z + 4\xi_x\eta_x\eta_z^2 + 4\xi_z\eta_z^3)] \quad (\text{A.16})$$

$$A5 = [\epsilon(\eta_x^4 + 2\eta_x^2\eta_z^2 + \eta_z^4)] \quad (\text{A.17})$$

$$A6 = [ \epsilon(6\xi_x^2\xi_{xx} + 2\xi_x^2\xi_{zz} + 8\xi_x\xi_z\xi_{xz} + 2\xi_{xx}\xi_z^2 + 6\xi_z^2\xi_{zz}) + \epsilon_x(2\xi_x^3 + 2\xi_x\xi_z^2) + \epsilon_z(2\xi_x^2\xi_z + 2\xi_z^3) ] \quad (A.18)$$

$$A7 = [ \epsilon(12\xi_x\xi_{xx}\eta_x + 6\xi_x^2\eta_{xx} + 2\xi_x^2\eta_{zz} + 4\xi_{xx}\xi_z\eta_z + 8\xi_x\xi_{xz}\eta_z + 8\xi_{xz}\xi_z\eta_x + 8\xi_x\xi_z\eta_{xz} + 4\xi_x\xi_{zz}\eta_x + 2\xi_z^2\eta_{xx} + 6\xi_z^2\eta_{zz} + 12\xi_z\xi_{zz}\eta_z) + \epsilon_x(6\xi_x^2\eta_x + 2\xi_z^2\eta_x + 4\xi_x\xi_z\eta_z) + \epsilon_z(4\xi_x\xi_z\eta_x + 2\xi_x^2\eta_z + 6\xi_z^2\eta_z) ] \quad (A.19)$$

$$A8 = [ \epsilon(12\xi_x\eta_x\eta_{xx} + 6\xi_{xx}\eta_x^2 + 2\xi_{xx}\eta_z^2 + 4\xi_x\eta_x\eta_{zz} + 8\xi_x\eta_z\eta_{xz} + 8\xi_{xz}\eta_x\eta_z + 8\xi_z\eta_x\eta_{xz} + 4\xi_z\eta_{xx}\eta_z + 2\xi_{zz}\eta_x^2 + 6\xi_{zz}\eta_z^2 + 12\xi_z\eta_z\eta_{zz}) + \epsilon_x(6\xi_x\eta_x^2 + 2\xi_x\eta_z^2 + 4\xi_z\eta_x\eta_z) + \epsilon_z(4\xi_x\eta_x\eta_z + 2\xi_z\eta_x^2 + 6\xi_z\eta_z^2) ] \quad (A.20)$$

$$A9 = [ \epsilon(6\eta_x^2\eta_{xx} + 2\eta_x^2\eta_{zz} + 8\eta_x\eta_z\eta_{xz} + 2\eta_{xx}\eta_z^2 + 6\eta_z^2\eta_{zz}) + \epsilon_x(2\eta_x^3 + 2\eta_x\eta_z^2) + \epsilon_z(2\eta_x^2\eta_z + 2\eta_z^3) ] \quad (A.21)$$

$$A10 = [ \epsilon(3\xi_{xx}^2 + 4\xi_x\xi_{xxx} + 2\xi_{xx}\xi_{zz} + 4\xi_{xxx}\xi_z + 4\xi_{xz}^2 + 4\xi_x\xi_{xzz} + 4\xi_z\xi_{zzz} + 3\xi_{zz}^2) + \epsilon_x(6\xi_x\xi_{xx} + 2\xi_x\xi_{zz} + 4\xi_{xz}\xi_z) + \epsilon_z(4\xi_x\xi_{xz} + 2\xi_{xx}\xi_z + 6\xi_z\xi_{zz}) + \epsilon_{xx}(\xi_x^2 - \xi_z^2) + \epsilon_{xz}(4\xi_x\xi_z) + \epsilon_{zz}(\xi_z^2 - \xi_x^2) ] \quad (A.22)$$

$$A11 = [ \epsilon(4\xi_{xxx}\eta_x + 6\xi_{xx}\eta_{xx} + 4\xi_x\eta_{xxx} + 2\xi_{xx}\eta_{zz} + 4\xi_x\eta_{xzz} + 4\xi_{xxz}\eta_z + 8\xi_{xz}\eta_{xz} + 4\xi_{xzz}\eta_x + 4\xi_z\eta_{xxz} + 2\xi_{zz}\eta_{xx} + 4\xi_{zzz}\eta_z + 6\xi_{zz}\eta_{zz} + 4\xi_z\eta_{zzz}) + \epsilon_x(6\xi_x\eta_{xx} + 6\xi_{xx}\eta_x + 2\xi_x\eta_{zz} + 4\xi_{xz}\eta_z + 4\xi_z\eta_{xz} + 2\xi_{zz}\eta_x) + \epsilon_z(2\xi_{xx}\eta_z + 4\xi_x\eta_{xz} + 4\xi_{xz}\eta_x + 2\xi_z\eta_{xx} + 6\xi_z\eta_{zz} + 6\xi_{zz}\eta_z) + \epsilon_{xx}(2\xi_x\eta_x - 2\xi_z\eta_z) + \epsilon_{xz}(4\xi_x\eta_z + 4\xi_z\eta_x) + \epsilon_{zz}(2\xi_z\eta_z - \xi_x\eta_x) ] \quad (A.23)$$

$$A12 = [ \epsilon(3\eta_{xx}^2 + 4\eta_x\eta_{xxx} + 2\eta_{xx}\eta_{zz} + 4\eta_{xxx}\eta_z + 4\eta_{xz}^2 + 4\eta_x\eta_{xzz} + 4\eta_z\eta_{zzz} + 3\eta_{zz}^2) + \epsilon_x(6\eta_x\eta_{xx} + 2\eta_x\eta_{zz} + 4\eta_{xz}\eta_z) + \epsilon_z(4\eta_x\eta_{xz} + 2\eta_{xx}\eta_z + 6\eta_z\eta_{zz}) + \epsilon_{xx}(\eta_x^2 - \eta_z^2) + \epsilon_{xz}(4\eta_x\eta_z) + \epsilon_{zz}(\eta_z^2 - \eta_x^2) ] \quad (A.24)$$

$$A13 = [ \epsilon(\xi_{xxxx} + 2\xi_{xxxx} + \xi_{zzzz}) + \epsilon_x(2\xi_{xxx} + 2\xi_{zzz}) + \epsilon_z(2\xi_{xxz} + 2\xi_{zzz}) \\ + \epsilon_{xx}(\xi_{xx} - \xi_{zz}) + \epsilon_{xz}(4\xi_{xz}) + \epsilon_{zz}(\xi_{zz} - \xi_{xx}) ] \quad (A.25)$$

$$A14 = [ \epsilon(\eta_{xxxx} + 2\eta_{xxxx} + \eta_{zzzz}) + \epsilon_x(2\eta_{xxx} + 2\eta_{zzz}) + \epsilon_z(2\eta_{xxz} + 2\eta_{zzz}) \\ + \epsilon_{xx}(\eta_{xx} - \eta_{zz}) + \epsilon_{xz}(4\eta_{xz}) + \epsilon_{zz}(\eta_{zz} - \eta_{xx}) ] \quad (A.26)$$

$$B1 = [ \xi_x^2 + \xi_z^2 ] \quad (A.27)$$

$$B2 = [ 2(\xi_x\eta_x + \xi_z\eta_z) ] \quad (A.28)$$

$$B3 = [ \eta_x^2 + \eta_z^2 ] \quad (A.29)$$

$$B4 = [ \xi_{xx} + \xi_{zz} ] \quad (A.30)$$

$$B5 = [ \eta_{xx} + \eta_{zz} ] \quad (A.31)$$

The values of  $\epsilon_x$ ,  $\epsilon_z$ ,  $\epsilon_{xx}$ ,  $\epsilon_{zz}$ , and  $\epsilon_{xz}$  also must be expanded to account for the coordinate transformation. Eqs. (A.32) through (A.36) present the corresponding expansions of the spatial derivatives of the eddy viscosity.

$$\epsilon_x = \xi_x\epsilon_\xi + \eta_x\epsilon_\eta \quad (A.32)$$

$$\epsilon_z = \xi_z\epsilon_\xi + \eta_z\epsilon_\eta \quad (A.33)$$

$$\epsilon_{xx} = \xi_x^2\epsilon_{\xi\xi} + 2\xi_x\eta_x\epsilon_{\xi\eta} + \eta_x^2\epsilon_{\eta\eta} + \xi_{xx}\epsilon_\xi + \eta_{xx}\epsilon_\eta \quad (A.34)$$

$$\epsilon_{zz} = \xi_z^2 \epsilon_{\xi\xi} + 2\xi_z \eta_z \epsilon_{\xi\eta} + \eta_z^2 \epsilon_{\eta\eta} + \xi_{zz} \epsilon_\xi + \eta_{zz} \epsilon_\eta \quad (\text{A.35})$$

$$\epsilon_{xx} = \xi_x \xi_z \epsilon_{\xi\xi} + (\xi_x \eta_z + \xi_z \eta_x) \epsilon_{\xi\eta} + \eta_x \eta_z \epsilon_{\eta\eta} + \xi_{xz} \epsilon_\xi + \eta_{xz} \epsilon_\eta \quad (\text{A.36})$$

### A.2.2 Discretization of the Two-Dimensional PDE

Eq. (A.12) is now discretized for the numerical solution of  $\psi$  on the interior points of the grid (recall that the values of the stream function along the edges are specified as boundary conditions, as in the 1-D model). Figure A.4 compares the discretized solution cell for the  $x$ - $z$  domain versus the solution cell for the transformed  $\xi$ - $\eta$  domain. The transformation process adds an additional eight points to the finite-difference equation.

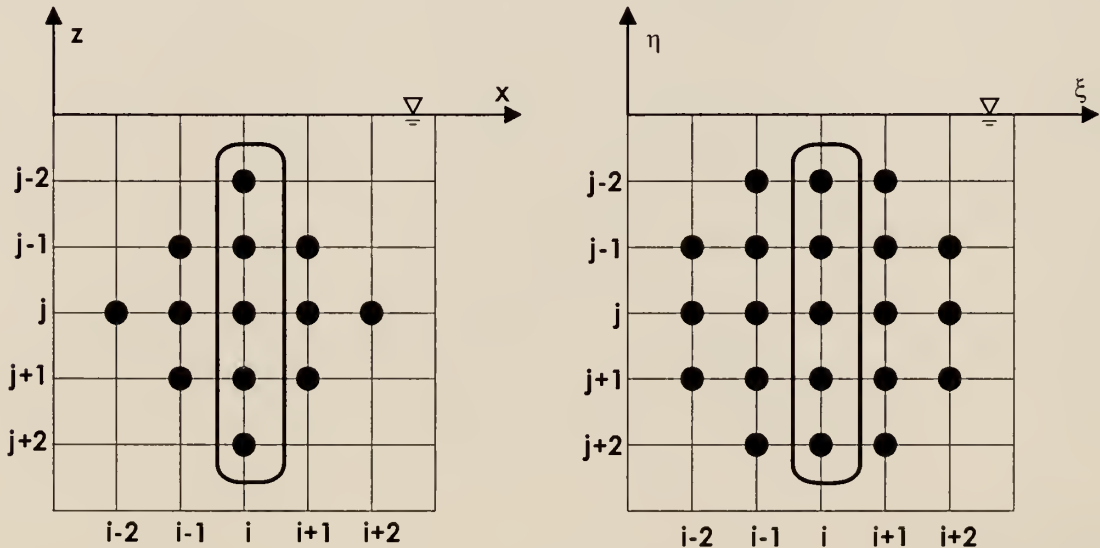


Figure A.4 Solution cells for the fourth-order finite difference equation in the  $x$ - $z$  domain and the transformed  $\xi$ - $\eta$  domain. The five circled points on column  $i$  represent the points solved for in the set of simultaneous equations. Note that row  $j=1$  corresponds to the surface row.

Eq. (A.12) is discretized using central difference spatial approximations of  $\psi$  with a forward difference approximation in time. As in the 1-D model, the equation includes a variable degree of implicitness in the solution, represented by the value of  $\theta$ . Again, efforts are made to separate those terms arising from the time derivative from those arising from the spatial derivatives. In a schematic way, the equation is discretized as follows:

$$[\text{time dep. terms}]^{n+1} - [\text{time dep. terms}]^n = \theta \Delta t [\text{s.s. solution terms}]^{n+1} + (1-\theta) \Delta t [\text{s.s. solution terms}]^n \quad (\text{A.37})$$

In Eq. (A.37) the time dependent terms on the left hand side are the discretized forms of the left hand side of Eq. (A.12), while the steady state (s.s.) solution terms are the discretized forms of the right hand side of Eq. (A.12). Written in full, the discretized equation is:

$$\begin{aligned} & [ DR1\psi_{j-1, i-1} + DR2\psi_{j, i-1} + DR3\psi_{j+1, i-1} \\ & \quad + DL1\psi_{j-1, i} + DL2\psi_{j, i} + DL3\psi_{j+1, i} \\ & \quad + DR4\psi_{j-1, i+1} + DR5\psi_{j, i+1} + DR6\psi_{j+1, i+1} ]^{n+1} \\ & - [ DR1\psi_{j-1, i-1} + DR2\psi_{j, i-1} + DR3\psi_{j+1, i-1} \\ & \quad + DL1\psi_{j-1, i} + DL2\psi_{j, i} + DL3\psi_{j+1, i} \\ & \quad + DR4\psi_{j-1, i+1} + DR5\psi_{j, i+1} + DR6\psi_{j+1, i+1} ]^n \\ & = \theta \Delta t [ CR1\psi_{j-1, i-2} + CR2\psi_{j, i-2} + CR3\psi_{j+1, i-2} \\ & \quad + CR4\psi_{j-2, i-1} + CR5\psi_{j-1, i-1} + CR6\psi_{j, i-1} + CR7\psi_{j+1, i-1} + CR8\psi_{j+2, i-1} \quad (\text{A.38}) \\ & \quad + CL1\psi_{j-2, i} + CL2\psi_{j-1, i} + CL3\psi_{j, i} + CL1\psi_{j+1, i} + CL5\psi_{j+2, i} \\ & \quad + CR9\psi_{j-2, i+1} + CR10\psi_{j-1, i+1} + CR11\psi_{j, i+1} + CR12\psi_{j+1, i+1} + CR13\psi_{j+2, i+1} \\ & \quad + CR14\psi_{j-1, i+2} + CR15\psi_{j, i+2} + CR16\psi_{j+1, i+2} ]^{n+1} \\ & \quad + (1-\theta) \Delta t [ CRI\psi_{j-1, i-2} + CR2\psi_{j, i-2} + CR3\psi_{j+1, i-2} \\ & \quad + CR4\psi_{j-2, i-1} + CR5\psi_{j-1, i-1} + CR6\psi_{j, i-1} + CR7\psi_{j+1, i-1} + CR8\psi_{j+2, i-1} \\ & \quad + CL1\psi_{j-2, i} + CL2\psi_{j-1, i} + CL3\psi_{j, i} + CL1\psi_{j+1, i} + CL5\psi_{j+2, i} \\ & \quad + CR9\psi_{j-2, i+1} + CR10\psi_{j-1, i+1} + CR11\psi_{j, i+1} + CR12\psi_{j+1, i+1} + CR13\psi_{j+2, i+1} \\ & \quad + CR14\psi_{j-1, i+2} + CR15\psi_{j, i+2} + CR16\psi_{j+1, i+2} ]^n \end{aligned}$$

As written, Eq. (A.38) would produce 21 points to solve for on the left hand side at the  $n+1$  time step, as opposed to the previous 5 points. This presents a problem in establishing a spatially consistent array of coefficients to solve for simultaneously. This problem is relieved by moving any points that do not reside on the  $i^{th}$  column to the right hand side and solving the system of equations iteratively at each time step. More details on the method of solution will be provided. To preface the following definitions of the coefficients in Eq. (A.38), it is noted that points on the  $i^{th}$  column in Eq. (A.38) are given coefficient labels  $CL1$  through  $CL5$  and  $DL1$  through  $DL3$  to indicate the points that may be solved for in the system of simultaneous equations (for the reason described above the labels use  $L$  for “*left-hand side*” points in the matrix equation of form  $Ax=B$ , where  $A$  is a square coefficient matrix of size  $N-2 \times N-2$ , and  $x$  and  $B$  are column vectors of dimensions  $N-2$ ). To clarify which coefficients apply to which points in the solution cell, Figure A.5 illustrates the various coefficient assignments. The equations that follow represent the 30 coefficients contained in Eq. (A.38) for the 21 points in the solution cell.

$$CL1 = [ A5 - A9 \frac{\Delta\eta}{2} ] \quad (A.39)$$

$$CL2 = [-4A5 - 2A3 \frac{(\Delta\eta)^2}{(\Delta\xi)^2} + A7 \frac{(\Delta\eta)^3}{(\Delta\xi)^2} + A9\Delta\eta + A12(\Delta\eta)^2 - A14 \frac{(\Delta\eta)^3}{2}] \quad (A.40)$$

$$CL3 = [ 6A1 \frac{(\Delta\eta)^4}{(\Delta\xi)^4} + 4A3 \frac{(\Delta\eta)^2}{(\Delta\xi)^2} + 6A5 - 2A10 \frac{(\Delta\eta)^4}{(\Delta\xi)^2} - 2A12(\Delta\eta)^2 ] \quad (A.41)$$

$$CL4 = [-4A5 - 2A3 \frac{(\Delta\eta)^2}{(\Delta\xi)^2} - A7 \frac{(\Delta\eta)^3}{(\Delta\xi)^2} - A9\Delta\eta + A12(\Delta\eta)^2 + A14 \frac{(\Delta\eta)^3}{2}] \quad (A.42)$$

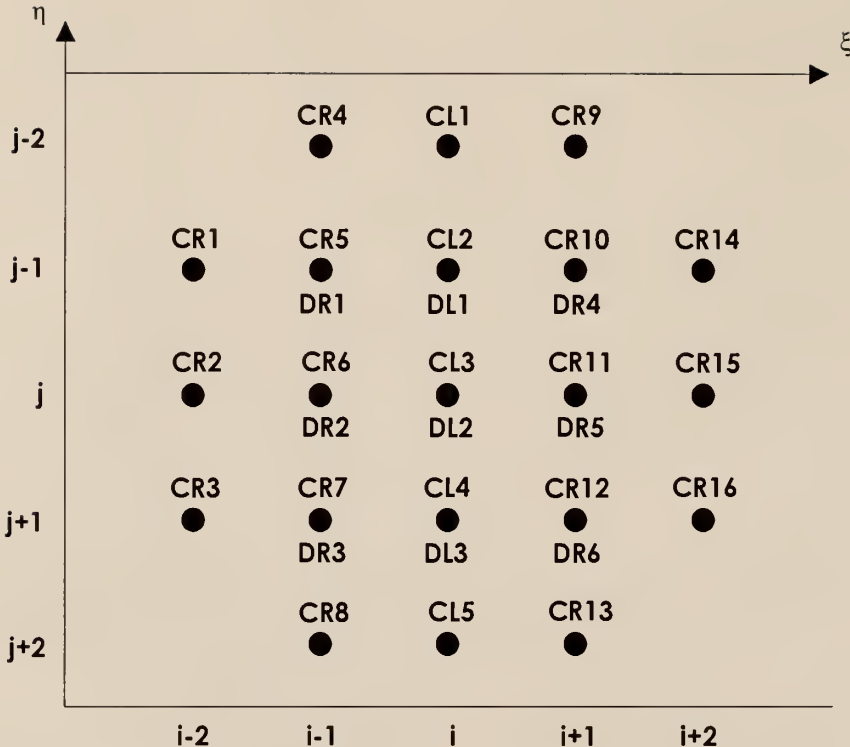


Figure A.5 Assignment of coefficient labels for each point in the solution cell. Note that points along the  $i^{\text{th}}$  row contain the letter  $L$ , while points off the  $i^{\text{th}}$  row are labeled with the letter  $R$ . Coefficients with  $C$  originate from the steady state solution terms, while coefficients with the letter  $D$  originate from the time dependent terms in the PDE.

$$CL5 = [ A5 + A9 \frac{\Delta\eta}{2} ] \quad (\text{A.43})$$

$$CR1 = [ A2 \frac{(\Delta\eta)^3}{4(\Delta\xi)^3} ] \quad (\text{A.44})$$

$$CR2 = [ A1 \frac{(\Delta\eta)^4}{(\Delta\xi)^4} - A6 \frac{(\Delta\eta)^4}{2(\Delta\xi)^3} ] \quad (\text{A.45})$$

$$CR3 = [ -A2 \frac{(\Delta\eta)^3}{4(\Delta\xi)^3} ] \quad (\text{A.46})$$

$$CR4 = [ A4 \frac{\Delta\eta}{4\Delta\xi} ] \quad (\text{A.47})$$

$$\begin{aligned}
CR5 = & [ -A2 \frac{(\Delta\eta)^3}{2(\Delta\xi)^3} + A3 \frac{(\Delta\eta)^2}{(\Delta\xi)^2} - A4 \frac{\Delta\eta}{2\Delta\xi} \\
& - A7 \frac{(\Delta\eta)^3}{2(\Delta\xi)^2} - A8 \frac{(\Delta\eta)^2}{2\Delta\xi} + A11 \frac{(\Delta\eta)^3}{4\Delta\xi} ]
\end{aligned} \tag{A.48}$$

$$\begin{aligned}
CR6 = & [ -4A1 \frac{(\Delta\eta)^4}{(\Delta\xi)^4} - 2A3 \frac{(\Delta\eta)^2}{(\Delta\xi)^2} + A6 \frac{(\Delta\eta)^4}{(\Delta\xi)^3} \\
& + A8 \frac{(\Delta\eta)^2}{\Delta\xi} + A10 \frac{(\Delta\eta)^4}{(\Delta\xi)^2} - A13 \frac{(\Delta\eta)^4}{2\Delta\xi} ]
\end{aligned} \tag{A.49}$$

$$\begin{aligned}
CR7 = & [ A2 \frac{(\Delta\eta)^3}{2(\Delta\xi)^3} + A3 \frac{(\Delta\eta)^2}{(\Delta\xi)^2} + A4 \frac{\Delta\eta}{2\Delta\xi} \\
& + A7 \frac{(\Delta\eta)^3}{2(\Delta\xi)^2} - A8 \frac{(\Delta\eta)^2}{2\Delta\xi} - A11 \frac{(\Delta\eta)^3}{4\Delta\xi} ]
\end{aligned} \tag{A.50}$$

$$CR8 = [ -A4 \frac{\Delta\eta}{4\Delta\xi} ] \tag{A.51}$$

$$CR9 = [ -A4 \frac{\Delta\eta}{4\Delta\xi} ] \tag{A.52}$$

$$\begin{aligned}
CR10 = & [ A2 \frac{(\Delta\eta)^3}{2(\Delta\xi)^3} + A3 \frac{(\Delta\eta)^2}{(\Delta\xi)^2} + A4 \frac{\Delta\eta}{2\Delta\xi} \\
& - A7 \frac{(\Delta\eta)^3}{2(\Delta\xi)^2} + A8 \frac{(\Delta\eta)^2}{2\Delta\xi} - A11 \frac{(\Delta\eta)^3}{4\Delta\xi} ]
\end{aligned} \tag{A.53}$$

$$\begin{aligned}
CR11 = & [ -4A1 \frac{(\Delta\eta)^4}{(\Delta\xi)^4} - 2A3 \frac{(\Delta\eta)^2}{(\Delta\xi)^2} - A6 \frac{(\Delta\eta)^4}{(\Delta\xi)^3} \\
& - A8 \frac{(\Delta\eta)^2}{\Delta\xi} + A10 \frac{(\Delta\eta)^4}{(\Delta\xi)^2} + A13 \frac{(\Delta\eta)^4}{2\Delta\xi} ]
\end{aligned} \tag{A.54}$$

$$\begin{aligned} CR12 = & [ -A2 \frac{(\Delta\eta)^3}{2(\Delta\xi)^3} + A3 \frac{(\Delta\eta)^2}{(\Delta\xi)^2} - A4 \frac{\Delta\eta}{2\Delta\xi} \\ & + A7 \frac{(\Delta\eta)^3}{2(\Delta\xi)^2} + A8 \frac{(\Delta\eta)^2}{2\Delta\xi} + A11 \frac{(\Delta\eta)^3}{4\Delta\xi} ] \end{aligned} \quad (A.55)$$

$$CR13 = [ A4 \frac{\Delta\eta}{4\Delta\xi} ] \quad (A.56)$$

$$CR14 = [ -A2 \frac{(\Delta\eta)^3}{4(\Delta\xi)^3} ] \quad (A.57)$$

$$CR15 = [ A1 \frac{(\Delta\eta)^4}{(\Delta\xi)^4} + A6 \frac{(\Delta\eta)^4}{2(\Delta\xi)^3} ] \quad (A.58)$$

$$CR16 = [ A2 \frac{(\Delta\eta)^3}{4(\Delta\xi)^3} ] \quad (A.59)$$

$$DL1 = [ B3(\Delta\eta)^2 - B5 \frac{(\Delta\eta)^3}{2} ] \quad (A.60)$$

$$DL2 = [ BI \frac{(\Delta\eta)^4}{(\Delta\xi)^2} - B4 \frac{(\Delta\eta)^4}{2\Delta\xi} ] \quad (A.61)$$

$$DL3 = [ B3(\Delta\eta)^2 + B5 \frac{(\Delta\eta)^3}{2} ] \quad (A.62)$$

$$DRI = B2 \frac{(\Delta\eta)^3}{4\Delta\xi} \quad (A.63)$$

$$DR2 = [ BI \frac{(\Delta\eta)^4}{(\Delta\xi)^2} - B4 \frac{(\Delta\eta)^4}{2\Delta\xi} ] \quad (A.64)$$

$$DR3 = - B2 \frac{(\Delta\eta)^3}{4\Delta\xi} \quad (A.65)$$

$$DR4 = - B2 \frac{(\Delta\eta)^3}{4\Delta\xi} \quad (A.66)$$

$$DR5 = [ BI \frac{(\Delta\eta)^4}{(\Delta\xi)^2} + B4 \frac{(\Delta\eta)^4}{2\Delta\xi} ] \quad (A.67)$$

$$DR6 = B2 \frac{(\Delta\eta)^3}{4\Delta\xi} \quad (A.68)$$

### A.2.3 Boundary Conditions for Two-Dimensional Model

For the two-dimensional model, the boundary conditions are essentially the same as in the one-dimensional case. The value of the stream function along the boundaries is specified, providing four of the eight boundary conditions needed. Along the bottom and side boundaries,  $\psi$  is generally set to zero, although inflow or outflow could be specified in the model by changing the value of  $\psi$  from one boundary grid point to the next. The value of  $\psi$  along the surface is specified by the modeling of the wave transformation across the surf zone. At each grid point the value of the volumetric transport created by the wave passage is used to establish  $\psi$  at the surface. The details of the wave transformation modeling are found in the main text.

The remaining four boundary conditions are also applied in a similar fashion to the 1-D model case. However, the transformation of coordinates used to achieve a rectangular model domain complicates their application. Figure A.6 illustrates the solution cell modifications needed to apply the various boundary conditions. At the surface, the gradient in  $\psi$  results in inflow or outflow of fluid to or from the model domain. Additionally, set-up or set-down of the water surface due to the waves alters the slope of the water surface from

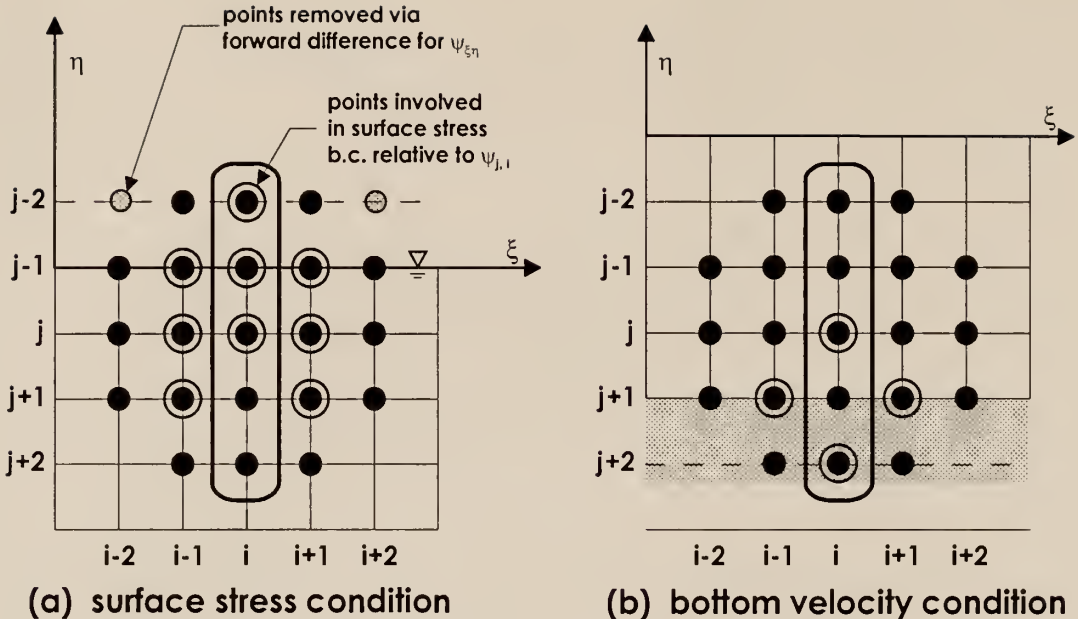


Figure A.6 Definition sketch of application of (a) applied surface shear stress, and (b) applied bottom velocity. The circled dots indicate the points in the solution cell needed to apply each condition for the  $\psi_{j,i}$  point only. The two shaded dots in plot (a) indicate the two points eliminated by using the forward difference approximation for  $\psi_{\xi\eta}$ .

the horizontal. To incorporate these effects and include a complete description of the surface shear stress, Eq. (A.5) is modified to read:

$$\tau_s = \rho\epsilon\left(\frac{\partial U}{\partial z} + \frac{\partial W}{\partial x}\right) = \rho\epsilon\left(-\frac{\partial^2 \psi}{\partial z^2} + \frac{\partial^2 \psi}{\partial x^2}\right) \quad (\text{A.69})$$

Eq. (A.69) is transformed, discretized, and reorganized to collect common terms in  $\psi$  (Figure A.6a). The boundary condition applies to three points in the solution cell, all of which lie on the surface, which is the  $j-1$  row ( $\sim 0$ ). One concession to the standard central difference spatial approximations is made at this stage. Central difference expansion of the  $\psi_{\xi\eta}$  term for the  $\psi_{j-1,i-1}$  and  $\psi_{j-1,i+1}$  points leads to the necessity of specifying  $\psi$  values above

the surface row that are not included in the 21-point solution cell. To circumvent this problem, a forward difference approximation of  $\psi_{\xi\eta}$  only was applied in the specification. The resultant boundary condition is:

$$\begin{aligned}\Psi_{j-2,i} &= \left( \frac{\tau_s}{\rho\epsilon} \right)_i / SC1_i - \left( \frac{SC2}{SC1} \right)_i \Psi_{j-1,i-1} + \left( \frac{SC3}{SC1} \right)_i \Psi_{j-1,i} \\ &- \left( \frac{SC4}{SC1} \right)_i \Psi_{j-1,i+1} + \left( \frac{SC5}{SC1} \right)_i \Psi_{j,i-1} - \left( \frac{SC6}{SC1} \right)_i \Psi_{j,i} - \left( \frac{SC7}{SC1} \right)_i \Psi_{j,i+1} \\ &- \left( \frac{SC8}{SC1} \right)_i \Psi_{j+1,i-1} + \left( \frac{SC9}{SC1} \right)_i \Psi_{j+1,i+1}\end{aligned}\quad (\text{A.70})$$

where the corresponding coefficients SC1 through SC9 are defined as follows:

$$SC1 = \frac{\eta_x^2 - \eta_z^2}{(\Delta\eta)^2} - \frac{\eta_{xx} - \eta_{zz}}{2\Delta\eta} \quad (\text{A.71})$$

$$SC2 = \frac{\xi_x^2 - \xi_z^2}{(\Delta\xi)^2} + \frac{3(\xi_x\eta_x - \xi_z\eta_z)}{2\Delta\xi\Delta\eta} - \frac{\xi_{xx} - \xi_{zz}}{2\Delta\xi} \quad (\text{A.72})$$

$$SC3 = 2\frac{\xi_x^2 - \xi_z^2}{(\Delta\xi)^2} + 2\frac{\eta_x^2 - \eta_z^2}{(\Delta\eta)^2} \quad (\text{A.73})$$

$$SC4 = \frac{\xi_x^2 - \xi_z^2}{(\Delta\xi)^2} - \frac{3(\xi_x\eta_x - \xi_z\eta_z)}{2\Delta\xi\Delta\eta} + \frac{\xi_{xx} - \xi_{zz}}{2\Delta\xi} \quad (\text{A.74})$$

$$SC5 = 2\frac{\xi_x\eta_x - \xi_z\eta_z}{\Delta\xi\Delta\eta} \quad (\text{A.75})$$

$$SC6 = \frac{\eta_x^2 - \eta_z^2}{(\Delta\eta)^2} + \frac{\eta_{xx} - \eta_{zz}}{2\Delta\eta} \quad (\text{A.76})$$

$$SC7 = 2\frac{\xi_x\eta_x - \xi_z\eta_z}{\Delta\xi\Delta\eta} \quad (\text{A.77})$$

$$SC8 = \frac{\xi_x \eta_x - \xi_z \eta_z}{2\Delta\xi\Delta\eta} \quad (A.78)$$

$$SC9 = \frac{\xi_x \eta_x - \xi_z \eta_z}{2\Delta\xi\Delta\eta} \quad (A.79)$$

Eq. (A.70) is solved for  $\psi_{j-2,i}$  and substituted into Eq. (A.38). Eq. (A.70) is then shifted and applied to the two adjacent points, solving for  $\psi_{j-2,i-1}$  and  $\psi_{j-2,i+1}$ , and substituting these values into Eq. (A.38) to remove all three points in the solution cell lying above the surface.

Along the sidewalls, the specification of  $\psi$  dictates the flow through the boundary. Specification of the tangential velocity at the wall satisfies the additional boundary conditions. The tangential velocity along the wall is specified by:

$$W_{wall} = (\Psi_x)_{wall} \quad (A.80)$$

which when discretized states (as an example):

$$\begin{aligned} \Psi_{j,wall-1} &= \Psi_{j,wall+1} + \left(\frac{\eta_x \Delta\xi}{\xi_x \Delta\eta}\right)_{j,wall} \Psi_{j+1,wall} \\ &\quad - \left(\frac{\eta_x \Delta\xi}{\xi_x \Delta\eta}\right)_{j,wall} \Psi_{j-1,wall} - \frac{2\Delta\xi}{\xi_x} W_{wall_j} \end{aligned} \quad (A.81)$$

Along the bottom boundary, the same options presented in the 1-D model development are applied. Again, the transformation of coordinates complicates the application of the boundary conditions. The specification of  $\psi$  controls the flow through the boundary, while the following equation specifies the bottom velocity tangential to the sloping bottom:

$$U - Wh_x = -\psi_z - \psi_x h_x = U_b \sqrt{h_x^2 + 1} \quad (\text{A.82})$$

where in Eq. (A.82)  $U_b$  represents the tangential bottom velocity and  $h_x$  is the bottom slope.

Transformation of Eq. (A.82) to  $\xi$ - $\eta$  coordinates and solution for the  $\psi$  value one point below the bottom, produces the following result:

$$\begin{aligned} \psi_{j+2,i} &= -(U_b)_i \sqrt{h_x^2 + 1} \left( \frac{2\Delta\eta}{h_x\eta_x + \eta_z} \right) - \frac{h_x\xi_x + \xi_z}{h_x\eta_x + \eta_z} \frac{\Delta\eta}{\Delta\xi} \psi_{j+1,i+1} \\ &\quad + \frac{h_x\xi_x + \xi_z}{h_x\eta_x + \eta_z} \frac{\Delta\eta}{\Delta\xi} \psi_{j+1,i-1} + \psi_{j,i} \end{aligned} \quad (\text{A.83})$$

As with the surface shear stress condition, Eq. (A.83) is applied to solve for  $\psi_{j+2,i}$ ,  $\psi_{j+2,i-1}$ , and  $\psi_{j+2,i+1}$ ; all three are substituted into Eq. (A.37) to solve for  $\psi_{j,i}$  (Figure A.6b).

For a bottom shear stress condition in the 2-D model, a procedure similar to the surface stress condition is employed. For  $j=N_j-1$ , the point just below the bed is found:

$$\begin{aligned} \psi_{j+2,i} &= \left( m \frac{\tau_s}{\rho\epsilon} \right)_i / BC1_i - \left( \frac{BC2}{BC1} \right)_i \psi_{j+1,i-1} + \left( \frac{BC3}{BC1} \right)_i \psi_{j+1,i} \\ &\quad - \left( \frac{BC4}{BC1} \right)_i \psi_{j+1,i+1} - \left( \frac{BC5}{BC1} \right)_i \psi_{j,i-1} - \left( \frac{BC6}{BC1} \right)_i \psi_{j,i} + \left( \frac{BC7}{BC1} \right)_i \psi_{j,i+1} \\ &\quad + \left( \frac{BC8}{BC1} \right)_i \psi_{j-1,i-1} - \left( \frac{BC9}{BC1} \right)_i \psi_{j-1,i+1} \end{aligned} \quad (\text{A.84})$$

While the coefficients for the nine points involved in Eq. (A.84) are fairly similar to those presented in Eqs. (A.71) through (A.79), they are defined at the  $j = N_j$  row for all i.

$$BC1 = \frac{\eta_x^2 - \eta_z^2}{\Delta\eta^2} + \frac{\eta_{xx} - \eta_{zz}}{2\Delta\eta} \quad (\text{A.85})$$

$$BC2 = \frac{\xi_x^2 - \xi_z^2}{(\Delta\xi)^2} - \frac{3(\xi_x\eta_x - \xi_z\eta_z)}{2\Delta\xi\Delta\eta} - \frac{\xi_{xx} - \xi_{zz}}{2\Delta\xi} \quad (\text{A.86})$$

$$BC3 = 2 \frac{\xi_x^2 - \xi_z^2}{(\Delta\xi)^2} + 2 \frac{\eta_x^2 - \eta_z^2}{(\Delta\eta)^2} \quad (A.87)$$

$$BC4 = \frac{\xi_x^2 - \xi_z^2}{(\Delta\xi)^2} + \frac{3(\xi_x\eta_x - \xi_z\eta_z)}{2\Delta\xi\Delta\eta} + \frac{\xi_{xx} - \xi_{zz}}{2\Delta\xi} \quad (A.88)$$

$$BC5 = 2 \frac{\xi_x\eta_x - \xi_z\eta_z}{\Delta\xi\Delta\eta} \quad (A.89)$$

$$BC6 = \frac{\eta_x^2 - \eta_z^2}{(\Delta\eta)^2} - \frac{\eta_{xx} - \eta_{zz}}{2\Delta\eta} \quad (A.90)$$

$$BC7 = 2 \frac{\xi_x\eta_x - \xi_z\eta_z}{\Delta\xi\Delta\eta} \quad (A.91)$$

$$BC8 = \frac{\xi_x\eta_x - \xi_z\eta_z}{2\Delta\xi\Delta\eta} \quad (A.92)$$

$$BC9 = \frac{\xi_x\eta_x - \xi_z\eta_z}{2\Delta\xi\Delta\eta} \quad (A.93)$$

Here Eq. (A.84) is applied three times to solve for  $\psi_{j+2, i}$ ,  $\psi_{j+2, i-1}$ , and  $\psi_{j+2, i+1}$ ; all three are substituted into Eq. (A.37) to solve for  $\psi_{j, i}$ .

**Corner Boundary Conditions.** Difficulties arise at the corners of the computational domain where the boundary conditions on the wall and on the surface or bottom share common points in the general solution cell that lie outside the computational domain. Generally speaking, the two conditions specify information at the virtual grid points one row and one column outside the corner point of the domain (refer to Figure A.6). To address this difficulty, the two boundary conditions are solved simultaneously for the two

outlying points, and the results applied in Eq. (A.37) along with the previously described boundary conditions for points away from the corner. As an example to demonstrate the nature of the substitutions, the following equations describe the corner boundary conditions where the bottom meets the sidewall for prescribed velocity values:

$$\Psi_{j+2,i-1} = \Psi_{j,i-1} - \frac{U_{b_{i-1}} \sqrt{h_x^2 + 1} \left( \frac{2\Delta\eta}{h_x\eta_x + \eta_z} \right)_{j+1,i-1}}{1 - \frac{\eta_x(h_x\xi_x + \xi_z)}{\xi_x(h_x\eta_x + \eta_z)}} - W_{wallNj} \frac{\frac{2\Delta\eta(h_x\xi_x + \xi_z)}{\xi_x(h_x\eta_x + \eta_z)}}{1 - \frac{\eta_x(h_x\xi_x + \xi_z)}{\xi_x(h_x\eta_x + \eta_z)}} \quad (\text{A.94})$$

$$\begin{aligned} \Psi_{j+1,i-2} &= \Psi_{j+1,i} - \frac{U_{b_{i-1}} \sqrt{h_x^2 + 1} \left( \frac{2\eta_x\Delta\xi}{\xi_x(h_x\eta_x + \eta_z)} \right)_{j+1,i-1}}{1 - \frac{\eta_x(h_x\xi_x + \xi_z)}{\xi_x(h_x\eta_x + \eta_z)}} \\ &\quad - W_{wallNj} \frac{\frac{2\Delta\xi}{\xi_x} [1 + \frac{\frac{\xi_x(h_x\eta_x + \eta_z)}{\eta_x(h_x\xi_x + \xi_z)}}{1 - \frac{\eta_x(h_x\xi_x + \xi_z)}{\xi_x(h_x\eta_x + \eta_z)}}]}{\xi_x} \end{aligned} \quad (\text{A.95})$$

While Eqs. (A.94) and (A.95) are quite cumbersome, the reader can appreciate that if the velocities near the corner are set to zero, the boundary conditions for the corner are greatly simplified. Nonetheless, to provide generality in the model and provide for the option of inflow or outflow at all the boundaries, these corner conditions are maintained.

#### A.2.4 Solution Scheme for Two-Dimensional Model

The solution technique for the 2-D model is similar to that used in the 1-D case. A simultaneous set of  $N_i-2$  equations is solved for the interior values of  $\psi$  along each vertical column (refer to Figure A.4). The same two subroutines used in the 1-D model are

employed in the 2-D model (BANDEC and BANBKS, Press et al., 1986). This process is swept horizontally from the offshore boundary to the shoreline for each time step.

As discussed previously, the method solves only for the points on the  $i^{\text{th}}$  column at the  $n+1$  time step. In the complete formulation, there would be points on five columns to solve for. This presents difficulties in creating a spatially consistent coefficient matrix. As a concession, the off-column points, those with  $R$  in their coefficient labels (Figure A.5), are moved to the right hand side of the equation and their respective  $\psi$  values are treated as known. The points moved from the solution side to the known side are then updated in a series of iterations for each time step. This entails tracking three different values of  $\psi$  at each point in the domain, the old value, the new intermediate value (known from the previous iteration at each time step), and the newly solved for value at each iteration.

The surface conditions represent the driving force in the model, that being the passage of waves across the profile. The model first determines the set-up/set-down and the wave height change across the profile, providing the initial surface boundary condition. The set-up/set-down is only used to determine the total water depth as the pressure gradient terms are implicit in the formulation.

The model runs through a series of time steps of the duration of a typical wave period (e.g., modal period). The model then changes the surface boundary conditions based on a randomly chosen wave height, and runs through the same number of time steps. The set-up/set-down are held fixed based on the first wave transformation. The model updates the average value of the stream function at each point in the model and periodically can record the instantaneous values in order to study the time evolution of the flow field. At each time step, the model compares the updated flow field to the previous flow field after each iteration and considers the maximum change in the value of  $\psi$  as a cutoff criteria.

## APPENDIX B

### FORTRAN CODE LISTING

#### RF\_PSI.F90

The following computer code is available from the author through the Coastal Engineering Archives at the Department of Civil & Coastal Engineering, University of Florida, Gainesville, FL, 32611.

```

PROGRAM rf_psi
! *****
! * TIME DEPENDENT/VARIABLE EDDY VISCOSITY MODEL IN TERMS OF PSI *
! * Numerical model to simulate the mean flows in the surf zone for *
! * a variable eddy viscosity field in the cross-differentiated 2-D *
! * Reynolds' equations of turbulent motion. Model translates the *
! * desired surf zone geometry to a rectangular grid, solves for the *
! * stream function in a 4th order PDE/FDE and then maps PSI back to *
! * the real geometry, solving for velocity and shear stress fields. *
! * 20 July, 1999 A.E. Browder *
! * Civil & Coastal Engineering Department - University of Florida *
! *
! * shoaling subroutine added - 14 August, 1999 *
! * inclusion of variable eddy viscosity (f(x,z)) - 23 August, 1999 *
! * added setup/setdown - 30 August, 1999 *
! * added surface roller option - 31 Aug 1999 *
! * added optional bottom stress B.C. - 5 Oct 1999 *
! * switched to x-sweep and double precision - 25 Oct 1999 *
! * added numerical routine for Dally et al. wave trans. - 8 Nov 1999 *
! * upgraded to time dependent (irregular wave) version - 17 Nov 1999 *
! * integrated Dally & Brown (1995) roller model - Feb 2000 *
! * added input file format - Mar 2000 *
! *****
USE MSFLIB
INTEGER, PARAMETER :: Ni = 79
INTEGER, PARAMETER :: Nj = 41
INTEGER, PARAMETER :: Nwaves = 15
INTEGER, DIMENSION(Nj-2,3:Ni-2) :: ALLindx
INTEGER, DIMENSION(Nj-2) :: indxA,indxB,indxC
INTEGER, DIMENSION(:, ), ALLOCATABLE :: indxj,p
DOUBLE PRECISION, DIMENSION(Nj,Ni) :: psiol,psinew,u,w,mag,theta,tau,adiff,z
DOUBLE PRECISION, DIMENSION(Nj,Ni) :: c11,c12,c13,c14,c15,e,ex,ez,exx,exz,ezz
DOUBLE PRECISION, DIMENSION(Nj,Ni) :: cr1,cr2,cr3,cr4,cr5,cr6,cr7,cr8,cr9,cr10
DOUBLE PRECISION, DIMENSION(Nj,Ni) :: cr11,cr12,cr13,cr14,cr15,cr16,thdist,sc99
DOUBLE PRECISION, DIMENSION(Nj,Ni) :: dr1,dr2,dr3,dr4,dr5,dr6,d11,d12,d13
DOUBLE PRECISION, DIMENSION(Nj,Ni) :: etax,etaxx,etaxz,etaxxx,etaxxz,etaxzz
DOUBLE PRECISION, DIMENSION(Nj,Ni) :: etaxxx,etaxxz,etaxzz,etaxzzz,psiave
DOUBLE PRECISION, DIMENSION(Nj,Ni) :: psinewi
DOUBLE PRECISION, DIMENSION(Nj,Ni,1) :: ua,wa,ta
DOUBLE PRECISION, DIMENSION(Ni) :: etaz,etazz,etazzz,etazzzz,ub,x,T,Tb,m,d,Ht
DOUBLE PRECISION, DIMENSION(Ni) :: setp,set0,dz,ubc1,ubc2,Hta,sxx,sxx0,sxxa
DOUBLE PRECISION, DIMENSION(Ni) :: scl,sc21,sc31,sc41,sc51,sc61,sc71,sc81,sc91
DOUBLE PRECISION, DIMENSION(Ni) :: bcl,bc21,bc31,bc41,bc51,bc61,bc71,bc81,bc91

```

```

DOUBLE PRECISION, DIMENSION(Nj-2,5) :: LHSA,LHSC,LB
DOUBLE PRECISION, DIMENSION(Nj-2,2) :: LLB,LWRA,LWRC
DOUBLE PRECISION, DIMENSION(Nj-2,2,3:Ni-2) :: LWRB
DOUBLE PRECISION, DIMENSION(Nj-2,5,3:Ni-2) :: ALLB
DOUBLE PRECISION, DIMENSION(Nj-2) :: rr
DOUBLE PRECISION, DIMENSION(Nj) :: ww
DOUBLE PRECISION, DIMENSION(:, ), ALLOCATABLE :: xp,zp
DOUBLE PRECISION, DIMENSION(:, ), ALLOCATABLE :: wvht
DOUBLE PRECISION, DIMENSION(:, :, ), ALLOCATABLE :: a1,a2,a3,a4,a5,a6,a7,a8,a9
DOUBLE PRECISION, DIMENSION(:, :, ), ALLOCATABLE :: a10,a11,a12,a13,a14
DOUBLE PRECISION, DIMENSION(:, :, ), ALLOCATABLE :: lhs,llhs,b1,b2,b3,b4,b5
DOUBLE PRECISION, DIMENSION(:, ), ALLOCATABLE :: d1,d2,d3,d4,d5,rhs
DOUBLE PRECISION kappa,da,db,dc,psibcRn,psibcRo,psibcLn,psibcLo,XXX
INTEGER isetd, ihotflag,ibbcflag,iwave
CHARACTER*80 fname, profile, hotfile, a

OPEN (unit = 16, file = "rf_psi_batch_nk_1d.inp",status='old')
!***** experiment to simulate: (1) Cox&Kobayashi (80x41) 1997'
!***** (2) Ting & Kirby (77x41)(1994) (3) Nadaoka&Kondoh (79x41) 1982'
!***** (4) Okayasu & Katayama(52x33)(1992) (5)Delta Flume 1-A (93,31) 1994'
!***** (6) Smith et al. (84x31) (1992) (7) Perdido Example (65,31)'

DO nsim = 1,50

psiold=0.0;psinew=0.0;adiff=0.0;resid=0.0;u=0.0;w=0.0;mag=0.0;x=0.0;m=0.0
LHSA=0.0;LHSC=0.0;LWRA=0.0;LLHSB=0.0;LWRC=0.0;theta=0.0;tau=0.0;psinewi=0.0
rr=0.0;indxA=0;indxB=0;indxC=0;ww=0.0;ub=0.0;T=0.0;z=0.0;x=0.0
zneg=0.0;set0=0.0;sxx=0.0 ; d = 0.0 ; setp = 0.0 ; sxx = 0.0 ; icc = 0
ua = 0.0 ; wa = 0.0 ; psiave = 0.0 ; ta = 0.0 ; Hta = 0.0 ; Ht = 0.0 ; sxxa = 0.0

READ (16,*) profile
READ (16,*) fname
READ (16,*) (a, i = 1,5)
READ (16,*) iexpflag
GOTO 1335
1336 READ (16,*) (a, i=1,3)
READ (16,*) isetq
dt = Twv/100.0
READ (16,*) (a, i=1,2)
READ (16,*) ieddy
READ (16,*) (a, i=1,2)
READ (16,*) e(1,1)
READ (16,*) (a, i=1,2)
READ (16,*) ibbcflag
READ (16,*) (a, i=1,2)
READ (16,*) isetd
READ (16,*) (a, i=1,2)
READ (16,*) ihotflag
READ (16,*) (a, i=1,1)
READ (16,*) hotfile
READ (16,*) (a, i=1,2)
READ (16,*) iofftau
READ (16,*) (a, i=1,2)
READ (16,*) itrans
READ (16,*) (a, i=1,2)
READ (16,*) iwave
IF (iwave.eq.0) THEN
    OPEN (unit=11,file="ok92wave.dat",status="old")
    ALLOCATE (wvht(Nwaves))
    DO k = 1,Nwaves
        READ (11,*) wvht(k)
    END DO
    CLOSE (11)
ENDIF
! *** Degree of implicitness of solution ***
th = 0.51
thc = 1.0 - th

```

```

OPEN (unit=11, file = TRIM(flname)//".dat", status = "REPLACE")
OPEN (unit=12, file = TRIM(flname)//".txt", status = "REPLACE")
OPEN (unit=13, file = TRIM(flname)//".bln", status = "REPLACE")
OPEN (unit=14, file = TRIM(flname)//".tau", status = "REPLACE")
OPEN (unit=15, file = TRIM(flname)//".csv", status = "REPLACE")

TOL = 1.e-07

ALLOCATE(xp(500),zp(500))
OPEN (unit=17 , file = TRIM(profile)//".dat", status='old')
DO i = 1,1000
    READ (17,* , END=21) xp(i),zp(i)
END DO
21 iprof = i-1
CLOSE(unit = 17)
deta = 1.0 / (Nj-1)
dx = dxi
CALL PROFSET(iprof,Ni,xp,zp,d,m,dzi)
DEALLOCATE(xp,zp)

! specify or estimate eddy viscosity on surface row
CALL SHOAL(Ni,Hinit,Ht,Twv,d,e(1,:),m,T,psiold(1,:),dzi,setup,ub,Tb,ib, &
           kappa,1,isetq,iofftau,sxx,itrans,ieddy)

DO i = 1,Ni
    x(i) = dxi*(i-1)
    d(i) = d(i) + setup(i)
    etaz(i) = -1.0 / d(i)
    dz(i) = d(i) / (Nj-1)
END DO

zix = 1.0 ; ziz = 0.0;zixx = 0.0;zixz = 0.0;zizz = 0.0;zixxx = 0.0
zixxz = 0.0;zixzz = 0.0;zizzz = 0.0;zixxxx = 0.0;zizzzz = 0.0
zixxxz = 0.0;zixxzz = 0.0;zixzzz = 0.0;etazz = 0.0;etaxzz = 0.0
etazzz = 0.0;etazzzz = 0.0;etaxzzz = 0.0;etaxzzzz = 0.0

CALL STB1(Ni,Nj,m,d,dx,z,etax,etaxz,etaxx,etaxxz,etaxxx,etaxxxz,etaxxxx,setup)
CALL EDDYVIS(Ni,Nj,e,ex,ez,exx,exz,ezz,Ht,ib,zix,zixx,ziz,zizz,zixz, &
            etax,etaxx,etaz,etazz,etaxz,dzi,deta,ieddy)

Tb = Tb * e(1,:)/e(Nj,:)
Tb = 0.0
ub = 0.0

GOTO 888      ;      ! *** routine to set up FDE coefficients
889 XXX = 1.0
GOTO 777      ;      ! *** routine to establish hot-start condition
778 psinew=psiold
IF (isetd.NE.0) GOTO 99
CALL SEED(RND$TIMESEED)
Nt = INT(Twv/dt)
sxx0 = sxx
300 FORMAT (3i6,2f17.15,f7.3)
icc = 0
! **** wave loop ****
! WAVES: DO Nw = 1,Nwaves
IF (iwave.NE.2) THEN
    IF (iwave.EQ.0) THEN
        Ho = wvht(Nw)
    ELSE
        CALL RANDOM(Fx)
        Ho = SQRT( - Hs*Hs*LOG(1 - Fx)/2.)
    ENDIF
    CALL SHOAL(Ni, Ho, Ht, Twv, d, e(1,:), m, T, psiold(1,:), dzi, setup, ub, Tb, ib, &
               kappa, 0, isetq, iofftau, sxx0, itrans, ieddy)
ENDIF
psinew(1,:) = psiold(1,:)
psinewi(1,:) = psiold(1,:)
Hta = Hta + Ht

```

```

sxxa = sxxa + sxx0
Tb = Tb * e(1,:)/e(Nj,:)
Tb = 0.0
ub = 0.0

! ***** dtloop runs the Twv seconds at dt intervals for each wave *****
DTLOOP: DO It = 1,Nt
  ! IF(XXX .EQ. 0.0) EXIT
  ic = 0
  adiffmax = 0.0
! ***** inner loop iterates on solution at each dt *****
  INNER: DO
    ! WRITE(*,300) Nw,It,ic,psiave(10,26)/(icc+1),xxx,Ho

! **** 2-D SOLUTION - ITERATION LOOP ****
  j = 2
  i = 2
  psibcLo = (T(i-1)/sc1(i-1)+sc21(i-1)*sc88*ww(j-1)-sc51(i-1)*sc88*ww(j) &
  + sc81(i-1)*sc88*ww(j+1) - (sc21(i-1)*sc99(j-1,i-1) &
  - sc81(i-1)*sc99(j+1,i-1)+sc61(i-1))*psiold(j,i-1) &
  + (sc31(i-1) - sc51(i-1)*sc99(j,i-1))*psiold(j-1,i-1) &
  + sc51(i-1)*sc99(j,i-1)*psiold(j+1,i-1) &
  - sc81(i-1)*sc99(j+1,i-1)*psiold(j+2,i-1)) / (1-sc21(i-1)*sc99(j-1,i-1))
  psibcLn = (T(i-1)/sc1(i-1)+sc21(i-1)*sc88*ww(j-1)-sc51(i-1)*sc88*ww(j) &
  + sc81(i-1)*sc88*ww(j+1) - (sc21(i-1)*sc99(j-1,i-1) &
  - sc81(i-1)*sc99(j+1,i-1)+sc61(i-1))*psinew(j,i-1) &
  + (sc31(i-1) - sc51(i-1)*sc99(j,i-1))*psinew(j-1,i-1) &
  + sc51(i-1)*sc99(j,i-1)*psinew(j+1,i-1) &
  - sc81(i-1)*sc99(j+1,i-1)*psinew(j+2,i-1)) / (1-sc21(i-1)*sc99(j-1,i-1))
  rr(j-1) = ( thc*dt*(cr5(j,i) - sc21(i)*c11(j,i) &
  - sc99(j,i-1)*cr2(j,i)) + dr1(j,i) )*psiold(j-1,i-1) &
  + ( thc*dt*(cr6(j,i) + sc51(i)*c11(j,i) - sc99(j+1,i-1)*cr3(j,i) &
  + sc99(j-1,i-1)*cr1(j,i)) + dr2(j,i) )*psiold(j,i-1) &
  + (thc*dt*(cr7(j,i) - sc81(i)*c11(j,i) &
  + sc99(j,i-1)*cr2(j,i)) + dr3(j,i))*psiold(j+1,i-1) &
  + thc*dt*(cr8(j,i) + sc99(j+1,i-1)*cr3(j,i))*psiold(j+2,i-1) &
  + ( dt*( c12(j,i) + sc31(i)*c11(j,i) - sc21(i+1)*cr9(j,i) &
  + cr1(j,i) - (cr4(j,i)-crl(j,i)*sc99(j-1,i-1)) &
  * (sc21(i-1)+sc41(i-1)) / (1-sc21(i-1)*sc99(1,i-1))) *psiold(j-1,i) &
  + ( thc*dt*( c13(j,i) - sc61(i)*c11(j,i) + sc51(i+1)*cr9(j,i) &
  + (cr4(j,i)-crl(j,i)*sc99(j-1,i-1))*(sc51(i-1)-sc71(i-1)) &
  / (1-sc21(i-1)*sc99(1,i-1)) + d12(j,i) )*psiold(j,i) &
  + ( thc*dt*( c14(j,i) - sc81(i+1)*cr9(j,i) + cr3(j,i) &
  + (cr4(j,i)-crl(j,i)*sc99(j-1,i-1))*(sc91(i-1)-sc81(i-1)) &
  / (1-sc21(i-1)*sc99(1,i-1)) + d13(j,i) )*psiold(j+1,i) &
  + thc*dt*c15(j,i)*psiold(j+2,i) &
  + ( thc*dt*( cr10(j,i) - sc41(i)*c11(j,i) &
  + sc31(i+1)*cr9(j,i) ) + dr4(j,i) )*psiold(j-1,i+1) &
  + ( thc*dt*( cr11(j,i) - sc71(i)*c11(j,i) &
  - sc61(i+1)*cr9(j,i) ) + dr5(j,i) )*psiold(j,i+1) &
  + (thc*dt*(cr12(j,i) + sc91(i)*c11(j,i)) + dr6(j,i))*psiold(j+1,i+1) &
  + thc*dt*cr13(j,i)*psiold(j+2,i+1) &
  + (thc*dt*(cr14(j,i) - sc41(i+1)*cr9(j,i))) *psiold(j-1,i+2) &
  + (thc*dt*(cr15(j,i) - sc71(i+1)*cr9(j,i))) *psiold(j,i+2) &
  + (thc*dt*(cr16(j,i) + sc91(i+1)*cr9(j,i))) *psiold(j+1,i+2) &
  + ( th*dt*( cr5(j,i) - sc21(i)*c11(j,i) &
  - sc99(j,i-1)*cr2(j,i) ) - dr1(j,i) )*psinew(j-1,i-1) &
  + (th*dt*( cr6(j,i) + sc51(i)*c11(j,i) - sc99(j+1,i-1)*cr3(j,i) &
  + sc99(j-1,i-1)*cr1(j,i) ) - dr2(j,i) )*psinew(j,i-1) &
  + (th*dt*(cr7(j,i) - sc81(i)*c11(j,i) &
  + sc99(j,i-1)*cr2(j,i)) + dr3(j,i))*psinew(j+1,i-1) &
  + th*dt*(cr8(j,i) + sc99(j+1,i-1)*cr3(j,i))*psinew(j+2,i-1) &
  + (th*dt*( cr10(j,i) - sc41(i)*c11(j,i) &
  + sc31(i+1)*cr9(j,i) ) - dr4(j,i) )*psinew(j-1,i+1) &
  + (th*dt*( cr11(j,i) - sc71(i)*c11(j,i) &
  - sc61(i+1)*cr9(j,i) ) - dr5(j,i) )*psinew(j,i+1) &
  + (th*dt*(cr12(j,i) + sc91(i)*c11(j,i)) - dr6(j,i))*psinew(j+1,i+1) &
  + th*dt*cr13(j,i)*psinew(j+2,i+1) &
  + (th*dt*(cr14(j,i) - sc41(i+1)*cr9(j,i))) *psinew(j-1,i+2) &
  + (th*dt*(cr15(j,i) - sc71(i+1)*cr9(j,i))) *psinew(j,i+2)

```

```

+ (th*dt*(cr15(j,i) - sc71(i+1)*cr9(j,i)))*psinew(j,i+2) &
+ (th*dt*(cr16(j,i) + sc91(i+1)*cr9(j,i)))*psinew(j+1,i+2) &
+ dt*T(i)/sc1(i)*cl1(j,i) + dt*T(i+1)/sc1(i+1)*cr9(j,i) &
- dt*sc88*(cr1(j,i)*ww(j-1) + cr2(j,i)*ww(j) + cr3(j,i)*ww(j+1) ) &
+ dt*(cr4(j,i)-cr1(j,i)*sc99(j-1,i-1))*(thc*psibcLo + th*psibcLn)

j = 3
rr(j-1) = (thc*dt*(cr4(j,i) - sc99(j-1,i-1)*cr1(j,i)))*psiold(j-2,i-1) &
+ (thc*dt*(cr5(j,i)-sc99(j,i-1)*cr2(j,i))+dr1(j,i))*psiold(j-1,i-1) &
+ (thc*dt*(cr6(j,i) + sc99(j-1,i-1)*cr1(j,i) &
- sc99(j,i-1)*cr3(j,i)) + dr2(j,i))*psiold(j,i-1) &
+ (thc*dt*(cr7(j,i)+sc99(j,i-1)*cr2(j,i))+dr3(j,i))*psiold(j+1,i-1) &
+ (thc*dt*(cr8(j,i)+sc99(j+1,i-1)*cr3(j,i)))*psiold(j+2,i-1) &
+ dt*c11(j,i)*psiold(j-2,i) &
+ (thc*dt*(c12(j,i) + cr1(j,i)) + dl1(j,i))*psiold(j-1,i) &
+ (thc*dt*(c13(j,i) + cr2(j,i)) + dl2(j,i))*psiold(j,i) &
+ (thc*dt*(c14(j,i) + cr3(j,i)) + dl3(j,i))*psiold(j+1,i) &
+ thc*dt*cl5(j,i)*psiold(j+2,i) + thc*dt*cr9(j,i)*psiold(j-2,i+1) &
+ (thc*dt*cr10(j,i) + dr4(j,i))*psiold(j-1,i+1) &
+ (thc*dt*cr11(j,i) + dr5(j,i))*psiold(j,i+1) &
+ (thc*dt*cr12(j,i) + dr6(j,i))*psiold(j+1,i+1) &
+ thc*dt*cr13(j,i)*psiold(j+2,i+1) + thc*dt*cr14(j,i)*psiold(j-1,i+2) &
+ thc*dt*cr15(j,i)*psiold(j,i+2) + thc*dt*cr16(j,i)*psiold(j+1,i+2) &
- dt*sc88*(cr1(j,i)*ww(j-1) + cr2(j,i)*ww(j) + cr3(j,i)*ww(j+1))

DO j= 4,Nj-3
rr(j-1) = (thc*dt*(cr4(j,i) - sc99(j-1,i-1)*cr1(j,i)))*psiold(j-2,i-1) &
+ (thc*dt*(cr5(j,i)-sc99(j,i-1)*cr2(j,i))+dr1(j,i))*psiold(j-1,i-1) &
+ (thc*dt*(cr6(j,i) + sc99(j-1,i-1)*cr1(j,i) &
- sc99(j,i-1)*cr3(j,i)) + dr2(j,i))*psiold(j,i-1) &
+ (thc*dt*(cr7(j,i)+sc99(j,i-1)*cr2(j,i))+dr3(j,i))*psiold(j+1,i-1) &
+ (thc*dt*(cr8(j,i)+sc99(j+1,i-1)*cr3(j,i)))*psiold(j+2,i-1) &
+ thc*dt*c11(j,i)*psiold(j-2,i) &
+ (thc*dt*(c12(j,i) + cr1(j,i)) + dl1(j,i))*psiold(j-1,i) &
+ (thc*dt*(c13(j,i) + cr2(j,i)) + dl2(j,i))*psiold(j,i) &
+ (thc*dt*(c14(j,i) + cr3(j,i)) + dl3(j,i))*psiold(j+1,i) &
+ thc*dt*cl5(j,i)*psiold(j+2,i) + thc*dt*cr9(j,i)*psiold(j-2,i+1) &
+ (thc*dt*cr10(j,i) + dr4(j,i))*psiold(j-1,i+1) &
+ (thc*dt*cr11(j,i) + dr5(j,i))*psiold(j,i+1) &
+ (thc*dt*cr12(j,i) - dr6(j,i))*psiold(j+1,i+1) &
+ thc*dt*cr13(j,i)*psiold(j+2,i+1) + thc*dt*cr14(j,i)*psiold(j-1,i+2) &
+ thc*dt*cr15(j,i)*psiold(j,i+2) + thc*dt*cr16(j,i)*psiold(j+1,i+2) &
- dt*sc88*(cr1(j,i)*ww(j-1) + cr2(j,i)*ww(j) + cr3(j,i)*ww(j+1))

END DO
j = Nj-2
rr(j-1) = (thc*dt*(cr4(j,i) - sc99(j-1,i-1)*cr1(j,i)))*psiold(j-2,i-1) &
+ (thc*dt*(cr5(j,i)-sc99(j,i-1)*cr2(j,i))+dr1(j,i))*psiold(j-1,i-1) &
+ (thc*dt*(cr6(j,i) + sc99(j-1,i-1)*cr1(j,i) &
- sc99(j,i-1)*cr3(j,i)) - dr2(j,i))*psiold(j,i-1) &
+ (thc*dt*(cr7(j,i)+sc99(j,i-1)*cr2(j,i))-dr3(j,i))*psiold(j+1,i-1) &
+ (thc*dt*(cr8(j,i)+sc99(j+1,i-1)*cr3(j,i)))*psiold(j+2,i-1) &
+ thc*dt*cr9(j,i)*psinew(j-2,i+1) &
+ (thc*dt*cr10(j,i) - dr4(j,i))*psinew(j-1,i+1) &
+ (thc*dt*cr11(j,i) - dr5(j,i))*psinew(j,i+1) &
+ (thc*dt*cr12(j,i) - dr6(j,i))*psinew(j+1,i+1) &
+ thc*dt*cr13(j,i)*psinew(j+2,i+1) + thc*dt*cr14(j,i)*psinew(j-1,i+2) &
+ thc*dt*cr15(j,i)*psinew(j,i+2) + thc*dt*cr16(j,i)*psinew(j+1,i+2) &
- dt*sc88*(cr1(j,i)*ww(j-1) + cr2(j,i)*ww(j) + cr3(j,i)*ww(j+1))

```

```

- sc99(j,i-1)*cr3(j,i)) + dr2(j,i))*psiold(j,i-1) &
+ (thc*dt*(cr7(j,i)+sc99(j,i-1)*cr2(j,i))+dr3(j,i))*psiold(j+1,i-1) &
+ (thc*dt*(cr8(j,i)+sc99(j+1,i-1)*cr3(j,i)))*psiold(j+2,i-1) &
+ thc*dt*c11(j,i)*psiold(j-2,i) &
+ (thc*dt*(c12(j,i) + cr1(j,i)) + dl1(j,i))*psiold(j-1,i) &
+ (thc*dt*(c13(j,i) + cr2(j,i)) + dl2(j,i))*psiold(j,i) &
+ (thc*dt*(c14(j,i) + cr3(j,i)) + dl3(j,i))*psiold(j+1,i) &
+ dt*c15(j,i)*psiold(j+2,i) &
+ thc*dt*cr9(j,i)*psiold(j-2,i+1) &
+ (thc*dt*cr10(j,i) + dr4(j,i))*psiold(j-1,i+1) &
+ (thc*dt*cr11(j,i) + dr5(j,i))*psiold(j,i+1) &
+ (thc*dt*cr12(j,i) + dr6(j,i))*psiold(j+1,i+1) &
+ thc*dt*cr13(j,i)*psiold(j+2,i+1) + thc*dt*cr14(j,i)*psiold(j-1,i+2) &
+ thc*dt*cr15(j,i)*psiold(j,i+2) + thc*dt*cr16(j,i)*psiold(j+1,i+2) &
+ (th*dt*(cr4(j,i)-sc99(j-1,i-1)*cr1(j,i)))*psinew(j-2,i-1) &
+ (th*dt*(cr5(j,i)-sc99(j,i-1)*cr2(j,i)) - dr1(j,i))*psinew(j-1,i-1) &
+ (th*dt*(cr6(j,i) + sc99(j-1,i-1)*cr1(j,i)) &
- sc99(j,i-1)*cr3(j,i)) - dr2(j,i))*psinew(j,i-1) &
+ (th*dt*(cr7(j,i)+sc99(j,i-1)*cr2(j,i))-dr3(j,i))*psinew(j+1,i-1) &
+ (th*dt*(cr8(j,i)+sc99(j+1,i-1)*cr3(j,i)))*psinew(j+2,i-1) &
+ th*dt*cr9(j,i)*psinew(j-2,i+1) &
+ (th*dt*cr10(j,i) - dr4(j,i))*psinew(j-1,i+1) &
+ (th*dt*cr11(j,i) - dr5(j,i))*psinew(j,i+1) &
+ (th*dt*cr12(j,i) - dr6(j,i))*psinew(j+1,i+1) &
+ th*dt*cr13(j,i)*psinew(j+2,i+1) + th*dt*cr14(j,i)*psinew(j-1,i+2) &
+ th*dt*cr15(j,i)*psinew(j,i+2) + th*dt*cr16(j,i)*psinew(j+1,i+2) &
- dt*sc88*(cr1(j,i)*ww(j-1) + cr2(j,i)*ww(j) + cr3(j,i)*ww(j+1))

j = Nj-1
IF (ibbcflag.EQ.0) THEN
  rr(j-1) = (thc*dt*(cr4(j,i) - sc99(j-1,i-1)*cr1(j,i)))*psiold(j-2,i-1) &
+ (thc*dt*(cr5(j,i)-sc99(j,i-1)*cr2(j,i))+dr1(j,i))*psiold(j-1,i-1) &
+ (thc*dt*(cr6(j,i) + sc99(j-1,i-1)*cr1(j,i)) &
+ cr8(j,i)) + dr2(j,i))*psiold(j,i-1) &
+ (thc*dt*(cr7(j,i) + sc99(j,i-1)*cr2(j,i)) &
+ c15(j,i)*ubc2(i)) + dr3(j,i))*psiold(j+1,i-1) &
+ thc*dt*c11(j,i)*psiold(j-2,i) &
+ (thc*dt*(c12(j,i) + cr1(j,i)) + dl1(j,i))*psiold(j-1,i) &
+ (thc*dt*(c13(j,i) + cr2(j,i) + c15(j,i)) + dl2(j,i))*psiold(j,i) &
+ (dt*(c14(j,i) + cr3(j,i) + cr13(j,i)*ubc2(i+1)))*psiold(j+1,i) &
+ thc*dt*cr9(j,i)*psiold(j-2,i+1) &
+ (thc*dt*cr10(j,i) + dr4(j,i))*psiold(j-1,i+1) &
+ (thc*dt*(cr11(j,i) + cr13(j,i)) + dr5(j,i))*psiold(j,i+1) &
+ (thc*dt*(cr12(j,i) - c15(j,i)*ubc2(i)) + dr6(j,i))*psiold(j+1,i+1) &
+ thc*dt*cr14(j,i)*psiold(j-1,i+2) + thc*dt*cr15(j,i)*psiold(j,i+2) &
+ (thc*dt*(cr16(j,i) - cr13(j,i)*ubc2(i+1)))*psiold(j+1,i+2) &
+ (th*dt*(cr4(j,i)-sc99(j-1,i-1)*cr1(j,i)))*psinew(j-2,i-1) &
+ (th*dt*(cr5(j,i)-sc99(j,i-1)*cr2(j,i)) - dr1(j,i))*psinew(j-1,i-1) &
+ (th*dt*(cr6(j,i) + sc99(j-1,i-1)*cr1(j,i)) &
+ cr8(j,i)) - dr2(j,i))*psinew(j,i-1) &
+ (th*dt*(cr7(j,i) + sc99(j,i-1)*cr2(j,i)) &
+ c15(j,i)*ubc2(i)) - dr3(j,i))*psinew(j+1,i-1) &
+ th*dt*cr9(j,i)*psinew(j-2,i+1) &
+ (th*dt*cr10(j,i) - dr4(j,i))*psinew(j-1,i+1) &
+ (th*dt*(cr11(j,i) + cr13(j,i)) - dr5(j,i))*psinew(j,i+1) &
+ (th*dt*(cr12(j,i) - c15(j,i)*ubc2(i)) - dr6(j,i))*psinew(j+1,i+1) &
+ th*dt*cr14(j,i)*psinew(j-1,i+2) + th*dt*cr15(j,i)*psinew(j,i+2) &
+ th*dt*(cr16(j,i) - cr13(j,i)*ubc2(i+1))*psinew(j+1,i+2) &
+ dt*(-c15(j,i)*ub(i)*ubc1(i) - cr13(j,i)*ub(i+1)*ubc1(i+1)) &
- dt*sc88*(cr1(j,i)*ww(j-1) + cr2(j,i)*ww(j) + cr3(j,i)*ww(j+1)) &
- cr8(j,i)*( ((1+sc99(j+1,i-1)*ubc2(i-1) &
/ (1.-sc99(j+1,i-1)*ubc2(i-1)))*ubc1(i-1)*ub(i-1)) &
- ww(j+1)*(sc88*ubc2(i-1)/(1.-sc99(j+1,i-1)*ubc2(i-1))) ) &
- cr3(j,i)*( sc88*ww(j+1)/(1.-sc99(j+1,i-1)*ubc2(i-1)) &
+ sc99(j+1,i-1)*ubc1(i-1)*ub(i-1)/(1.-sc99(j+1,i-1)*ubc2(i-1)) )

ELSE
  bbcLbo = (Tb(i-1)/bc1(i-1)+bc21(i-1)*sc88*ww(j+1)+bc51(i-1)*sc88*ww(j) &
- bc81(i-1)*sc88*ww(j-1) &
+ (bc21(i-1)*sc99(j+1,i-1)+bc81(i-1)*sc99(j-1,i-1) &
- bc61(i-1))*psiold(j,i-1) &
+ (bc31(i-1) - bc51(i-1)*sc99(j,i-1))*psiold(j+1,i-1) &

```

```

+ bc51(i-1)*sc99(j,i-1)*psiold(j-1,i-1) &
- bc81(i-1)*sc99(j-1,i-1)*psiold(j-2,i-1)) / (1+bc21(i-1)*sc99(j+1,i-1))
bbcLbn = (Tb(i-1)/bc1(i-1)+bc21(i-1)*sc88*ww(j+1)+bc51(i-1)*sc88*ww(j) &
- bc81(i-1)*sc88*ww(j-1) &
+ (bc21(i-1)*sc99(j+1,i-1)+bc81(i-1)*sc99(j-1,i-1) &
- bc61(i-1))*psinew(j,i-1) &
+ (bc31(i-1) - bc51(i-1)*sc99(j,i-1))*psinew(j+1,i-1) &
+ bc51(i-1)*sc99(j,i-1)*psinew(j-1,i-1) &
- bc81(i-1)*sc99(j-1,i-1)*psinew(j-2,i-1)) / (1+bc21(i-1)*sc99(j+1,i-1))
rr(j-1) = thc*dt*c11(j,i)*psiold(j-2,i) &
+ (thc*dt*( cl2(j,i) + cr1(j,i) + bc81(i+1)*cr13(j,i) &
+ (cr8(j,i)+cr3(j,i)*sc99(j+1,i-1)) &
* ((bc81(i-1)-bc91(i-1))/(1+bc21(i-1)*sc99(j+1,i-1))) ) &
+ d11(j,i))*psiold(j-1,i) &
+ (thc*dt*( cl3(j,i) + cr2(j,i) - bc51(i+1)*cr13(j,i) &
+ bc61(i)*c15(j,i) + (cr8(j,i)+cr3(j,i)*sc99(j+1,i-1)) &
* ((bc71(i-1)-bc71(i-1))/(1+bc21(i-1)*sc99(j+1,i-1))) ) &
+ d12(j,i))*psiold(j,i) &
+ thc*dt*cr9(j,i)*psiold(j-2,i+1) &
+ (thc*dt*(cr10(j,i) - bc91(i)*c15(j,i)) + dr4(j,i))*psiold(j-1,i+1) &
+ (thc*dt*(cr11(j,i) + bc71(i)*c15(j,i) - bc61(i+1)*cr13(j,i)) &
+ dr5(j,i))*psiold(j,i+1) &
+ thc*dt*(cr14(j,i)-bc91(i+1)*cr13(j,i))*psiold(j-1,i+2) &
+ thc*dt*(cr15(j,i)+bc71(i+1)*cr13(j,i))*psiold(j,i+2) &
+ th*dt*cr9(j,i)*psinew(j-2,i+1) &
+ (th*dt*(cr10(j,i) - bc91(i)*c15(j,i)) - dr4(j,i))*psinew(j-1,i+1) &
- dr5(j,i))*psinew(j,i+1) &
+ th*dt*(cr14(j,i)-bc91(i+1)*cr13(j,i))*psinew(j-1,i+2) &
+ th*dt*(cr15(j,i)+bc71(i+1)*cr13(j,i))*psinew(j,i+2) &
+ dt*Tb(i)/bc1(i)*c15(j,i) + dt*Tb(i+1)/bc1(i+1)*cr13(j,i) &
+ dt*(cr8(j,i)+cr3(j,i)*sc99(j+1,i-1))*(thc*bbcLbo + th*bbcLbn)
ENDIF
CALL banbks(LHSA,Nj-2,2,2,Nj-2,5,LWRA,2,indxA,rr)
DO j = 1,Nj-2
    psinewi(j+1,i) = rr(j)
END DO
rr = 0.0
!***** solve for Psi's along columns i = 3 to Ni-2
! solve for Psi's along columns i = 3 to Ni-2
DO i = 3,Ni-2
j = 2
rr(j-1) = (thc*dt*(cr1(j,i) - sc21(i-1)*cr4(j,i)))*psiold(j-1,i-2) &
+ (thc*dt*(cr2(j,i) + sc51(i-1)*cr4(j,i)))*psiold(j,i-2) &
+ (thc*dt*(cr3(j,i) - sc81(i-1)*cr4(j,i)))*psiold(j+1,i-2) &
+ (thc*dt*(cr5(j,i) - sc21(i)*c11(j,i) &
+ sc31(i-1)*cr4(j,i)) + dr1(j,i))*psiold(j-1,i-1) &
+ (thc*dt*(cr6(j,i) + sc51(i)*c11(j,i) &
- sc61(i-1)*cr4(j,i)) + dr2(j,i))*psiold(j,i-1) &
+ (thc*dt*(cr7(j,i) - sc81(i)*c11(j,i)) + dr3(j,i))*psiold(j+1,i-1) &
+ thc*dt*cr8(j,i)*psiold(j+2,i-1) &
+ (dt*(cl2(j,i) + sc31(i)*c11(j,i) - sc21(i+1)*cr9(j,i) &
- sc41(i-1)*cr4(j,i)))*psiold(j-1,i) &
+ (thc*dt*( cl3(j,i) - sc61(i)*c11(j,i) + sc51(i+1)*cr9(j,i) &
- sc71(i-1)*cr4(j,i) ) + d12(j,i))*psiold(j,i) &
+ (thc*dt*(cl4(j,i) + sc91(i-1)*cr4(j,i) &
- sc81(i+1)*cr9(j,i) ) + d13(j,i))*psiold(j+1,i) &
+ thc*dt*c15(j,i)*psiold(j+2,i) &
+ (thc*dt*( cr10(j,i) - sc41(i)*c11(j,i) &
+ sc31(i+1)*cr9(j,i) ) + dr4(j,i))*psiold(j-1,i+1) &
+ (thc*dt*( cr11(j,i) - sc71(i)*c11(j,i) &
- sc61(i+1)*cr9(j,i) ) + dr5(j,i))*psiold(j,i+1) &
+ (thc*dt*(cr12(j,i) + sc91(i)*c11(j,i)) + dr6(j,i))*psiold(j+1,i+1) &
+ thc*dt*cr13(j,i)*psiold(j+2,i+1) &
+ (thc*dt*(cr14(j,i) - sc41(i+1)*cr9(j,i)))*psiold(j-1,i+2) &
+ (thc*dt*(cr15(j,i) - sc71(i+1)*cr9(j,i)))*psiold(j,i+2) &
+ (thc*dt*(cr16(j,i) + sc91(i+1)*cr9(j,i)))*psiold(j+1,i+2) &

```

```

+ (th*dt*(crl(j,i) - sc21(i-1)*cr4(j,i)))*psinew(j-1,i-2) &
+ (th*dt*(cr2(j,i) + sc51(i-1)*cr4(j,i)))*psinew(j,i-2) &
+ (th*dt*(cr3(j,i) - sc81(i-1)*cr4(j,i)))*psinew(j+1,i-2) &
+ (th*dt*(cr5(j,i) - sc21(i)*cl1(j,i)) &
+ sc31(i-1)*cr4(j,i)) - dr1(j,i) )*psinew(j-1,i-1) &
+ (th*dt*(cr6(j,i) + sc51(i)*cl1(j,i) &
- sc61(i-1)*cr4(j,i)) - dr2(j,i) )*psinew(j,i-1) &
+ (th*dt*(cr7(j,i) - sc81(i)*cl1(j,i)) - dr3(j,i))*psinew(j+1,i-1) &
+ th*dt*cr8(j,i)*psinew(j+2,i-1) &
+ (th*dt*(cr10(j,i) - sc41(i)*cl1(j,i) &
+ sc31(i+1)*cr9(j,i)) - dr4(j,i) )*psinew(j-1,i+1) &
+ (th*dt*(cr11(j,i) - sc71(i)*cl1(j,i) &
- sc61(i+1)*cr9(j,i)) - dr5(j,i) )*psinew(j,i+1) &
+ (th*dt*(cr12(j,i)+sc91(i)*cl1(j,i))-dr6(j,i))*psinew(j+1,i+1) &
+ th*dt*cr13(j,i)*psinew(j+2,i+1) &
+ (th*dt*(cr14(j,i) - sc41(i+1)*cr9(j,i)))*psinew(j-1,i+2) &
+ (th*dt*(cr15(j,i) - sc71(i+1)*cr9(j,i)))*psinew(j,i+2) &
+ (th*dt*(cr16(j,i) + sc91(i+1)*cr9(j,i)))*psinew(j+1,i+2) &
+ dt*T(i)/sc1(i)*cl1(j,i) + dt*T(i+1)/sc1(i+1)*cr9(j,i) &
+ dt*T(i-1)/sc1(i-1)*cr4(j,i)

j = 3
rr(j-1) = thc*dt*cr1(j,i)*psiol(j-1,i-2) + thc*dt*cr2(j,i)*psiol(j,i-2) &
+ thc*dt*cr3(j,i)*psiol(j+1,i-2) + thc*dt*cr4(j,i)*psiol(j-2,i-1) &
+ (thc*dt*cr5(j,i) + dr1(j,i))*psiol(j-1,i-1) &
+ (thc*dt*cr6(j,i) + dr2(j,i))*psiol(j,i-1) &
+ (thc*dt*cr7(j,i) + dr3(j,i))*psiol(j+1,i-1) &
+ thc*dt*cr8(j,i)*psiol(j+2,i-1) + dt*cl1(j,i)*psiol(j-2,i) &
+ (thc*dt*cl2(j,i) + dl1(j,i))*psiol(j-1,i) &
+ (thc*dt*cl3(j,i) + dl2(j,i))*psiol(j,i) &
+ (thc*dt*cl4(j,i) + dl3(j,i))*psiol(j+1,i) &
+ thc*dt*cl5(j,i)*psiol(j+2,i) + thc*dt*cr9(j,i)*psiol(j-2,i+1) &
+ (thc*dt*cr10(j,i) + dr4(j,i))*psiol(j-1,i+1) &
+ (thc*dt*cr11(j,i) + dr5(j,i))*psiol(j,i+1) &
+ (thc*dt*cr12(j,i) + dr6(j,i))*psiol(j+1,i+1) &
+ thc*dt*cr13(j,i)*psiol(j+2,i+1) + thc*dt*cr14(j,i)*psiol(j-1,i+2) &
+ thc*dt*cr15(j,i)*psiol(j,i+2) + thc*dt*cr16(j,i)*psiol(j+1,i+2)
! *** THIS IS THE BASE FORM OF FDE ***
DO j = 4,Nj-3
rr(j-1) = thc*dt*cr1(j,i)*psiol(j-1,i-2) + thc*dt*cr2(j,i)*psiol(j,i-2) &
+ thc*dt*cr3(j,i)*psiol(j+1,i-2) + thc*dt*cr4(j,i)*psiol(j-2,i-1) &
+ (thc*dt*cr5(j,i) + dr1(j,i))*psiol(j-1,i-1) &
+ (thc*dt*cr6(j,i) + dr2(j,i))*psiol(j,i-1) &
+ (thc*dt*cr7(j,i) + dr3(j,i))*psiol(j+1,i-1) &
+ thc*dt*cr8(j,i)*psiol(j+2,i-1) + thc*dt*cl1(j,i)*psiol(j-2,i) &
+ (thc*dt*cl2(j,i) + dl1(j,i))*psiol(j-1,i) &
+ (thc*dt*cl3(j,i) + dl2(j,i))*psiol(j,i) &
+ (thc*dt*cl4(j,i) + dl3(j,i))*psiol(j+1,i) &
+ thc*dt*cl5(j,i)*psiol(j+2,i) + thc*dt*cr9(j,i)*psiol(j-2,i+1) &
+ (thc*dt*cr10(j,i) + dr4(j,i))*psiol(j-1,i+1) &
+ (thc*dt*cr11(j,i) + dr5(j,i))*psiol(j,i+1) &
+ (thc*dt*cr12(j,i) + dr6(j,i))*psiol(j+1,i+1) &
+ thc*dt*cr13(j,i)*psiol(j+2,i+1) + thc*dt*cr14(j,i)*psiol(j-1,i+2) &
+ thc*dt*cr15(j,i)*psiol(j,i+2) + thc*dt*cr16(j,i)*psiol(j+1,i+2)
+ thc*dt*cr1(j,i)*psinew(j-1,i-2) + thc*dt*cr2(j,i)*psinew(j,i-2) &
+ thc*dt*cr3(j,i)*psinew(j+1,i-2) + thc*dt*cr4(j,i)*psinew(j-2,i-1) &
+ (thc*dt*cr5(j,i) - dr1(j,i))*psinew(j-1,i-1) &
+ (thc*dt*cr6(j,i) - dr2(j,i))*psinew(j,i-1) &
+ (thc*dt*cr7(j,i) - dr3(j,i))*psinew(j+1,i-1) &
+ thc*dt*cr8(j,i)*psinew(j+2,i-1) + thc*dt*cr9(j,i)*psinew(j-2,i+1) &

```

```

+ (th*dt*cr10(j,i) - dr4(j,i))*psinew(j-1,i+1) &
+ (th*dt*cr11(j,i) - dr5(j,i))*psinew(j,i+1) &
+ (th*dt*cr12(j,i) - dr6(j,i))*psinew(j+1,i+1) &
+ th*dt*cr13(j,i)*psinew(j+2,i+1) + th*dt*cr14(j,i)*psinew(j-1,i+2) &
+ th*dt*cr15(j,i)*psinew(j,i+2) + th*dt*cr16(j,i)*psinew(j+1,i+2)
END DO
j = Nj-2
rr(j-1) = thc*dt*cr1(j,i)*psiold(j-1,i-2) + thc*dt*cr2(j,i)*psiold(j,i-2) &
+ thc*dt*cr3(j,i)*psiold(j+1,i-2) + thc*dt*cr4(j,i)*psiold(j-2,i-1) &
+ (thc*dt*cr5(j,i) + dr1(j,i))*psiold(j-1,i-1) &
+ (thc*dt*cr6(j,i) + dr2(j,i))*psiold(j,i-1) &
+ (thc*dt*cr7(j,i) + dr3(j,i))*psiold(j+1,i-1) &
+ thc*dt*cr8(j,i)*psiold(j+2,i-1) + thc*dt*cl1(j,i)*psiold(j-2,i) &
+ (thc*dt*cl2(j,i) + dl1(j,i))*psiold(j-1,i) &
+ (thc*dt*cl3(j,i) + dl2(j,i))*psiold(j,i) &
+ (thc*dt*cl4(j,i) + dl3(j,i))*psiold(j+1,i) &
+ dt*c15(j,i)*psiold(j+2,i) + thc*dt*cr9(j,i)*psiold(j-2,i+1) &
+ (thc*dt*cr10(j,i) + dr4(j,i))*psiold(j-1,i+1) &
+ (thc*dt*cr11(j,i) + dr5(j,i))*psiold(j,i+1) &
+ (thc*dt*cr12(j,i) + dr6(j,i))*psiold(j+1,i+1) &
+ thc*dt*cr13(j,i)*psiold(j+2,i+1) + thc*dt*cr14(j,i)*psiold(j-1,i+2) &
+ thc*dt*cr15(j,i)*psiold(j,i+2) + thc*dt*cr16(j,i)*psiold(j+1,i+2)

j = Nj-1
IF (ibbcflag.EQ.0) THEN
rr(j-1) = thc*dt*cr1(j,i)*psiold(j-1,i-2) + thc*dt*cr2(j,i)*psiold(j,i-2) &
+ (thc*dt*(cr3(j,i) + cr8(j,i)*ubc2(i-1)))*psiold(j+1,i-2) &
+ thc*dt*cr4(j,i)*psiold(j-2,i-1) &
+ (thc*dt*cr5(j,i) + dr1(j,i))*psiold(j-1,i-1) &
+ (thc*dt*(cr6(j,i) + cr8(j,i)) + dr2(j,i))*psiold(j,i-1) &
+ (thc*dt*(cr7(j,i) + c15(j,i)*ubc2(i)) + dr3(j,i))*psiold(j+1,i-1) &
+ thc*dt*cl1(j,i)*psiold(j-2,i) &
+ (thc*dt*cl2(j,i) + dl1(j,i))*psiold(j-1,i) &
+ (thc*dt*(cl3(j,i) + c15(j,i)) + dl2(j,i))*psiold(j,i) &
+ dt*(c14(j,i) - cr8(j,i)*ubc2(i-1) + cr13(j,i)*ubc2(i+1))*psiold(j+1,i) &
+ thc*dt*cr9(j,i)*psiold(j-2,i+1) &
+ (thc*dt*cr10(j,i) + dr4(j,i))*psiold(j-1,i+1) &
+ (thc*dt*(cr11(j,i) + cr13(j,i)) + dr5(j,i))*psiold(j,i+1) &
+ (thc*dt*(cr12(j,i) - c15(j,i)*ubc2(i)) + dr6(j,i))*psiold(j+1,i+1) &
+ thc*dt*cr14(j,i)*psiold(j-1,i+2) &
+ thc*dt*cr15(j,i)*psiold(j,i+2) &
+ (thc*dt*(cr16(j,i) - cr13(j,i)*ubc2(i+1)))*psiold(j+1,i+2) &
+ dt*(-c15(j,i)*ub(i)*ubc1(i) - cr8(j,i)*ub(i-1)*ubc1(i-1) &
- cr13(j,i)*ub(i+1)*ubc1(i+1))
ELSE
rr(j-1) = thc*dt*( cr1(j,i) + bc81(i-1)*cr8(j,i) )*psiold(j-1,i-2) &
+ thc*dt*( cr2(j,i) - bc51(i-1)*cr8(j,i) )*psiold(j,i-2) &

```

```

+ thc*dt*cr4(j,i)*psiold(j-2,i-1) &
+ ( thc*dt*( cr5(j,i) + bc81(i)*cl5(j,i) ) + dr1(j,i) )*psiold(j-1,i-1) &
+ ( thc*dt*(cr6(j,i) - bc51(i)*cl5(j,i) - bc61(i-1)*cr8(j,i) ) &
+ dr2(j,i))*psiold(j,i-1) &
+ thc*dt*c11(j,i)*psiold(j-2,i) &
+ ( thc*dt*(cl2(j,i) - bc91(i-1)*cr8(j,i) + bc81(i+1)*cr13(j,i)) &
+ d11(j,i) )*psiold(j-1,i) &
+ ( thc*dt*( cl3(j,i) - bc61(i)*cl5(j,i) + bc71(i-1)*cr8(j,i) &
- bc51(i+1)*cr13(j,i) ) + d12(j,i) )*psiold(j,i) &
+ thc*dt*cr9(j,i)*psiold(j-2,i+1) &
+ ( thc*dt*( cr10(j,i) - bc91(i)*cl5(j,i) ) + dr4(j,i))*psiold(j-1,i+1) &
+ ( thc*dt*( cr11(j,i) + bc71(i)*cl5(j,i) - bc61(i+1)*cr13(j,i) ) &
+ dr5(j,i) )*psiold(j,i+1) &
+ thc*dt*( cr14(j,i) - bc91(i+1)*cr13(j,i) ) * psiold(j-1,i+2) &
+ thc*dt*( cr15(j,i) + bc71(i+1)*cr13(j,i) ) * psiold(j,i+2) &
+ th*dt*( cr1(j,i) + bc81(i-1)*cr8(j,i) )*psinew(j-1,i-2) &
+ th*dt*( cr2(j,i) - bc51(i-1)*cr8(j,i) )*psinew(j,i-2) &
+ th*dt*cr4(j,i)*psinew(j-2,i-1) &
+ ( th*dt*( cr5(j,i) + bc81(i)*cl5(j,i) ) - dr1(j,i))*psinew(j-1,i-1) &
+ ( th*dt*( cr6(j,i) - bc51(i)*cl5(j,i) - bc61(i-1)*cr8(j,i) ) &
- dr2(j,i) )*psinew(j,i-1) &
+ th*dt*cr9(j,i)*psinew(j-2,i+1) &
+ (th*dt*( cr10(j,i) - bc91(i)*cl5(j,i) ) - dr4(j,i))*psinew(j-1,i+1) &
+ (th*dt*( cr11(j,i) + bc71(i)*cl5(j,i) - bc61(i+1)*cr13(j,i) ) &
- dr5(j,i) )*psinew(j,i+1) &
+ th*dt*(cr14(j,i) - bc91(i+1)*cr13(j,i))*psinew(j-1,i+2) &
+ th*dt*(cr15(j,i) + bc71(i+1)*cr13(j,i))*psinew(j,i+2) &
+ thc*dt*( cr3(j,i) - bc21(i-1)*cr8(j,i) )*psiold(j+1,i-2) &
+ (thc*dt*(cr7(j,i) - bc21(i)*cl5(j,i) + bc31(i-1)*cr8(j,i)) &
+ dr3(j,i))*psiold(j+1,i-1) &
+ ( dt*(cl4(j,i) + bc31(i)*cl5(j,i) - bc41(i-1)*cr8(j,i) &
- bc21(i+1)*cr13(j,i)) + d13(j,i))*psiold(j+1,i) &
+ (thc*dt*(cr12(j,i) - bc41(i)*cl5(j,i) + bc31(i-1)*cr13(j,i)) &
+ dr6(j,i))*psiold(j+1,i+1) &
+ thc*dt*(cr16(j,i) - bc41(i+1)*cr13(j,i))*psiold(j+1,i+2) &
+ th*dt*( cr3(j,i) - bc21(i-1)*cr8(j,i) )*psinew(j+1,i-2) &
+ (th*dt*(cr7(j,i) - bc21(i)*cl5(j,i) + bc31(i-1)*cr8(j,i)) &
- dr3(j,i) )*psinew(j+1,i-1) &
+ (th*dt*(cr12(j,i) - bc41(i)*cl5(j,i) + bc31(i-1)*cr13(j,i)) &
- dr6(j,i) )*psinew(j+1,i+1) &
+ th*dt*(cr16(j,i) - bc41(i+1)*cr13(j,i))*psinew(j+1,i+2) &
+ dt*Tb(i)/bc1(i)*cl5(j,i) + dt*Tb(i+1)/bc1(i+1)*cr13(j,i) &
+ dt*Tb(i-1)/bc1(i-1)*cr8(j,i)
ENDIF
LB = ALLB(:,:,i)
LLB = LWRB(:,:,i)
indxR = ALLindx(:,i)
CALL banbks(LB,Nj-2,2,2,Nj-2,5,LLB,2,indxR,rr)
DO j = 2,Nj-1
    psinewi(j,i) = rr(j-1)
END DO
    rr = 0.0
END DO
!*****
! set RHS array and solve for psinew(2:Nj-1,Ni-1)
j = 2
i = Ni-1
psibcRo = (T(i+1)/sc1(i+1) - sc41(i+1)*sc88*ww(j-1) &
- sc71(i+1)*sc88*ww(j) + sc91(i+1)*sc88*ww(j+1) &
+ (sc31(i+1) - sc71(i+1)*sc99(j,i+1))*psiold(j-1,i+1) &
+ (sc41(i+1)*sc99(j-1,i+1) - sc61(i+1) &
+ sc91(i+1)*sc99(j+1,i+1))*psiold(j,i+1) &
+ sc71(i+1)*sc99(j,i+1)*psiold(j+1,i+1) &
- sc91(i+1)*sc99(j+1,i+1)*psiold(j+2,i+1))/(1+sc41(i+1)*sc99(j-1,i+1))
psibcRn = (T(i+1)/sc1(i+1) - sc41(i+1)*sc88*ww(j-1) &
- sc71(i+1)*sc88*ww(j) + sc91(i+1)*sc88*ww(j+1) &
+ (sc31(i+1) - sc71(i+1)*sc99(j,i+1))*psinew(j-1,i+1) &
+ (sc41(i+1)*sc99(j-1,i+1) - sc61(i+1) &
+ sc91(i+1)*sc99(j+1,i+1))*psinew(j,i+1) &
+ sc71(i+1)*sc99(j,i+1)*psinew(j+1,i+1) &

```

```

- sc91(i+1)*sc99(j+1,i+1)*psinew(j+2,i+1))/(1+sc41(i+1)*sc99(j-1,i+1))
rr(j-1) = (thc*dt*(cr1(j,i) - sc21(i-1)*cr4(j,i)))*psiold(j-1,i-2) &
+ (thc*dt*(cr2(j,i) + sc51(i-1)*cr4(j,i)))*psiold(j,i-2) &
+ (thc*dt*(cr3(j,i) - sc81(i-1)*cr4(j,i)))*psiold(j+1,i-2) &
+ (thc*dt*(cr5(j,i) - sc21(i)*cl1(j,i)) &
+ sc31(i-1)*cr4(j,i)) + dr1(j,i))*psiold(j-1,i-1) &
+ (thc*dt*(cr6(j,i) + sc51(i)*cl1(j,i)) &
- sc61(i-1)*cr4(j,i)) + dr2(j,i))*psiold(j,i-1) &
+ (thc*dt*(cr7(j,i) - sc81(i)*cl1(j,i)) + dr3(j,i))*psiold(j+1,i-1) &
+ thc*dt*cr8(j,i)*psiold(j+2,i-1) &
+ (dt*(cl2(j,i) + sc31(i)*cl1(j,i) - sc41(i-1)*cr4(j,i) &
+ cr14(j,i) - (cr9(j,i) + cr14(j,i)*sc99(j-1,i+1))) *psiold(j-1,i) &
* (sc21(i+1)+sc41(i+1))/(1.+sc41(i+1)*sc99(j-1,i+1))) *psiold(j-1,i) &
+ (thc*dt*(c13(j,i) - sc61(i)*cl1(j,i) - sc71(i-1)*cr4(j,i) &
+ cr15(j,i) + (cr9(j,i) + cr14(j,i)*sc99(j-1,i+1)) &
* (sc51(i+1)-sc71(i+1))/(1.+sc41(i+1)*sc99(j-1,i+1))) &
+ dl2(j,i))*psiold(j,i) &
+ (thc*dt*(c14(j,i) + sc91(i-1)*cr4(j,i) &
+ cr16(j,i) + (cr9(j,i) + cr14(j,i)*sc99(j-1,i+1)) &
* (sc91(i+1)-sc81(i+1))/(1.+sc41(i+1)*sc99(j-1,i+1))) &
+ dl3(j,i))*psiold(j+1,i) + thc*dt*cl5(j,i)*psiold(j+2,i) &
+ (thc*dt*(cr10(j,i) - sc41(i)*cl1(j,i) &
+ sc99(j,i+1)*cr15(j,i)) + dr4(j,i))*psiold(j-1,i+1) &
+ (thc*dt*(cr11(j,i) - sc71(i)*cl1(j,i) &
+ sc99(j+1,i+1)*cr16(j,i) - sc99(j-1,i+1)*cr14(j,i)) &
+ dr5(j,i))*psiold(j,i+1) &
+ (thc*dt*(cr12(j,i) + sc91(i)*cl1(j,i) - sc99(j,i+1)*cr15(j,i)) &
+ dr6(j,i))*psiold(j+1,i+1) &
+ thc*dt*(cr13(j,i) - sc99(j+1,i+1)*cr16(j,i))*psiold(j+2,i+1) &
+ (th*dt*(cr1(j,i) - sc21(i-1)*cr4(j,i)))*psinew(j-1,i-2) &
+ (th*dt*(cr2(j,i) + sc51(i-1)*cr4(j,i)))*psinew(j,i-2) &
+ (th*dt*(cr3(j,i) - sc81(i-1)*cr4(j,i)))*psinew(j+1,i-2) &
+ (th*dt*(cr5(j,i) - sc21(i)*cl1(j,i) &
+ sc31(i-1)*cr4(j,i)) - dr1(j,i))*psinew(j-1,i-1) &
+ (th*dt*(cr6(j,i) + sc51(i)*cl1(j,i) &
- sc61(i-1)*cr4(j,i)) - dr2(j,i))*psinew(j,i-1) &
+ (th*dt*(cr7(j,i) - sc81(i)*cl1(j,i)) - dr3(j,i))*psinew(j+1,i-1) &
+ th*dt*cr8(j,i)*psinew(j+2,i-1) &
+ (th*dt*(cr10(j,i) - sc41(i)*cl1(j,i)) - dr4(j,i))*psinew(j-1,i+1) &
+ (th*dt*(cr11(j,i) - sc71(i)*cl1(j,i) + sc99(j+1,i+1)*cr16(j,i) &
- sc99(j-1,i+1)*cr14(j,i)) - dr5(j,i))*psinew(j,i+1) &
+ (th*dt*(cr12(j,i) + sc91(i)*cl1(j,i) - sc99(j,i+1)*cr15(j,i)) &
- dr6(j,i))*psinew(j+1,i+1) &
+ th*dt*(cr13(j,i) - sc99(j+1,i+1)*cr16(j,i))*psinew(j+2,i+1) &
+ dt*T(i)/sc1(i)*cl1(j,i) + dt*T(i-1)/sc1(i-1)*cr4(j,i) &
+ dt*sc88*(cr15(j,i)*ww(j) + cr14(j,i)*ww(j-1) + cr16(j,i)*ww(j+1)) &
+ dt*(cr9(j,i)+cr14(j,i)*sc99(j-1,i+1))*(psibcRo*thc + psibcRn*th)
j = 3
rr(j-1) = thc*dt*cr1(j,i)*psiold(j-1,i-2) + thc*dt*cr2(j,i)*psiold(j,i-2) &
+ thc*dt*cr3(j,i)*psiold(j+1,i-2) + thc*dt*cr4(j,i)*psiold(j-2,i-1) &
+ (thc*dt*cr5(j,i) + dr1(j,i))*psiold(j-1,i-1) &
+ (thc*dt*cr6(j,i) + dr2(j,i))*psiold(j,i-1) &
+ (thc*dt*cr7(j,i) + dr3(j,i))*psiold(j+1,i-1) &
+ thc*dt*cr8(j,i)*psiold(j+2,i-1) + dt*cl1(j,i)*psiold(j-2,i) &
+ (thc*dt*(c12(j,i) + cr14(j,i)) + dl1(j,i))*psiold(j-1,i) &
+ (thc*dt*(c13(j,i) + cr15(j,i)) + dl2(j,i))*psiold(j,i) &
+ (thc*dt*(c14(j,i) + cr16(j,i)) + dl3(j,i))*psiold(j+1,i) &
+ thc*dt*cl5(j,i)*psiold(j+2,i) &
+ (thc*dt*(cr9(j,i) + sc99(j-1,i+1)*cr14(j,i)))*psiold(j-2,i+1) &
+ (thc*dt*(cr10(j,i)+sc99(j,i+1)*cr15(j,i))+dr4(j,i))*psiold(j-1,i+1) &
+ (thc*dt*(cr11(j,i) + sc99(j+1,i-1)*cr16(j,i) &
- sc99(j-1,i+1)*cr14(j,i)) + dr5(j,i))*psiold(j,i+1) &
+ (thc*dt*(cr12(j,i)-sc99(j,i+1)*cr15(j,i))+dr6(j,i))*psiold(j+1,i+1) &
+ (thc*dt*(cr13(j,i) - sc99(j+1,i+1)*cr16(j,i)))*psiold(j+2,i+1) &
+ th*dt*cr1(j,i)*psinew(j-1,i-2) + th*dt*cr2(j,i)*psinew(j,i-2) &
+ th*dt*cr3(j,i)*psinew(j+1,i-2) + th*dt*cr4(j,i)*psinew(j-2,i-1) &
+ (th*dt*cr5(j,i) - dr1(j,i))*psinew(j-1,i-1) &
+ (th*dt*cr6(j,i) - dr2(j,i))*psinew(j,i-1) &
+ (th*dt*cr7(j,i) - dr3(j,i))*psinew(j+1,i-1) &
+ th*dt*cr8(j,i)*psinew(j+2,i-1) &

```

```

+ (th*dt*(cr9(j,i) + sc99(j-1,i+1)*cr14(j,i)))*psinew(j-2,i+1) &
+ (th*dt*(cr10(j,i)+sc99(j,i+1)*cr15(j,i))-dr4(j,i))*psinew(j-1,i+1) &
+ (th*dt*(cr11(j,i) + sc99(j+1,i-1)*cr16(j,i)) &
- sc99(j-1,i+1)*cr14(j,i)) - dr5(j,i))*psinew(j,i+1) &
+ (th*dt*(cr12(j,i)-sc99(j,i+1)*cr15(j,i))-dr6(j,i))*psinew(j+1,i+1) &
+ (th*dt*(cr13(j,i)-sc99(j+1,i+1)*cr16(j,i)))*psinew(j+2,i+1) &
+ dt*sc88*(cr15(j,i)*ww(j) + cr14(j,i)*ww(j-1) + cr16(j,i)*ww(j+1))

DO j = 4,Nj-3
  rr(j-1) = thc*dt*cr1(j,i)*psiold(j-1,i-2) + thc*dt*cr2(j,i)*psiold(j,i-2) &
+ thc*dt*cr3(j,i)*psiold(j+1,i-2) + thc*dt*cr4(j,i)*psiold(j-2,i-1) &
+ (thc*dt*cr5(j,i) + dr1(j,i))*psiold(j-1,i-1) &
+ (thc*dt*cr6(j,i) + dr2(j,i))*psiold(j,i-1) &
+ (thc*dt*cr7(j,i) + dr3(j,i))*psiold(j+1,i-1) &
+ thc*dt*cr8(j,i)*psiold(j+2,i-1) + thc*dt*cl1(j,i)*psiold(j-2,i) &
+ (thc*dt*(c12(j,i) + cr14(j,i)) + dl1(j,i))*psiold(j-1,i) &
+ (thc*dt*(c13(j,i) + cr15(j,i)) + dl2(j,i))*psiold(j,i) &
+ (thc*dt*(c14(j,i) + cr16(j,i)) + dl3(j,i))*psiold(j+1,i) &
+ thc*dt*c15(j,i)*psiold(j+2,i) &
+ (thc*dt*(cr9(j,i) + sc99(j-1,i+1)*cr14(j,i)))*psiold(j-2,i+1) &
+ (thc*dt*(cr10(j,i)+sc99(j,i+1)*cr15(j,i))+dr4(j,i))*psiold(j-1,i+1) &
+ (thc*dt*(cr11(j,i) + sc99(j+1,i-1)*cr16(j,i)) &
- sc99(j-1,i+1)*cr14(j,i)) + dr5(j,i))*psiold(j,i+1) &
+ (thc*dt*(cr12(j,i)-sc99(j,i+1)*cr15(j,i))-dr6(j,i))*psiold(j+1,i+1) &
+ (thc*dt*(cr13(j,i)-sc99(j+1,i+1)*cr16(j,i)))*psiold(j+2,i+1) &
+ dt*sc88*(cr15(j,i)*ww(j) + cr14(j,i)*ww(j-1) + cr16(j,i)*ww(j+1))

END DO
j = Nj-2
rr(j-1) = thc*dt*cr1(j,i)*psiold(j-1,i-2) + thc*dt*cr2(j,i)*psiold(j,i-2) &
+ thc*dt*cr3(j,i)*psiold(j+1,i-2) + thc*dt*cr4(j,i)*psiold(j-2,i-1) &
+ (thc*dt*cr5(j,i) + dr1(j,i))*psiold(j-1,i-1) &
+ (thc*dt*cr6(j,i) + dr2(j,i))*psiold(j,i-1) &
+ (thc*dt*cr7(j,i) + dr3(j,i))*psiold(j+1,i-1) &
+ thc*dt*cr8(j,i)*psiold(j+2,i-1) + thc*dt*cl1(j,i)*psiold(j-2,i) &
+ (thc*dt*(c12(j,i) + cr14(j,i)) + dl1(j,i))*psiold(j-1,i) &
+ (thc*dt*(c13(j,i) + cr15(j,i)) + dl2(j,i))*psiold(j,i) &
+ (thc*dt*(c14(j,i) + cr16(j,i)) + dl3(j,i))*psiold(j+1,i) &
+ dt*c15(j,i)*psiold(j+2,i) &
+ (thc*dt*(cr9(j,i) + sc99(j-1,i+1)*cr14(j,i)))*psiold(j-2,i+1) &
+ (thc*dt*(cr10(j,i)+sc99(j,i+1)*cr15(j,i))+dr4(j,i))*psiold(j-1,i+1) &
+ (thc*dt*(cr11(j,i) + sc99(j+1,i-1)*cr16(j,i)) &
- sc99(j-1,i+1)*cr14(j,i)) + dr5(j,i))*psiold(j,i+1) &
+ (thc*dt*(cr12(j,i)-sc99(j,i+1)*cr15(j,i))-dr6(j,i))*psiold(j+1,i+1) &
+ (thc*dt*(cr13(j,i)-sc99(j+1,i+1)*cr16(j,i)))*psiold(j+2,i+1) &
+ dt*sc88*(cr15(j,i)*ww(j) + cr14(j,i)*ww(j-1) + cr16(j,i)*ww(j+1))

IF (ibbcflag.EQ.0) THEN
  j = Nj-1

```

```

rr(j-1) = thc*dt*cr1(j,i)*psiold(j-1,i-2) + thc*dt*cr2(j,i)*psiold(j,i-2) &
+ (thc*dt*(cr3(j,i) + cr8(j,i)*ubc2(i-1)))*psiold(j+1,i-2) &
+ thc*dt*cr4(j,i)*psiold(j-2,i-1) &
+ (thc*dt*(cr5(j,i) + dr1(j,i))*psiold(j-1,i-1) &
+ (thc*dt*(cr6(j,i) + cr8(j,i)) + dr2(j,i))*psiold(j,i-1) &
+ (thc*dt*(cr7(j,i) + cl5(j,i)*ubc2(i)) + dr3(j,i))*psiold(j+1,i-1) &
+ thc*dt*c11(j,i)*psiold(j-2,i) &
+ (thc*dt*(cl2(j,i) + cr14(j,i)) + dl1(j,i))*psiold(j-1,i) &
+ (thc*dt*(cl3(j,i) + cr15(j,i) + cl5(j,i)) + dl2(j,i))*psiold(j,i) &
+ (dt*(+cl4(j,i) + cr16(j,i) - cr8(j,i)*ubc2(i-1)) &
+ dl3(j,i))*psiold(j+1,i) &
+ (thc*dt*(cr9(j,i) + sc99(j-1,i+1)*cr14(j,i)))*psiold(j-2,i+1) &
+ (thc*dt*(cr10(j,i)+sc99(j,i+1)*cr15(j,i))+dr4(j,i))*psiold(j-1,i+1) &
+ (thc*dt*(cr11(j,i) + cr13(j,i) &
- sc99(j-1,i+1)*cr14(j,i)) + dr5(j,i))*psiold(j,i+1) &
+ (thc*dt*(cr12(j,i) - cl5(j,i)*ubc2(i) &
- sc99(j,i+1)*cr15(j,i)) + dr6(j,i))*psiold(j+1,i+1) &
+ th*dt*cr1(j,i)*psinew(j-1,i-2) + th*dt*cr2(j,i)*psinew(j,i-2) &
+ (th*dt*(cr3(j,i) + cr8(j,i)*ubc2(i-1)))*psinew(j+1,i-2) &
+ th*dt*cr4(j,i)*psinew(j-2,i-1) &
+ (th*dt*cr5(j,i) - dr1(j,i))*psinew(j-1,i-1) &
+ (th*dt*(cr6(j,i) + cr8(j,i)) - dr2(j,i))*psinew(j,i-1) &
+ (th*dt*(cr7(j,i) + cl5(j,i)*ubc2(i)) - dr3(j,i))*psinew(j+1,i-1) &
+ (th*dt*(cr9(j,i) + sc99(j-1,i+1)*cr14(j,i)))*psinew(j-2,i+1) &
+ (th*dt*(cr10(j,i)+sc99(j,i+1)*cr15(j,i))-dr4(j,i))*psinew(j-1,i+1) &
+ (th*dt*(cr11(j,i) - sc99(j-1,i+1)*cr14(j,i) &
+ cr13(j,i)) - dr5(j,i) )*psinew(j,i+1) &
+ (th*dt*(cr12(j,i) - sc99(j,i+1)*cr15(j,i) &
- cl5(j,i)*ubc2(i)) - dr6(j,i))*psinew(j+1,i+1) &
+ dt*sc88*(cr15(j,i)*ww(j) + cr14(j,i)*ww(j-1)) &
+ dt*(-cl5(j,i)*ub(i)*ubc1(i) - cr8(j,i)*ub(i-1)*ubc1(i-1)) &
+ cr13(j,i)*dt*((1+sc99(j+1,i+1)*ubc2(i+1)) *ubc1(i+1)*ub(i+1)) &
/ (1.-sc99(j+1,i+1)*ubc2(i+1))/(1.-sc99(j+1,i+1)*ubc2(i+1))) ) &
+ cr16(j,i)*dt*( sc88*ww(j+1)/(1.-sc99(j+1,i+1)*ubc2(i+1)) &
- sc99(j+1,i+1)*ubc1(i+1)*ub(i+1)/(1.-sc99(j+1,i+1)*ubc2(i+1)) )

ELSE
bbcRbo = (Tb(i+1)/bc1(i+1) - bc41(i+1)*sc88*ww(j+1)+bc71(i+1)*sc88*ww(j) &
- bc91(i+1)*sc88*ww(j-1) &
+ (bc31(i+1) - bc71(i+1)*sc99(j,i+1))*psiold(j+1,i+1) &
+ (-bc41(i+1)*sc99(j+1,i+1)+bc61(i+1) &
+ bc91(i+1)*sc99(j-1,i+1))*psiold(j,i+1) &
+ bc71(i+1)*sc99(j,i+1)*psiold(j-1,i+1) &
- bc91(i+1)*sc99(j-1,i+1)*psiold(j-2,i+1)) / (1-bc41(i+1)*sc99(j+1,i+1))
bbcRbn = (Tb(i+1)/bc1(i+1) - bc41(i+1)*sc88*ww(j+1)+bc71(i+1)*sc88*ww(j) &
- bc91(i+1)*sc88*ww(j-1) &
+ (bc31(i+1) - bc71(i+1)*sc99(j,i+1))*psinew(j+1,i+1) &
+ (-bc41(i+1)*sc99(j+1,i+1)+bc61(i+1) &
+ bc91(i+1)*sc99(j-1,i+1))*psinew(j,i+1) &
+ bc71(i+1)*sc99(j,i+1)*psinew(j-1,i+1) &
- bc91(i+1)*sc99(j-1,i+1)*psinew(j-2,i+1)) / (1-bc41(i+1)*sc99(j+1,i+1))

rr(j-1) = thc*dt*( cr1(j,i) + bc81(i-1)*cr8(j,i) )*psiold(j-1,i-2) &
+ thc*dt*( cr2(j,i) - bc51(i-1)*cr8(j,i) )*psiold(j,i-2) &
+ thc*dt*cr4(j,i)*psiold(j-2,i-1) &
+ ( thc*dt*( cr5(j,i) + bc81(i)*cl5(j,i) + dr1(j,i) )*psiold(j-1,i-1) &
+ ( thc*dt*(cr6(j,i) - bc51(i)*cl5(j,i) - bc61(i-1)*cr8(j,i) ) &
+ dr2(j,i))*psiold(j,i-1) &
+ thc*dt*c11(j,i)*psiold(j-2,i) &
+ ( thc*dt*(cl2(j,i) - bc91(i-1)*cr8(j,i) +cr14(j,i) &
+ (cr13(j,i)-cr16(j,i)*sc99(j+1,i+1))*(bc81(i+1)-bc91(i+1)) &
/ (1-bc41(i+1)*sc99(j+1,i+1)) ) + dl1(j,i) )*psiold(j-1,i) &
+ ( thc*dt*( cl3(j,i) - bc61(i)*cl5(j,i) + bc71(i-1)*cr8(j,i) &
+ cr15(j,i)+(cr13(j,i)-cr16(j,i)*sc99(j+1,i+1))*(bc71(i+1)-bc51(i+1)) &
/ (1-bc41(i+1)*sc99(j+1,i+1)) ) + dl2(j,i) )*psiold(j,i) &
+ th*dt*( cr1(j,i) + bc81(i-1)*cr8(j,i) )*psinew(j-1,i-2) &
+ th*dt*( cr2(j,i) - bc51(i-1)*cr8(j,i) )*psinew(j,i-2) &
+ th*dt*cr4(j,i)*psinew(j-2,i-1) &
+ ( th*dt*( cr5(j,i) + bc81(i)*cl5(j,i) ) - dr1(j,i))*psinew(j-1,i-1) &
+ ( th*dt*( cr6(j,i) - bc51(i)*cl5(j,i) - bc61(i-1)*cr8(j,i) ) &
- dr2(j,i) )*psinew(j,i-1) &

```

```

        + dt*sc88*(cr15(j,i)*ww(j) + cr14(j,i)*ww(j-1) + cr16(j,i)*ww(j+1) ) &
        + (cr13(j,i) - cr16(j,i)*sc99(j+1,i+1))*(thc*bbcRbo + th*bbcRbn) &
        + dt*Tb(i)/bc1(i)*cl5(j,i) + dt*Tb(i-1)/bc1(i-1)*cr8(j,i)

ENDIF
CALL banbks(LHSC,Nj-2,2,2,Nj-2,5,LWRC,2,indxC,rr)
DO j = 2,Nj-1
    psinewi(j,i) = rr(j-1)
END DO
rr = 0.0
! ****
adiff= abs(psinewi - psinew)
XXX = MAXVAL(adiff)
DO jjj = 1,Nj
    DO iii = 1,Ni
        IF (ABS(psinewi(jjj,iii)-psinew(jjj,iii)).EQ.XXX) THEN
            jmax = jjj
            imax = iii
        ENDIF
    END DO
END DO
! WRITE(*,*) psinew(39,40),psinew(jmax,imax),jmax,imax
IF ( XXX .LT. TOL ) EXIT
ic = ic + 1
psinew = psinewi
END DO INNER
IF (Nw.GT.10) THEN
    psiave = psiave + psinew
    icc = icc + 1
ENDIF
psiold = psinew
END DO DTLOOP
IF (NW.GT.10) THEN
    WRITE(*,*) Nsim,Nw,psiave(2,45)/(icc*1.),Ho
ELSE
    WRITE(*,*) Nsim,Nw,Ho
ENDIF
END DO WAVES
! ****
! create products
! ****
99 rho = 1000.0
Hta = Hta / Nwaves
sxxa = sxxa / Nwaves
IF (isetz.eq.2) THEN
    DO i = 2, Ni-1
        DO j = 2,Nj-1
            u(j,i) = -(-psinew(j+1,i) + psinew(j-1,i))/(2.*dz(i))
            tau(j,i) = -rho*e(j,i) * (psinew(j-1,i) - 2.*psinew(j,i) &
                                         + psinew(j+1,i))/(dz(i)**2.)
        END DO
        tau(1,i) = -rho*e(1,i)*(2.*psinew(1,i) - 5.*psinew(2,i) &
                               + 4.*psinew(3,i) - psinew(4,i))/(dz(i)**2.)
        tau(Nj,i) = -rho*e(Nj,i)*(2.*psinew(Nj,i) - 5.*psinew(Nj-1,i) &
                               + 4.*psinew(Nj-2,i)-psinew(Nj-3,i))/(dz(i)**2.)
        u(1,i) = (-3.*psinew(1,i) + 4.*psinew(2,i) - psinew(3,i))/(2.*dz(i))
        u(Nj,i) = (3.*psinew(Nj,i) - 4.*psinew(Nj-1,i) + psinew(Nj-2,i))/(2.*dz(i))
        IF (ibbcflag.EQ.0) u(Nj,i) = ub(i)
    END DO
    ua(:,:,1) = u
    ta(:,:,1) = tau
    psiave = psinew
ELSE
    ! ***compute the average velocity and shear stress fields
    psiave = psiave/icc
    DO j = 2,Nj-1
        DO i = 2,Ni-1
            u(j,i) = -(-psiave(j,i-1)+psiave(j,i+1))*ziz/(2*dzi) &
                      -(-psiave(j-1,i)+psiave(j+1,i))*etaz(i)/(2*data)
        END DO
    END DO
END IF

```

```

w(j,i) = ( -psiave(j,i-1) + psiave(j,i+1) ) * zix / (2*dzi) &
         - ( -psiave(j-1,i) + psiave(j+1,i) ) * etax(j,i) / (2*data)
tau(j,i) = rho*e(j,i) * ( &
    (zix**2.-ziz**2.)*(psiave(j,i-1)-2*psiave(j,i)+psiave(j,i+1))/(dxi*2.) &
    + (zix*etax(j,i)-ziz*etaz(i))*(psiave(j-1,i-1)-psiave(j-1,i+1)) &
    - psiave(j+1,i-1)+psiave(j+1,i+1)/(2*dzi*data) &
    + (etax(j,i)**2. - etaz(i)**2.)*(psiave(j-1,i)-2*psiave(j,i) &
    + psiave(j+1,i))/(data**2.) + (zixx-zizz)*(-psiave(j,i-1) &
    + psiave(j,i+1))/(2*dzi) + (etaxx(j,i)-etazz(i))*(-psiave(j-1,i) &
    + psiave(j+1,i))/(2*data) )
END DO
END DO
j = 1;
DO i = 2,Ni-1
    u(j,i) = -(-psiave(j,i-1) + psiave(j,i+1))*ziz/(2*dzi) &
              -(-3.*psiave(j,i) + 4.*psiave(j+1,i) &
              - psiave(j+2,i))*etaz(i)/(2*data)
    w(j,i) = (-psiave(j,i-1) + psiave(j,i+1))*zix/(2*dzi) &
              + (-3.*psiave(j,i) + 4.*psiave(j+1,i) &
              - psiave(j+2,i))*etax(j,i)/(2*data)
    tau(j,i) = rho*e(j,i) * ( &
        (zix**2.-ziz**2.)*(psiave(j,i-1)-2*psiave(j,i)+psiave(j,i+1))/(dxi**2.) &
        + (zix*etax(j,i)-ziz*etaz(i))*(psiave(j+2,i-1)-4*psiave(j+1,i-1) &
        + 3*psiave(j,i-1)-psiave(j+2,i+1)+4*psiave(j+1,i+1) &
        - 3*psiave(j,i+1))/(2*dzi*data) + (etax(j,i)**2. &
        - etaz(i)**2.)*(-psiave(j+3,i)+4*psiave(j+2,i)-5*psiave(j+1,i) &
        + 2*psiave(j,i))/(data**2.) + (zixx-zizz)*(-psiave(j,i-1) &
        + psiave(j,i+1))/(2*dzi) + (etaxx(j,i)-etazz(i))*(-psiave(j+2,i) &
        + 4*psiave(j+1,i)-3*psiave(j,i))/(2*data) )
END DO
j = Nj
DO i = 2,Ni-1
    u(j,i) = -(-psiave(j,i-1)+psiave(j,i+1))*ziz/(2*dzi) &
              -(3.*psiave(j,i) - 4.*psiave(j-1,i) + psiave(j-2,i)) &
              *etaz(i)/(2*data)
    w(j,i) = (-psiave(j,i-1)+psiave(j,i+1))*zix/(2*dzi) &
              + (-3.*psiave(j,i)+4.*psiave(j-1,i)-psiave(j-2,i)) &
              *etax(j,i)/(2*data)
    tau(j,i) = rho*e(j,i) / COS(m(i)) * ( &
        (zix**2.-ziz**2.)*(psiave(j,i-1)-2*psiave(j,i)+psiave(j,i+1))/(dxi**2.) &
        + (zix*etax(j,i)-ziz*etaz(i))*(-psiave(j-2,i-1) + 4*psiave(j-1,i-1) &
        - 3*psiave(j,i-1)+psiave(j-2,i+1)-4*psiave(j-1,i+1)+3*psiave(j,i+1)) &
        / (2*dzi*data) + (etax(j,i)**2.-etaz(i)**2.)*(-psiave(j-3,i) &
        + 4*psiave(j-2,i)-5*psiave(j-1,i)+2*psiave(j,i))/(data**2.) &
        + (zixx-zizz)*(-psiave(j,i-1)+psiave(j,i+1))/(2*dzi) &
        + (etaxx(j,i)-etazz(i))*(psiave(j-2,i)-4*psiave(j-1,i)&
        + 3*psiave(j,i))/(2*data) )
END DO
IF (ibbcflag.EQ.0) u(Nj,:) = ub(:)
ua(:,:,1) = u
wa(:,:,1) = w
ta(:,:,1) = tau
ENDIF
DO j = 1,Nj
    DO i = 1,Ni
        mag(j,i) = sqrt(ua(j,i,1)*ua(j,i,1) + wa(j,i,1)*wa(j,i,1))
        IF (wa(j,i,1).eq.0.0.and.ua(j,i,1).eq.0.0) THEN
            theta(j,i) = 0.0
        ELSE
            theta(j,i)= atan2d(wa(j,i,1),ua(j,i,1))
            thdist(j,i) = atan2d(wa(j,i,1)*10.0,ua(j,i,1))
        ENDIF
    END DO
END DO
! create output data file for SURFER
100 FORMAT(1x,2f8.3,e12.4,2I5,3f10.5,2f8.1,2f12.4)
DO i = 1,Ni
    DO j = 1,Nj

```

```

      WRITE (11,100) x(i)-toe,z(j,i),psiave(j,i),i,j,ua(j,i,1),wa(j,i,1), &
                    mag(j,i),theta(j,i),thdist(j,i),ta(j,i,1),Hta(i)
      END DO
      END DO
! *** Cut out velocity profiles to match
200 FORMAT (1x,22f9.3)
DO j = 1,Nj
      WRITE (12,200) (-100.0*(z(Nj,p(i))-z(j,p(i))),ua(j,p(i),1)*100.0, i=1,nml)
      WRITE (14,200) (-100.0*(z(Nj,p(i))-z(j,p(i))),ta(j,p(i),1), i=1,nml)
END DO

! *** Create SURFER blanking files ***
WRITE (13,*) Ni+3,1
WRITE (13,*) x(1)-toe,1.0
WRITE (15,*) Ni,'',1
DO i = 1,Ni
      WRITE (13,*) x(i)-toe,z(1,i)
      WRITE (15,*) x(i)-toe,'',z(Nj,i)
END DO
WRITE (15,*) Ni,'',1
DO i = 1,Ni
      WRITE (15,*) x(i)-toe,'',Hta(i)*100.0
END DO
WRITE (15,*) Ni,'',1
DO i = 1,Ni
      WRITE (15,*) x(i)-toe,'',setp(i)*100.0
END DO
WRITE (15,*) Ni,'',1
DO i = 1,Ni
      WRITE (15,*) x(i)-toe,'',psiave(1,i)*100.0*100.0
END DO
WRITE (15,*) Ni,1
DO i = 1,Ni
      WRITE (15,*) x(i)-toe,'',sxxa(i)
END DO
WRITE (13,*) x(Ni)-toe,1.0
WRITE (13,*) x(1)-toe,1.0
GOTO 999

! **** Hot start routine ****
777 IF (ihotflag.EQ.0) THEN
      OPEN (unit=10, file = TRIM(hotfile)//".dat", status = "OLD")
      DO ii = 1,Ni
          READ(10,*) xx,xx,skip,i,j,xx,xx,xx,xx,xx,xx,xx
          DO jj = 2,Nj
              READ(10,*) xx,xx,psiold(jj,ii),i,j,xx,xx,xx,xx,xx,xx,xx
          END DO
      END DO
      CLOSE(10)
ELSEIF (ihotflag.eq.1) THEN
      ALLOCATE(d1(Nj),d2(Nj),d3(Nj),d4(Nj),d5(Nj),rhs(Nj-2) &
               ,lhs(Nj-2,5),llhs(Nj-2,2),indxj(Nj-2))
      DO i = 2,Ni-1
          d1=0.0;d2=0.0;d3=0.0;d4=0.0;d5=0.0;lhs=0.0;llhs=0.0;rhs=0.0;indxj=0.0
          DO j=1,Nj
              d1(j) = e(Nj-1-j,i) - dz(i)*ez(Nj-1-j,i)
              d2(j) = -4.*e(Nj-1-j,i) + 2.*dz(i)*ez(Nj-1-j,i) &
                      + dz(i)**2.*ezz(Nj-1-j,i)
              d3(j) = 6.*e(Nj-1-j,i) - 2.*dz(i)**2.*ezz(Nj-1-j,i)
              d4(j) = -4.*e(Nj-1-j,i) - 2.*dz(i)*ez(Nj-1-j,i) &
                      + dz(i)**2.*ezz(Nj-1-j,i)
              d5(j) = e(Nj-1-j,i) + dz(i)*ez(Nj-1-j,i)
          END DO
          DO j = 2,Nj-1
              lhs(j-1,1) = d1(j)
              lhs(j-1,2) = d2(j)
              lhs(j-1,3) = d3(j)
              lhs(j-1,4) = d4(j)
              lhs(j-1,5) = d5(j)
          END DO
      END DO
  
```

```

    END DO
    IF (ibbcflag.EQ.0) THEN
        lhs(1,3) = d3(2) + d1(2)
        rhs(1) = -2.*dz(i)*d1(2)*ub(i) - d2(2)*psiold(Nj,i)
    ELSE
        lhs(1,3) = d3(2) - d1(2)
        rhs(1) = -(2.*d1(2) + d2(2))*psiold(Nj,i) + d1(2)*Tb(i)*dz(i)**2.
    ENDIF
    rhs(2) = -d1(3)*psiold(Nj,i)
    rhs(Nj-3) = -d5(Nj-2)*psiold(1,i)
    lhs(Nj-2,3) = d3(Nj-1) - d5(Nj-1)
    rhs(Nj-2) = -(2.*d5(Nj-1) + d4(Nj-1))*psiold(1,i) &
                + d5(Nj-1)*T(i)*dz(i)*dz(i)
    CALL bandec(lhs,Nj-2,2,2,Nj-2,5,llhs,2,indxj,da)
    CALL banbks(lhs,Nj-2,2,2,Nj-2,5,llhs,2,indxj,rhs)
    DO j = 1,Nj-2
        psiold(Nj-j,i) = rhs(j)
    END DO
    END DO
    DEALLOCATE(d1,d2,d3,d4,d5,rhs,lhs,llhs,indxj)
ELSE
    psiold = 0.0
ENDIF
GOTO 778
! ****
! ***** Routine to set up FDE coefficients *****
888 rat1 = dzi/deta
    rat2 = (dzi/deta)**2.
    rat3 = (dzi/deta)**3.
    rat4 = (dzi/deta)**4.
    sc88 = 2.*dzi/zix
    goz = 1. / (rat4)
! *** change to multiply thru by data^4 rather than dzi^4
ALLOCATE(a1(Nj,Ni),a2(Nj,Ni),a3(Nj,Ni),a4(Nj,Ni),a5(Nj,Ni),a6(Nj,Ni) &
, a7(Nj,Ni),a8(Nj,Ni),a9(Nj,Ni),a10(Nj,Ni),a11(Nj,Ni),a12(Nj,Ni) &
, a13(Nj,Ni),a14(Nj,Ni),b1(Nj,Ni),b2(Nj,Ni),b3(Nj,Ni),b4(Nj,Ni),b5(Nj,Ni))
DO ii = 1,Ni
    sc1(ii) = (etax(1,ii)**2. - etaz(ii)**2.)/data**2. &
                - (etaxx(1,ii)-etazz(ii))/2/data
    sc21(ii) = ((zix**2.-ziz**2.)/dzi**2. + 3./2.* (zix*etax(1,ii) &
                - ziz*etaz(ii))/dzi/deta - (zixx-zizz)/2.0/dzi)/sc1(ii)
    sc31(ii) = (2.*(zix**2.-ziz**2.)/dzi**2. &
                + 2.* (etax(1,ii)**2.-etaz(ii)**2.)/data**2.)/sc1(ii)
    sc41(ii) = sc21(ii)
    sc51(ii) = (4./2.* (zix*etax(1,ii)-ziz*etaz(ii))/dzi/deta)/sc1(ii)
    sc61(ii) = ((etax(1,ii)**2.-etaz(ii)**2.)/data**2. + &
                (etaxx(1,ii)-etazz(ii))/2/data)/sc1(ii)
    sc71(ii) = sc51(ii)
    sc81(ii) = (1./2.* (zix*etax(1,ii)-ziz*etaz(ii))/dzi/deta)/sc1(ii)
    sc91(ii) = sc81(ii)
    bc1(ii) = (etax(Nj,ii)**2.-etaz(ii)**2.)/data**2. - &
                (etaxx(Nj,ii)-etazz(ii))/2/data
    bc21(ii) = ((zix**2.-ziz**2.)/dzi**2. - 3./2.* (zix*etax(Nj,ii) &
                - ziz*etaz(ii))/dzi/deta - (zixx-zizz)/2.0/dzi)/bc1(ii)
    bc31(ii) = (2.*(zix**2.-ziz**2.)/dzi**2. + 2.* (etax(Nj,ii)**2. &
                - etaz(ii)**2.)/data**2.)/bc1(ii)
    bc41(ii) = ((zix**2.-ziz**2.)/dzi**2. + 3./2.* (zix*etax(Nj,ii) &
                - ziz*etaz(ii))/dzi/deta + (zixx-zizz)/2.0/dzi)/bc1(ii)
    bc51(ii) = (2.* (zix*etax(Nj,ii)-ziz*etaz(ii))/dzi/deta)/bc1(ii)
    bc61(ii) = ((etax(Nj,ii)**2.-etaz(ii)**2.)/data**2. - &
                (etaxx(Nj,ii)-etazz(ii))/2/data)/bc1(ii)
    bc71(ii) = bc51(ii)
    bc81(ii) = (1./2.* (zix*etax(Nj,ii)-ziz*etaz(ii))/dzi/deta)/bc1(ii)
    bc91(ii) = bc81(ii)
    ubc1(ii) = SQRT(m(ii)**2.+1)*2*deta/(m(ii)*etax(Nj,ii)+etaz(ii))
    ubc2(ii) = (m(ii)*zix+ziz)/(m(ii)*etax(Nj,ii)+etaz(ii))*deta/dzi
DO jj = 1,Nj
    sc99(jj,ii) = etax(jj,ii)/zix*dzi/deta
    a1(jj,ii) = goz*( e(jj,ii)*(zix**4. + 2.*zix**2.*ziz**2. + ziz**4.) )
    a2(jj,ii) = goz*(e(jj,ii)*(4.*zix**3.*etax(jj,ii)+4*zix**2.*ziz*etaz(ii) &

```

```

+ 4.*ziz**2.*zix*etax(jj,ii) + 4.*ziz**3.*etaz(ii)))
a3(jj,ii) = goz*(e(jj,ii)*(6.*zix**2.*etax(jj,ii)**2. &
+ 2.*zix**2.*etaz(ii)**2. + 8.*zix*ziz*etax(jj,ii)*etaz(ii) &
+ 2.*ziz**2.*etax(jj,ii)**2. + 6.*ziz**2.*etaz(ii)**2.))
a4(jj,ii) = goz*(e(jj,ii)*(4*zix*etax(jj,ii)**3. + 4.*ziz*etaz(ii)**3. &
+ 4.*zix*etax(jj,ii)*etaz(ii)**2. + 4.*ziz*etax(jj,ii)**2.*etaz(ii)))
a5(jj,ii) = goz*(e(jj,ii)*(etax(jj,ii)**4. + etaz(ii)**4. &
+ 2.*etax(jj,ii)**2.*etaz(ii)**2.))
a6(jj,ii) = goz*(e(jj,ii)*(6.*zix**2.*zixx + 2.*zix**2.*zizz &
+ 8.*zix*ziz*zixz + 2.*zixx*ziz**2. + 6.*ziz**2.*zizz) &
+ 2.*ex(jj,ii)*zix**3. + 2.*ez(jj,ii)*zix**2.*ziz &
+ 2.*ex(jj,ii)*zix*ziz**2. + 2.*ez(jj,ii)*ziz**3.)
a7(jj,ii) = goz*(e(jj,ii)*(12.*zix*zixx*etax(jj,ii) &
+ 6.*zix**2.*etaxx(jj,ii) + 2.*zix**2.*etazz(ii) &
+ 8.*zix*zixz*etaz(ii) + 8.*zix*ziz*etaxz(jj,ii) &
+ 4.*zix*zizz*etax(jj,ii) + 8.*zixz*ziz*etax(jj,ii) &
+ 4.*zixx*ziz*etaz(ii) + 2.*ziz**2.*etaxx(jj,ii) &
+ 12.*ziz*zizz*etaz(ii) + 6.*ziz**2.*etazz(ii)) &
+ 6.*ex(jj,ii)*zix**2.*etax(jj,ii) + 2.*ez(jj,ii)*(zix**2.*etaz(ii) &
+ 2.*zix*ziz*etax(jj,ii)) + 2.*ex(jj,ii)*(ziz**2.*etax(jj,ii) &
+ 2.*zix*ziz*etaz(ii)) + 6.*ez(jj,ii)*ziz**2.*etaz(ii))
a8(jj,ii) = goz*(e(jj,ii)*(12.*zix*etax(jj,ii)*etaxx(jj,ii) &
+ 6.*zixx*etax(jj,ii)**2. + 2.*zizz*etax(jj,ii)**2. &
+ 8.*zix*etax(jj,ii)*etaxz(jj,ii) + 4.*zix*etax(jj,ii)*etazz(ii) &
+ 8.*zix*etaz(ii)*etaxz(jj,ii) + 8.*zixz*etax(jj,ii)*etaz(ii) &
+ 4.*ziz*etaxx(jj,ii)*etaz(ii) + 2.*zixx*etaz(ii)**2. &
+ 12.*ziz*etaz(ii)*etazz(ii) + 6.*ziz**2.*etaz(ii)**2.) &
+ 6.*ex(jj,ii)*zix*etax(jj,ii)**2. + 2.*ez(jj,ii) &
* (ziz*etax(jj,ii)**2. + 2.*zix*etax(jj,ii)*etaz(ii)) &
+ 2.*ex(jj,ii)*(zix*etaz(ii)**2. + 2.*ziz*etax(jj,ii)*etaz(ii)) &
+ 6.*ez(jj,ii)*ziz*etaz(ii)**2.)
a9(jj,ii) = goz*(e(jj,ii)*(6.*etax(jj,ii)**2.*etaxx(jj,ii) &
+ 2.*etax(jj,ii)**2.*etazz(ii) + 8.*etax(jj,ii)*etaz(ii)*etaxz(jj,ii) &
+ 2.*etaxx(jj,ii)*etaz(ii)**2. + 6.*etaz(ii)**2.*etazz(ii)) &
+ 2.*ex(jj,ii)*etax(jj,ii)**3. + 2.*ez(jj,ii)*etax(jj,ii)**2.*etaz(ii) &
+ 2.*ex(jj,ii)*etax(jj,ii)*etaz(ii)**2. + 2.*ez(jj,ii)*etaz(ii)**3.)
a10(jj,ii) = goz*(e(jj,ii)*(4.*zix*zixxx + 3.*zixx**2. + 2.*zixx*zizz &
+ 4.*zixxx*ziz+4.*zixz**2.+4.*zix*zixzz+4.*ziz*zizz+3.*zizz**2.) &
+ (exx(jj,ii)-ezz(jj,ii))*zix**2. + 4.*exx(jj,ii)*zix*ziz &
- (exx(jj,ii)-ezz(jj,ii))*ziz**2. + 6.*ex(jj,ii)*zix*zixx &
+ 2.*ez(jj,ii)*(2.*zix*zixz + zixx*ziz) &
+ 2.*ex(jj,ii)*(2*zixz*ziz+zix*ziz) + 6.*ez(jj,ii)*ziz*zizz)
a11(jj,ii) = goz*(e(jj,ii)*(4.*zixxx*etax(jj,ii) + 6.*zixx*etaxx(jj,ii) &
+ 4.*zix*etaxxx(jj,ii) + 2.*zixx*etazz(ii) + 4.*zixx*etazz(ii) &
+ 4.*ziz*etaxxx(jj,ii) + 2.*zizz*etaxx(jj,ii) + 4.*zix*etaxzz(jj,ii) &
+ 8.*zixz*etaxz(jj,ii) + 4.*zixz*etax(jj,ii) + 4.*zizzz*etaz(ii) &
+ 6.*zizz*etazz(ii) + 4.*ziz*etazzz(ii)) &
+ (exx(jj,ii)-ezz(jj,ii))*2*zix*etax(jj,ii) &
+ 4.*exx(jj,ii)*(zix*etaz(ii) + ziz*etax(jj,ii)) &
- (exx(jj,ii)-ezz(jj,ii))*2.*ziz*etaz(ii) &
+ 6.*ex(jj,ii)*(zix*etaxx(jj,ii) + zixx*etax(jj,ii)) &
+ 2.*ez(jj,ii)*(zixx*etaz(ii)+ziz*etaxx(jj,ii)+2.*zix*etaxz(jj,ii) &
+ 2.*zixz*etax(jj,ii)) + 2.*ex(jj,ii)*(zizz*etax(jj,ii)+zix*etazz(ii) &
+ 2.*zixz*etaz(ii) + 2.*ziz*etaxz(jj,ii)) &
+ 6.*ez(jj,ii)*(ziz*etazz(ii) + zizz*etaz(ii)) )
a12(jj,ii) = goz*(e(jj,ii)*(4.*etax(jj,ii)*etaxxx(jj,ii) &
+ 3.*etaxx(jj,ii)*etaxx(jj,ii) + 2.*etaxx(jj,ii) &
+ 4.*etaxxz(jj,ii)*etaz(ii) + 4.*etaxz(jj,ii)*etaxz(jj,ii) &
+ 4.*etax(jj,ii)*etaxzz(jj,ii) &
+ 4.*etaz(ii)*etazzz(ii) + 3.*etazzz(ii)*etazzz(ii)) &
+ (exx(jj,ii)-ezz(jj,ii))*etax(jj,ii)*etax(jj,ii) &
+ 4.*exx(jj,ii)*etax(jj,ii)*etaz(ii) &
- (exx(jj,ii)-ezz(jj,ii))*etaz(ii)*etaz(ii) &
+ 6.*ex(jj,ii)*etax(jj,ii)*etaxx(jj,ii) &
+ 6.*ez(jj,ii)*etaz(ii)*etazzz(ii) &
+ 2.*ez(jj,ii)*(2.*etax(jj,ii)*etaxz(jj,ii)+etaxx(jj,ii)*etaz(ii)) &
+ 2.*ex(jj,ii)*(2.*etaxx(jj,ii)*etaz(ii) + etax(jj,ii)*etazz(ii)))
a13(jj,ii) = goz*(e(jj,ii)*(zixxxx + 2.*zixxzz + zizzzz) &
+ (exx(jj,ii)-ezz(jj,ii))*zixx + 4.*exx(jj,ii)*zixz &
- (exx(jj,ii)-ezz(jj,ii))*zizz + 2.*ex(jj,ii)*zixxx &

```

```

    + 2.*ez(jj,ii)*zixxz + 2.*ex(jj,ii)*zixzz + 2.*ez(jj,ii)*zizzz)
a14(jj,ii) = goz*( e(jj,ii)*(etaxxxx(jj,ii) + 2.*etaxxzz(jj,ii)) &
    + etazzzz(ii)) + (exx(jj,ii)-ezz(jj,ii))*etaxx(jj,ii) &
    + 4.*exz(jj,ii)*etaxz(jj,ii) - (exx(jj,ii)-ezz(jj,ii))*etazz(ii) &
    + 2.*ex(jj,ii)*etaxxx(jj,ii) + 2.*ez(jj,ii)*etaxxzz(jj,ii) &
    + 2.*ex(jj,ii)*etaxzz(jj,ii) + 2.*ez(jj,ii)*etazzz(ii) )
b1(jj,ii) = (zix**2. + ziz**2.)
b2(jj,ii) = 2.*(zix*etax(jj,ii) + ziz*etaz(ii))
b3(jj,ii) = etax(jj,ii)**2. + etaz(ii)**2.
b4(jj,ii) = zixx + zizz
b5(jj,ii) = etaxx(jj,ii) + etazz(ii)
c11(jj,ii) = (a5(jj,ii)*rat4 - a9(jj,ii)/2.*rat4*data)
c12(jj,ii) = (-4.*a5(jj,ii)*rat4 - 2.*a3(jj,ii)*rat2 &
    + a7(jj,ii)*rat2*data + a9(jj,ii)*rat4*data &
    + a12(jj,ii)*rat4*data**2. - a14(jj,ii)/2.*rat4*data**3.)
c13(jj,ii) = (6.*a1(jj,ii) + 4.*a3(jj,ii)*rat2 + 6.*a5(jj,ii)*rat4 &
    - 2.*a10(jj,ii)*dzi**2. - 2.*a12(jj,ii)*rat4*data**2.)
c14(jj,ii) = (-4.*a5(jj,ii)*rat4 - 2.*a3(jj,ii)*rat2 &
    - a7(jj,ii)*rat2*data - a9(jj,ii)*rat4*data &
    + a12(jj,ii)*rat4*data**2. + a14(jj,ii)/2.*rat4*data**3.)
c15(jj,ii) = (a5(jj,ii)*rat4 + a9(jj,ii)/2.*rat4*data)
cr1(jj,ii) = a2(jj,ii)/4.*rat1
cr2(jj,ii) = (a1(jj,ii) - a6(jj,ii)*dzi/2)
cr3(jj,ii) = -a2(jj,ii)/4.*rat1
cr4(jj,ii) = a4(jj,ii)/4.*rat3
cr5(jj,ii) = (-a2(jj,ii)/2.*rat1 + a3(jj,ii)*rat2 - a4(jj,ii)/2.*rat3 &
    - a7(jj,ii)/2.*rat2*data - a8(jj,ii)/2.*rat3*data &
    + a11(jj,ii)/4.*rat3*data**2.)
cr6(jj,ii) = (-4.*a1(jj,ii) - 2.*a3(jj,ii)*rat2 + a6(jj,ii)*dzi &
    + a8(jj,ii)*rat3*data + a10(jj,ii)*dzi**2. - a13(jj,ii)/2.*dzi**3.)
cr7(jj,ii) = (a2(jj,ii)/2.*rat1 + a3(jj,ii)*rat2 + a4(jj,ii)/2.*rat3 &
    + a7(jj,ii)/2.*rat2*data - a8(jj,ii)/2.*rat3*data &
    - a11(jj,ii)/4.*rat3*data**2.)
cr8(jj,ii) = -a4(jj,ii)/4.*rat3
cr9(jj,ii) = -a4(jj,ii)/4.*rat3
cr10(jj,ii) = (a2(jj,ii)/2.*rat1+a3(jj,ii)*rat2 + a4(jj,ii)/2.*rat3 &
    - a7(jj,ii)/2.*rat2*data + a8(jj,ii)/2.*rat3*data &
    - a11(jj,ii)/4.*rat3*data**2.)
cr11(jj,ii) = (-4.*a1(jj,ii) - 2.*a3(jj,ii)*rat2 - a6(jj,ii)*dzi &
    - a8(jj,ii)*rat3*data + a10(jj,ii)*dzi**2. + a13(jj,ii)/2.*dzi**3.)
cr12(jj,ii) = (-a2(jj,ii)/2.*rat1 + a3(jj,ii)*rat2 - a4(jj,ii)/2.*rat3 &
    + a7(jj,ii)/2.*rat2*data + a8(jj,ii)/2.*rat3*data &
    + a11(jj,ii)/4.*rat3*data**2.)
cr13(jj,ii) = a4(jj,ii)/4.*rat3
cr14(jj,ii) = -a2(jj,ii)/4.*rat1
cr15(jj,ii) = (a1(jj,ii) + a6(jj,ii)*dzi/2.)
cr16(jj,ii) = a2(jj,ii)/4.*rat1
d11(jj,ii) = b3(jj,ii)*data**2. - b5(jj,ii)*data**3./2.
d12(jj,ii) = -2.*b1(jj,ii)/rat2*data**2. - 2.*b3(jj,ii)*data**2.
d13(jj,ii) = b3(jj,ii)*data**2. + b5(jj,ii)*data**3./2.
dr1(jj,ii) = b2(jj,ii)/rat1*data**2./4.
dr2(jj,ii) = b1(jj,ii)/rat2*data**2. - b4(jj,ii)/2./rat1*data**3.
dr3(jj,ii) = -b2(jj,ii)/rat1*data**2./4.
dr4(jj,ii) = -b2(jj,ii)/rat1*data**2./4.
dr5(jj,ii) = b1(jj,ii)/rat2*data**2. + b4(jj,ii)/2./rat1*data**3.
dr6(jj,ii) = b2(jj,ii)/rat1*data**2./4.

END DO
END DO
DEALLOCATE(a1,a2,a3,a4,a5,a6,a7,a8,a9,a10,a11,a12,a13,a14,b1,b2,b3,b4,b5)

! *****COLUMN 2 LHS matrix from j = 2 to j = Nj-1:
i = 2
DO j = 2,Nj-1
    LHSA(j-1,1)=-th*dt*c11(j,i)
    LHSA(j-1,2)=d11(j,i) + th*dt*(-cl2(j,i) - cr1(j,i))
    LHSA(j-1,3)=d12(j,i) + th*dt*(-cl3(j,i) - cr2(j,i))
    LHSA(j-1,4)=d13(j,i) + th*dt*(-cl4(j,i) - cr3(j,i))
    LHSA(j-1,5)=-th*dt*c15(j,i)
END DO
j = 2

```

```

LHSA(1,3) = dl2(j,i) + th*dt*(-cl3(j,i) - cr2(j,i) + cl1(j,i)*sc61(i) &
           - cr9(j,i)*sc51(i+1) - (cr4(j,i)-cr1(j,i)*sc99(j-1,i-1)) &
           *(sc51(i-1)-sc71(i-1))/(1-sc21(i-1)*sc99(j-1,i-1)) )
LHSA(1,4) = dl3(j,i) + th*dt*(-cl4(j,i) - cr3(j,i) + cr9(j,i)*sc81(i+1) &
           - (cr4(j,i)-cr1(j,i)*sc99(j-1,i-1))*(sc91(i-1)-sc81(i-1)) &
           /(1-sc21(i-1)*sc99(j-1,i-1)) )

j = Nj-1
IF (ibbcflag.EQ.0) THEN
    LHSA(Nj-2,3) = dl2(j,i) + th*dt*(-cl3(j,i) - cr2(j,i) - cl5(j,i))
ELSE
    LHSA(Nj-2,3)=dl2(j,i)-th*dt*cl3(j,i) + th*dt*( cl5(j,i)*bc61(i) &
           - cr2(j,i) + cr13(j,i)*bc51(i+1) &
           - (cr8(Nj-1,i)+cr3(Nj-1,i)*sc99(j+1,i-1)) &
           *(bc71(i-1)-bc51(i-1))/(1+bc21(i-1)*sc99(j+1,i-1)) )
    LHSA(Nj-2,2)= dl1(j,i)-th*dt*c12(j,i) + th*dt*( &
           - cr13(j,i)*bc81(i+1) - cr1(j,i) &
           - (cr8(Nj-1,i)+cr3(Nj-1,i)*sc99(j+1,i-1)) &
           *(bc81(i-1)-bc91(i-1))/(1+bc21(i-1)*sc99(j+1,i-1)) )
ENDIF
CALL bandec(LHSA,Nj-2,2,2,Nj-2,5,LWRA,2,indxA,da)

! ***** COLUMN 3>>Ni-2 LHS *****
! ALLB >> LHS in compact form, the third dimension is the column #
DO i = 3,Ni-2
    DO j = 2,Nj-1
        ALLB(j-1,1,i) = -th*dt*c11(j,i)
        ALLB(j-1,2,i) = dl1(j,i) - th*dt*c12(j,i)
        ALLB(j-1,3,i) = dl2(j,i) - th*dt*c13(j,i)
        ALLB(j-1,4,i) = dl3(j,i) - th*dt*c14(j,i)
        ALLB(j-1,5,i) = -th*dt*c15(j,i)
    END DO
    j=2
    ALLB(1,3,i) = dl2(j,i)-th*dt*c13(j,i) + th*dt*( cl1(j,i)*sc61(i) &
           + cr4(j,i)*sc71(i-1) - cr9(j,i)*sc51(i+1))
    ALLB(1,4,i) = dl3(j,i)-th*dt*c14(j,i) + th*dt*( &
           - cr4(j,i)*sc91(i-1) + cr9(j,i)*sc81(i+1))

    j = Nj-1
    IF (ibbcflag.EQ.0) THEN
        ALLB(j-1,3,i) = dl2(j,i) - th*dt*c13(Nj-1,i) - th*dt*c15(Nj-1,i)
    ELSE
        ALLB(j-1,3,i)=dl2(j,i)-th*dt*c13(j,i) + th*dt*( cl5(j,i)*bc61(i) &
           - cr8(j,i)*bc71(i-1) + cr13(j,i)*bc51(i+1))
        ALLB(j-1,2,i) = dl1(j,i)-th*dt*c12(j,i) + th*dt*( &
           - cr13(j,i)*bc81(i+1) + cr8(j,i)*bc91(i-1))
    END IF
    LB = ALLB(:,:,i)
    CALL bandec(LB,Nj-2,2,2,Nj-2,5,LLB,2,indxB,db)
    ALLB(:,:,i) = LB
    LWRB(:,:,i) = LLB
    ALLindx(:,:,i) = indxB
END DO

! ***** column Ni-1 LHS: *****
i = Ni-1
DO j = 2,Nj-1
    LHSC(j-1,1)=-th*dt*c11(j,i)
    LHSC(j-1,2)=dl1(j,i) + th*dt*(-cl2(j,i) - cr14(j,i))
    LHSC(j-1,3)=dl2(j,i) + th*dt*(-cl3(j,i) - cr15(j,i))
    LHSC(j-1,4)=dl3(j,i) + th*dt*(-cl4(j,i) - cr16(j,i))
    LHSC(j-1,5)=-th*dt*c15(j,i)
END DO
j = 2
LHSC(1,3) = dl2(j,i) - th*dt*c13(j,i) + th*dt*( cl1(j,i)*sc61(i) &
           + cr4(j,i)*sc71(i-1) - cr15(j,i) - (cr9(j,i) + cr14(j,i)*sc99(j-1,i+1))* &
           (sc51(i+1)-sc71(i+1))/(1+sc41(i+1)*sc99(j-1,i+1)))
LHSC(1,4) = dl3(j,i) - th*dt*c14(j,i) + th*dt*( &
           - cr4(j,i)*sc91(i-1) - cr16(j,i) - (cr9(j,i) + cr14(j,i)*sc99(j-1,i+1))* &
           (sc91(i+1)-sc81(i+1))/(1+sc41(i+1)*sc99(j-1,i+1)) )

j = Nj-1
IF (ibbcflag.EQ.0) THEN

```

```

LHSC(Nj-2,3) = dl2(j,i) + th*dt*(-cl3(j,i) - cr15(j,i) - cl5(j,i))
ELSE
  LHSC(Nj-2,3)=dl2(j,i)-th*dt*cl3(j,i) + th*dt*( cl5(j,i)*bc61(i) &
    - cr15(j,i) - cr8(j,i)*bc71(i-1) &
    - (cr13(Nj-1,i)-cr16(Nj-1,i)*sc99(j+1,i+1)) &
    + (bc71(i+1)-bc51(i+1))/(1-bc41(i+1)*sc99(j+1,i+1)) )
  LHSC(Nj-2,2)= dl1(j,i)-th*dt*c12(j,i) + th*dt*( &
    + cr8(j,i)*bc91(i-1) - cr14(j,i) &
    - (cr13(Nj-1,i)-cr16(Nj-1,i)*sc99(j+1,i+1)) &
    + (bc71(i+1)-bc51(i+1))/(1-bc41(i+1)*sc99(j+1,i+1)) )
ENDIF
CALL bandec(LHSC,Nj-2,2,2,Nj-2,5,LWRC,2,indxC,dc)
GOTO 889
! *****
1335 WRITE (*,*) "set up experimental parameters"
! *** Cox & Kobayashi, 1997 *** 1/35 slope, rough bottom
! 80x41
IF (iexpflag.EQ.1) THEN
  Hs = 0.113
  Hinit = Hs
  dzi = 0.2
  Twv = 2.2
  kappa = 0.84
  toe = 2.0
  nml = 8
  ALLOCATE (p(nml))
  p = (/32,44,50,56,62,68,45,46/)
  nml = 8
ENDIF
! *** Ting & Kirby, 1994 *** 1/35 slope, smooth bottom
! 77x41
IF (iexpflag.EQ.2) THEN
  Hs = 0.116
  Hinit = Hs
  dzi = 0.2
  Twv = 2.0
  kappa = 0.90
  toe = 2.0
  nml = 8
  ALLOCATE (p(nml))
  p = (/8,41,45,48,51,54,57,61/)
ENDIF
! *** Nadaokah and Kondoh, 1982 *** 1/20 slope, smooth bottom
! 79x41
IF (iexpflag.EQ.3) THEN
  Hs = 0.223
  Hinit = Hs
  dzi = 0.2
  Twv = 1.32
  kappa = 0.75
  toe = 2.0
  nml = 8
  ALLOCATE (p(nml))
  p = (/46,50,51,55,60,65,70,75/)
ENDIF
! *** Okayasu & Katayama, 1992 *** 1/20 barred lab beach
! 52x33
IF (iexpflag.EQ.4) THEN
  Hs = 0.11
  Hinit = Hs / 1.416
  Twv = 1.14
  dzi = 0.2
  kappa = 0.90
  toe = 2.0
  nml = 8
  ALLOCATE (p(nml))
  p = (/23,31,35,39,43,47,51,32/)
ENDIF
! *** Delta Flume Experiment Test #1A
! 93x31

```

```

IF (iexpflag.EQ.5) THEN
    Hs = 0.94
    Hinit = Hs / 1.416
    dzi = 2.0
    Twv = 4.82
    kappa = 0.9
    toe = 0.0
    nml = 11
    ALLOCATE (p(nml))
    p = (/33,51,52,58,66,70,71,73,77,79,81/)
ENDIF
! *** Smith, Svendsen, Putrevu 1992 *** DELILAH DUCK
!84x31
IF (iexpflag.EQ.6) THEN
    Hs = 0.60
    Hinit = Hs / 1.416
    Twv = 9.7
    dzi = 2.0
    kappa = 0.78
    toe = 0.0
    nml = 6
    ALLOCATE (p(nml))
    p = (/19,27,36,46,55,68/)
ENDIF
! *** Perdido Key example R-38 ***
! 65x31
IF (iexpflag.EQ.7) THEN
    Hs = 1.00
    Hinit = Hs / 1.416
    Twv = 6.0
    dzi = 3.0
    kappa = 0.78
    toe = 0.0
    nml = 6
    ALLOCATE (p(nml))
    p = (/19,27,36,41,46,55/)
ENDIF
GOTO 1336
! ****
! ****
999      WRITE(*,*) 'Simulation Complete'
WRITE (*,*) "Now Run simulation # ",nsim+1
READ (16,*) (a, i=1,1)
CLOSE(11)
CLOSE(12)
CLOSE(13)
CLOSE(14)
CLOSE(15)
DEALLOCATE (P)
IF(iwave.EQ.0) DEALLOCATE (wvht)

END DO
END

! ****
! ****
! SUBROUTINE for LU decomposition (from Numerical Recipes, Press et al. 1986)
! -----
SUBROUTINE bandec(a,n,m1,m2,np,mp,al,mp1,indx,d)
INTEGER m1,m2,mp,mp1,n,np,indx(n)
DOUBLE PRECISION d,a(np,mp),al(np,mp1),TINY
PARAMETER (TINY=1.e-20)
INTEGER i,j,k,l,mm
DOUBLE PRECISION dum
mm=m1+m2+1
if (mm.gt.mp.or.m1.gt.mp1.or.n.gt.mp) pause 'bad args in bandec'
l=m1
do 13 i=m1,m1
    do 11 j=m1+2-i,mm
        a(i,j-1)=a(i,j)
11    continue
13    continue

```

```

11      continue
12      l=l-1
13      do 12 j=mm-1,mm
14          a(i,j)=0.
15      continue
16      d=1.
17      l=m1
18      do 18 k=1,n
19          dum=a(k,1)
20          i=k

21          if(l.lt.n)l=l+1
22          do 14 j=k+1,l
23              if(abs(a(j,1)).gt.abs(dum))then
24                  dum=a(j,1)
25                  i=j
26              endif
27          continue
28          indx(k)=i
29          if(dum.eq.0.) a(k,1)=TINY
30          if(i.ne.k)then
31              d=-d
32              do 15 j=1,mm
33                  dum=a(k,j)
34                  a(k,j)=a(i,j)
35                  a(i,j)=dum
36              continue
37          endif
38          do 17 i=k+1,l
39              dum=a(i,1)/a(k,1)
40              al(k,i-k)=dum
41              do 16 j=2,mm
42                  a(i,j-1)=a(i,j)-dum*a(k,j)

43          continue
44          a(i,mm)=0.
45      continue
46      continue
47      return
48  END
! ****
! subroutine to solve Ax=b for b (from Numerical Recipes, Press et al. 1986)
! -----
SUBROUTINE banbks(a,n,m1,m2,np,mp,al,mpl,indx,b)
INTEGER m1,m2,mp,mp1,n,np,indx(n)
DOUBLE PRECISION a(np,mp),al(np,mp1),b(n)
INTEGER i,k,l,mm
DOUBLE PRECISION dum
mm=m1+m2+1
if(mm.gt.mp.or.m1.gt.mpl.or.n.gt.mp) pause 'bad args in banbks'
l=m1
do 12 k=1,n
    i=indx(k)
    if(i.ne.k)then
        dum=b(k)
        b(k)=b(i)
        b(i)=dum
    endif
    if(l.lt.n)l=l+1
    do 11 i=k+1,l
        b(i)=b(i)-al(k,i-k)*b(k)
    continue
11    continue
12    l=1
    do 14 i=n,1,-1

        dum=b(i)
        do 13 k=2,l
            dum=dum-a(i,k)*b(k+i-1)

```

```

13      continue
14      b(i)=dum/a(i,1)
           if(l.lt.mm) l=l+1
14      continue
      return
END

! ****
! SUBROUTINES for wave height variation, psi at the surface, stress at surface
! and setup/setdown
SUBROUTINE SHOAL(nn,Ho,Ht,pd,h,eps,m,dEdx,psis,dzi,setup,ub,taurat,ib,kappa,im, &
               isetq1,iofftau1,sxx,itrans,iddy1)
DOUBLE PRECISION, DIMENSION(nn) :: h,dEdx,psis,Ht,m,eps,setup,ub,taurat,sxx
DOUBLE PRECISION, DIMENSION(nn) :: Aroll,ECg,wvlsf,mfluxact,efluxact
DOUBLE PRECISION, DIMENSION(10,4) :: psi,sfe,mflux,lol,eflux
DOUBLE PRECISION, DIMENSION(10) :: hlol
DOUBLE PRECISION, DIMENSION(4) :: HHB
DOUBLE PRECISION Lo,kappa,BB,AA,AB,AC,AD,AE,AF,gamma,Htold,hLo,HoLo,kapact
DOUBLE PRECISION mfluxup,mfluxdown,lolup,loldown,efluxup,efluxdown

psis = 0.0;Ht = 0.0 ; dEdx = 0.0 ; jj = 0 ; kk = 0
wvnum = 0.1
wvnum2 = 0.1
g = 9.81
rho = 1000.0
pi = ACOS(-1.0)
Lo = g * pd * pd / 2.0 / pi
HoLo = Ho / Lo
hLo = h(1)/Lo
Eprev = 0.0
setup = 0.0
CALL sfheight(hLo,HoLo,Lo,Ht(1))
CALL psitable(psi,hlol,HHB,sfe,eflux,mflux,lol)
DO i = 2,nn-1
    hLo = (h(i)+setup(i-1)) / Lo
    CALL sfheight(hLo,HoLo,Lo,Ht(i))
    CALL dsp((h(i)+setup(i-1)),pd,wvnum)
    IF (abs(Ht(i)-Ht(i-1)).GT.1e-6.AND.im.EQ.1) THEN
        setup(i) = -Ht(i)*Ht(i)*wvnum/8.0/SINH(2.0*h(i)*wvnum)
    ENDIF
    IF ( ( Ht(i)/ (h(i)+setup(i)) ) .GT. kappa) GOTO 6
    hLo = (h(i)+setup(i))/Lo      ; ! relative depth
    htr = Ht(i)/(kappa*(h(i)+setup(i)))   ; ! local height ratio
    IF (htr.GT.1.0) htr = 1.0
    DO jj = 1,10
        IF (hLo.LT.hlol(jj)) THEN
            phLo = (hLo-hlol(jj-1))/(hlol(jj)-hlol(jj-1))
            GOTO 2
        ENDIF
    END DO
2   DO kk = 1,4
        IF (htr.LE.HHB(kk)) THEN
            phhb = (htr-HHB(kk-1))/(HHB(kk)-HHB(kk-1))
            GOTO 3
        ENDIF
    END DO
3   IF (kk.eq.1) THEN
        psidown = psi(jj-1,kk)
        edown = sfe(jj-1,kk)
        efluxdown = eflux(jj-1,kk)
        mfluxdown = mflux(jj-1,kk)
        loldown = lol(jj-1,kk)
    ELSE
        psidown = psi(jj-1,kk-1) + phLo*(psi(jj,kk-1)-psi(jj-1,kk-1))
        edown = sfe(jj-1,kk-1) + phLo*(sfe(jj,kk-1)-sfe(jj-1,kk-1))
        efluxdown = eflux(jj-1,kk-1) + phLo*(eflux(jj,kk-1)-eflux(jj-1,kk-1))
        mfluxdown = mflux(jj-1,kk-1) + phLo*(mflux(jj,kk-1)-mflux(jj-1,kk-1))
        loldown = lol(jj-1,kk-1) + phLo*(lol(jj,kk-1)-lol(jj-1,kk-1))
    ENDIF

```

```

psiup = psi(jj-1,kk) + phLo*(psi(jj,kk)-psi(jj-1,kk))
eup = sfe(jj-1,kk) + phLo*(sfe(jj,kk)-sfe(jj-1,kk))
efluxup = eflux(jj-1,kk) + phLo*(eflux(jj,kk)-eflux(jj-1,kk))
mfluxup = mflux(jj-1,kk) + phLo*(mflux(jj,kk)-mflux(jj-1,kk))
lolup = lol(jj-1,kk) + phLo*(lol(jj,kk)-lol(jj-1,kk))
psiactual = psidown + phhb*(psiup-psidown)
efluxact(i) = efluxdown + phhb*(efluxup-efluxdown)
mfluxact(i) = mfluxdown + phhb*(mfluxup-mfluxdown)
wvlsf(i) = (loldown + phhb*(lolup-loldown))*Lo
psis(i) = -psiactual*pd*g*Ht(i)
sxx(i) = mfluxact(i)*rho*g*Ht(i)*Ht(i)/8.
E = rho*g*8.*Ht(i)*Ht(i)*(edown + phhb*(eup-edown))
ECg(i) = efluxact(i)*rho*g*Ht(i)*Ht(i)/8./pd*wvlsf(i)

IF (ieddy1.LT.2) THEN
    eps(i) = eps(1)
ELSE
    eps(i) = 0.01* (h(i)+setp(i))* SQRT(g*(h(i)+setp(i)))
ENDIF

IF (Ht(i).NE.Ht(i-1)) THEN
    dEdx(i) = ((-sxx(i-1)+sxx(i))/(dzi)/3.)/rho/eps(i)
    IF (iofftaul.eq.1) dEdx(i) = 0.0 ; ! option: no offshore stress
    taurat(i) = 0.1 *dEdx(i)
ENDIF
Eprev = E
ub(i) = -psis(i)/(h(i)+setp(i))
END DO
6   i = i - 1
Hb = Ht(i)
kapact = Ht(i)/(h(i)+setp(i))
db = h(i) ; ! stillwater breaking depth for Dally's model
setpb = setp(i)

! *** After break, apply Dally, Dean, & Dalrymple (1985) breaker model
xkappa = 0.15
gamma = 0.4
ib=i
Htold = 0.0
Aroll(i) = 0.0 ; ! initial value for Dally's surface roller area
betac = 1.0
betad = 0.15
! *** Numerical version of Dally's breaker model
ibb = 0

DO j=i+1,nn
    IF (im.EQ.1) setp(j) = setpb + 0.186*((h(i)+setp(i)) - (h(j)))
34  ZZ=1.0
    ZZ2 = 1.0
    BB=Ht(j-1)/kapact
    IF(BB.LT.(h(j-1)+setp(j-1)).AND.ibb.EQ.0) GOTO 36
    ibb = 1
    GOTO 38
36  ZZ=0.0
38  IF (Ht(j-1)/GAMMA.LT.(h(j-1)+setp(j-1))) ZZ2 = 0.0
    AA=ZZ2*ZZ*xkappa*dzi/(      h(j-1)+setp(j-1)      +      h(j)+setp(j)      )
    AB=1.0+AA
    AC=1.0-AA
    AD=Ht(j-1)**2.*SQRT((h(j-1)+setp(j-1)))
    AE=AA*GAMMA**2.*((      h(j-1)+setp(j-1)      ) **2.5 + ( h(j)+setp(j) )**2.5 )
    AF=(AD*AC+AE)/AB
    Ht(j)=SQRT(AF/SQRT((h(j)+setp(j))))
    wvdiff = (Ht(j) - Htold)/Ht(j)*100.0
    IF (ABS(wvdiff).GT.0.01) THEN
        Htold = Ht(j)
        GOTO 34
    ENDIF
    IF (ieddy1.LT.2) THEN
        eps(j) = eps(1)
    ELSE

```

```

    eps(j) = 0.01* (h(j)+setp(j))* SQRT(g*(h(j)+setp(j)))
ENDIF

IF (isetql.EQ.4.OR.isetql.EQ.5) THEN
! Dally and Brown (1995) surface roller model & stream function theory i.s.z.
    hLo = (h(j)+setp(j))/Lo      ; ! relative depth
    htr = Ht(j)/(kappa*(h(j)+setp(j)))   ; ! local height ratio
    IF (htr.GT.1.0) htr = 1.0
    DO jj = 1,10
        IF (hLo.LT.hlol(jj)) THEN
            phLo = (hLo-hlol(jj-1))/(hlol(jj)-hlol(jj-1))
            GOTO 62
        ENDIF
    END DO
    DO kk = 1,4
        IF (htr.LE.HHB(kk)) THEN
            phhb = (htr-HHB(kk-1))/(HHB(kk)-HHB(kk-1))
            GOTO 63
        ENDIF
    END DO
62   IF (kk.eq.1) THEN
        psidown = psi(jj-1,kk)
        edown = sfe(jj-1,kk)
        efluxdown = eflux(jj-1,kk)
        mfluxdown = mflux(jj-1,kk)
        loldown = lol(jj-1,kk)
    ELSE
        psidown = psi(jj-1,kk-1) + phLo*(psi(jj,kk-1)-psi(jj-1,kk-1))
        edown = sfe(jj-1,kk-1) + phLo*(sfe(jj,kk-1)-sfe(jj-1,kk-1))
        efluxdown = eflux(jj-1,kk-1) + phLo*(eflux(jj,kk-1)-eflux(jj-1,kk-1))
        mfluxdown = mflux(jj-1,kk-1) + phLo*(mflux(jj,kk-1)-mflux(jj-1,kk-1))
        loldown = lol(jj-1,kk-1) + phLo*(lol(jj,kk-1)-lol(jj-1,kk-1))
    ENDIF
    psiup = psi(jj-1,kk) + phLo*(psi(jj,kk)-psi(jj-1,kk))
    eup = sfe(jj-1,kk) + phLo*(sfe(jj,kk)-sfe(jj-1,kk))
    efluxup = eflux(jj-1,kk) + phLo*(eflux(jj,kk)-eflux(jj-1,kk))
    mfluxup = mflux(jj-1,kk) + phLo*(mflux(jj,kk)-mflux(jj-1,kk))
    lolup = lol(jj-1,kk) + phLo*(lol(jj,kk)-lol(jj-1,kk))
    psiactual = psidown + phhb*(psiup-psidown)
    efluxact(j) = efluxdown + phhb*(efluxup-efluxdown)
    mfluxact(j) = (mfluxdown + phhb*(mfluxup-mfluxdown))*rho*g*Ht(j)*Ht(j)/8.
    wvlsf(j) = (loldown + phhb*(lolup-loldown))*Lo
    psis(j) = -psiactual*pd*g*Ht(j)

! *** this psis(j) is the volume transport associated with the organized motion
    ECg(j) = efluxact(j)*rho*g*Ht(j)*Ht(j)/8./pd*wvlsf(j)
    E = rho*g/8.*Ht(j)*Ht(j)*(edown + phhb*(eup-edown))
! *** compute volume transport and Sxx associated with roller
    Aroll(j) =-((Ecg(j)-Ecg(j-1))+Aroll(j-1)*(-wvlsf(j-1)/pd)**2.&
*betac**2.+g*betad*dzi/2.)/(g*betad*dzi/2.+betac*betac*(wvlsf(j)/pd)**2.)
    IF (isetql.EQ.5) THEN
        psis(j) = psis(j) + Aroll(j)/rho
        sxx(j) = mfluxact(j) + Aroll(j)*betac*(wvlsf(j)/pd)
    ELSE
        psis(j) = psis(j)
        sxx(j) = mfluxact(j)
    ! just stream function description in the surf zone (and no need to patch)
    ENDIF
    dEdx(j) = -((-sxx(j-1)+sxx(j))/(dzi)/3.)/rho/eps(j)
    taurat(j) = 0.1 *dEdx(j)
ELSE
    CALL dsp((h(j)+setp(j)),pd,wvk)
    wvl = 2.*pi/wvk
    IF (isetql.EQ.1) THEN
        E = 0.125 * rho * g * Ht(j) * Ht(j)
        sxx(j) = 1.5*E
        psis(j) = E / rho / (wvl/pd)
        linear theory
    ELSEIF (isetql.EQ.2) THEN
        E = 0.125 * rho * g * Ht(j) * Ht(j) * 2./3.
    ENDIF
END

```

```

        sxx(j) = 1.5*E
        psis(j) = E / rho / (wvl/pd)
!      sawtooth wave theory
        ELSE
            sxx(j) = rho*g*Ht(j)*Ht(j)*(1.5*0.075 + 0.9*(h(j)+setp(j))/wvl)
            psis(j) = 0.1*SQRT(g/(h(j)+setp(j)))*Ht(j)*(h(j)+setp(j))
!      ^^^^ Svendsen (1984) surface roller approximation ^^^^
        ENDIF
        dEdx(j) = -((-sxx(j-1)+sxx(j))/(dzi)/3.)/rho/eps(j)
        taurat(j) = 0.1 *dEdx(j)
    ENDIF
END DO

! routine to attempt to bridge the transition region quantities
IF (isetq1.LT.4.AND.itrans.EQ.1) THEN
    psiref=psis(ib+1)
    sxxref=sxx(ib+1)
    DO n = i+1,nn
        IF (sxx(n).LT.sxx(ib)) GOTO 42
    END DO
42  nend = n - 1
    xfold = (nend-ib)*dzi
    IF (xfold.LE.dzi) xfold = 2.*dzi
    DO n = i+1,nn
        psis(n) = psis(n) - (psiref-psis(ib))*(exp(-(n-ib-1)*dzi/(xfold-dzi)))
        sxx(n)=sxx(n)-(sxxref-sxx(ib))*(exp(-(n-ib-1)*dzi/(xfold-dzi)))
    END DO
    DO n = i+1,nn
        dEdx(n) = -((-sxx(n-1)+sxx(n))/dzi/3.)/rho/eps(n)
    END DO
ENDIF
dEdx(1:2) = 0.0
dEdx(nn) = 0.0
psis(1) = 0.0
RETURN
END

! *****
SUBROUTINE dsp(dpth,prd,wvnumk)
    DOUBLE PRECISION :: wvdiff,wvnumold,wvnumkdp,dpth
    pi = ACOS(-1.0)
    g = 9.81
    wvnumold = 1.0
300   wvnumkdp = (2*pi/prd)**2 / (g*TANH(wvnumold*dpth))
    wvdiff = ABS(wvnumkdp - wvnumold)
    IF (wvdiff.lt.0.00001) THEN
        wvnumk = wvnumkdp
        RETURN
    ENDIF
    wvnumold = wvnumkdp
    GOTO 300
END
! *****
! *****STREAM FUNCTION WAVE THEORY - lookup tables for psi, H/Hb, and E
SUBROUTINE psitable(psi,hlol,HHB,sfe,eflux1,mflux1,lol1)
    INTEGER :: a,b,c,d
    DOUBLE PRECISION, DIMENSION(10,4) :: psi,sfe,eflux1,mflux1,lol1
    DOUBLE PRECISION, DIMENSION(10) :: hlol
    DOUBLE PRECISION, DIMENSION(4) :: HHB
    a=1;b=2;c=3;d=4
    psi(1,a)=-0.000178; psi(1,b)=-0.000246; psi(1,c)=-0.000286; psi(1,d)=-0.000312
    psi(2,a)=-0.000405; psi(2,b)=-0.000574; psi(2,c)=-0.000638; psi(2,d)=-0.000632
    psi(3,a)=-0.000724; psi(3,b)=-0.001075; psi(3,c)=-0.001219; psi(3,d)=-0.001185
    psi(4,a)=-0.001206; psi(4,b)=-0.001938; psi(4,c)=-0.002233; psi(4,d)=-0.002296
    psi(5,a)=-0.002188; psi(5,b)=-0.003854; psi(5,c)=-0.004620; psi(5,d)=-0.004386
    psi(6,a)=-0.003155; psi(6,b)=-0.005873; psi(6,c)=-0.007567; psi(6,d)=-0.007316
    psi(7,a)=-0.004328; psi(7,b)=-0.008220; psi(7,c)=-0.010950; psi(7,d)=-0.010896
    psi(8,a)=-0.005178; psi(8,b)=-0.009830; psi(8,c)=-0.013381; psi(8,d)=-0.013882
    psi(9,a)=-0.005255; psi(9,b)=-0.009933; psi(9,c)=-0.013501; psi(9,d)=-0.015022

```

```

psi(10,a)=-0.005282;psi(10,b)=-0.00993;psi(10,c)=-0.013600;psi(10,d)=-0.015407
hlol(1) = 0.002 ; hlol(2) = 0.005 ; hlol(3) = 0.01 ; hlol(4) = 0.02
hlol(5) = 0.05 ; hlol(6) = 0.1 ; hlol(7) = 0.2 ; hlol(8) = 0.5
hlol(9) = 1.0 ; hlol(10) = 2.0
HHB(1) = 0.25 ; HHB(2) = 0.50 ; HHB(3) = 0.75 ; HHB(4) = 1.0
sfe(1,a)=0.424; sfe(1,b)=0.308; sfe(1,c)=0.249; sfe(1,d)=0.213
sfe(2,a)=0.605; sfe(2,b)=0.446; sfe(2,c)=0.344; sfe(2,d)=0.263
sfe(3,a)=0.755; sfe(3,b)=0.580; sfe(3,c)=0.455; sfe(3,d)=0.342
sfe(4,a)=0.880; sfe(4,b)=0.722; sfe(4,c)=0.577; sfe(4,d)=0.467
sfe(5,a)=0.966; sfe(5,b)=0.873; sfe(5,c)=0.753; sfe(5,d)=0.527
sfe(6,a)=0.988; sfe(6,b)=0.939; sfe(6,c)=0.830; sfe(6,d)=0.618
sfe(7,a)=0.995; sfe(7,b)=0.966; sfe(7,c)=0.887; sfe(7,d)=0.686
sfe(8,a)=0.998; sfe(8,b)=0.979; sfe(8,c)=0.928; sfe(8,d)=0.750
sfe(9,a)=0.998; sfe(9,b)=0.979; sfe(9,c)=0.932; sfe(9,d)=0.811
sfe(10,a)=0.998;sfe(10,b)=0.979;sfe(10,c)=0.933;sfe(10,d)=0.836
eflux1(1,a)=0.417; eflux1(1,b)=0.303; eflux1(1,c)=0.247; eflux1(1,d)=0.215
eflux1(2,a)=0.591; eflux1(2,b)=0.434; eflux1(2,c)=0.335; eflux1(2,d)=0.260
eflux1(3,a)=0.730; eflux1(3,b)=0.558; eflux1(3,c)=0.438; eflux1(3,d)=0.334
eflux1(4,a)=0.835; eflux1(4,b)=0.682; eflux1(4,c)=0.545; eflux1(4,d)=0.447
eflux1(5,a)=0.866; eflux1(5,b)=0.783; eflux1(5,c)=0.663; eflux1(5,d)=0.488
eflux1(6,a)=0.803; eflux1(6,b)=0.775; eflux1(6,c)=0.704; eflux1(6,d)=0.545
eflux1(7,a)=0.673; eflux1(7,b)=0.682; eflux1(7,c)=0.665; eflux1(7,d)=0.548
eflux1(8,a)=0.521; eflux1(8,b)=0.542; eflux1(8,c)=0.557; eflux1(8,d)=0.491
eflux1(9,a)=0.509; eflux1(9,b)=0.528; eflux1(9,c)=0.542; eflux1(9,d)=0.513
eflux1(10,a)=0.509;eflux1(10,b)=0.528;eflux1(10,c)=0.542;eflux1(10,d)=0.531
mflux1(1,a)=0.606; mflux1(1,b)=0.428; mflux1(1,c)=0.344; mflux1(1,d)=0.297
mflux1(2,a)=0.859; mflux1(2,b)=0.613; mflux1(2,c)=0.461; mflux1(2,d)=0.354
mflux1(3,a)=1.060; mflux1(3,b)=0.789; mflux1(3,c)=0.604; mflux1(3,d)=0.454
mflux1(4,a)=1.211; mflux1(4,b)=0.962; mflux1(4,c)=0.749; mflux1(4,d)=0.603
mflux1(5,a)=1.238; mflux1(5,b)=1.095; mflux1(5,c)=0.903; mflux1(5,d)=0.654
mflux1(6,a)=1.106; mflux1(6,b)=1.055; mflux1(6,c)=0.941; mflux1(6,d)=0.720
mflux1(7,a)=0.844; mflux1(7,b)=0.858; mflux1(7,c)=0.838; mflux1(7,d)=0.694
mflux1(8,a)=0.537; mflux1(8,b)=0.572; mflux1(8,c)=0.604; mflux1(8,d)=0.548
mflux1(9,a)=0.513; mflux1(9,b)=0.544; mflux1(9,c)=0.572; mflux1(9,d)=0.558
mflux1(10,a)=0.513;mflux1(10,b)=0.543;mflux1(10,c)=0.574;mflux1(10,d)=0.580
lol1(1,a)=0.119648; lol1(1,b)=0.128262; lol1(1,c)=0.137070; lol1(1,d)=0.146465
lol1(2,a)=0.186504; lol1(2,b)=0.199023; lol1(2,c)=0.210547; lol1(2,d)=0.222852
lol1(3,a)=0.259570; lol1(3,b)=0.276172; lol1(3,c)=0.291992; lol1(3,d)=0.308203
lol1(4,a)=0.358594; lol1(4,b)=0.379687; lol1(4,c)=0.401172; lol1(4,d)=0.422461
lol1(5,a)=0.541016; lol1(5,b)=0.566016; lol1(5,c)=0.597070; lol1(5,d)=0.627344
lol1(6,a)=0.718164; lol1(6,b)=0.743750; lol1(6,c)=0.783203; lol1(6,d)=0.824414
lol1(7,a)=0.899219; lol1(7,b)=0.931055; lol1(7,c)=0.981055; lol1(7,d)=1.035156
lol1(8,a)=1.013086; lol1(8,b)=1.059180; lol1(8,c)=1.125195; lol1(8,d)=1.193750
lol1(9,a)=1.017578; lol1(9,b)=1.065234; lol1(9,c)=1.132813; lol1(9,d)=1.210937
lol1(10,a)=1.017773;lol1(10,b)=1.065234;lol1(10,c)=1.134375;lol1(10,d)=1.222070
RETURN
END

```

```

! ****
! ***** Subroutine to interpolate the stream function shoaling table *****
SUBROUTINE sfheight(hLo,HoLo,Lo,height)
DOUBLE PRECISION hLo,HoLo,Lo,height
IF (hLo.GT.0.4) THEN
    height = HoLo * Lo
    RETURN
ENDIF
IF (hLo.GT.0.15) THEN
    IF (HoLo.GT.0.04) THEN
        Ht1Lo = 0.0170230*EXP(0.646433*hLo) + 0.0179098
        Ht2Lo = 0.03383149*EXP(0.713807*hLo) + 0.03534899
        Height = Lo * ((Ht2Lo-Ht1Lo)/0.04*(HoLo - 0.04) + Ht1Lo)
        RETURN
    ELSEIF (HoLo.GT.0.02) THEN
        Ht1Lo = 0.00818234*EXP(0.9492775*hLo) + 0.00829363
        Ht2Lo = 0.0170230*EXP(0.646433*hLo) + 0.0179098
        Height = Lo * ((Ht2Lo-Ht1Lo)/0.02*(HoLo - 0.02) + Ht1Lo)
        RETURN
    ELSEIF (HoLo.GT.0.01) THEN
        Ht1Lo = 0.0041714*EXP(0.87871707*hLo) + 0.004248363
        Ht2Lo = 0.00818234*EXP(0.9492775*hLo) + 0.00829363
    ENDIF
END

```

```

        Height = Lo * ((Ht2Lo-Ht1Lo)/0.01*(HoLo - 0.01) + Ht1Lo)
        RETURN
    ELSE
        Ht1Lo = 0.000815246*EXP(.95880886*hLo) + 0.00082576
        Ht2Lo = 0.0041714*EXP(0.87871707*hLo) + 0.004248363
        Height = Lo * ((Ht2Lo-Ht1Lo)/0.008*(HoLo - 0.008) + Ht1Lo)
        RETURN
    ENDIF
    RETURN
ENDIF
IF (HoLo.GT.0.04) THEN
    Ht1Lo = 0.2327783*EXP(-56.487485*hLo) + 0.03770144
    Ht2Lo = 0.40633356*EXP(-44.893344*hLo) + 0.07251580
    Height = Lo * ((Ht2Lo-Ht1Lo)/0.04*(HoLo - 0.04) + Ht1Lo)
    RETURN
ELSEIF (HoLo.GT.0.02) THEN
    Ht1Lo = 0.1486142*EXP(-90.7945497*hLo) + 0.0195859
    Ht2Lo = 0.2327783*EXP(-56.487485*hLo) + 0.03770144
    Height = Lo * ((Ht2Lo-Ht1Lo)/0.02*(HoLo - 0.02) + Ht1Lo)
    RETURN
ELSEIF (HoLo.GT.0.01) THEN
    Ht1Lo = 0.0641560*EXP(-116.9087785*hLo) + 0.009943302
    Ht2Lo = 0.1486142*EXP(-90.7945497*hLo) + 0.0195859
    Height = Lo * ((Ht2Lo-Ht1Lo)/0.01*(HoLo - 0.01) + Ht1Lo)
    RETURN
ELSE
    Ht1Lo = 0.299490*EXP(-493.7068724*hLo) + 0.002213177
    Ht2Lo = 0.0641560*EXP(-116.9087785*hLo) + 0.009943302
    Height = Lo * ((Ht2Lo-Ht1Lo)*(HoLo - 0.002)/0.008 + Ht1Lo)
    RETURN
ENDIF
RETURN
END

! ****
! SUBROUTINE to establish the profile at evenly spaced increments, determine
! Still Water Depth, d(i), and bottom slope m(i) at each x location.
! Done numerically to accomodate arbitrary beach profiles....
SUBROUTINE PROFSET(iprof,Ni,xp,zp,d,m,dzi)
DOUBLE PRECISION, DIMENSION(Ni) :: d,m,xa
DOUBLE PRECISION, DIMENSION(500) :: xp,zp
d(1) = ABS(zp(1))
DO i = 1,Ni
    xa(i) = xp(1) + dzi*(i-1)
END DO
ic = 2
DO ii = 1,iprof-1
    SLOPE = (zp(ii+1)-zp(ii))/(xp(ii+1)-xp(ii))
    BINT = zp(ii) - SLOPE * xp(ii)
    DO j = 1,1500
        IF (xa(ic).GT.xp(ii+1)) GOTO 9
        d(ic) = ABS(SLOPE * xa(ic) + BINT)
        ic = ic + 1
        IF (ic.GT.Ni) GOTO 12
    END DO
9 END DO
12 d(Ni) = ABS(zp(iprof))
DO ii = 2,Ni-1
    m(ii) = (d(ii+1)-d(ii-1))/(2.*dzi)
END DO
m(1) = m(2)
m(Ni) = m(Ni-1)
RETURN
END

! ****
! Subroutine to set the spatial derivatives involved in the coordinate
! transformation. 1-26-00 AEB
SUBROUTINE STB1(NNi,NNj,mm,h,dxx,zz,etx,etxz,etxx,etxxz,etxxx,etxxxxz, &
etxxxx,setup)

```

```

DOUBLE PRECISION, DIMENSION(NNj,NNi) :: etx,etxz,etxx,etxxz,etxxx,etxxxxz
DOUBLE PRECISION, DIMENSION(NNj,NNi) :: etxxxxx,zz
DOUBLE PRECISION, DIMENSION(NNi) :: mm,h,setup
DO i = 3,NNi-2
  DO j = 1,NNj
    zz(j,i) = - h(i)*(j-1)/(NNj-1) + setup(i)
    etx(j,i) = -zz(j,i)/h(i)**2. * mm(i)
    etxz(j,i) = -mm(i)/h(i)**2.
    etxx(j,i) = -zz(j,i)/h(i)**2. * ((h(i-1)-2.*h(i)+h(i+1))/dxx**2. &
      - 2./h(i)*mm(i)**2.)
    etxxz(j,i) = -( ( h(i-1)-2.*h(i)+h(i+1) )/dxx**2. &
      - 2./h(i)*mm(i)**2. )/h(i)**2.
    etxxx(j,i) = -zz(j,i)*( 1./h(i)**2.*(-h(i-2)+2.*h(i-1)-2.*h(i+1)+h(i+2)) &
      / (2.*dxx**3.) - 6./h(i)**3.* (h(i-1)-2.*h(i)+h(i+1))/dxx**2. * mm(i) &
      + 6./h(i)**4.*mm(i)**3. )
    etxxxxz(j,i) = -( 1./h(i)**2.*(-h(i-2)+2.*h(i-1)-2.*h(i+1)+h(i+2)) &
      / (2.*dxx**3.) - 6./h(i)**3.* (h(i-1)-2.*h(i)+h(i+1))/dxx**2. * mm(i) &
      + 6./h(i)**4.*mm(i)**3. )
    etxxxxx(j,i) = -zz(j,i)*( 1./h(i)**2.* (h(i-1)-4.*h(i-1)+6.*h(i)-4.*h(i+1) &
      + h(i+2))/dxx**4. - 8.*mm(i)/h(i)**3.* (-h(i-2)+2.*h(i-1)-2.*h(i+1)+h(i+2)) &
      / (2.*dxx**3.) + 18./h(i)**4*mm(i)**2.* (h(i-1)-2.*h(i)+h(i+1))/dxx**2. &
      - 6./h(i)**3.* ((h(i-1)-2.*h(i)+h(i+1))/dxx**2. )**2. &
      - 24./h(i)**5. * mm(i)**4. )
  END DO
END DO
i = 1
DO j = 1, NNj
  zz(j,i) = - h(i)*(j-1)/(NNj-1) + setup(i)
  etx(j,i) = -zz(j,i)/h(i)**2. * mm(i)
  etxz(j,i) = -mm(i)/h(i)**2.
  etxx(j,i) = -zz(j,i)/h(i)**2. * ((2.*h(i)-5.*h(i+1)+4.*h(i+2)-h(i+3)) &
    /dxx**2. - 2./h(i)*mm(i)**2.)
  etxxz(j,i) = -( (2.*h(i)-5.*h(i+1)+4.*h(i+2)-h(i+3))/dxx**2. &
    - 2./h(i)*mm(i)**2. )/h(i)**2.
  etxxx(j,i) = -zz(j,i)*( 1./h(i)**2.* (-5.*h(i)+18.*h(i+1)-24.*h(i+2) &
    + 14.*h(i+3)-3.*h(i+4))/(2.*dxx**3.) &
    - 6./h(i)**3.* (2.*h(i)-5.*h(i+1)+4.*h(i+2)-h(i+3))/dxx**2. * mm(i) &
    + 6./h(i)**4.*mm(i)**3. )
  etxxxxz(j,i) = -( 1./h(i)**2.* (-5.*h(i)+18.*h(i+1)-24.*h(i+2) &
    + 14.*h(i+3)-3.*h(i+4))/(2.*dxx**3.) &
    - 6./h(i)**3.* (2.*h(i)-5.*h(i+1)+4.*h(i+2)-h(i+3))/dxx**2. * mm(i) &
    + 6./h(i)**4.*mm(i)**3. )
  etxxxxx(j,i) = -zz(j,i)*( 1./h(i)**2.* (3.*h(i)-14.*h(i+1)+26.*h(i+2) &
    - 24.*h(i+3)+11.*h(i+4)-2.*h(i+5))/dxx**4. - 8.*mm(i)/h(i)**3. &
    * (-5.*h(i)+18.*h(i+1)-24.*h(i+2)+14.*h(i+3)-3.*h(i+4))/(2.*dxx**3.) &
    + 18./h(i)**4*mm(i)**2.* (2.*h(i)-5.*h(i+1)+4.*h(i+2)-h(i+3))/dxx**2. &
    - 6./h(i)**3.* ((2.*h(i)-5.*h(i+1)+4.*h(i+2)-h(i+3))/dxx**2. )**2. &
    - 24./h(i)**5. * mm(i)**4. )
END DO
i = 2
DO j = 1,NNj
  zz(j,i) = - h(i)*(j-1)/(NNj-1) + setup(i)
  etx(j,i) = -zz(j,i)/h(i)**2. * mm(i)
  etxz(j,i) = -mm(i)/h(i)**2.
  etxx(j,i) = (etxx(j,i-1)+etxx(j,i+1))/2.
  etxxz(j,i) = (etxxz(j,i-1)+etxxz(j,i+1))/2.
  etxxx(j,i) = (etxxx(j,i-1)+etxxx(j,i+1))/2.
  etxxxxz(j,i) = (etxxxxz(j,i-1)+etxxxxz(j,i+1))/2.
  etxxxxx(j,i) = (etxxxxx(j,i-1)+etxxxxx(j,i+1))/2.
END DO
i = NNi
DO j = 1,NNj
  zz(j,i) = - h(i)*(j-1)/(NNj-1) + setup(i)
  etx(j,i) = -zz(j,i)/h(i)**2. * mm(i)
  etxz(j,i) = -mm(i)/h(i)**2.
  etxx(j,i) = -zz(j,i)/h(i)**2. * ((2.*h(i)-5.*h(i-1)+4.*h(i-2)-h(i-3)) &
    /dxx**2. - 2./h(i)*mm(i)**2.)
  etxxz(j,i) = -( (2.*h(i)-5.*h(i-1)+4.*h(i-2)-h(i-3))/dxx**2. &
    - 2./h(i)*mm(i)**2. )/h(i)**2.
  etxxx(j,i) = -zz(j,i)*( 1./h(i)**2.* (5.*h(i)-18.*h(i-1)+24.*h(i-2) &
    - 24.*h(i)-11.*h(i+1)+2.*h(i+2))/dxx**3. &
    - 6./h(i)**3.* (5.*h(i)-18.*h(i-1)+24.*h(i-2)+14.*h(i-3)-3.*h(i+1))/dxx**2. &
    + 18./h(i)**4*mm(i)**2.* (2.*h(i)-5.*h(i-1)+4.*h(i-2)-h(i-3))/dxx**2. &
    - 6./h(i)**3.* ((2.*h(i)-5.*h(i-1)+4.*h(i-2)-h(i-3))/dxx**2. )**2. &
    - 24./h(i)**5. * mm(i)**4. )
END DO

```

```

-14.*h(i-3)+3.*h(i-4))/(2.*dxx**3.) &
- 6./h(i)**3.* (2.*h(i)-5.*h(i-1)+4.*h(i-2)-h(i-3))/dxx**2. * mm(i) &
+ 6./h(i)**4.*mm(i)**3. )
etxxxz(j,i) = - ( 1./h(i)**2.* (5.*h(i)-18.*h(i-1)+24.*h(i-2) &
-14.*h(i-3)+3.*h(i-4))/(2.*dxx**3.) &
- 6./h(i)**3.* (2.*h(i)-5.*h(i-1)+4.*h(i-2)-h(i-3))/dxx**2. * mm(i) &
+ 6./h(i)**4.*mm(i)**3. )
etxxxx(j,i) = -zz(j,i)*( 1./h(i)**2.* (3.*h(i)-14.*h(i-1)+26.*h(i-2) &
-24.*h(i-3)+11.*h(i-4)-2.*h(i-5))/dxx**4. - 8.*mm(i)/h(i)**3. &
* (5.*h(i)-18.*h(i-1)+24.*h(i-2)-14.*h(i-3)+3.*h(i-4))/(2.*dxx**3.) &
+ 18./h(i)**4*mm(i)**2.* (2.*h(i)-5.*h(i-1)+4.*h(i-2)-h(i-3))/dxx**2. &
- 6./h(i)**3.* ((2.*h(i)-5.*h(i-1)+4.*h(i-2)-h(i-3))/dxx**2.)**2. &
- 24./h(i)**5. * mm(i)**4. )
END DO
i = NNI-1
DO j = 1,NNj
  zz(j,i) = - h(i)*(j-1)/(NNj-1) + setup(i)
  etx(j,i) = -zz(j,i)/h(i)**2. * mm(i)
  etxz(j,i) = -mm(i)/h(i)**2.
  etxx(j,i) = (etxx(j,i-1)+etxx(j,i+1))/2.
  etxxz(j,i) = (etxxz(j,i-1)+etxxz(j,i+1))/2.
  etxxx(j,i) = (etxxx(j,i-1)+etxxx(j,i+1))/2.
  etxxxx(j,i) = (etxxxx(j,i-1)+etxxxx(j,i+1))/2.
END DO
RETURN
END

! ****
! SUBROUTINE to set up the eddy viscosity variation across the x-z domain
! **** derivative terms must be written in terms of the xi-eta coords!!!
! **** for the variable case, the vertical profile is similar across the
! **** model
SUBROUTINE eddyvis(nn,mm,e1,ex1,ez1,exx1,exz1,ezz1,wv,ibr,zix1,zixx1, &
ziz1,zizz1,zixz1,etax1,etaxx1,etaz1,etazz1,etaxz1,dzi1,detal,ieddy1)
DOUBLE PRECISION, DIMENSION(nn) :: wv,etaz1,etazz1
DOUBLE PRECISION, DIMENSION(mm,nn) :: e1,ex1,ez1,exx1,exz1,ezz1
DOUBLE PRECISION, DIMENSION(mm,nn) :: etax1,etaxx1,etaxz1
IF (ieddy1.EQ.0) THEN
  e1 = e1(1,1)
  ex1 = 0.0
  ez1 = 0.0
  exx1 = 0.0
  ezz1 = 0.0
  exz1 = 0.0
ELSEIF (ieddy1.EQ.2) THEN
  DO i = 1,nn
    e1(:,i) = e1(1,i)
  END DO
ELSE
  DO i = 1,ibr
    DO j = 1,mm
      e1(mm-(j-1),i) = e1(1,i)*(0.01 + 2.5479*(j-1)/(mm-1) &
      + 5.23881*(1.*(j-1)/(mm-1))**2. - 6.793936*(1.*(j-1)/(mm-1))**3.)
    END DO
  END DO
  DO i = ibr+1,nn
    DO j = 1,mm
      e1(mm-(j-1),i) = e1(1,i)*(0.01 + 2.5479*(j-1)/(mm-1) &
      + 5.23881*(1.*(j-1)/(mm-1))**2. - 6.793936*(1.*(j-1)/(mm-1))**3.)
    END DO
  END DO
ENDIF
DO i = 2,nn-1
  DO j = 2,mm-1
    ex1(j,i) = zix1 * ( (-e1(j,i-1)+e1(j,i+1))/(2.*dzi1) ) &
    + etax1(j,i)* ( (-e1(j-1,i)+e1(j+1,i))/(2.*detal) )
    ez1(j,i) = ziz1 * ( (-e1(j,i-1)+e1(j,i+1))/(2.*dzi1) ) &
    + etaz1(i)* ( (-e1(j-1,i)+e1(j+1,i))/(2.*detal) )
    exx1(j,i) = zix1**2. * ( ( e1(j,i-1)-2.*e1(j,i)+e1(j,i+1) )/dzi1**2. ) &
  END DO
END DO

```

```

+ etax1(j,i)**2.*( (e1(j-1,i)-2.*e1(j,i)+e1(j+1,i))/deta1**2.) &
+ 2.*zix1*etax1(j,i)*((e1(j+1,i+1)-e1(j+1,i-1)-e1(j-1,i+1)+e1(j-1,i-1)) &
/(4.*deta1*dzi1)) + zixx1* ( (-e1(j,i-1)+e1(j,i+1))/(2.*dzi1)) &
+ etaxx1(j,i) * ( (-e1(j-1,i)+e1(j+1,i)) /(2.*deta1))
ezz1(j,i) = ziz1**2.* ( (e1(j,i-1)-2.*e1(j,i)+e1(j,i+1))/dzi1**2.) &
+ etaz1(i)**2.*( (e1(j-1,i)-2.*e1(j,i)+e1(j+1,i))/deta1**2.) &
+ 2.*ziz1*etaz1(i)*((e1(j+1,i+1)-e1(j+1,i-1)-e1(j-1,i+1)+e1(j-1,i-1)) &
/(4.*deta1*dzi1)) + zizz1*(( -e1(j,i-1)+e1(j,i+1))/(2.*dzi1)) &
+ etazz1(i)* ( (-e1(j-1,i)+e1(j+1,i)) /(2.*deta1) )
exz1(j,i) = zix1*ziz1*( (e1(j,i-1)-2.*e1(j,i)+e1(j,i+1))/dzi1**2.) &
+ etax1(j,i)*etaz1(i)*((e1(j-1,i)-2.*e1(j,i)+e1(j+1,i))/deta1**2.) &
+ (zix1*etaz1(i)+ziz1*etax1(j,i))*((e1(j+1,i+1)-e1(j+1,i-1)-e1(j-1,i+1) &
+ e1(j-1,i-1))/(4.*deta1*dzi1)) + zixz1*(( -e1(j,i-1)+e1(j,i+1)) &
/(2.*dzi1)) + etaxz1(j,i)*(( -e1(j-1,i)+e1(j+1,i)) /(2.*deta1))

END DO
END DO
ex1(1,:) = ex1(2,:)
ez1(1,:) = ez1(2,:)
exx1(1,:) = exx1(2,:)
ezz1(1,:) = ezz1(2,:)
exz1(1,:) = exz1(2,:)
ex1(mm,:) = ex1(mm-1,:)
ez1(mm,:) = ez1(mm-1,:)
exx1(mm,:) = exx1(mm-1,:)
ezz1(mm,:) = ezz1(mm-1,:)
exz1(mm,:) = exz1(mm-1,:)
RETURN
END

```

## REFERENCES

Abbott, M.B. (1979). *Computational hydraulics: elements of the theory of free surface flows*. Pitman Publishers, Boston, MA.

Börećki, O.S. (1982) Distribution of wave-induced momentum fluxes over depth and application within the surf zone. Ph.D. Dissertation, University of Delaware, Newark, DE.

Brinch-Nielsen, U., and Jonsson, I.G. (1985). The angular momentum equation and its application to water waves; Part 2: Applications. Institute of Hydrodynamics and Hydraulic Engineering, Technical University of Denmark, Lyngby, Denmark, Progress Report No. 62, 47-60.

Carslaw, H.S., and Jaeger, J.C. (1986). *Conduction of heat in solids*, 2<sup>nd</sup> Ed. Oxford University Press, Oxford, UK.

Cokelet, E.D. (1977). Breaking Waves. *Nature*, Vol., 267 (5614), 769-774.

Cox, D.T., Kobayashi, N., and Okayasu, A. (1995). Experimental and numerical modeling of surf zone hydrodynamics. Center for Applied Coastal Research, Research Report No. CACR-95-07, Ocean Engineering Laboratory, University of Delaware, Newark, DE.

Cox, D.T., Kobayashi, N., and Okayasu, A. (1996). Bottom shear stress in the surf zone. *Journal of Geophysical Research*, 101 (C6), 14,337-14,348.

Cox, D.T., and Kobayashi, N. (1997). Kinematic undertow model with logarithmic boundary layer. *Journal of Waterway, Port, Coastal, and Ocean Engineering*, 123(6), 354-360.

Cox, D.T., and Kobayashi, N. (1998). Application of an undertow model to irregular waves on plane and barred beaches. *Journal Coastal Research*, 14(4), 1314-1324.

Crank, J., and Nicolson, P. (1947). A practical method for numerical evaluation of solutions of partial differential equations of the heat conduction type. *Proceedings of the Cambridge Philosophical Society of London*, 43, 50-67.

Dally, W.R. (1980). A numerical model for beach profile evolution. M.S. Thesis, University of Delaware, Newark, DE.

Dally, W.R., and Brown, C.A. (1995). A modeling investigation of the breaking wave roller with application to cross-shore currents. *Journal of Geophysical Research*, 100 (C12), 24,873-24,883.

Dally, W.R., and Dean, R.G. (1984). Suspended sediment transport and beach profile evolution. *Journal of Waterway, Port, Coastal, and Ocean Engineering*, 110(1), 15-33.

Dally, W.R., and Dean, R.G. (1984). Mass flux and undertow in a surf zone, by I.A. Svendsen — discussion (closure by I.A. Svendsen). *Coastal Engineering*, 10, 289-307.

Dally, W.R., Dean, R.G., and Dalrymple, R.A. (1985). Wave height variation across beaches of arbitrary profile. *Journal of Geophysical Research*, 90 (C6), 11,917-11,927.

Dalrymple, R.A., and Dean, R.G. (1975). Waves of maximum height on uniform currents. *Journal of the Waterways, Port, Harbors, and Coastal Engineering Division*, 101(3), 259-268.

Dean, R.G. (1974). Evaluation and development of water wave theories for engineering application, 1 & 2. U.S. Army Corps of Engineers, Coastal Engineering Research Center, Vicksburg, MS, Special Report No. 1.

Dean, R.G. (1995). Cross-shore sediment transport processes. In P.L.F. Liu ed., *Advances in Coastal and Ocean Engineering*, Vol. 1, World Scientific Press, Ltd., Singapore.

Diegaard, R., Bro Mikkelsen, M., and Fredsoe, J. (1991). Measurements of the bed shear stress in a surf zone. Institute of Hydrodynamics and Hydraulic Engineering, Technical University of Denmark, Lyngby, Denmark. Progress Report No. 73, 21-30.

Diegaard, R., Justesen, P., and Fredsoe, J. (1991). Modeling of undertow by a one-equation turbulence model. *Coastal Engineering*, 15, 431-458.

Duncan, J.H. (1981). An experimental investigation of breaking waves produced by a towed hydrofoil. *Proceedings of the Royal Society of London*, London, UK, Series A 377, 331-348.

Dyhr-Nielsen, M., and Sorensen, T. (1970). Some sand transport phenomena on coasts with bars. *Proceedings of the 11<sup>th</sup> International Conference on Coastal Engineering*, Chap. 54, 855-865.

Haines, J.W., and Sallenger, A.H. (1994). Vertical structure of mean cross-shore currents across a barred surf zone. *Journal of Geophysical Research*, 99 (C7), 14,223-14,242.

Hansen, J.B., and Svendsen, I.A. (1984). A theoretical and experimental study of undertow. *Proceedings of the 19<sup>th</sup> International Conference on Coastal Engineering*. Chap. 151, 2246-2262.

Hoffman, K.A. (1989). *Computational fluid dynamics for engineers*. Engineering Education System, Austin TX.

Johnson, D.W. (1919). *Shore processes and shoreline development*. Hafner Publishing Company, New York, NY. (1965 facsimile of original 1919 ed.).

Longuet-Higgins, M.S. (1953). Mass transport in water waves. *Proceedings of the Royal Society of London*, Series A 245, 535-581.

Longuet-Higgins, M.S. (1975). Integral properties of periodic gravity waves of finite amplitude. *Proceedings of the Royal Society of London*, Series A 342, 157-174.

Longuet-Higgins, M.S., and Stewart, R.W. (1962). Radiation stress and mass transport in gravity waves, with application to 'surf beats.' *Journal of Fluid Mechanics*, Vol. 13(4), 481-504.

Longuet-Higgins, M.S. and Stewart, R.W. (1964). Radiation stresses in water waves; a physical discussion, with applications. *Deep-Sea Research*, Vol. 11, 529-562

Nadaoka, K., and Kondoh, T. (1982). Laboratory measurements of velocity field structure in the surf zone by LDV. *Coastal Engineering in Japan*, Vol. XXV, 125-145.

Okayasu, A., and Katayama, H. (1992). Distribution of undertow and long-wave component velocity due to random waves. *Proceedings of the 17<sup>th</sup> International Conference on Coastal Engineering*, 883-893.

Press, W.H., Flannery, B.P., Teukolsky, S.A., Vetterling, W.T. (1986). *Numerical recipes: the art of scientific computing*. Cambridge University Press, Cambridge, UK.

Putrevu, U., and Svendsen, I.A. (1993). Vertical structure of the undertow outside the surf zone. *Journal of Geophysical Research*, 98 (C12), 22,707-22,716.

Rivero, F.J., and Arcilla, A.S., (1995). On the vertical distribution of  $\langle \tilde{u} \tilde{w} \rangle$ . *Coastal Engineering*, 25, 137-152.

Roelvink, J.A., and Reniers, A.J.H.M. (1995). LIP 11D Delta Flume experiments - A data set for profile model validation, Delft Hydraulics Laboratory, Delft, The Netherlands, Report # H 2130.

Russell, R.C.H., and Osorio, J.D.C. (1957). An experimental investigation of drift profiles in a closed channel. *Proceedings of the 6<sup>th</sup> International Conference on Coastal Engineering*, Chap. 10, 171-193.

Schlichting, H. (1968). *Boundary-layer theory*. McGraw-Hill Book Company, New York, NY.

Smith, G.D., (1985). *Numerical solution of partial differential equations: finite difference methods*. Oxford University Press, Oxford, UK.

Smith, J.M., Svendsen, I.A., and Putrevu, U. (1992). Velocity and pressure field of spilling breakers. *Proceedings of the 24<sup>th</sup> International Conference on Coastal Engineering*, 547-566.

Sobey, R.J, Goodwin, P., Thieke, R.J., and Westberg, R.J. (1987). Application of Stokes, Cnoidal, and Fourier Wave Theories. *Journal of Waterway, Port, Coastal, and Ocean Engineering*, 113(6), 565-574.

Stive, M.J.F. (1980). Velocity and pressure field of spilling breakers. *Proceedings of the 17<sup>th</sup> International Conference on Coastal Engineering*, 547-566.

Stive, M.J.F.(1984). Energy dissipation in waves breaking on gentle slopes. *Coastal Engineering*, 8, 99-127.

Stive, M.J.F., and Wind, H.G. (1986). Cross-shore mean flow in the surf zone. *Coastal Engineering*, 10, 325-340.

Svendsen, I.A. (1984a). Wave heights and set-up in a surf zone. *Coastal Engineering*, 8, 303-329.

Svendsen, I.A. (1984b). Mass flux and undertow in a surf zone. *Coastal Engineering*, 8, 347-365.

Svendsen, I.A., Schaffer, H.A., Hansen, J.B. (1987). The Interaction between the undertow and the boundary layer flow on a beach. *Journal of Geophysical Research*, 92 (C11), 11,845-11,856.

Ting, F.C.K., and Kirby, J.T. (1994). Observations of undertow and turbulence in a laboratory surf zone. *Coastal Engineering*, 24, 51-80.

## BIOGRAPHICAL SKETCH

Albert E. Browder was born in 1969 and raised in Colonial Heights, Virginia, where he developed an interest in engineering at an early age, primarily from the intensive study of toys that he had recently broken. Family vacations to Neptune Beach, Florida, throughout his childhood introduced him to coastal engineering and beach restoration. Further motivated in math and physics in high school, Browder pursued a bachelor's degree in mechanical engineering from Clemson University, where his life-long love of the Tigers was firmly established. As a senior M.E., Browder was introduced to the technical side of coastal engineering, and after graduation in 1992 pursued a Master's degree from the University of Florida in Coastal and Oceanographic Engineering. Just before graduation in 1994, the author was lucky enough to run into his future wife (at a bar no less). After UF Browder took a position as a coastal engineer at Olsen Associates, Inc., in Jacksonville, and pursued the practical application of coastal engineering work. The desire to improve his technical skills and achieve the final educational goal of a Ph.D. sent the author back to UF in 1997 to pursue doctoral studies. Following graduation, the author will continue pursuing his interests in coastal engineering.

I certify that I have read this study and that in my opinion it conforms to acceptable standards of scholarly presentation and is fully adequate, in scope and quality, as a dissertation for the degree of Doctor of Philosophy.

Robert G. Dean  
Robert G. Dean, Chairman  
Graduate Research Professor of Civil  
& Coastal Engineering

I certify that I have read this study and that in my opinion it conforms to acceptable standards of scholarly presentation and is fully adequate, in scope and quality, as a dissertation for the degree of Doctor of Philosophy.

Daniel M. Hanes  
Daniel M. Hanes  
Professor of Civil & Coastal  
Engineering

I certify that I have read this study and that in my opinion it conforms to acceptable standards of scholarly presentation and is fully adequate, in scope and quality, as a dissertation for the degree of Doctor of Philosophy.

Ashish J. Mehta  
Ashish J. Mehta  
Professor of Civil & Coastal  
Engineering

I certify that I have read this study and that in my opinion it conforms to acceptable standards of scholarly presentation and is fully adequate, in scope and quality, as a dissertation for the degree of Doctor of Philosophy.

Robert J. Thieke  
Robert J. Thieke  
Assistant Professor of Civil & Coastal  
Engineering

I certify that I have read this study and that in my opinion it conforms to acceptable standards of scholarly presentation and is fully adequate, in scope and quality, as a dissertation for the degree of Doctor of Philosophy.

Ulrich H. Kurzweg

Ulrich H. Kurzweg

Professor of Aerospace Engineering,  
Mechanics, & Engineering  
Science

This dissertation was submitted to the Graduate Faculty of the College of Engineering and to the Graduate School and was accepted as partial fulfillment of the requirements for the degree of Doctor of Philosophy.

August 2000



M.J. Ohanian  
Dean, College of Engineering

---

Winfred M. Phillips  
Dean, Graduate School

937 F8 T 5951C  
10/16/00 34760 SCL INFORMATION CONFINEMENT